Science | Science Advances | Science Immunology | Science Signaling | Science Translational Medicine

[SPECIAL EDITION]

CANCER

AAAS

aaas.org/science-journals

Science | AAAS

Submit Your Research for Publication in the *Science* Family of Journals

The *Science* family of journals are among the most highly-regarded journals in the world for quality and selectivity. Our peer-reviewed journals are committed to publishing cutting-edge research, incisive scientific commentary, and insights on what's important to the scientific world at the highest standards.

Submit your research today!
Learn more at www.sciencemag.org/journals

Science AAAS
Science Advances AAAS
Science Immunology AAAS
Science Robotics AAAS
Science Signaling AAAS
Science Translational Medicine AAAS

Enzo

Step Up Your Game

CYTO-ID® Autophagy 2.0 Kit

Visit Us at AACR, Booth #1048

Why Transfect…When You Can Simply Detect?

Rapidly Quantify Autophagy Without Transfection

CYTO-ID Autophagy Detection Kits are the simplest, most specific fluorescent assays for quantifying autophagy in live cells. The CYTO-ID Kits include a unique cell-permeable dye that selectively stains pre-autophagosomes, autophagosomes, and autolysosomes, with minimal staining of lysosomes.

No Transfection Needed – Our cell-permeable dye detects autophagosomes and autolysosomes in 100% of cells without transfection or selection

Rapid Staining – Eliminates need for time and effort-consuming transfection efficiency validation

Study Intact Pathways – Monitor autophagy in homogeneous cell populations without overexpressing LC3

Low Background – Minimize non-specific staining seen with MDC and other dye-based methods

Fully Quantitative – Quantify changes in autophagy by flow cytometry and microscopic imaging platforms

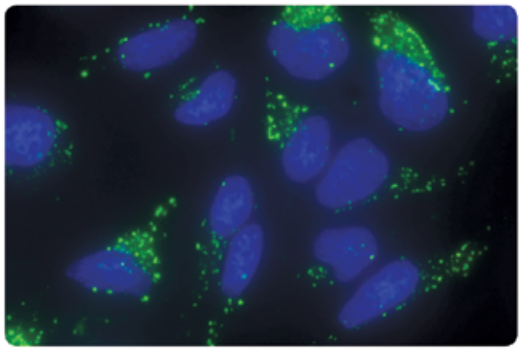

Autophagic vesicles stained with CYTO-ID Autophagy Dye in HeLa cells induced by starvation.

Microscopy | Flow Cytometry | Microplate Reader

scientists *enabling* scientists™

www.enzolifesciences.com/autophagy

© 2018 Enzo Life Sciences.
For Research Use Only.

NEW ENGLAND BioLabs® Inc.

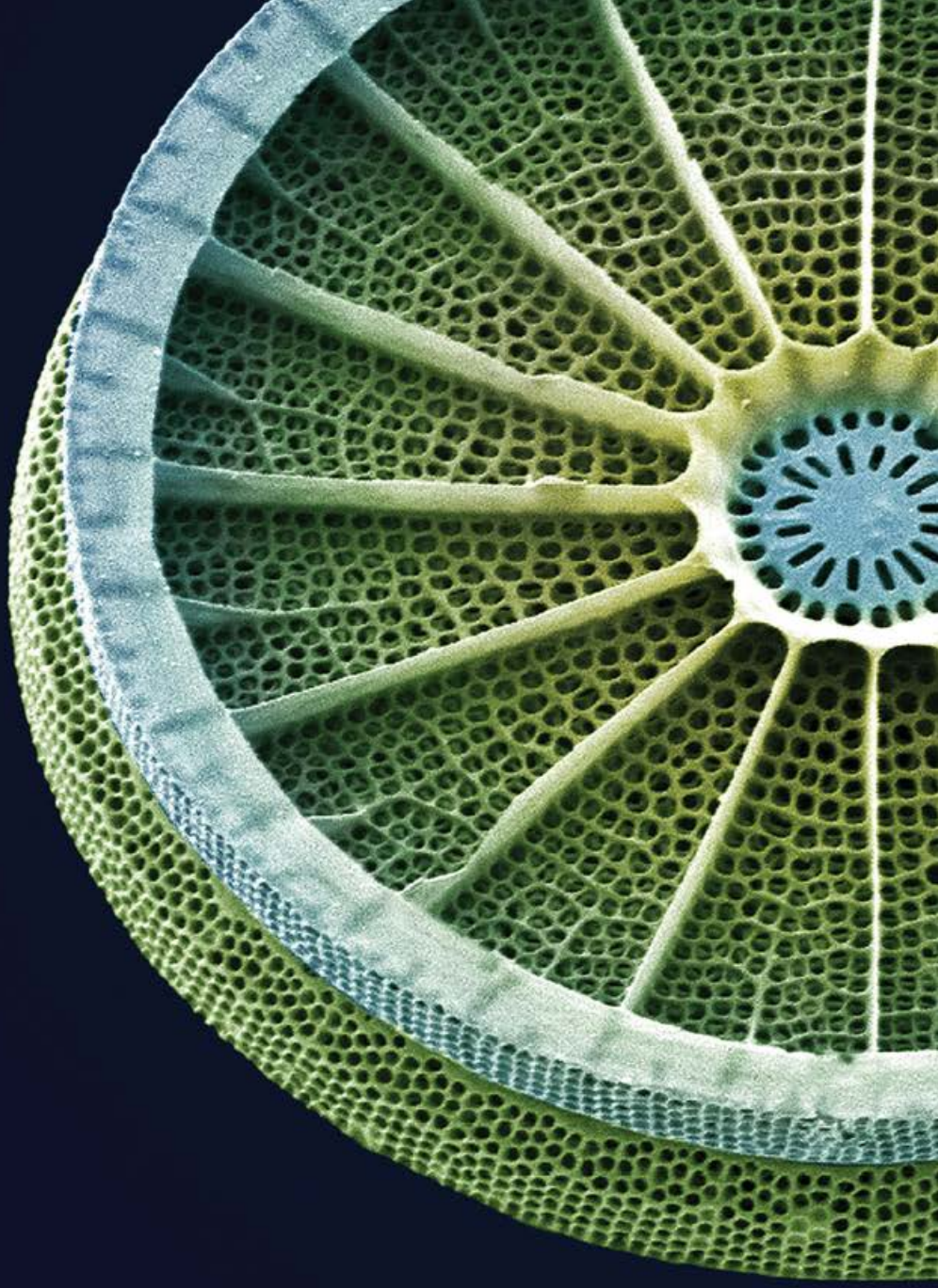

Target with precision.

Introducing the NEBNext Direct™ Cancer HotSpot Panel

Using a unique approach, the NEBNext Direct Cancer HotSpot Panel enriches for 190 common cancer targets from 50 genes prior to next generation sequencing. Combining a novel method for hybridization-based target enrichment with library preparation, the NEBNext Direct technology reduces processing time and minimizes sample loss. Ideal for automation, NEBNext Direct enables highly-specific deep sequencing of genomic regions of interest for the discovery and identification of low frequency variants from challenging sample types.

Visit **NEBNextDirect.com** to learn more and to inquire about sampling this product.

TARGETS INCLUDE REGIONS FROM THE FOLLOWING CANCER-RELATED GENES, INCLUDING >18,000 COSMIC FEATURES:

ABL1	EGFR	GNAQ	KRAS	PTPN11
AKT1	ERBB2	GNAS	MET	RB1
ALK	ERBB4	HNF1A	MLH1	RET
APC	EZH2	HRAS	MPL	SMAD4
ATM	FBXW7	IDH1	NOTCH1	SMARCB1
BRAF	FGFR1	IDH2	NPM1	SMO
CDH1	FGFR2	JAK2	NRAS	SRC
CDKN2A	FGFR3	JAK3	PDGFRA	STK11
CSF1R	FLT3	KDR	PIK3CA	TP53
CTNNB1	GNA11	KIT	PTEN	VHL

For research use only; not intended for diagnostic use.

NEW ENGLAND BIOLABS® and NEB® are registered trademarks of New England Biolabs, Inc.
NEBNEXT DIRECT™ is a trademark of New England Biolabs, Inc.

SPECIAL EDITION: Cancer

Select research published in *Science*, *Science Advances*, *Science Immunology*, *Science Signaling*, and *Science Translational Medicine*

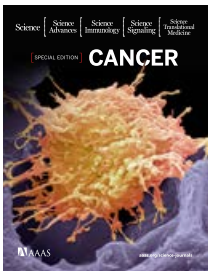

Cancer remains one of the leading causes of death worldwide, but the rapid pace of innovation and discovery in this field is increasingly transforming cancer into a survivable and sometimes even curable condition. In this booklet are samples of empirical research from five featured journals from the *Science* family, showcasing various discoveries in cancer biology and treatment.

Image: Steve Gschmeissner/Science Photo Library

Editor-in-Chief
Jeremy Berg, Ph.D.
Science family of journals
AAAS, Washington, DC

Science | AAAS

Science is a leading outlet for scientific news, commentary, and cutting-edge research. The journal publishes original peer-reviewed research across the sciences, with articles that consistently rank among the most cited in the world.

Deputy Editors
Lisa D. Chong, Ph.D.
Andrew M. Sugden, Ph.D.
Valda J. Vinson, Ph.D.
Jake S. Yeston, Ph.D.

Cancer Editors
Priscilla Kelly, Ph.D.
Paula Kiberstis, Ph.D.

Science Advances | AAAS OPEN ACCESS

Science Advances is the digital, open access expansion of *Science* magazine. The journal publishes significant, innovative original research that advances the frontiers of science across a broad range of disciplines, from bioscience and medicine to neuroscience, physics, ecology, and material sciences.

Managing Editor
Philippa Benson, Ph.D.

Editorial Team
Lynden Archer, Ph.D.
Aaron Clauset, Ph.D.
Sarah M. Fortune, M.D.
Kip V. Hodges, Ph.D.
Jeremy Jackson, Ph.D.
Zakya H. Kafafi, Ph.D.
Kevin S. LaBar, Ph.D.
Shahid Naeem, Ph.D.
Ali Shilatifard, Ph.D.
Philip Yeagle, Ph.D.
Warren Warren, Ph.D.

Science Immunology | AAAS

Science Immunology publishes original, peer-reviewed, science-based research articles that report critical advances in all areas of immunological research, including important new tools and techniques.

Chief Scientific Advisors
Abul K. Abbas, M.D.
University of California, San Francisco
Federica Sallusto, Ph.D.
Università della Svizzera Italiana

Editor
Ifor Williams, M.D., Ph.D.

Editorial Team
Anand Balasubramani, Ph.D.

Science Signaling | AAAS

Science Signaling publishes peer-reviewed, original research investigating cell signaling that underlies physiology and disease, on the molecular, cellular, intercellular and organismal levels.

Chief Scientific Editor
Michael B. Yaffe, M.D., Ph.D.
Massachusetts Institute of Technology

Editor
John F. Foley, Ph.D.

Editorial Team
Leslie K. Ferrarelli, Ph.D.
Annalisa M. VanHook, Ph.D.
Erin R. Williams, Ph.D.
Wei Wong, Ph.D.

Science Translational Medicine | AAAS

Science Translational Medicine is an interdisciplinary journal that publishes translational research with impact for human health that fills the knowledge gaps between preclinical studies and clinical applications.

Chief Scientific Advisors
Elazer R. Edelman, M.D., Ph.D.
Massachusetts Institute of Technology
Garret FitzGerald, M.D.
University of Pennsylvania

Editor
Orla M. Smith, Ph.D.

Editorial Team
Catherine A. Charneski, Ph.D.
Caitlin A. Czajka, Ph.D.
Mattia Maroso, Ph.D.
Yevgeniya Nusinovich, M.D., Ph.D.
Lindsey Pujanandez, Ph.D.

Learn more and submit your research today: aaas.org/science-journals

IN THIS BOOKLET

Science

4 REPORT
Detection and localization of surgically resectable cancers with a multi-analyte blood test
Joshua D. Cohen *et al.* (Nickolas Papadopoulos)

12 RESEARCH | REPORT
Analysis of *Fusobacterium* persistence and antibiotic response in colorectal cancer
Susan Bullman *et al.* (Mathew Meyerson)

Science Advances

18 REVIEW
Fundamentals of cancer metabolism
Ralph J. DeBerardinis and Navdeep S. Chandel

36 RESEARCH ARTICLE
The DNA cytosine deaminase APOBEC3B promotes tamoxifen resistance in ER-positive breast cancer
Emily K. Law *et al.* (Reuben S. Harris)

Science Immunology

45 RESEARCH ARTICLE
A melanin-mediated cancer immunotherapy patch
Yanqui Ye *et al.* (Zhen Gu)

57 RESEARCH ARTICLE
Platelets subvert T cell immunity against cancer via GARP-TGFβ axis
Saleh Rachidi *et al.* (Zihai Li)

Science Signaling

69 RESEARCH ARTICLE
Blockade of TNFR2 signaling enhances the immunotherapeutic effect of CpG ODN in a mouse model of colon cancer
Yingjie Nie *et al.* (Joost J. Oppenheim, Xin Chen)

78 RESEARCH ARTICLE
Androgen receptor inhibitor–induced "BRCAness" and PARP inhibition are synthetically lethal for castration-resistant prostate cancer
Likun Li Park *et al.* (Timothy C. Thompson)

Science Translational Medicine

89 RESEARCH ARTICLE
Identifying DNA methylation biomarkers for non-endoscopic detection of Barrett's esophagus
Helen R. Moinova *et al.* (Sanford D. Markowitz)

100 RESEARCH ARTICLE
A precision therapy against cancers driven by *KIT/PDGFRA* mutations
Erica K. Evans *et al.* (Christoph Lengauer)

Publisher: **Bill Moran**
AD/Business Development: **Justin Sawyers**
Marketing Manager: **Shawana Arnold**
Layout/Design: **Kim Huynh**

© 2018 by The American Association for the Advancement of Science. All Rights Reserved.

Learn more and submit your research today: aaas.org/science-journals

FORCEFORSCIENCE.ORG

STAND TOGETHER
Be a Force for Science

GET THE FACTS

Understand the science behind the issues that matter.

FOLLOW AAAS ADVOCACY

Champion public discussion and evidence-based policy.

TAKE ACTION

Learn ways you can become an advocate and stand up for science.

AMERICAN ASSOCIATION FOR THE ADVANCEMENT OF SCIENCE

AAAS

Detection and localization of surgically resectable cancers with a multi-analyte blood test

Joshua D. Cohen,[1,2,3,4,5] Lu Li,[6] Yuxuan Wang,[1,2,3,4] Christopher Thoburn,[3] Bahman Afsari,[7] Ludmila Danilova,[7] Christopher Douville,[1,2,3,4] Ammar A. Javed,[8] Fay Wong,[1,2,3,4] Austin Mattox,[1,2,3,4] Ralph. H. Hruban,[3,4,9] Christopher L. Wolfgang,[8] Michael G. Goggins,[3,4,9,10,11] Marco Dal Molin,[4] Tian-Li Wang,[3,9] Richard Roden,[3,9] Alison P. Klein,[3,4,12] Janine Ptak,[1,2,3,4] Lisa Dobbyn,[1,2,3,4] Joy Schaefer,[1,2,3,4] Natalie Silliman,[1,2,3,4] Maria Popoli,[1,2,3,4] Joshua T. Vogelstein,[13] James D. Browne,[14] Robert E. Schoen,[15,16] Randall E. Brand,[15] Jeanne Tie,[17,18,19,20] Peter Gibbs,[17,18,19,20] Hui-Li Wong,[17] Aaron S. Mansfield,[21] Jin Jen,[22] Samir M. Hanash,[23] Massimo Falconi,[24] Peter J. Allen,[25] Shibin Zhou,[1,3,4] Chetan Bettegowda,[1,2,3,4] Luis Diaz,[1,3,4] Cristian Tomasetti,[3,6,7*] Kenneth W. Kinzler,[1,3,4*] Bert Vogelstein,[1,2,3,4*] Anne Marie Lennon,[3,4,8,10,11*] Nickolas Papadopoulos[1,3,4*]

[1]Ludwig Center for Cancer Genetics and Therapeutics, Johns Hopkins University School of Medicine, Baltimore, MD 21205, USA. [2]Howard Hughes Medical Institute, Johns Hopkins University School of Medicine, Baltimore, MD 21205, USA. [3]Sidney Kimmel Cancer Center, Johns Hopkins University School of Medicine, Baltimore, MD 21205, USA. [4]Sol Goldman Pancreatic Cancer Research Center, Johns Hopkins University School of Medicine, Baltimore, MD 21205, USA. [5]Department of Biomedical Engineering, Johns Hopkins University School of Medicine, Baltimore, MD 21205, USA. [6]Department of Biostatistics, Johns Hopkins University Bloomberg School of Public Health, Baltimore, MD 21205, USA. [7]Division of Biostatistics and Bioinformatics, Department of Oncology, Johns Hopkins Medical Institutions, Baltimore, MD 21287, USA. [8]Department of Surgery, Johns Hopkins Medical Institutions, Baltimore, MD 21287, USA. [9]Department of Pathology, Johns Hopkins Medical Institutions, Baltimore, MD 21287, USA. [10]Department of Medicine, Johns Hopkins Medical Institutions, Baltimore, MD 21287, USA. [11]Department of Oncology, Johns Hopkins Medical Institutions, Baltimore, MD 21287, USA. [12]Department of Epidemiology, Johns Hopkins University Bloomberg School of Public Health, Baltimore, MD 21205, USA. [13]Institute for Computational Medicine, Johns Hopkins University School of Medicine, Baltimore, MD 21205, USA. [14]Department of Computer Science, Johns Hopkins University Whiting School of Engineering, Baltimore, MD 21218 USA. [15]Department of Medicine, University of Pittsburgh, Pittsburgh, PA 15260 USA. [16]Department of Epidemiology, University of Pittsburgh, Pittsburgh, PA 15260 USA. [17]Division of Systems Biology and Personalized Medicine, Walter and Eliza Hall Institute of Medical Research, Parkville, VIC 3021, Australia. [18]Faculty of Medicine, Dentistry and Health Sciences, University of Melbourne, Melbourne, VIC 3010, Australia. [19]Department of Medical Oncology, Western Health, Melbourne, VIC 3021, Australia. [20]Department of Medical Oncology, Peter MacCallum Cancer Center, Melbourne, VIC 3000, Australia. [21]Division of Medical Oncology, Department of Oncology, Mayo Clinic, Rochester, MN 55902 USA. [22]Division of Experimental Pathology, Department of Laboratory Medicine and Pathology, Mayo Clinic, Rochester, MN 55902 USA. [23]Sheikh Ahmed Center for Pancreatic Cancer Research, University of Texas MD Anderson Cancer Center, Houston, TX 77030 USA. [24]Division of Pancreatic Surgery, Department of Surgery, San Raffaele Scientific Institute Research Hospital, 20132 Milan, Italy. [25]Department of Surgery, Memorial Sloan-Kettering Cancer Center, New York, NY 10065 USA.

***Corresponding author. Email: ctomasetti@jhu.edu (C.T.); amlennon@jhmi.edu (A.M.L.); kinzlke@jhmi.edu (K.W.K); bertvog@gmail.com (B.V.); npapado1@jhmi.edu (N.P.)**

Earlier detection is key to reducing cancer deaths. Here we describe a blood test that can detect eight common cancer types through assessment of the levels of circulating proteins and mutations in cell-free DNA. We applied this test, called CancerSEEK, to 1,005 patients with non-metastatic, clinically detected cancers of the ovary, liver, stomach, pancreas, esophagus, colorectum, lung, or breast. CancerSEEK tests were positive in a median of 70% of the eight cancer types. The sensitivities ranged from 69% to 98% for the detection of five cancer types (ovary, liver, stomach, pancreas, and esophagus) for which there are no screening tests available for average-risk individuals. The specificity of CancerSEEK was > 99%: only 7 of 812 healthy controls scored positive. In addition, CancerSEEK localized the cancer to a small number of anatomic sites in a median of 83% of the patients.

The majority of localized cancers can be cured by surgery alone, without any systemic therapy (*1*). Once distant metastasis has occurred, however, surgical excision is rarely curative. One major goal in cancer research is therefore the detection of cancers before they metastasize to distant sites. For many adult cancers, it takes 20 to 30 years for incipient neoplastic lesions to progress to late-stage disease (*2*–*4*). Only in the last few years of this long process do neoplastic cells appear to successfully seed and give rise to metastatic lesions (*2*–*5*). Thus, there is a wide window of opportunity to detect cancers prior to the onset of metastasis. Even when metastasis has initiated but is not yet evident radiologically, cancers can be cured in up to 50% of cases with systemic therapies, such as cytotoxic drugs and immunotherapy (*6*–*9*). Once large, metastatic tumors are formed, however, current therapies are rarely effective (*6*–*9*).

The only widely used blood test for earlier cancer detection is based on measurement of prostate specific antigen (PSA), and the proper use of this test is still being debated (*10*). The approved tests for cancer detection are not blood-based, and include colonoscopy, mammography, and cervical

cytology. New blood tests for cancer must have very high specificity; otherwise, too many healthy individuals will receive positive test results, leading to unnecessary follow-up procedures and anxiety. Blood tests that detect somatic mutations ("liquid biopsies") offer the promise of exquisite specificity because they are based on driver gene mutations that are expected to be found only in abnormal clonal proliferations of cells, such as cancers (*11*–*18*). To date, the vast majority of cancer patients evaluated with mutation-based liquid biopsies have advanced-stage disease. In addition, no studies have examined a large number of healthy control individuals, which is essential for evaluation of the specificity of such tests (*19*). Diagnostic sensitivity is also an issue for liquid biopsies. Available evidence indicates that patients with early-stage cancers can harbor < 1 mutant template molecule per ml of plasma (*11*, *20*), which is often beyond the limit of detection of previously reported technologies that assess multiple mutations simultaneously (*19*, *21*). Yet another issue with liquid biopsies is the identification of the underlying tissue of origin. Because the same gene mutations drive multiple tumor types, liquid biopsies based on genomic analysis alone generally cannot identify the anatomical location of the primary tumor.

We describe here a new blood test, called CancerSEEK, which addresses the issues described above. The test utilizes combined assays for genetic alterations and protein biomarkers and has the capacity not only to identify the presence of relatively early cancers but also to localize the organ of origin of these cancers.

Initial studies demonstrated that the maximum sensitivity of plasma DNA-based tests ("liquid biopsies") was limited for localized cancers (*11*). A subsequent study suggested that the combination of four protein biomarkers with one genetic marker (*KRAS*) could enhance sensitivity for the detection of pancreatic cancers (*20*). We sought to generalize this approach by evaluating a panel of protein and gene markers that might be used to detect many solid tumors at a stage prior to the emergence of distant metastases. We began by designing a polymerase chain reaction (PCR)-based assay that could simultaneously assess multiple regions of driver genes that are commonly mutated in a variety of cancer types. In designing this test, we were confronted by four competing challenges. First, the test must query a sufficient number of bases to allow detection of a large number of cancers. Second, each base queried in the test must be sequenced thousands of times to detect low prevalence mutations (*11*, *19*, *21*, *22*). Third, there must be a limit on the number of bases queried in the test because the more bases queried, the more likely that artifactual mutations would be identified, reducing the signal-to-noise ratio. And fourth, for implementation in a screening setting, the test must be cost effective and amenable to high throughput, factors that limit the amount of sequencing that can be performed. To overcome these challenges, we searched for the minimum number of short amplicons that would allow us to detect at least one driver gene mutation in each of the eight tumor types evaluated. Using publicly available sequencing data, we found that there was a fractional power law relationship between the number of amplicons required and the sensitivity of detection, with a plateau at ~ 60 amplicons (Fig. 1). Once this plateau was reached, raising the number of amplicons would not detect substantially more cancers but would increase the probability of false positive results. This decreasing marginal utility defined the optimal number of amplicons.

Based on these data, we designed a 61-amplicon panel, with each amplicon querying an average of 33 bp within one of 16 genes (table S1). As shown in Fig. 1, this panel would theoretically detect 41% (liver) to 95% (pancreas) of the cancers in the Catalog of Somatic Mutations in Cancer (COSMIC) dataset (*23*). In practice, the panel performed considerably better, detecting at least one mutation in 82%, two mutations in 47%, and more than two mutations in 8% of the 805 cancers evaluated in our study (Fig. 1, colored dots; fig. S1; and table S2). We were able to detect a larger fraction of tumors than predicted by the COSMIC dataset because the PCR-based sequencing assay we used was more sensitive for detecting mutations than conventional genome-wide sequencing. Based on this analysis of the DNA from primary tumors, the predicted maximum detection capability of circulating tumor DNA (ctDNA) in our study varied by tumor type, ranging from 60% for liver cancers to 100% for ovarian cancers (Fig. 1).

Armed with this small but robust panel of amplicons, we developed two approaches that enabled the detection of the rare mutations expected to be present in plasma ctDNA. First, we used multiplex-PCR to directly and uniquely label each original template molecule with a DNA barcode. This design minimizes the errors inherent to massively parallel sequencing (*24*) and makes efficient use of the small amount of cell-free DNA present in plasma. Additionally, we divided the total amount of DNA recovered from plasma into multiple aliquots and performed independent assays on each replicate. In effect, this decreases the number of DNA molecules per well; however, it increases the fraction of each mutant molecule per well, making the mutants easier to detect. Because the sensitivity of detection is often limited by the fraction of mutant alleles in each replicate, this partitioning strategy allowed us to increase the signal-to-noise ratio and identify mutations present at lower prevalence than possible if all of the plasma DNA was evaluated at once.

The second component of CancerSEEK is based on protein biomarkers. Previous studies have demonstrated that a major fraction of early-stage tumors do not release detectable

amounts of ctDNA, even when extremely sensitive techniques are used to identify them (*11*, *20*). Many proteins potentially useful for early detection and diagnosis of cancer have been described in the literature (*25*–*27*). We searched this literature to find proteins that had previously been shown to detect at least one of the eight cancer types described above with sensitivities > 10% and specificities > 99%. We identified 41 potential protein biomarkers (table S3) and evaluated them in preliminary studies on plasma samples from normal individuals as well as from cancer patients. We found that 39 of these proteins could be reproducibly evaluated through a single immunoassay platform and we then used this platform to assay all plasma samples (table S3). Eight of the 39 proteins proved to be particularly useful for discriminating cancer patients from healthy controls (table S3).

We then used CancerSEEK to study 1,005 patients who had been diagnosed with Stage I to III cancers of the ovary, liver, stomach, pancreas, esophagus, colorectum, lung, or breast. No patient received neo-adjuvant chemotherapy prior to blood sample collection and none had evident distant metastasis at the time of study entry. The median age at diagnosis was 64 (range 22 to 93). The eight cancer types were chosen because they are common in western populations and because no blood-based tests for their earlier detection are in common clinical use. The histopathological and clinical characteristics of the patients are summarized in table S4. The most common stage at presentation was American Joint Commission on Cancer (AJCC) stage II, accounting for 49% of patients, with the remaining patients harboring stage I (20%) or stage III (31%) disease. The number of samples per stage for each of the eight tumor types is summarized in table S11. The healthy control cohort consisted of 812 individuals of median age 55 (range 17 to 88) with no known history of cancer, high-grade dysplasia, autoimmune disease, or chronic kidney disease.

CancerSEEK evaluates levels of 8 proteins and the presence of mutations in 2,001 genomic positions; each genomic position could be mutated in several ways (single base substitutions, insertions, or deletions). The presence of a mutation in an assayed gene or an elevation in the level of any of these proteins would classify a patient as positive. It was therefore imperative to employ rigorous statistical methods to ensure the accuracy of the test. We used log ratios to evaluate mutations and incorporated them into a logistic regression algorithm that took into account both mutation data and protein biomarker levels to score CancerSEEK test results (Supplementary Materials). The mean sensitivities and specificities were determined by ten iterations of 10-fold cross-validations. The receiver operating characteristic (ROC) curves for the entire cohort of cancer patients and controls in one representative iteration is shown in Fig. 2A.

The median sensitivity of CancerSEEK among the eight cancer types evaluated was 70% ($P < 10^{-96}$ one-sided binomial test) and ranged from 98% in ovarian cancers to 33% in breast cancers (Fig. 2C). At this sensitivity, the specificity was > 99%; i.e., only 7 of the 812 individuals without known cancers scored positive. We could not be certain that the few "false positive" individuals identified among the healthy cohort did not actually have an as yet undetected cancer, but classifying them as false positives provided the most conservative approach to classification and interpretation of the data.

The features of the test that were most important to the algorithm were the presence of a ctDNA mutation followed by elevations of cancer antigen 125 (CA-125), carcinoembryonic antigen (CEA), cancer antigen 19-9 (CA19-9), prolactin (PRL), hepatocyte growth factor (HGF), osteopontin (OPN), myeloperoxidase (MPO), and tissue inhibitor of metalloproteinases 1 (TIMP-1) protein levels (table S9). Waterfall plots for each of the ctDNA and protein features used in CancerSEEK illustrate their distribution among individuals with and without cancer (fig. S2). The importance ranking of the ctDNA and protein features used in CancerSEEK are provided in table S9 and a principal component analysis displaying the clustering of individuals with and without cancer is shown in fig. S3. The complete dataset, including the levels of all proteins studied and the mutations identified in the plasma samples, are provided in tables S5 and S6. The probabilistic rather than deterministic nature of the approach used here to call a sample positive is evident from fig S4; each panel represents the sensitivity of CancerSEEK when one specific feature was excluded from the analysis.

One of the most important attributes of a screening test is the ability to detect cancers at relatively early stages. The median sensitivity of CancerSEEK was 73% for the most common stage evaluated (Stage II), similar (78%) for Stage III cancers, and lower (43%) for Stage I cancers (Fig. 2B). The sensitivity for the earliest stage cancers (Stage I) was highest for liver cancer (100%) and lowest for esophageal cancer (20%).

The basis of liquid biopsy is that mutant DNA templates in plasma are derived from dying cancer cells and thus serve as exquisitely specific markers for neoplasia. To investigate whether CancerSEEK meets this expectation, we evaluated tumor tissue from 153 patients in whom ctDNA could be detected at statistically significant levels (Supplementary Materials) and for whom primary tumors were available. We found that the mutation in the plasma was identical to a mutation found in the primary tumor of the same individual in 138 (90%) of these 153 cases (table S7). This concordance between plasma and primary tumor was evident in all eight cancer types, and ranged from 100% in ovarian and pancreatic cancers to 82% in stomach cancers.

One limitation of liquid biopsies is their inability to determine the cancer type in patients who test positive, which poses challenges for clinical follow-up. To examine whether the CancerSEEK test can help identify a cancer's tissue of origin, we used supervised machine learning to predict the underlying cancer type in patients with positive CancerSEEK tests. The input algorithm took into account the ctDNA and protein biomarker levels as well as the gender of the patient (Supplementary Materials). One of the main purposes of such predictions is to determine the most appropriate follow-up test for cancer diagnosis or monitoring after a positive CancerSEEK test. We therefore grouped together patients with esophageal and gastric cancers, as endoscopy would be the optimal follow-up in both instances. We then used this algorithm (Supplementary Materials) to study the 626 cancer patients scoring positive in the CancerSEEK Test. Without any clinical information about the patients, we were able to localize the source of the cancer to two anatomic sites in a median of 83% of these patients (Fig. 3, table S8; $P < 10^{-77}$ one-sided binomial test). Furthermore, we were able to localize the source of the positive test to a single organ in a median of 63% of these patients (Fig. 3, table S8; $P < 10^{-47}$ one-sided binomial test). Given that driver gene mutations are usually not tissue-specific, the vast majority of the localization information was derived from protein markers. The accuracy of prediction varied with tumor type; it was highest for colorectal cancers and lowest for lung cancers (Fig. 3 and table S10).

In summary, we have designed a multi-analyte blood test that can detect the presence of eight common solid tumor types. The advantage of combining completely different agents, with distinct mechanisms of action, is widely recognized in therapeutics (*28*–*30*) but has not been routinely applied to diagnostics. Here, we combined protein biomarkers with genetic biomarkers to increase sensitivity without substantially decreasing specificity. Other cancer biomarkers, such as metabolites, mRNA transcripts, miRNAs, or methylated DNA sequences could be similarly combined to increase sensitivity and localization of cancer site. Such multi-analyte tests would not be not meant to replace other non-blood based screening tests, such as those for breast or colorectal cancers, but to provide additional information that could help identify those patients most likely to harbor a malignancy.

Several limitations of our study should be acknowledged. First, the patient cohort in our study was composed of individuals with known cancers, most diagnosed on the basis of symptoms of disease. Though none of our patients had clinically evident metastatic disease at the time of study entry, most individuals in a true screening setting would have less advanced disease and the sensitivity of detection is likely to be less than reported here. Second, our controls were limited to healthy individuals whereas in a true cancer screening setting, some individuals might have inflammatory or other diseases which could result in a greater proportion of false positive results than observed in our study. Third, although multiple-fold cross-validation is a powerful and widely used technique for demonstrating robust sensitivity and specificity on a cohort of this study's scale, we were not able to use a completely independent set of cases for testing, which would have been optimal. Finally, the proportion of cancers of each type in our cohort was purposefully not representative of those in the U.S. as a whole because we wanted to evaluate at least 50 examples of each cancer type with the resources available to us. When weighted for actual incidence in the U.S., we estimate the sensitivity of CancerSEEK to be 55% among all eight cancer types. Importantly, this weighting would not affect the high sensitivities of CancerSEEK (69% to 98%) to detect five cancer types (ovary, liver, stomach, pancreas, and esophagus) for which there are no screening tests available for average-risk individuals.

Our study lays the conceptual and practical foundation for a single, multi-analyte blood test for cancers of many types. We estimate the cost of the test to be less than $500, which is comparable or lower than other screening tests for single cancers, such as colonoscopy. The eight cancer types studied here account for 360,000 (60%) of the estimated cancer deaths in the U.S. in 2017 and their earlier detection could conceivably reduce deaths from these diseases. To actually establish the clinical utility of CancerSEEK and to demonstrate that it can save lives, prospective studies of all incident cancer types in a large population will be required.

REFERENCES AND NOTES

1. R. L. Siegel, K. D. Miller, A. Jemal, Cancer Statistics, 2017. *CA Cancer J. Clin.* **67**, 7–30 (2017). doi:10.3322/caac.21387 Medline
2. B. Vogelstein, N. Papadopoulos, V. E. Velculescu, S. Zhou, L. A. Diaz Jr., K. W. Kinzler, Cancer genome landscapes. *Science* **339**, 1546–1558 (2013). doi:10.1126/science.1235122 Medline
3. S. Jones, W. D. Chen, G. Parmigiani, F. Diehl, N. Beerenwinkel, T. Antal, A. Traulsen, M. A. Nowak, C. Siegel, V. E. Velculescu, K. W. Kinzler, B. Vogelstein, J. Willis, S. D. Markowitz, Comparative lesion sequencing provides insights into tumor evolution. *Proc. Natl. Acad. Sci. U.S.A.* **105**, 4283–4288 (2008). doi:10.1073/pnas.0712345105 Medline
4. S. Yachida, C. M. White, Y. Naito, Y. Zhong, J. A. Brosnan, A. M. Macgregor-Das, R. A. Morgan, T. Saunders, D. A. Laheru, J. M. Herman, R. H. Hruban, A. P. Klein, S. Jones, V. Velculescu, C. L. Wolfgang, C. A. Iacobuzio-Donahue, Clinical significance of the genetic landscape of pancreatic cancer and implications for identification of potential long-term survivors. *Clin. Cancer Res.* **18**, 6339–6347 (2012). doi:10.1158/1078-0432.CCR-12-1215 Medline
5. B. Vogelstein, K. W. Kinzler, The Path to Cancer —Three Strikes and You're Out. *N. Engl. J. Med.* **373**, 1895–1898 (2015). doi:10.1056/NEJMp1508811 Medline
6. I. Bozic, J. G. Reiter, B. Allen, T. Antal, K. Chatterjee, P. Shah, Y. S. Moon, A. Yaqubie, N. Kelly, D. T. Le, E. J. Lipson, P. B. Chapman, L. A. Diaz Jr., B. Vogelstein, M. A. Nowak, Evolutionary dynamics of cancer in response to targeted combination therapy. *eLife* **2**, e00747 (2013). doi:10.7554/eLife.00747 Medline
7. T. J. Semrad, A. R. Fahrni, I. Y. Gong, V. P. Khatri, Integrating Chemotherapy into the Management of Oligometastatic Colorectal Cancer: Evidence-Based Approach Using Clinical Trial Findings. *Ann. Surg. Oncol.* **22** (Suppl 3), S855–S862 (2015). doi:10.1245/s10434-015-4610-4 Medline

8. C. G. Moertel, T. R. Fleming, J. S. Macdonald, D. G. Haller, J. A. Laurie, C. M. Tangen, J. S. Ungerleider, W. A. Emerson, D. C. Tormey, J. H. Glick, M. H. Veeder, J. A. Mailliard, Fluorouracil plus levamisole as effective adjuvant therapy after resection of stage III colon carcinoma: A final report. *Ann. Intern. Med.* **122**, 321–326 (1995). doi:10.7326/0003-4819-122-5-199503010-00001 Medline
9. A. C. Huang, M. A. Postow, R. J. Orlowski, R. Mick, B. Bengsch, S. Manne, W. Xu, S. Harmon, J. R. Giles, B. Wenz, M. Adamow, D. Kuk, K. S. Panageas, C. Carrera, P. Wong, F. Quagliarello, B. Wubbenhorst, K. D'Andrea, K. E. Pauken, R. S. Herati, R. P. Staupe, J. M. Schenkel, S. McGettigan, S. Kothari, S. M. George, R. H. Vonderheide, R. K. Amaravadi, G. C. Karakousis, L. M. Schuchter, X. Xu, K. L. Nathanson, J. D. Wolchok, T. C. Gangadhar, E. J. Wherry, T-cell invigoration to tumour burden ratio associated with anti-PD-1 response. *Nature* **545**, 60–65 (2017). doi:10.1038/nature22079 Medline
10. P. F. Pinsky, P. C. Prorok, B. S. Kramer, Prostate Cancer Screening - A Perspective on the Current State of the Evidence. *N. Engl. J. Med.* **376**, 1285–1289 (2017). doi:10.1056/NEJMsb1616281 Medline
11. C. Bettegowda, M. Sausen, R. J. Leary, I. Kinde, Y. Wang, N. Agrawal, B. R. Bartlett, H. Wang, B. Luber, R. M. Alani, E. S. Antonarakis, N. S. Azad, A. Bardelli, H. Brem, J. L. Cameron, C. C. Lee, L. A. Fecher, G. L. Gallia, P. Gibbs, D. Le, R. L. Giuntoli, M. Goggins, M. D. Hogarty, M. Holdhoff, S.-M. Hong, Y. Jiao, H. H. Juhl, J. J. Kim, G. Siravegna, D. A. Laheru, C. Lauricella, M. Lim, E. J. Lipson, S. K. N. Marie, G. J. Netto, K. S. Oliner, A. Olivi, L. Olsson, G. J. Riggins, A. Sartore-Bianchi, K. Schmidt, M. Shih, S. M. Oba-Shinjo, S. Siena, D. Theodorescu, J. Tie, T. T. Harkins, S. Veronese, T.-L. Wang, J. D. Weingart, C. L. Wolfgang, L. D. Wood, D. Xing, R. H. Hruban, J. Wu, P. J. Allen, C. M. Schmidt, M. A. Choti, V. E. Velculescu, K. W. Kinzler, B. Vogelstein, N. Papadopoulos, L. A. Diaz Jr., Detection of circulating tumor DNA in early- and late-stage human malignancies. *Sci. Transl. Med.* **6**, 224ra24 (2014). doi:10.1126/scitranslmed.3007094 Medline
12. D. A. Haber, V. E. Velculescu, Blood-based analyses of cancer: Circulating tumor cells and circulating tumor DNA. *Cancer Discov.* **4**, 650–661 (2014). doi:10.1158/2159-8290.CD-13-1014 Medline
13. S. J. Dawson, D. W. Y. Tsui, M. Murtaza, H. Biggs, O. M. Rueda, S.-F. Chin, M. J. Dunning, D. Gale, T. Forshew, B. Mahler-Araujo, S. Rajan, S. Humphray, J. Becq, D. Halsall, M. Wallis, D. Bentley, C. Caldas, N. Rosenfeld, Analysis of circulating tumor DNA to monitor metastatic breast cancer. *N. Engl. J. Med.* **368**, 1199–1209 (2013). doi:10.1056/NEJMoa1213261 Medline
14. Y. Wang, S. Springer, C. L. Mulvey, N. Silliman, J. Schaefer, M. Sausen, N. James, E. M. Rettig, T. Guo, C. R. Pickering, J. A. Bishop, C. H. Chung, J. A. Califano, D. W. Eisele, C. Fakhry, C. G. Gourin, P. K. Ha, H. Kang, A. Kiess, W. M. Koch, J. N. Myers, H. Quon, J. D. Richmon, D. Sidransky, R. P. Tufano, W. H. Westra, C. Bettegowda, L. A. Diaz Jr., N. Papadopoulos, K. W. Kinzler, B. Vogelstein, N. Agrawal, Detection of somatic mutations and HPV in the saliva and plasma of patients with head and neck squamous cell carcinomas. *Sci. Transl. Med.* **7**, 293ra104 (2015). doi:10.1126/scitranslmed.aaa8507 Medline
15. T. Forshew, M. Murtaza, C. Parkinson, D. Gale, D. W. Y. Tsui, F. Kaper, S.-J. Dawson, A. M. Piskorz, M. Jimenez-Linan, D. Bentley, J. Hadfield, A. P. May, C. Caldas, J. D. Brenton, N. Rosenfeld, Noninvasive identification and monitoring of cancer mutations by targeted deep sequencing of plasma DNA. *Sci. Transl. Med.* **4**, 136ra68 (2012). doi:10.1126/scitranslmed.3003726 Medline
16. C. Abbosh, N. J. Birkbak, G. A. Wilson, M. Jamal-Hanjani, T. Constantin, R. Salari, J. Le Quesne, D. A. Moore, S. Veeriah, R. Rosenthal, T. Marafioti, E. Kirkizlar, T. B. K. Watkins, N. McGranahan, S. Ward, L. Martinson, J. Riley, F. Fraioli, M. Al Bakir, E. Grönroos, F. Zambrana, R. Endozo, W. L. Bi, F. M. Fennessy, N. Sponer, D. Johnson, J. Laycock, S. Shafi, J. Czyzewska-Khan, A. Rowan, T. Chambers, N. Matthews, S. Turajlic, C. Hiley, S. M. Lee, M. D. Forster, T. Ahmad, M. Falzon, E. Borg, D. Lawrence, M. Hayward, S. Kolvekar, N. Panagiotopoulos, S. M. Janes, R. Thakrar, A. Ahmed, F. Blackhall, Y. Summers, D. Hafez, A. Naik, A. Ganguly, S. Kareht, R. Shah, L. Joseph, A. Marie Quinn, P. A. Crosbie, B. Naidu, G. Middleton, G. Langman, S. Trotter, M. Nicolson, H. Remmen, K. Kerr, M. Chetty, L. Gomersall, D. A. Fennell, A. Nakas, S. Rathinam, G. Anand, S. Khan, P. Russell, V. Ezhil, B. Ismail, M. Irvin-Sellers, V. Prakash, J. F. Lester, M. Kornaszewska, R. Attanoos, H. Adams, H. Davies, D. Oukrif, A. U. Akarca, J. A. Hartley, H. L. Lowe, S. Lock, N. Iles, H. Bell, Y. Ngai, G. Elgar, Z. Szallasi, R. F. Schwarz, J. Herrero, A. Stewart, S. A. Quezada, K. S. Peggs, P. Van Loo, C. Dive, C. J. Lin, M. Rabinowitz, H. J. W. L. Aerts, A. Hackshaw, J. A. Shaw, B. G. Zimmermann, C. Swanton, M. Jamal-Hanjani, C. Abbosh, S. Veeriah, S. Shafi, J. Czyzewska-Khan, D. Johnson, J. Laycock, L. Bosshard-Carter, G. Goh, R. Rosenthal, P. Gorman, N. Murugaesu, R. E. Hynds, G. A. Wilson, N. J. Birkbak, T. B. K. Watkins, N. McGranahan, S. Horswell, M. A. Bakir, E. Grönroos, R. Mitter, M. Escudero, A. Stewart, P. Van Loo, A. Rowan, H. Xu, S. Turajlic, C. Hiley, J. Goldman, R. K. Stone, T. Denner, N. Matthews, G. Elgar, S. Ward, J. Biggs, M. Costa, S. Begum, B. Phillimore, T. Chambers, E. Nye, S. Graca, K. Joshi, A. Furness, A. Ben Aissa, Y. N. S. Wong, A. Georgiou, S. A. Quezada, K. S. Peggs, J. A. Hartley, H. L. Lowe, J. Herrero, D. Lawrence, M. Hayward, N. Panagiotopoulos, S. Kolvekar, M. Falzon, E. Borg, T. Marafioti, C. Simeon, G. Hector, A. Smith, M. Aranda, M. Novelli, D. Oukrif, A. U. Akarca, S. M. Janes, R. Thakrar, M. D. Forster, T. Ahmad, S. M. Lee, D. Papadatos-Pastos, D. Carnell, R. Mendes, J. George, N. Navani, A. Ahmed, M. Taylor, J. Choudhary, Y. Summers, R. Califano, P. Taylor, R. Shah, P. Krysiak, K. Rammohan, E. Fontaine, R. Booton, M. Evison, P. A. Crosbie, S. Moss, F. Idries, L. Joseph, P. Bishop, A. Chaturvedi, A. M. Quinn, H. Doran, A. Leek, P. Harrison, K. Moore, R. Waddington, J. Novasio, F. Blackhall, J. Rogan, E. Smith, C. Dive, J. Tugwood, G. Brady, D. G. Rothwell, F. Chemi, J. Pierce, S. Gulati, B. Naidu, G. Langman, S. Trotter, M. Bellamy, H. Bancroft, A. Kerr, S. Kadiri, J. Webb, G. Middleton, M. Djearaman, D. A. Fennell, J. A. Shaw, J. L. Quesne, D. A. Moore, A. Thomas, H. Walter, J. Riley, L. Martinson, A. Nakas, S. Rathinam, W. Monteiro, H. Marshall, L. Nelson, J. Bennett, L. Primrose, G. Anand, S. Khan, A. Amadi, M. Nicolson, K. Kerr, S. Palmer, H. Remmen, J. Miller, K. Buchan, M. Chetty, L. Gomersall, J. F. Lester, A. Edwards, F. Morgan, H. Adams, H. Davies, M. Kornaszewska, R. Attanoos, S. Lock, A. Verjee, M. MacKenzie, M. Wilcox, H. Bell, N. Iles, A. Hackshaw, Y. Ngai, S. Smith, N. Gower, C. Ottensmeier, S. Chee, B. Johnson, A. Alzetani, E. Shaw, E. Lim, P. De Sousa, M. T. Barbosa, A. Bowman, S. Jordan, A. Rice, H. Raubenheimer, C. Proli, M. E. Cufari, J. C. Ronquillo, A. Kwayie, H. Bhayani, M. Hamilton, Y. Bakar, N. Mensah, L. Ambrose, A. Devaraj, S. Buderi, J. Finch, L. Azcarate, H. Chavan, S. Green, H. Mashinga, A. G. Nicholson, K. Lau, M. Sheaff, P. Schmid, J. Conibear, V. Ezhil, B. Ismail, M. Irvin-Sellers, V. Prakash, P. Russell, T. Light, T. Horey, S. Danson, J. Bury, J. Edwards, J. Hill, S. Matthews, Y. Kitsanta, K. Suvarna, P. Fisher, A. D. Keerio, M. Shackcloth, J. Gosney, P. Postmus, S. Feeney, J. Asante-Siaw, T. Constantin, R. Salari, N. Sponer, A. Naik, B. G. Zimmermann, M. Rabinowitz, H. J. W. L. Aerts, S. Dentro, C. Dessimoz, C. Swanton; TRACERx consortium; PEACE consortium, Phylogenetic ctDNA analysis depicts early-stage lung cancer evolution. *Nature* **545**, 446–451 (2017). doi:10.1038/nature22364 Medline
17. E. Beddowes, S. J. Sammut, M. Gao, C. Caldas, Predicting treatment resistance and relapse through circulating DNA. *Breast* **34** (Suppl 1), S31–S35 (2017). doi:10.1016/j.breast.2017.06.024 Medline
18. J. Phallen, M. Sausen, V. Adleff, A. Leal, C. Hruban, J. White, V. Anagnostou, J. Fiksel, S. Cristiano, E. Papp, S. Speir, T. Reinert, M. W. Orntoft, B. D. Woodward, D. Murphy, S. Parpart-Li, D. Riley, M. Nesselbush, N. Sengamalay, A. Georgiadis, Q. K. Li, M. R. Madsen, F. V. Mortensen, J. Huiskens, C. Punt, N. van Grieken, R. Fijneman, G. Meijer, H. Husain, R. B. Scharpf, L. A. Diaz Jr., S. Jones, S. Angiuoli, T. Ørntoft, H. J. Nielsen, C. L. Andersen, V. E. Velculescu, Direct detection of early-stage cancers using circulating tumor DNA. *Sci. Transl. Med.* **9**, eaan2415 (2017). doi:10.1126/scitranslmed.aan2415 Medline
19. I. A. Cree, L. Uttley, H. Buckley Woods, H. Kikuchi, A. Reiman, S. Harnan, B. L. Whiteman, S. T. Philips, M. Messenger, A. Cox, D. Teare, O. Sheils, J. Shaw; UK Early Cancer Detection Consortium, The evidence base for circulating tumour DNA blood-based biomarkers for the early detection of cancer: A systematic mapping review. *BMC Cancer* **17**, 697 (2017). doi:10.1186/s12885-017-3693-7 Medline
20. J. D. Cohen, A. A. Javed, C. Thoburn, F. Wong, J. Tie, P. Gibbs, C. M. Schmidt, M. T. Yip-Schneider, P. J. Allen, M. Schattner, R. E. Brand, A. D. Singhi, G. M. Petersen, S.-M. Hong, S. C. Kim, M. Falconi, C. Doglioni, M. J. Weiss, N. Ahuja, J. He, M. A. Makary, A. Maitra, S. M. Hanash, M. Dal Molin, Y. Wang, L. Li, J. Ptak, L. Dobbyn, J. Schaefer, N. Silliman, M. Popoli, M. G. Goggins, R. H. Hruban, C. L. Wolfgang, A. P. Klein, C. Tomasetti, N. Papadopoulos, K. W. Kinzler, B. Vogelstein, A. M. Lennon, Combined circulating tumor DNA and protein biomarker-based liquid biopsy for the earlier detection of pancreatic cancers. *Proc. Natl. Acad. Sci. U.S.A.* **114**, 10202–10207 (2017). doi:10.1073/pnas.1704961114 Medline
21. A. Bardelli, K. Pantel, Liquid Biopsies, What We Do Not Know (Yet). *Cancer Cell* **31**, 172–179 (2017). doi:10.1016/j.ccell.2017.01.002 Medline

22. F. Diehl, M. Li, D. Dressman, Y. He, D. Shen, S. Szabo, L. A. Diaz Jr., S. N. Goodman, K. A. David, H. Juhl, K. W. Kinzler, B. Vogelstein, Detection and quantification of mutations in the plasma of patients with colorectal tumors. *Proc. Natl. Acad. Sci. U.S.A.* **102**, 16368–16373 (2005). doi:10.1073/pnas.0507904102 Medline
23. S. A. Forbes, D. Beare, H. Boutselakis, S. Bamford, N. Bindal, J. Tate, C. G. Cole, S. Ward, E. Dawson, L. Ponting, R. Stefancsik, B. Harsha, C. Y. Kok, M. Jia, H. Jubb, Z. Sondka, S. Thompson, T. De, P. J. Campbell, COSMIC: Somatic cancer genetics at high-resolution. *Nucleic Acids Res.* **45** (D1), D777–D783 (2017). doi:10.1093/nar/gkw1121 Medline
24. I. Kinde, J. Wu, N. Papadopoulos, K. W. Kinzler, B. Vogelstein, Detection and quantification of rare mutations with massively parallel sequencing. *Proc. Natl. Acad. Sci. U.S.A.* **108**, 9530–9535 (2011). doi:10.1073/pnas.1105422108 Medline
25. L. A. Liotta, E. F. Petricoin 3rd, The promise of proteomics. *Clin. Adv. Hematol. Oncol.* **1**, 460–462 (2003). Medline
26. H. Wang, T. Shi, W.-J. Qian, T. Liu, J. Kagan, S. Srivastava, R. D. Smith, K. D. Rodland, D. G. Camp 2nd, The clinical impact of recent advances in LC-MS for cancer biomarker discovery and verification. *Expert Rev. Proteomics* **13**, 99–114 (2016). doi:10.1586/14789450.2016.1122529 Medline
27. E. F. Patz Jr., M. J. Campa, E. B. Gottlin, I. Kusmartseva, X. R. Guan, J. E. Herndon 2nd, Panel of serum biomarkers for the diagnosis of lung cancer. *J. Clin. Oncol.* **25**, 5578–5583 (2007). doi:10.1200/JCO.2007.13.5392 Medline
28. *Treatment of Tuberculosis: Guidelines* (World Health Organization, Geneva, 2010).
29. *Consolidated Guidelines on the Use of Antiretroviral Drugs for Treating and Preventing HIV Infection: Recommendations for a Public Health Approach* (World Health Organization, 2016).
30. A. B. Benson 3rd, A. P. Venook, L. Cederquist, E. Chan, Y.-J. Chen, H. S. Cooper, D. Deming, P. F. Engstrom, P. C. Enzinger, A. Fichera, J. L. Grem, A. Grothey, H. S. Hochster, S. Hoffe, S. Hunt, A. Kamel, N. Kirilcuk, S. Krishnamurthi, W. A. Messersmith, M. F. Mulcahy, J. D. Murphy, S. Nurkin, L. Saltz, S. Sharma, D. Shibata, J. M. Skibber, C. T. Sofocleous, E. M. Stoffel, E. Stotsky-Himelfarb, C. G. Willett, C. S. Wu, K. M. Gregory, D. Freedman-Cass, Colon Cancer, Version 1.2017, NCCN Clinical Practice Guidelines in Oncology. *J. Natl. Compr. Canc. Netw.* **15**, 370–398 (2017). doi:10.6004/jnccn.2017.0036 Medline
31. Y. Wang, K. Sundfeldt, C. Mateoiu, IeM. Shih, R. J. Kurman, J. Schaefer, N. Silliman, I. Kinde, S. Springer, M. Foote, B. Kristjansdottir, N. James, K. W. Kinzler, N. Papadopoulos, L. A. Diaz, B. Vogelstein, Diagnostic potential of tumor DNA from ovarian cyst fluid. *eLife* **5**, e15175 (2016). doi:10.7554/eLife.15175 Medline
32. H. Jung, D. Lee, J. Lee, D. Park, Y. J. Kim, W.-Y. Park, D. Hong, P. J. Park, E. Lee, Intron retention is a widespread mechanism of tumor-suppressor inactivation. *Nat. Genet.* **47**, 1242–1248 (2015). doi:10.1038/ng.3414 Medline
33. S. Jaiswal, P. Fontanillas, J. Flannick, A. Manning, P. V. Grauman, B. G. Mar, R. C. Lindsley, C. H. Mermel, N. Burtt, A. Chavez, J. M. Higgins, V. Moltchanov, F. C. Kuo, M. J. Kluk, B. Henderson, L. Kinnunen, H. A. Koistinen, C. Ladenvall, G. Getz, A. Correa, B. F. Banahan, S. Gabriel, S. Kathiresan, H. M. Stringham, M. I. McCarthy, M. Boehnke, J. Tuomilehto, C. Haiman, L. Groop, G. Atzmon, J. G. Wilson, D. Neuberg, D. Altshuler, B. L. Ebert, Age-related clonal hematopoiesis associated with adverse outcomes. *N. Engl. J. Med.* **371**, 2488–2498 (2014). doi:10.1056/NEJMoa1408617 Medline
34. J. Friedman, T. Hastie, R. Tibshirani, Regularization paths for generalized linear models via coordinate descent. *J. Stat. Softw.* **33**, 1–22 (2010). doi:10.18637/jss.v033.i01 Medline
35. A. Liaw, M. Wiener, Classification and regression by randomForest. *R News* **2**, 18–22 (2001).
36. A. P. Makohon-Moore, M. Zhang, J. G. Reiter, I. Bozic, B. Allen, D. Kundu, K. Chatterjee, F. Wong, Y. Jiao, Z. A. Kohutek, J. Hong, M. Attiyeh, B. Javier, L. D. Wood, R. H. Hruban, M. A. Nowak, N. Papadopoulos, K. W. Kinzler, B. Vogelstein, C. A. Iacobuzio-Donahue, Limited heterogeneity of known driver gene mutations among the metastases of individual patients with pancreatic cancer. *Nat. Genet.* **49**, 358–366 (2017). doi:10.1038/ng.3764 Medline
37. I. Kinde, N. Papadopoulos, K. W. Kinzler, B. Vogelstein, FAST-SeqS: A simple and efficient method for the detection of aneuploidy by massively parallel sequencing. *PLOS ONE* **7**, e41162 (2012). doi:10.1371/journal.pone.0041162 Medline

ACKNOWLEDGMENTS

We thank our patients for their courage and generosity. We are grateful to C. Blair and K. Judge for expert technical and administrative assistance. We thank H. Ren, J. Olson, M. Hathcok, H. Zeh, A. Singhi, S. Crippa, M. Ryan, and L. Ryan for their assistance with this study. This work was supported by the Lustgarten Foundation for Pancreatic Cancer Research, The Virginia and D.K. Ludwig Fund for Cancer Research, The Commonwealth Fund, The John Templeton Foundation, the Clinomics Program, Mayo Clinic Center for Individualized Medicine, the Mayo Clinic Biobank, The Sol Goldman Center for Pancreatic Cancer Research, The Michael Rolfe Pancreatic Cancer Research Foundation, The Benjamin Baker Scholarship, The Gray Foundation, The Early Detection Research Network, Susan Wojcicki and Dennis Troper, The Marcus Foundation, and National Institutes of Health Grants P50-CA62924, P50-CA102701, CA06973, GM-07309, and U01CA152753. N.P., S. Z., K.W.K., L.D., and B.V. are founders of Personal Genome Diagnostics, Inc. and PapGene, Inc. B.V. and K.W.K are on the Scientific Advisory Board of Sysmex-Inostics. B.V. is also on the Scientific Advisory Boards of Exelixis GP. R.H.H. is on the Board of Directors of MiDiagnostics. These companies and others have licensed technologies from Johns Hopkins, and N.P., K.W.K., L.D., B.V, and R.H.H. receive equity or royalties from these licenses. The terms of these arrangements are being managed by Johns Hopkins University in accordance with its conflict of interest policies. L.D. is on the Board of Directors of Jounce Therapeutics and is a Scientific Advisor for Genocea, Cell Design Labs, and Merck. A.S.M. is a consultant for Abbvie, Genentech, Bristol-Myers Squibb, and Trovagene. B.V., N.P. and K.W.K. are inventors on a patent (US 20140227705 A1) held by Johns Hopkins University that covers basic aspects of the SafeSeqS technology used in this paper. B.V., K.W.K., N.P., J.D.C., C. T. and A.M.L. are inventors on a patent application to be submitted by Johns Hopkins University that covers other aspects of SafeSeqS as well as the multi-analyte approach described in this paper. All data needed to evaluate the conclusions in the paper are present in the paper and/or the supplementary materials. Contact C.T. for questions about the algorithms; A.M.L. for questions about clinically related issues; K.W.K about the sequencing analyses; B.V. about experimental procedures; and N.P. about the overall design of the study.

SUPPLEMENTARY MATERIALS

www.sciencemag.org/cgi/content/full/science.aar3247/DC1
Material and Methods
Figs. S1 to S4
Tables S1 to S11
References (*31*–*37*)

31 October 2017; accepted 8 January 2018
Published online 18 January 2018
10.1126/science.aar3247

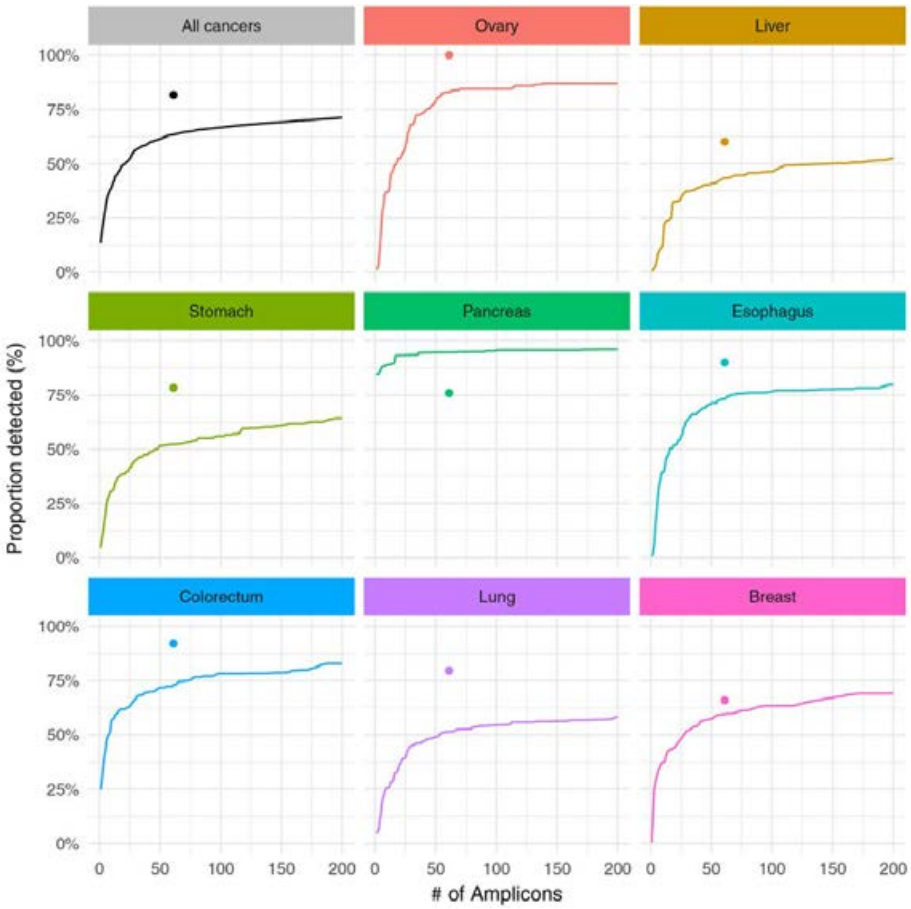

Fig. 1. Development of a PCR-based assay to identify tumor-specific mutations in plasma samples. Colored curves indicate the proportion of cancers of the eight types evaluated in this study that can be detected with an increasing number of short (< 40 bp) amplicons. The sensitivity of detection increases with the number of amplicons but plateaus at ~ 60 amplicons. Colored dots indicate the fraction of cancers detected using the 61-amplicon panel used in 805 cancers evaluated in our study, which averaged 82% (see main text). Publicly available sequencing data were obtained from the Catalog of Somatic Mutations in Cancer (COSMIC) repository.

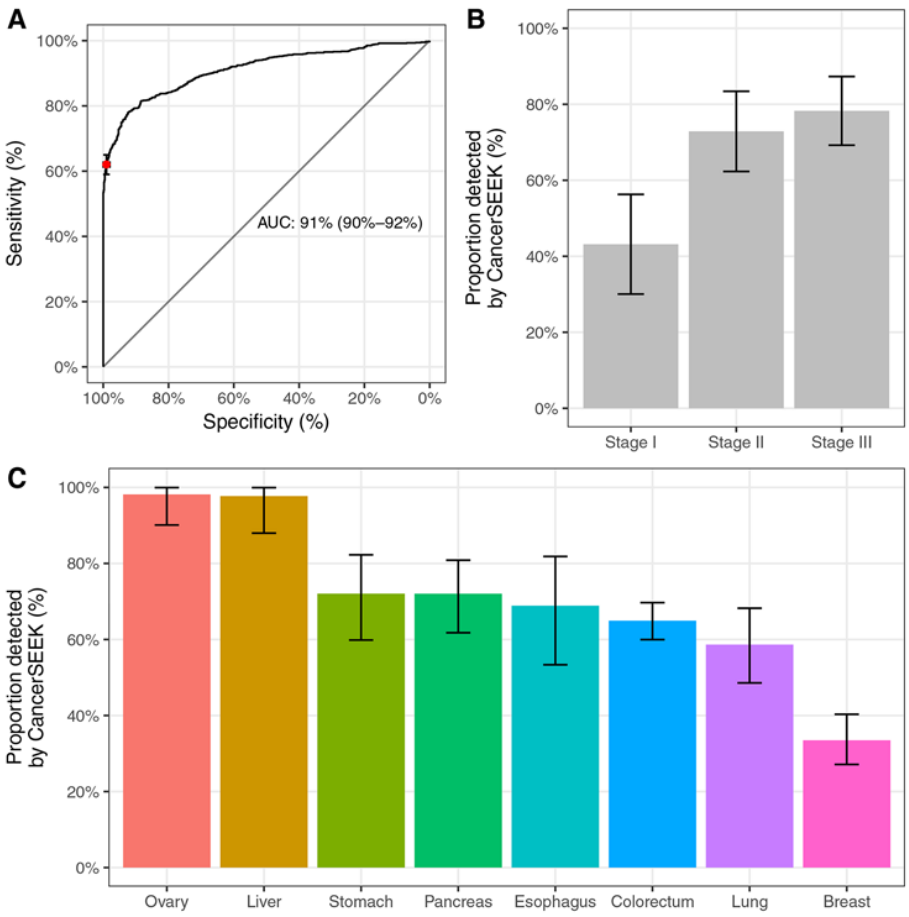

Fig. 2. Performance of CancerSEEK. (**A**) Receiver operator characteristic (ROC) curve for CancerSEEK. The red point on the curve indicate the test's average performance (62%) at > 99% specificity. Error bars represent 95% confidence intervals for sensitivity and specificity at this particular point. The median performance among the 8 cancer types assessed was 70%, as noted in the main text. (**B**) Sensitivity of CancerSEEK by stage. Bars represent the median sensitivity of the eight cancer types and error bars represent standard errors of the median. (**C**) Sensitivity of CancerSEEK by tumor type. Error bars represent 95% confidence intervals.

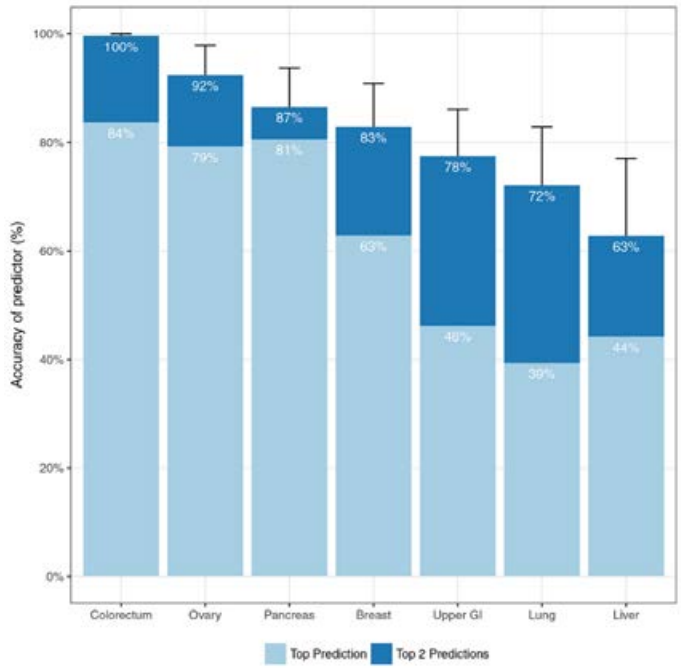

Fig. 3. Identification of cancer type by supervised machine learning for patients classified as positive by CancerSEEK. Percentages correspond to the proportion of patients correctly classified by one of the two most likely types (sum of light and dark blue bars) or the most likely type (light blue bar). Predictions for all patients for all cancer types are provided in table S8. Error bars represent 95% confidence intervals.

CANCER

Analysis of *Fusobacterium* persistence and antibiotic response in colorectal cancer

Susan Bullman,[1,2] Chandra S. Pedamallu,[1,2] Ewa Sicinska,[1] Thomas E. Clancy,[3] Xiaoyang Zhang,[1,2] Diana Cai,[1,2] Donna Neuberg,[1] Katherine Huang,[2] Fatima Guevara,[1] Timothy Nelson,[1] Otari Chipashvili,[1] Timothy Hagan,[1] Mark Walker,[2] Aruna Ramachandran,[1,2] Begoña Diosdado,[1,2] Garazi Serna,[4] Nuria Mulet,[4] Stefania Landolfi,[4] Santiago Ramon y Cajal,[4] Roberta Fasani,[4] Andrew J. Aguirre,[1,2,3] Kimmie Ng,[1] Elena Élez,[4] Shuji Ogino,[1,3,5] Josep Tabernero,[4] Charles S. Fuchs,[6] William C. Hahn,[1,2,3] Paolo Nuciforo,[4] Matthew Meyerson[1,2,3]*

Colorectal cancers comprise a complex mixture of malignant cells, nontransformed cells, and microorganisms. *Fusobacterium nucleatum* is among the most prevalent bacterial species in colorectal cancer tissues. Here we show that colonization of human colorectal cancers with *Fusobacterium* and its associated microbiome—including *Bacteroides*, *Selenomonas*, and *Prevotella* species—is maintained in distal metastases, demonstrating microbiome stability between paired primary and metastatic tumors. In situ hybridization analysis revealed that *Fusobacterium* is predominantly associated with cancer cells in the metastatic lesions. Mouse xenografts of human primary colorectal adenocarcinomas were found to retain viable *Fusobacterium* and its associated microbiome through successive passages. Treatment of mice bearing a colon cancer xenograft with the antibiotic metronidazole reduced *Fusobacterium* load, cancer cell proliferation, and overall tumor growth. These observations argue for further investigation of antimicrobial interventions as a potential treatment for patients with *Fusobacterium*-associated colorectal cancer.

The cancer-associated microbiota are known to influence cancer development and progression, most notably for colorectal cancer (*1*–*5*). Unbiased genomic analyses have revealed an enrichment of *Fusobacterium nucleatum* in human colon cancers and adenomas relative to noncancerous colon tissues (*6*, *7*). These observations have been confirmed in studies of multiple colon cancer patient cohorts from around the world (*8*–*12*). Increased tumor levels of *F. nucleatum* have been correlated with lower T cell infiltration (*13*); with advanced disease stage and poorer patient survival (*10*, *11*, *14*); and with clinical and molecular characteristics such as right-sided anatomic location, *BRAF* mutation, and hypermutation with microsatellite instability (*9*, *12*, *15*).

Studies in diverse experimental models have suggested a pro-tumorigenic role for *Fusobacterium*. Feeding mice with *Fusobacterium* (*16*–*18*), infection of colorectal cancer cell lines with *Fusobacterium* (*19*–*21*), and generation of xenografts derived from *Fusobacterium*-infected colorectal cancer cell lines (*17*) were all observed to potentiate tumor cell growth. Suggested mechanisms have ranged from enhanced tumor cell adhesion and invasion (*17*, *19*, *22*) to modulation of the host immune response (*16*, *23*) to activation of the Toll-like receptor 4 pathway (*17*, *20*, *21*). However, not all animal or cellular studies of *Fusobacterium* have demonstrated a cancer-promoting effect (*24*). A recent editorial has highlighted the importance of studying *Fusobacterium* infection in colon cancer as a component of the diverse microbiota within the native tumor microenvironment (*25*).

To investigate the role of *Fusobacterium* and its associated microbiota in native human colorectal cancers, we analyzed five independent cohorts of patient-derived colorectal cancers for *Fusobacterium* and microbiome RNA and/or DNA. Where technically possible, we performed *Fusobacterium* culture and tested the effect of antibiotic treatment upon the growth of propagated patient-derived colon cancer xenografts. These cohorts (table S1) include: (i) 11 fresh-frozen primary colorectal cancers and paired liver metastases (frozen paired cohort); (ii) 77 fresh-frozen primary colorectal cancers with detailed recurrence information (frozen primary cohort); (iii) published data from 430 resected fresh-frozen colon carcinomas from The Cancer Genome Atlas (*26*) (TCGA cohort), together with data from 201 resected fresh-frozen hepatocellular carcinomas from TCGA (*27*); (iv) 101 formalin-fixed paraffin-embedded colorectal carcinomas and paired liver metastases (FFPE paired cohort); and (v) 13 fresh primary colorectal cancers used for patient-derived xenograft studies (xenograft cohort).

Using the frozen paired cohort, we tested whether we could culture viable *Fusobacterium* species from primary colorectal carcinomas and corresponding liver metastases. Quantitative polymerase chain reaction (qPCR) analysis showed that 9 of 11 (82%) snap-frozen primary tumors (table S2) were positive for *Fusobacterium* in the primary tumor [patients one through nine (P1 through P9)]; we could isolate *Fusobacterium* species from 73% of these tumors (n = 8 of 11 tumors; P1 through P8) (Fig. 1A). In addition, we cultured *Fusobacterium* species from two liver metastases (P1 and P2) from *Fusobacterium*-positive primary tumors. Five metastatic specimens had inadequate amounts of tissue for culture but were positive for *Fusobacterium* by qPCR (P3 through P7), for a total of seven primary-metastatic tumor pairs (64%) testing positive for *Fusobacterium* by qPCR (Fig. 1A). This finding extends previous results showing the presence of *Fusobacterium* nucleic acids in hepatic and lymph node metastases of colon cancer (*7*, *22*, *28*) to now demonstrate that viable *Fusobacterium* species are present in distant metastases.

To address whether the same *Fusobacterium* is present in primary cancers and metastases, we performed whole-genome sequencing of pure *Fusobacterium* isolates from primary and metastatic tumors from two patients (P1 and P2). For both patients, the primary-metastatic tumor pairs harbored highly similar strains of *Fusobacterium*, with >99.9% average nucleotide identity, despite the tissue being collected months (P2) or even years (P1) apart (Fig. 1B and fig. S1). We cultured *Fusobacterium necrophorum* subsp. *funduliforme* from the primary colorectal tumor and liver metastasis of P1 and *F. nucleatum* subsp. *animalis* from the primary tumor and metastasis of P2. We also cultured other anaerobes, including *Bacteroides* species, from the primary-metastasis pairs (table S3). Our finding of nearly identical, viable *Fusobacterium* strains in matched primary and metastatic colorectal cancers confirms the persistence of viable *Fusobacterium* species through the metastatic process and suggests that *Fusobacterium* species may migrate with the colorectal cancer cells to the metastatic site.

To quantitate the relative abundance of *Fusobacterium* and to evaluate the overall microbiome in the paired primary and metastatic tumors, we performed RNA sequencing of 10 primary cancers and their matched liver metastases from the frozen paired cohort (P1 to P6 and P8 to P11). PathSeq analysis (*29*) of the RNA sequencing data showed that the same *Fusobacterium* species were present, at a similar relative abundance, in the paired primary-metastatic tumors (Fig. 1C, samples P1 to P6) and that the overall dominant microbiome was also qualitatively similar. In addition to *F. nucleatum* and *F. necrophorum*, primary cancer microbes that persisted in the liver metastases included *Bacteroides fragilis*, *Bacteroides thetaiotaomicron*, and several typically oral anaerobes such as *Prevotella intermedia* and *Selenomonas sputigena* (Fig. 1C). In contrast, there

[1]Dana-Farber Cancer Institute, Harvard Medical School, Boston, MA 02115, USA. [2]Broad Institute of MIT and Harvard, Cambridge, MA 02142, USA. [3]Brigham and Women's Hospital, Harvard Medical School, Boston, MA 02115, USA. [4]Vall d'Hebron University Hospital, Vall d'Hebron Institute of Oncology, Barcelona, CIBERONC, Universitat Autònoma de Barcelona, Spain. [5]Harvard T.H. Chan School of Public Health, Boston, MA 02115, USA. [6]Yale Cancer Center, Yale School of Medicine, New Haven, CT 06520, USA.
***Corresponding author. Email: matthew_meyerson@dfci.harvard.edu**

was little similarity between bacterial sequences in the primary colorectal cancer and liver metastasis in the lone sample where *Fusobacterium* was present in the primary cancer but not detected in the metastasis (Fig. 1C, sample P8) or in the three samples with low or undetectable levels of *Fusobacterium* in the primary cancer (Fig. 1C, samples P9 to P11). Jaccard index analysis revealed a high correlation between the dominant bacterial genera in the primary tumor and metastasis for *Fusobacterium*-positive pairs, but a low correlation between bacterial genera in the primary tumor and metastasis for *Fusobacterium*-negative pairs (Fig. 1D and fig. S2).

Targeted bacterial 16*S* ribosomal RNA (rRNA) gene sequencing on DNA from the 11 frozen paired samples confirmed that (i) *Fusobacterium* species are present in paired primary-metastatic

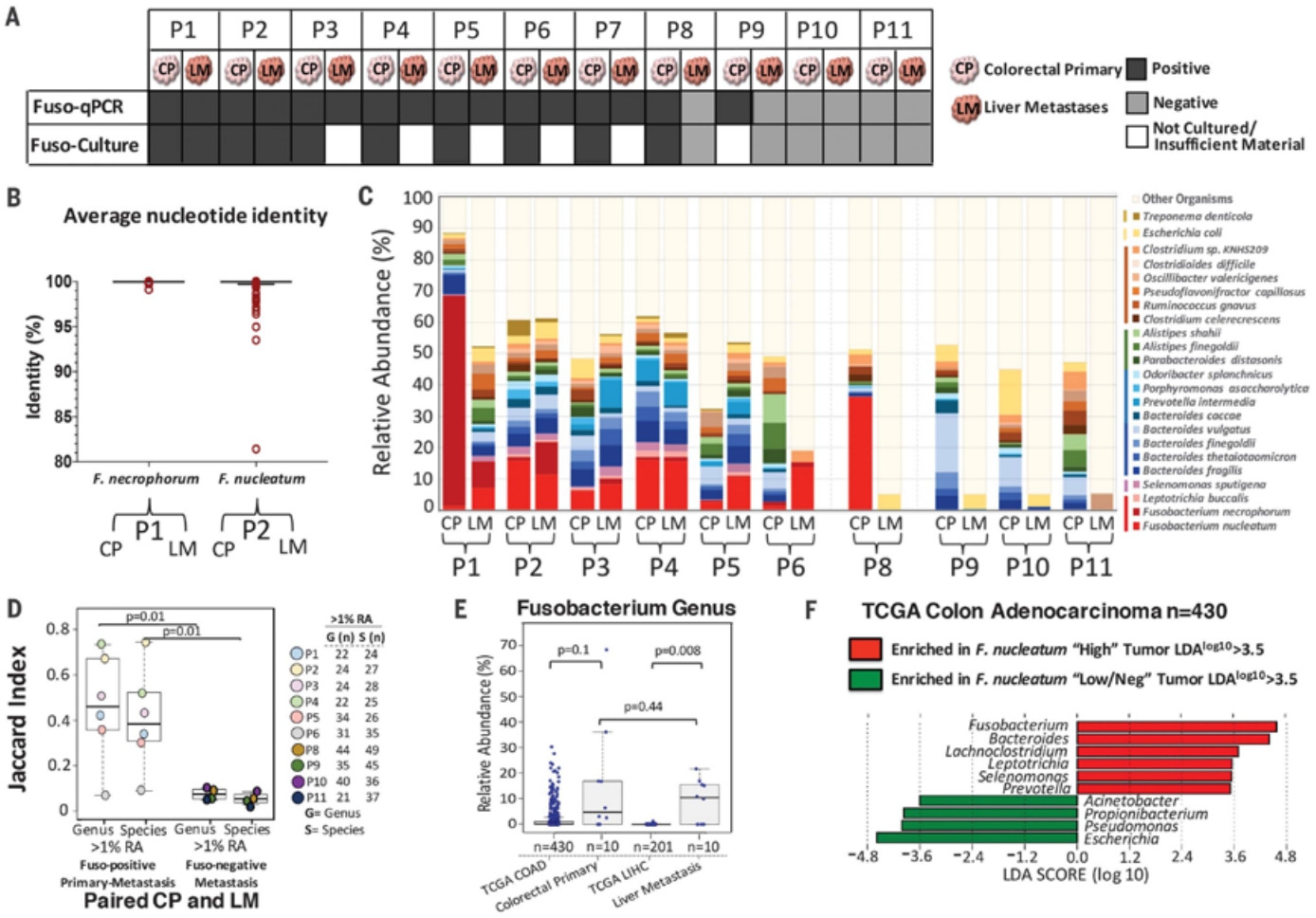

Fig. 1. *Fusobacterium* colonizes liver metastases of *Fusobacterium*-associated colorectal primary tumors. (**A**) Schematic of *Fusobacterium* culture and *Fusobacterium*-targeted qPCR status of paired snap-frozen colorectal primary tumors and liver metastases from 11 patients (P1 to P11) from the frozen paired cohort. (**B**) Aligned dot plot representing the average nucleotide identity (ANI) of whole-genome sequencing data from *F. necrophorum* isolated from paired primary colorectal tumor (CP) and liver metastasis (LM) of P1 and *F. nucleatum* isolate cultured from paired primary tumors and liver metastasis of P2. *F. necrophorum* P1 two-way ANI: 100% (SD: 0.01%) from 10,220 fragments; *F. nucleatum* P2 two-way ANI: 99.99% (SD: 0.23%) from 7334 fragments. (**C**) Species-level microbial composition of paired colorectal primary tumors and liver metastases (frozen paired cohort), assayed by RNA sequencing followed by PathSeq analysis for microbial identification. For simplicity, only organisms with >2% relative abundance (RA) in at least one tumor are shown. The colors correspond to bacterial taxonomic class. Red, Fusobacteriia; pink, Negativicutes; blue/green, Bacteroidia; orange, Clostridia; yellow, Gamma-proteobacteria; dark brown, Spirochaetes. The samples are separated into three groups: *Fusobacterium*-positive primary tumor and metastases (n = 6 pairs), *Fusobacterium*-positive primary tumor and *Fusobacterium*-negative metastases (n = 1 pair), and *Fusobacterium*-negative primary tumor and metastases (n = 3 pairs). P7 had insufficient tissue for RNA sequencing analysis. (**D**) Box plots represent the Jaccard index (proportion of shared genera or species) between paired colorectal primary tumors and liver metastases at both the genus and species level at 1% RA. The box represents the first and third quartiles, and error bars indicate the 95% confidence level of the median. Paired samples that were positive for *Fusobacterium* in both the primary tumor and metastasis were compared with paired samples where the metastasis was *Fusobacterium*-negative. *P* values were determined using Welch's two-sample *t* test. (**E**) Box plots of *Fusobacterium* RA in primary colon adenocarcinoma (COAD) (n = 430) and primary liver hepatocellular carcinoma (LIHC) (n = 201) from TCGA (TCGA cohort) and primary-metastasis pairs from 10 patients. The box represents the first and third quartiles, and error bars indicate the 95% confidence level of the median. *P* values were determined using Welch's two-sample *t* test with correction for unequal variances. (**F**) Identification of bacteria that co-occur with *Fusobacterium* in primary COAD (TCGA cohort). Primary COAD tumors were subset into two groups: *Fusobacterium* "High" if *Fusobacterium* RA was >1% (n = 110, median RA = 5%, mean RA = 7.4%) and *Fusobacterium* "Low/Neg" if RA was <1% (n = 320, median RA = 0.06%, mean RA = 0.16%). The bar plot illustrates genera enriched (red) and depleted (green) in COAD with >1% *Fusobacterium* RA. LDA, linear discriminant analysis.

tumors, (ii) the relative abundance of *Fusobacterium* is correlated between primary tumors and metastases, and (iii) the dominant microbial genera in the liver metastases correspond to those in the primary tumors, demonstrating microbiome stability between paired *Fusobacterium*-positive primary-metastatic tumors (P = 0.01) (fig. S3).

To investigate the relationship between *Fusobacterium* and cancer recurrence, we performed microbial culture and bacterial 16*S* rRNA gene sequencing in a blinded fashion on the frozen primary cohort of 77 snap-frozen colorectal cancers lacking paired metastases (n = 21 with recurrence, n = 56 without recurrence) (table S4). We discovered that 44 of 77 tumors (57%) had cultivable *Fusobacterium* species and 45 of 77 had >1% *Fusobacterium* relative abundance. We found no correlation between *Fusobacterium* load or culture with either recurrence or stable disease in this cohort (fig. S4).

To assess *Fusobacterium* persistence and its correlation with clinical parameters, we analyzed the 101 primary-metastasis pairs from the FFPE paired cohort (table S5). We found that 43% (n = 44 of 101) of primary colorectal cancers tested positive for *Fusobacterium* by qPCR and 45% (n = 20 of 44) of liver metastases arising from these primary tumors were *Fusobacterium*-positive (fig. S5A).

To determine the spatial distribution of *Fusobacterium* in these tumors, *Fusobacterium* RNA in situ hybridization (ISH) analysis was performed on five qPCR-positive primary-metastasis pairs from this cohort (table S6, Fig. 2, and fig. S6). Both biofilm and invasive *F. nucleatum* were observed in primary colorectal cancer (Fig. 2, A to D). Invasive *F. nucleatum* distribution was highly heterogeneous and focal, found in isolated or small groups of cells with morphology consistent with that of malignant cells and located close to the lumen and ulcerated regions. *F. nucleatum* was also observed in glandular structures present in the tumor center and invasive margins, but to a lesser extent. In adjacent normal mucosa (when present), *F. nucleatum* was exclusively located in the biofilm. In liver metastasis, *F. nucleatum* was predominantly localized in isolated cells whose histomorphology is consistent with colon cancer cells (Fig. 2, E to H), although occasional stromal *F. nucleatum* could be observed as well. No *F. nucleatum* was detected in the adjacent residual liver parenchyma.

Notably, none of the 57 *Fusobacterium*-negative primary colorectal tumors were associated with a *Fusobacterium*-positive liver metastasis (n = 0 of 57; P = 0) (fig. S5A). Consistent with previous reports (*15*), the presence of *Fusobacterium* in paired primary tumors and corresponding metastases was enriched in metastatic cancers of the cecum and ascending colon (n = 10 of 20 *Fusobacterium*-positive primary-metastasis pairs, P = 0.002), (fig. S5B), whereas cancers that were *Fusobacterium*-negative in both primary and metastatic lesions were more likely to be rectal cancers (n = 29 of 57 of the *Fusobacterium*-negative primary-metastasis pairs, P = 0.016) (fig. S5B).

To assess the relationship between patient survival and *Fusobacterium* presence in the primary cecum and ascending colon, we carried out PathSeq (*29*) analysis on RNA sequencing data from the 430 primary colon adenocarcinomas in the TCGA cohort. Patients with cancer of the cecum and ascending colon exhibited worse overall survival than patients with non-cecum ascending colon cancer (P = 0.01) (fig. S5C). Among patients with cecum and ascending colon tumors, we observed poorer overall survival in correlation with tumor *Fusobacterium* load (fig. S5D) (P = 0.004).

To determine whether *Fusobacterium* is associated with primary liver hepatocellular carcinoma, we performed PathSeq analysis (*29*) of RNA sequencing data from 201 primary liver tumors from the TCGA cohort. This analysis demonstrated that *Fusobacterium* is rare in primary liver carcinomas and that the relative abundance of *Fusobacterium* is significantly enriched in liver metastases arising from colorectal cancers compared with primary liver cancers (P = 0.008) (Fig. 1E).

PathSeq analysis of data from the TCGA cohort also confirmed that the microbes present in liver metastases of *Fusobacterium*-positive colorectal carcinomas are similar to those associated with *Fusobacterium* in primary colorectal carcinoma. *Selenomonas*, *Bacteroides*, and *Prevotella*

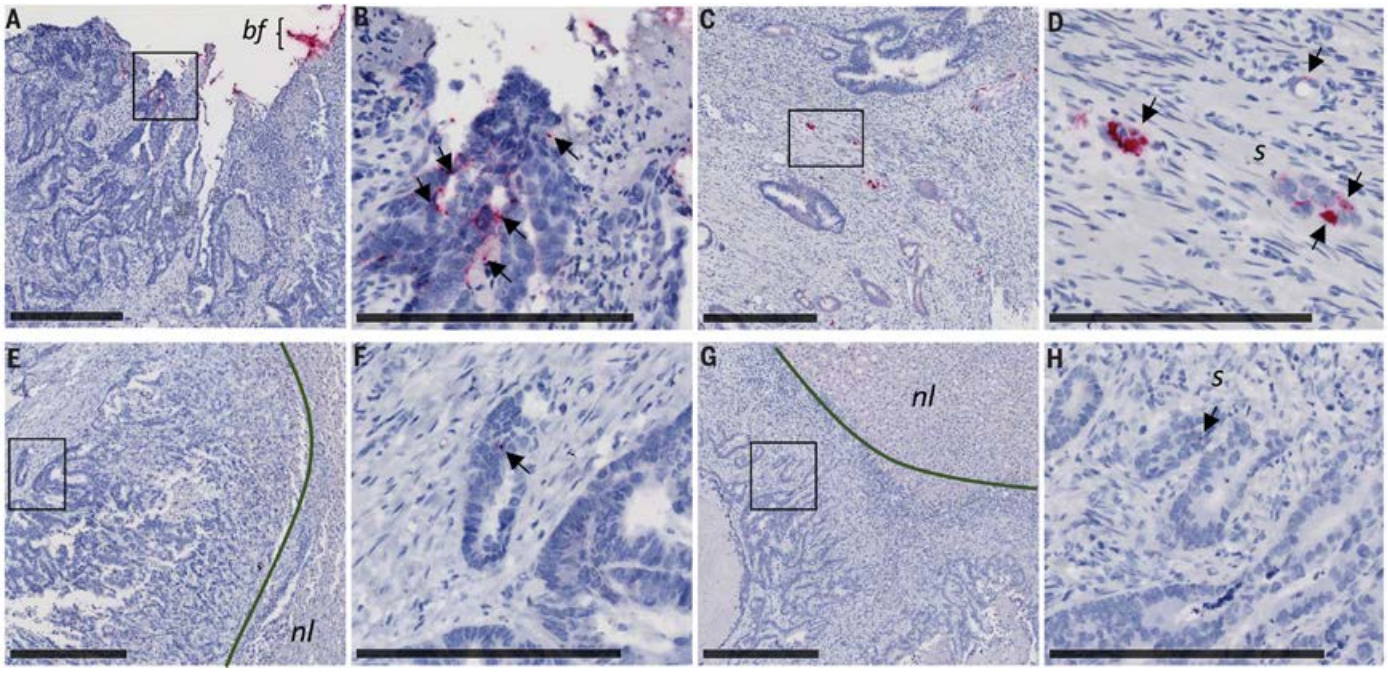

Fig. 2. *F. nucleatum* RNA ISH analysis of matched primary colorectal tumors and liver metastases. Representative images of *F. nucleatum* spatial distribution in paired samples from P187 primary colorectal tumor (**A** and **B**) and liver metastasis (**E** and **F**) and P188 primary colorectal tumor (**C** and **D**) and liver metastasis (**G** and **H**) from the FFPE paired cohort are shown. Arrows indicate cells with histomorphology consistent with that of colon cancer cells infected by invasive *F. nucleatum* (red dots) in both primary colorectal tumors (B and D) and matched liver metastases (F and H). *Fusobacterium*-containing biofilm (bf) is highlighted in the colorectal tumor of P187 (A). *Fusobacterium* was not detected in normal liver (nl) tissue [(E) and (F)]. s, stroma. Panels (B), (D), (F), and (H) show magnification of the boxed areas in (A), (C), (E), and (G), respectively. Scale bars: 500 μm in (A), (C), (E), and (G); 250 μm in (B), (D), (F), and (H).

genera were shared between primary and metastatic colorectal cancers and also correlated with *Fusobacterium* abundance in primary colon adenocarcinoma (Fig. 1F, fig. S7, and table S7).

Given that metastatic colorectal carcinomas harbored cultivable *Fusobacterium* species, we wondered whether viable *Fusobacterium* could persist in xenografts from human colorectal cancers, which would provide a valuable model system for evaluating the effects of microbiota modulation on cancer growth. In a double-blinded approach, 13 fresh human primary colorectal tumors from the xenograft cohort were evaluated, by culture or qPCR, for the presence of *Fusobacterium*. In parallel, these tumors were implanted subcutaneously, by an independent investigator, into Nu/Nu mice to establish patient-derived xenografts (PDXs) (table S8). All five *Fusobacterium*–culture positive tumors resulted in successful xenografts (fig. S8), one of four qPCR-positive but culture-negative tumors gave rise to a successful xenograft, and none of the four *Fusobacterium*-negative tumors generated successful xenografts (P = 0.003). Tumor grade did not appear to significantly influence successful xenograft formation (P = 0.1) (fig. S9A), although we noted a modest association between *Fusobacterium* cultivability and high-grade tumors in this cohort (n = 4 of 5 tumors, P = 0.03) (fig. S9B).

Next, we sought to determine whether *Fusobacterium* species would remain viable and stably associated with a xenograft. A PDX derived from an *F. nucleatum* culture–positive colon cancer (COCA36) was passaged to xenograft generation F8 over 29 weeks and tested for *F. nucleatum*. We cultured *F. nucleatum* from this PDX for up to four generations and 124 days in vivo. All xenograft generations, from F1 through F8, were positive for *Fusobacterium* by qPCR (Fig. 3A). Additionally, we cultured other anaerobic bacteria, including *B. fragilis* and *B. thetaiotaomicron*, from both the primary tumor and PDXs. We further cultured *Fusobacterium* species from PDXs generated from two additional patient tumors (table S9). qPCR and microbiome analysis of fecal pellets and oral swabs from the PDX-bearing animals were negative for *Fusobacterium* species (fig. S10), arguing against the possibility of *Fusobacterium* species arising from the endogenous murine microbiota.

To evaluate the overall microbiome stability and to identify bacteria that are persistently associated with the primary colorectal tumor and derived xenografts, we carried out unbiased total RNA sequencing followed by PathSeq analysis, which revealed that *F. nucleatum* and other Gram-negative anaerobes, including *B. fragilis* and *S. sputigena*, persist in these PDX models for multiple generations (Fig. 3B). The bacteria that persist within the PDX include the genera that we report to persist in distant-site metastases to the liver (Fig. 1C) and that are enriched in *Fusobacterium*-associated colorectal cancer from analysis of TCGA data (Fig. 1F). Bacterial 16*S* rRNA gene sequencing further confirmed the persistence of *Fusobacterium* and co-occurring anaerobes in these primary colorectal tumors and derived xenografts (fig. S11).

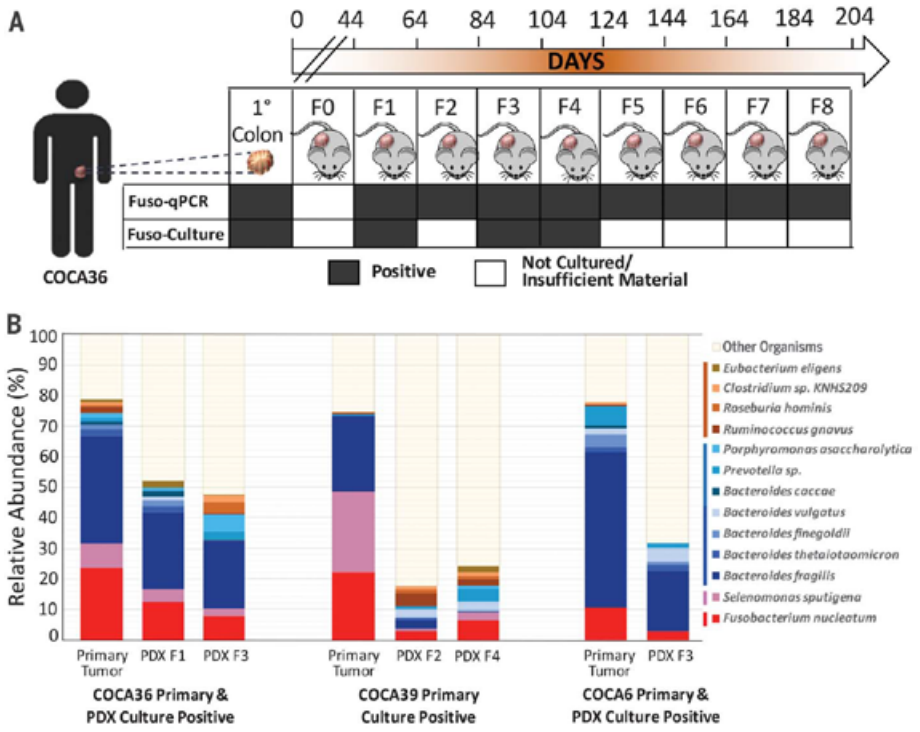

Fig. 3. *Fusobacterium* and co-occurring anaerobes persist in colon adenocarcinoma PDXs. (**A**) Assessment of *Fusobacterium* persistence in PDX COCA36 over a period of 204 days. *Fusobacterium* persistence was determined via microbial culture and *Fusobacterium*-targeted qPCR. F0 denotes the first implantation of the tumor into mice; F1 to F8 represent sequential xenograft passages after F0. (**B**) Species-level microbial composition of three patient primary colon adenocarcinomas (COCA36, COCA39, and COCA6) and subsequent PDXs. Total RNA sequencing was carried out, followed by PathSeq analysis for microbial identification. For simplicity, selected species with >1% relative abundance in the primary tumor and either corresponding PDX are shown. The colors correspond to bacterial taxonomic class. Red, Fusobacteriia; pink, Negativicutes; blue/green, Bacteroidia; orange, Clostridia.

Transmission electron microscopy showed that *F. nucleatum* isolates from both the primary colon carcinoma and PDX were invasive when incubated with human colon cancer cell lines HT-29 and HCT-116. Upon infection with *F. nucleatum*, we saw evidence of bacterial cells within vesicle-like structures in the cancer cell (fig. S12, A to C). We also observed evidence of bacterial adhesion and invasion in the respective patient xenograft tissue (fig. S12D).

Finally, we asked whether treatment of *Fusobacterium*-positive colon cancer xenografts with either (i) an antibiotic to which *Fusobacterium* is resistant or (ii) an antibiotic to which *Fusobacterium* is sensitive would affect tumor growth. We chose erythromycin as a resistant antibiotic because the *F. nucleatum* clinical isolates were resistant to high concentrations of erythromycin (minimum inhibitory concentration >25 μg/ml) (fig. S13A). After oral gavage of the *Fusobacterium*-harboring PDX COCA36, with erythromycin, we observed a slight decrease in tumor volume compared with mice treated with the vehicle control. However, erythromycin did not significantly affect the trajectory of tumor growth (P = 0.073) (fig. S13B), *Fusobacterium* tumor load (P = 0.98) (fig. S13C), or tumor cell proliferation (P = 0.3) (fig. S13D).

For a *Fusobacterium*-killing antibiotic, we chose metronidazole because fusobacteria are known to be highly sensitive to this drug (*30*). We then confirmed sensitivity of the *F. nucleatum* isolate from PDX COCA36 (minimum inhibitory concentration < 0.01 μg/ml) (fig. S14). Because PDXs could not be generated from *Fusobacterium*-negative primary tumors, we treated *Fusobacterium*-free xenografts derived from HT-29 colon adenocarcinoma cells with metronidazole to assess whether metronidazole inhibits the growth of *Fusobacterium*-negative colorectal carcinomas. This experiment revealed no significant change in tumor growth (P = 0.88) (Fig. 4A).

Finally, oral administration of metronidazole to mice bearing *Fusobacterium*-positive PDXs resulted in a statistically significant decrease in the trajectory of tumor growth, compared with PDXs in mice treated with vehicle (P = 0.0005) (Fig. 4A). Treatment with metronidazole was associated with a significant decrease in *Fusobacterium* load in the

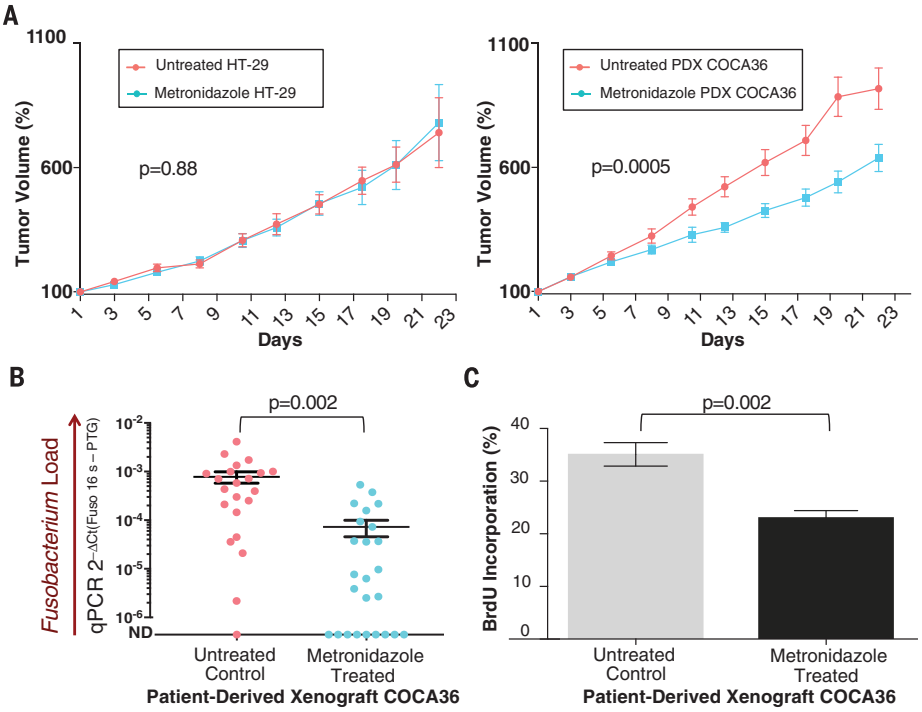

Fig. 4. Treatment of *Fusobacterium*-colonized PDXs with metronidazole reduces tumor growth in vivo. (**A**) (Left) Tumor volume percentage of *Fusobacterium*-free xenografts derived from HT-29 cells treated with metronidazole (treated; 19 animals) or with vehicle (untreated; 20 animals). (Right) Tumor volume percentage of *Fusobacterium*-positive PDX tumors (COCA36) treated with metronidazole (treated; 25 animals) or with vehicle (untreated; 22 animals). *P* values were determined by the Wald test. Tumors were measured in a blinded fashion on Mondays, Wednesdays, and Fridays each week. Error bars represent mean ± SEM. The remaining number of HT-29-derived xenografts and PDX-implanted animals at each time point is included in the supplementary materials. (**B**) Assessment of *Fusobacterium* tissue load. *Fusobacterium*-targeted qPCR on PDX tissue (COCA36) after treatment with metronidazole (treated) or with vehicle (untreated). ND, not detected. The center bar represents the mean; error bars indicate SEM. *P* values were determined using Welch's two-sample *t* test. ΔCt, delta cycle threshold; PTG, prostaglandin transporter. (**C**) Bromodeoxyuridine (BrdU) immunohistochemistry of PDX tumors to assess cell proliferation. The bar plot represents the percentage of cells with BrdU incorporation in treated and untreated PDXs (*n* = 6 animals per arm); error bars denote mean ± SEM. *P* values were determined using the Welch's two-sample *t* test.

tumor tissue ($P = 0.002$) (Fig. 4B), as well as a significant reduction in tumor cell proliferation ($P = 0.002$) (Fig. 4C and fig. S15).

We have shown that (i) *Fusobacterium* is persistently associated with distant metastases from primary human colorectal cancers; (ii) invasive *Fusobacterium* can be detected in liver metastases by ISH; (iii) *Fusobacterium* co-occurs with other Gram-negative anaerobes in primary and matched metastatic tumors; (iv) *Fusobacterium* survives in colorectal cancer PDXs through multiple generations; and (v) treatment of a *Fusobacterium*-harboring PDX model with the antibiotic metronidazole decreases *Fusobacterium* load, cancer cell proliferation, and tumor growth.

The persistence of *Fusobacterium* and its associated microbiome in both metastasis and PDXs, as well as the ability of antibiotic treatment to reduce PDX growth, point to the potential of *Fusobacterium*, and its associated microbiota, to contribute to colorectal cancer growth and metastasis. On the basis of our observation that the dominant microbiome is highly similar in primary-metastatic pairs and the concordance of *Fusobacterium* strains found in primary tumors and paired metastases, we hypothesize that *Fusobacterium* travels with the primary tumor cells to distant sites, as part of metastatic tissue colonization. This suggests that the tumor microbiota are intrinsic and essential components of the cancer microenvironment.

Our results highlight the need for further studies on microbiota modulation as a potential treatment for *Fusobacterium*-associated colorectal carcinomas. One concern is the negative effect of broad spectrum antibiotics on the healthy intestinal microbiota. Given that metronidazole targets a range of anaerobic bacteria, including co-occurring anaerobes that persist with *Fusobacterium*, one would ideally want to develop a *Fusobacterium*-specific antimicrobial agent to assess the effect of selective targeting of *Fusobacterium* on tumor growth. Important questions raised by our findings are whether conventional chemotherapeutic regimens for colorectal cancer will affect the colon cancer microbiota and whether the microbiota will modulate the response to such therapies. A recent study, reporting that colorectal tumors with a high *Fusobacterium* load are more likely to develop recurrence (*21*), supports the concept that *Fusobacterium*-positive tumors may benefit from anti-fusobacterial therapy. Our results provide a strong foundation for pursuing targeted approaches for colorectal cancer treatment directed against *Fusobacterium* and other key constituents of the cancer microbiota.

REFERENCES AND NOTES

1. J. C. Arthur *et al.*, *Science* **338**, 120–123 (2012).
2. M. E. Hope, G. L. Hold, R. Kain, E. M. El-Omar, *FEMS Microbiol. Lett.* **244**, 1–7 (2005).
3. I. R. Rowland, *Curr. Pharm. Des.* **15**, 1524–1527 (2009).
4. S. Wu *et al.*, *Nat. Med.* **15**, 1016–1022 (2009).
5. L. Yang, Z. Pei, *World J. Gastroenterol.* **12**, 6741–6746 (2006).
6. M. Castellarin *et al.*, *Genome Res.* **22**, 299–306 (2012).
7. A. D. Kostic *et al.*, *Genome Res.* **22**, 292–298 (2012).
8. A. N. McCoy *et al.*, *PLOS ONE* **8**, e53653 (2013).
9. T. Tahara *et al.*, *Cancer Res.* **74**, 1311–1318 (2014).
10. L. Flanagan *et al.*, *Eur. J. Clin. Microbiol. Infect. Dis.* **33**, 1381–1390 (2014).
11. M. Ito *et al.*, *Int. J. Cancer* **137**, 1258–1268 (2015).
12. Y. Y. Li *et al.*, *World J. Gastroenterol.* **22**, 3227–3233 (2016).
13. K. Mima *et al.*, *JAMA Oncol.* **1**, 653–661 (2015).
14. K. Mima *et al.*, *Gut* **65**, 1973–1980 (2016).
15. K. Mima *et al.*, *Clin. Transl. Gastroenterol.* **7**, e200 (2016).
16. A. D. Kostic *et al.*, *Cell Host Microbe* **14**, 207–215 (2013).
17. Y. Yang *et al.*, *Gastroenterology* **152**, 851–866.e24 (2017).
18. Y. N. Yu *et al.*, *Oncotarget* **6**, 32013–32026 (2015).
19. M. R. Rubinstein *et al.*, *Cell Host Microbe* **14**, 195–206 (2013).
20. Y. Chen *et al.*, *Oncotarget* **8**, 31802–31814 (2017).
21. T. Yu *et al.*, *Cell* **170**, 548–563.e16 (2017).
22. J. Abed *et al.*, *Cell Host Microbe* **20**, 215–225 (2016).
23. C. Gur *et al.*, *Immunity* **42**, 344–355 (2015).
24. S. Tomkovich *et al.*, *Cancer Res.* **77**, 2620–2632 (2017).
25. R. A. Holt, K. Cochrane, *Gastroenterology* **152**, 694–696 (2017).
26. The Cancer Genome Atlas Network, *Nature* **487**, 330–337 (2012).
27. The Cancer Genome Atlas Research Network, *Cell* **169**, 1327–1341.e23 (2017).
28. J. Yu *et al.*, *Int. J. Cancer* **139**, 1318–1326 (2016).
29. A. D. Kostic *et al.*, *Nat. Biotechnol.* **29**, 393–396 (2011).
30. S. Löfmark, C. Edlund, C. E. Nord, *Clin. Infect. Dis.* **50** (suppl. 1), S16–S23 (2010).

ACKNOWLEDGMENTS

This work was supported by NIH grants (R35 CA197568 to M.M., R35 CA197735 to S.O., K07 CA148894 to K.N., and R01 CA118553 and R01 CA169141 to C.S.F.) and Dana-Farber/Harvard Cancer Center GI SPORE P50 grant CA 127003 to C.S.F. (this grant also supports S.B., A.J.A., W.C.H., K.N., and S.O.). In addition, M.M. is supported by an American Cancer Society Research Professorship; W.C.H. is supported by the Hale Family Center for Pancreatic Cancer; C.S.F. is supported by the Project P Fund for Colorectal Cancer Research, Stand-up-to-Cancer (Colorectal Cancer Dream Team), the Chambers Family Fund for Colorectal Cancer Research, the Team Perry Fund, and the Clark Family Fund for GI Cancer Research; S.B. is supported by a Prevent Cancer Foundation Figdor Family Fellowship; G.S., N.M., E.E., P.N., and J.T. are supported by the Cellex Private Foundation; and P.N. is supported by the Banco Bilbao Vizcaya Argentaria Foundation. M.M. is on the Scientific Advisory Board of and holds stock in OrigiMed, a biotechnology company that provides sequencing information for cancer diagnostics. C.S.F. is on the Board of CytomX Therapeutics, a biotechnology company that is developing therapeutic antibodies for cancer, and is a paid consultant

for Eli Lilly, Genentech, Merck, Sanofi, Five Prime Therapeutics, Merrimack Pharmaceuticals, Bayer, Agios Pharmaceuticals, Taiho Oncology, and KEW Group. M.M. and S.B. are inventors on U.S. Provisional Patent Application no. 62/534,672, submitted by the Broad Institute and Dana-Farber Cancer Institute, that covers targeting of *Fusobacterium* for treatment of colorectal cancer. All raw sequencing data from this study can be accessed at the National Center for Biotechnology Information (NCBI) under the bioproject PRJNA362951. Bacterial whole-genome sequences have been deposited at DNA Data Bank of Japan/European Nucleotide Archive/GenBank, with the following NCBI accession, GenBank assembly accession, and BioSample numbers, respectively: *F. necrophorum* subsp. *funduliforme* P1_CP patient P1 primary colorectal tumor (NPNF00000000, GCA_002761995.1, and SAMN07448029), *F. necrophorum* subsp. *funduliforme* P1_LM patient P1 liver metastasis (NPNE00000000, GCA_002762025.1, and SAMN07448030), *F. nucleatum* subsp. *animalis* P2_CP patient P2 primary colorectal tumor (NPND00000000, GCA_002762005.1, and SAMN07448031), and *F. nucleatum* subsp. *animalis* P2_LM patient P2 liver metastasis (NPNC00000000, GCA_002762015.1, and SAMN07448032).

SUPPLEMENTARY MATERIALS

www.sciencemag.org/content/358/6369/1443/suppl/DC1
Materials and Methods
Figs. S1 to S15
Tables S1 to S9
References (*31*–*43*)

2 December 2016; resubmitted 17 August 2017
Accepted 13 November 2017
Published online 23 November 2017
10.1126/science.aal5240

THIS IS NOT SCIENCE FICTION

This is captivating, impactful *Science*

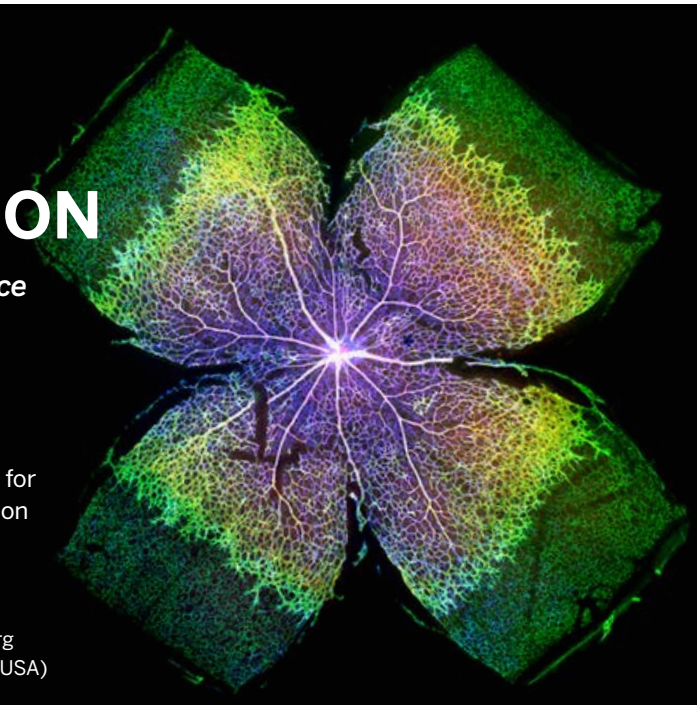

Contact us today to discuss pricing options for adding any of these journals to your collection of *Science* resources.

Institutional Licensing
ScienceMag.org/request | scienceonline@aaas.org
1-866-265-4152 (USA) | +1-202-326-6730 (outside USA)

Science AAAS | Science Advances | Science Immunology | Science Robotics | Science Signaling | Science Translational Medicine

ONCOLOGY

Fundamentals of cancer metabolism

Ralph J. DeBerardinis[1]* and Navdeep S. Chandel[2]*

2016 © The Authors, some rights reserved; exclusive licensee American Association for the Advancement of Science. Distributed under a Creative Commons Attribution NonCommercial License 4.0 (CC BY-NC).
10.1126/sciadv.1600200

Tumors reprogram pathways of nutrient acquisition and metabolism to meet the bioenergetic, biosynthetic, and redox demands of malignant cells. These reprogrammed activities are now recognized as hallmarks of cancer, and recent work has uncovered remarkable flexibility in the specific pathways activated by tumor cells to support these key functions. In this perspective, we provide a conceptual framework to understand how and why metabolic reprogramming occurs in tumor cells, and the mechanisms linking altered metabolism to tumorigenesis and metastasis. Understanding these concepts will progressively support the development of new strategies to treat human cancer.

INTRODUCTION AND OVERARCHING PRINCIPLES

Cancer metabolism is one of the oldest areas of research in cancer biology, predating the discovery of oncogenes and tumor suppressors by some 50 years. The field is based on the principle that metabolic activities are altered in cancer cells relative to normal cells, and that these alterations support the acquisition and maintenance of malignant properties. Because some altered metabolic features are observed quite generally across many types of cancer cells, reprogrammed metabolism is considered a hallmark of cancer (*1*, *2*). Precisely how metabolism becomes reprogrammed in cancer cells, whose functions or malignant properties are enabled by these activities, and how to exploit metabolic changes for therapeutic benefit are among the key questions driving research in the field.

This review covers several fundamental principles in cancer metabolism, with the goal of introducing non-experts to the concepts motivating ongoing research. With the explosion of research in cancer metabolism over the past decade, no single review can possibly cover it all. The sections below highlight some of the essential, recent papers supporting these core principles. An overarching theme in cancer metabolism is that reprogrammed activities improve cellular fitness to provide a selective advantage during tumorigenesis. Most of the classical examples of reprogrammed activities either support cell survival under stressful conditions or allow cells to grow and proliferate at pathologically elevated levels. Three of these—altered bioenergetics, enhanced biosynthesis, and redox balance—are discussed at length below. It logically flows that if these activities provide benefit to the malignant cell, then some of them might be suitable therapeutic targets. This rendering of cancer metabolism is supported by many examples in which inhibition of an enhanced metabolic activity results in impaired growth of experimental tumors (*3*, *4*). In some cases, the particular metabolic liabilities of cancer cells have been translated into effective therapies in human cancer. Asparaginase, an enzyme that converts the amino acid asparagine to aspartic acid and ammonia, is an essential component of treatment for acute lymphoblastic leukemia (ALL) (*5*). Because of their high rates of protein synthesis and poor ability to synthesize asparagine de novo, ALL cells require a constant supply of asparagine from the plasma. This supply is essentially eliminated by systemic administration of asparaginase. Ultimately, effective metabolic therapy will require defining the stage of tumor progression in which each pathway provides its benefit to the cancer cell. Some activities first become essential very early in tumorigenesis as the nascent tumor begins to experience nutrient limitations (*6*). In other cases, altered pathways may be dispensable in primary tumors but essential for metastasis (*7*, *8*). Because new therapeutic targets are nominated from simple experimental models like cultured cells, it will be essential to define their context-specific roles in biologically accurate models of tumor initiation and progression.

METABOLIC REPROGRAMMING AND ONCOMETABOLITES IN CANCER

Altered metabolic activity supports anabolic growth during nutrient-replete conditions, catabolism to support cell survival during nutrient limitation, and fortification of redox homeostatic systems to counteract the metabolic effects of oncogene activation, tumor suppressor loss, and other stresses (*9*). Discovery and characterization of reprogrammed activities may provide opportunities to image tumor tissue noninvasively, predict tumor behavior, and prevent tumor progression by blocking essential pathways. It is important to differentiate "metabolic reprogramming" from "oncometabolites," two terms widely used in the recent cancer metabolism literature (*10*). We propose that the term metabolic reprogramming be used to describe conventional metabolic pathways whose activities are enhanced or suppressed in tumor cells relative to benign tissues as a consequence of tumorigenic mutations and/or other factors. Oncometabolite is a relatively new term that refers to metabolites whose abundance increases markedly in tumors. We suggest that this term be reserved for metabolites for which (i) there is a clear mechanism connecting a specific mutation in the tumor to accumulation of the metabolite, and (ii) there is compelling evidence for involvement of the metabolite in the development of malignancy.

The classical example of a reprogrammed metabolic pathway in cancer is the Warburg effect or aerobic glycolysis (*11*). Glycolysis is a physiological response to hypoxia in normal tissues, but Otto Warburg in the 1920s observed that tumor slices and ascites cancer cells constitutively take up glucose and produce lactate regardless of oxygen availability, an observation that has been seen in many types of cancer cells and tumors (*12*). The increase in glycolytic flux allows glycolytic

[1]Children's Medical Center Research Institute, University of Texas Southwestern Medical Center, Dallas, TX 75390, USA. [2]Department of Medicine, Northwestern University Feinberg School of Medicine, Chicago, IL 60611, USA.
*Corresponding author. Email: Ralph.Deberardinis@UTSouthwestern.edu (R.J.D.); nav@northwestern.edu (N.S.C.)

intermediates to supply subsidiary pathways to fulfill the metabolic demands of proliferating cells (*11*). Like glycolytic intermediates, tricarboxylic acid (TCA) cycle intermediates are also used as precursors for macromolecule synthesis (*13*). Their utilization in biosynthetic pathways requires that carbon be resupplied to the cycle so that intermediate pools are maintained; pathways that "refill" the cycle are termed anaplerotic pathways, and they generate TCA cycle intermediates that can enter the cycle at sites other than acetyl-CoA (coenzyme A) (*14*). Two activities that provide anaplerotic fluxes in cancer cells are glutaminolysis, which produces α-ketoglutarate from glutamine, and pyruvate carboxylation, which produces oxaloacetate from glucose/pyruvate. Oxidation of the branched-chain amino acids (BCAAs) isoleucine and valine also provides an anaplerotic flux in some tissues.

Despite the incredible genetic and histological heterogeneity of tumors, malignancy seems to involve the common induction of a finite set of pathways to support core functions like anabolism, catabolism, and redox balance (*15*). The general induction of these pathways may reflect their regulation by signaling pathways that are commonly perturbed in cancer cells (Fig. 1). Normal cells, upon stimulation by growth factors, activate phosphatidylinositol 3-kinase (PI3K) and its downstream pathways AKT and mammalian target of rapamycin (mTOR), thereby promoting a robust anabolic program involving increased glycolytic flux and fatty acid synthesis through activation of hypoxia-inducible factor–1 (HIF-1) and sterol regulatory element–binding protein (SREBP), respectively (*16*). Tumor cells very frequently contain mutations that allow the PI3K-AKT-mTOR network to achieve high levels of signaling with minimal dependence on extrinsic stimulation by growth factors (*17*). Many of the best-characterized oncogenes and tumor suppressors reside in the PI3K-AKT-mTOR network, and aberrant activation of this pathway is among the most frequent alterations seen in a diverse set of cancers.

Another commonly deregulated pathway in cancer is gain of function of MYC by chromosomal translocations, gene amplification, and single-nucleotide polymorphisms. MYC increases the expression of many genes that support anabolic growth, including transporters and enzymes involved in glycolysis, fatty acid synthesis, glutaminolysis, serine metabolism, and mitochondrial metabolism (*18*). Oncogenes like Kras, which is frequently mutated in lung, colon, and pancreatic cancers, co-opt the physiological functions of PI3K and MYC pathways to promote tumorigenicity. Aside from oncogenes, tumor suppressors such as the p53 transcription factor can also regulate metabolism (*19*). The p53 protein–encoding gene *TP53* (tumor protein p53) is mutated or deleted in 50% of all human cancers. The tumor-suppressive functions of p53 have been ascribed to execution of DNA repair, cell cycle arrest, senescence, and apoptosis. However, recent studies indicate that p53 tumor-suppressive actions might be independent of these canonical p53 activities but rather dependent on the regulation of metabolism and oxidative stress (*20*, *21*). Loss of p53 increases glycolytic flux to promote anabolism and redox balance, two key processes that promote tumorigenesis (*19*).

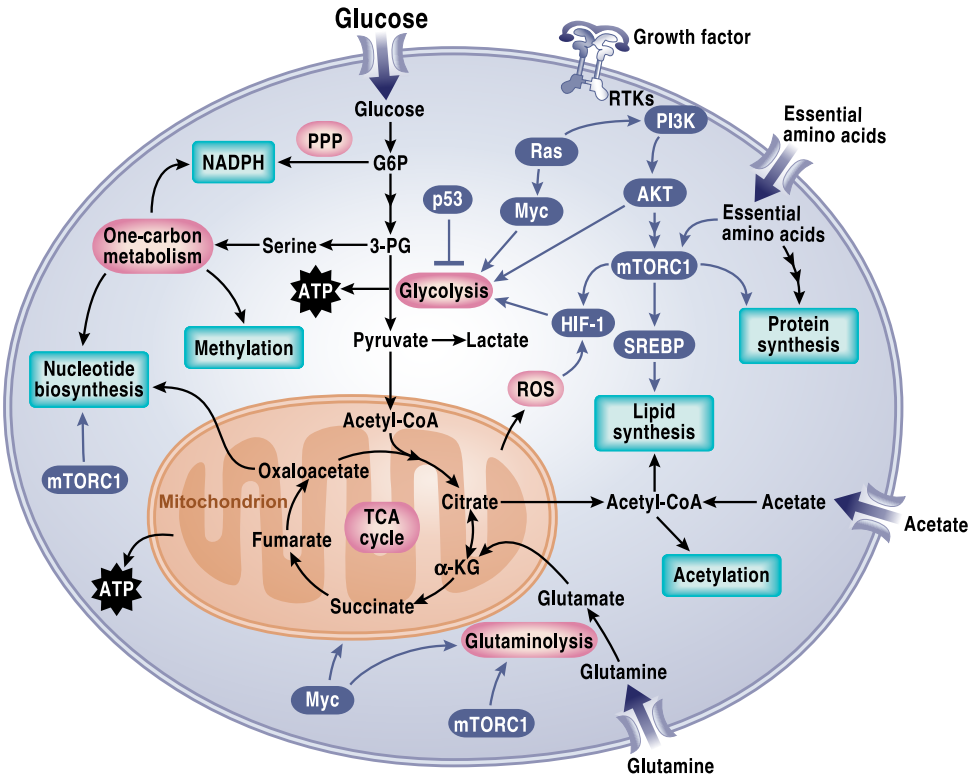

Fig. 1. Signaling pathways that regulate cancer metabolism. Tumor cells have aberrant activation of mTORC1 that induces an anabolic growth program resulting in nucleotide, protein, and lipid synthesis. Loss of tumor suppressors like p53 or activation of oncogenes like MYC further promotes anabolism through transcriptional regulation of metabolic genes. Metabolism controls signaling through regulating reactive oxygen species (ROS), acetylation, and methylation. PPP, pentose phosphate pathway; G6P, glucose-6-phosphate; 3-PG, 3-phosphoglycerate; ATP, adenosine 5′-triphosphate; mTORC1, mTOR complex 1; α-KG, α-ketoglutarate; RTK, receptor tyrosine kinase.

A salient feature of many tumors is that they reside in a low-oxygen environment (hypoxia) ranging from 0 to 2% O_2 because the tumor cell proliferation rate often exceeds the rate of new blood vessel formation (angiogenesis) (*22*). The metabolic adaptation to hypoxia is coordinated by HIF-1, which induces metabolic genes involved in increasing glycolytic flux (*23*). Some tumors display constitutive activation of HIF-1 under normoxic conditions through a variety of mechanisms, including (i) hyperactivation of mTORC1, (ii) loss of von Hippel–Lindau, (iii) accumulation of ROS, and (iv) accumulation of the TCA cycle metabolites succinate or fumarate due to cancer-specific mutations in succinate dehydrogenase (SDH) or fumarate hydratase (FH), respectively (*24*).

The robust coordinated induction of metabolic pathways that support tumorigenesis by combination of deregulation of PI3K-AKT-mTOR signaling pathways, loss of tumor suppressors, and activation of oncogenes alleviates the necessity of having mutations or amplifications in metabolic enzymes per se. Thus, examples of metabolic enzyme deregulation through genetic mutation are rare. One example is the elevated expression of phosphoglycerate dehydrogenase (PHGDH) due to amplification in a fraction of breast cancer and melanoma (*25*, *26*). PHGDH catalyzes the conversion of the glycolytic intermediate 3-phosphoglycerate to 3-phosphohydroxypyruvate in the first step of the serine biosynthesis pathway. Serine metabolism supplies methyl groups to the one-carbon and folate pools contributing to nucleotide synthesis, methylation reactions, and NADPH (reduced nicotinamide adenine dinucleotide phosphate) production (*27*). Inhibiting serine biosynthesis by silencing PHGDH in cells with high levels of this enzyme results in growth suppression, and the enzyme displays oncogenic properties in gain of function assays (*25*, *26*).

The other examples of mutational deregulation of metabolic enzymes are those that generate oncometabolites. The current list of true oncometabolites is short (*28*). The term is most commonly and appropriately applied to D-2-hydroxyglutarate (D2HG), a reduced form of the TCA cycle intermediate α-ketoglutarate. D2HG is scarce in normal tissues but rises to millimolar concentrations in tumors with mutations in isocitrate dehydrogenase 1 or 2 (IDH1 or IDH2). These mutations occur commonly in gliomas, acute myelogenous leukemias (AMLs), and other types of cancer (*29*–*31*). D2HG and its relationship to mutant IDH1 and IDH2 have been reviewed extensively elsewhere (*32*). The most relevant point here is that D2HG production requires a neomorphic enzyme activity imparted to IDH1/IDH2 by specific active-site mutations (*33*, *34*). High levels of D2HG interfere with the function of dioxygenases requiring α-ketoglutarate as a cosubstrate. These include prolyl hydroxylases, cytosine hydroxylases, and histone demethylases, whose inhibition influences gene expression in part via an altered epigenetic state characterized by a failure to express differentiation programs (*35*–*41*). Thus, although D2HG arises from an alteration of the metabolic network, its role in cancer seems to depend on nonmetabolic effects. Currently, D2HG is being used as a biomarker for disease monitoring, and inhibitors specific to mutants IDH1/IDH2 are in clinical trials for AML and solid tumors.

The metabolite 2HG also exists as the enantiomer L-2HG (L2HG), which is not produced by mutant forms of IDH1/IDH2. This metabolite arises from the noncanonical activity of various dehydrogenases, including malate dehydrogenase and lactate dehydrogenase, whose promiscuous behavior reduces α-ketoglutarate to L2HG (*42*–*44*). L2HG may be oxidized back to α-ketoglutarate by a FAD-linked enzyme, L2HG dehydrogenase (L2HGDH). L2HGDH deficiency, also called L2HG aciduria, is a rare neurometabolic disease of childhood caused by the inheritance of biallelic mutations in the gene encoding L2HGDH (*45*). Affected children have seizures, mental retardation, white matter abnormalities of the brain, and systemically elevated levels of L2HG. Remarkably, a number of these children have developed malignant brain tumors (*46*), providing an early clue to the significance of D2HG in IDH1/IDH2-mutant gliomas and raising the question of whether L2HG is also an oncometabolite. L2HG and D2HG exhibit different effects on dioxygenase function (*38*), suggesting that the sensitivity of a particular tissue to the presence of either metabolite may depend on which dioxygenases are expressed. Recent work has demonstrated modest accumulation of L2HG in cells experiencing hypoxia or electron transport chain (ETC) dysfunction (*42*, *47*) and in human renal cell carcinomas, which frequently display epigenetic silencing of L2HGDH (*48*). It is unknown whether reducing L2HG levels in these settings will promote cellular differentiation or suppress tumor progression.

The principle that oncometabolites exert their effects outside of the conventional metabolic network also applies to the other two molecules that can reasonably be called oncometabolites: fumarate and succinate (*28*). Both are TCA cycle intermediates found throughout the body, but some tumors accumulate massive levels of fumarate and/or succinate as a consequence of loss-of-function mutations in FH or the SDH complex, respectively (*49*–*51*). Although these mutations markedly reprogram metabolism by impairing TCA cycle flux, the extent to which fumarate and succinate participate in cancer development likely involves their nonmetabolic functions (*28*). Like D2HG, evidence indicates that succinate and fumarate interfere with dioxygenase activity, supporting the notion that a general property of oncometabolites is the ability to regulate epigenetics (*52*, *53*). PHGDH overexpression and mutations in IDH1/IDH2, SDH, and FH all alter metabolite levels that control epigenetics (*54*). Several other metabolites, including acetyl-CoA, α-ketoglutarate, and *S*-adenosylmethionine also participate in epigenetic reprogramming, and time will tell whether genetically specific alterations of these metabolites in tumors promote tumorigenesis (*54*). Some metabolites, notably fumarate, covalently bind to sulfhydryl groups in glutathione, proteins, and peptides, altering their function and perhaps accounting for another mechanism by which oncometabolites promote or perpetuate malignant phenotypes (*55*–*58*).

BIOENERGETICS

Otto Warburg's hypothesis that cancer cells take up glucose and generate a substantial amount of lactate in the presence of ambient oxygen due to impaired mitochondrial function led to the widely held misconception that cancer cells rely on glycolysis as their major source of ATP (*59*, *60*). Today, it is clear that cancer cells exhibit aerobic glycolysis due to activation of oncogenes, loss of tumor suppressors, and up-regulation of the PI3K pathway, and that one advantage of high glycolytic rates is the availability of precursors for anabolic pathways (*2*, *61*). Warburg's observation that tumors display a high rate of glucose consumption has been validated in many human cancers with fluorodeoxyglucose positron emission tomography, which uses a radioactive glucose analog to image glucose uptake in tumors and adjacent normal tissue. Nevertheless, many studies have demonstrated that the great majority of tumor cells have the capacity to produce energy through glucose oxidation (that is, the process by which glucose-derived carbons enter the TCA cycle and are oxidized to CO_2, producing ATP through oxidative phosphorylation). Furthermore, limiting glycolytic ATP production by inhibiting

the activity of pyruvate kinase fails to prevent tumorigenesis, suggesting that the major role of glycolysis is not to supply ATP (*62*). Moreover, mitochondrial metabolism is necessary for cancer cell proliferation and tumorigenesis (*63*–*65*). Thus, despite their high glycolytic rates, most cancer cells generate the majority of ATP through mitochondrial function, with the likely exception of tumors bearing mutations in enzymes involved in mitochondrial respiration (for example, SDH and FH) (*66*). Nevertheless, cells harboring mutations in FH or SDH still rely on mitochondrial metabolism by metabolically rewiring themselves to provide the necessary TCA cycle intermediates and ROS for cell proliferation (*55*, *67*–*70*).

In addition to pyruvate derived from glycolysis, fatty acids and amino acids can supply substrates to the TCA cycle to sustain mitochondrial ATP production in cancer cells (Fig. 2). The breakdown of fatty acids (β-oxidation) in the mitochondria generates acetyl-CoA and the reducing equivalents NADH and $FADH_2$, which are used by the ETC to produce mitochondrial ATP. The amino acid glutamine can generate glutamate and subsequently α-ketoglutarate to fuel the TCA cycle through a series of biochemical reactions termed glutaminolysis (*71*). Furthermore, the BCAAs isoleucine, valine, and leucine, which are elevated in plasma of patients with pancreatic cancers, can be converted into acetyl-CoA and other organic molecules that also enter the TCA cycle (*72*). The metabolic flexibility afforded by multiple inputs into the TCA cycle allows cancer cells to adequately respond to the fuels available in the changing microenvironment during the evolution of the tumor (*9*). A combination of the local tumor microenvironment and oncogenic lesions is likely to dictate the fuel used by mitochondria to sustain tumor growth.

Solid tumors contain significant heterogeneity of perfusion, such that many tumor cells reside in nutrient- and oxygen-poor environments. Cancer cells have therefore adapted multiple mechanisms to sustain mitochondrial function for survival. For example, the mitochondrial ETC can function optimally at oxygen levels as low as 0.5% (*73*). Moreover, hypoxic tumor cells (<2% O_2) can continue to cycle and use glutamine as a fuel for oxidative ATP production (*74*–*76*). Kras-driven pancreatic cancer cells in nutrient-depleted conditions use proteins scavenged from the extracellular space to produce glutamine and other amino acids to fuel the TCA cycle for cell survival and growth (Fig. 2) (*77*). Furthermore, if pyruvate oxidation to acetyl-CoA is compromised by hypoxia or ETC impairment, glutamine can provide acetyl-CoA as a biosynthetic precursor to sustain tumor growth (*69*, *78*, *79*).

When tumor cells become nutrient-deprived, they adapt to the microenvironment by decreasing their demand for ATP. The resultant increase in ATP availability maintains an adequate ATP/ADP (adenosine 5′-diphosphate) ratio to drive unfavorable biological reactions. The anabolic kinase mTOR, discussed in greater detail below, drives the energetically demanding growth of tumor cells. This kinase is inhibited when amino acids and oxygen levels are diminished (*80*). Furthermore, decreased mTOR activity increases autophagic flux. In oncogenic Kras- or Braf-driven non–small-cell lung cancer (NSCLC) cells, autophagy provides an intracellular glutamine supply to sustain mitochondrial function (*81*, *82*). To survive the hypoxic tumor microenvironment, cancer cells also diminish their demand for ATP by decreasing highly demanding ATP-dependent processes, such as running the Na/K-dependent adenosine triphosphatase. If diminishing ATP demand is not sufficient to maintain ATP/ADP ratio, the rise in ADP activates adenylate kinase, a phosphotransferase enzyme that buffers the fall in ATP levels by converting two ADP molecules into adenosine 5′-monophosphate (AMP) and ATP (*83*). The rise in AMP during nutrient deprivation triggers the activation of AMP kinase (AMPK), which activates catabolic pathways like fatty acid oxidation to stimulate ATP production (*84*). In conditions of metabolic stress, certain Ras-driven cancer cells scavenge lipids to support ATP production (*85*). Ovarian cancer cells use fatty acids from neighboring adipocytes to fuel mitochondrial ATP production (*86*). Thus, there are multiple mechanisms by which cancer cells maintain their ATP/ADP ratio to sustain viability in nutrient- and oxygen-poor environments.

BIOSYNTHESIS OF MACROMOLECULES

Biosynthetic or anabolic pathways are an essential aspect of cancer metabolism because they enable cells to produce the macromolecules required for replicative cell division and tumor growth. As a general theme, these pathways involve the acquisition of simple nutrients (sugars, essential amino acids, etc.) from the extracellular space, followed by their conversion into biosynthetic intermediates through core metabolic pathways like glycolysis, the PPP, the TCA cycle, and nonessential amino acid synthesis, and finally the assembly of larger and more complex molecules through ATP-dependent processes (Fig. 3). The three macromolecular classes most commonly studied in cancer metabolism are proteins, lipids, and nucleic acids, which comprise approximately 60, 15, and 5% of the dry mass of mammalian cells, respectively. Evidence indicates that biosynthesis of all three classes is under the control of the same signaling pathways that govern cell growth and are activated in cancer via tumorigenic mutations, particularly PI3K-mTOR signaling.

Protein biosynthesis is highly regulated and requires access to a full complement of essential and nonessential amino acids. Cancer cells and other cells under the influence of growth factor signaling express surface transporters that allow them to acquire amino acids from the extracellular space (*87*). This not only provides cells with the raw materials needed for protein synthesis but also allows them to maintain activity of the mTOR signaling system, specifically mTORC1. mTORC1 is stimulated by the presence of amino acids and activates protein synthesis via its effects on translation and ribosome biogenesis (*80*). Most nonessential amino acids are produced through transamination reactions, which transfer the amino group from glutamate to a ketoacid. Proliferating cancer cells take up glutamine and convert it to glutamate through a variety of deamidation and transamidation reactions, most notably the mitochondrial amidohydrolase glutaminase (*71*). Together, these enzymes generate a large intracellular glutamate pool available for nonessential amino acid synthesis. Both glutamine uptake and glutaminase activity are stimulated by mTORC1, providing glutamate for transamination reactions and/or maintenance of the TCA cycle, which also contributes to amino acid synthesis. Furthermore, when the intracellular glutamine supply exceeds the cell's demands, glutamine can be exported in exchange for essential amino acids to stimulate mTORC1 and protein synthesis (*88*). Thus, growth conditions in which glutamine and essential amino acids are abundant enable mTORC1-mediated activation of protein synthesis.

When nutrients are scarce, cells have access to a number of catabolic pathways to degrade macromolecules and resupply key pools of intracellular metabolic intermediates. Protein degradation pathways have been characterized extensively as mechanisms to supply amino acids in cancer cells. Intracellular proteins and other macromolecules can be recycled through autophagy, a highly regulated process through which proteins and organelles are delivered to the lysosome and degraded (*89*). Autophagy is an essential survival pathway during nutrient or growth factor deprivation, and genetic studies demonstrate that it contributes to

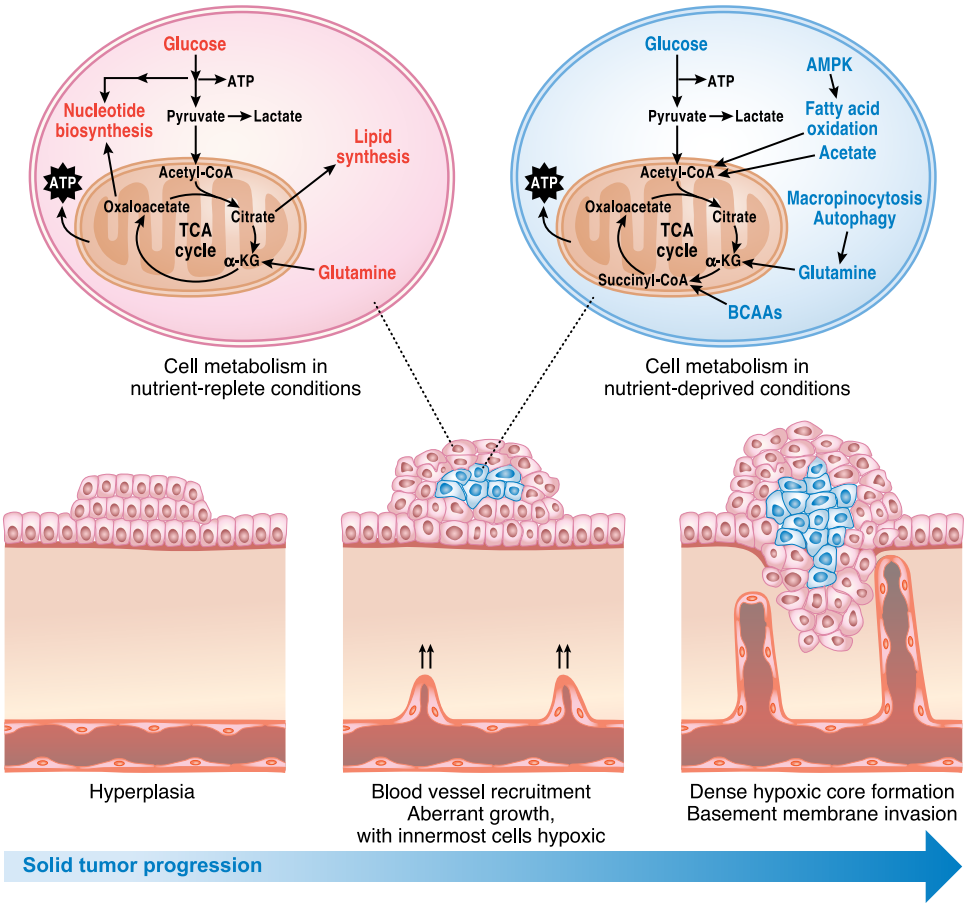

Fig. 2. Metabolic pathways under nutrient-replete and nutrient-deprived conditions. Accessibility to nutrients within solid tumors is regulated by proximity to the vasculature. Cells located adjacent to the vasculature use nutrients and oxygen to fuel anabolic pathways that support proliferation. However, cells distant from the vasculature have diminished accessibility to nutrients and oxygen and may engage in alternative forms of metabolism including oxidation of fatty acids and BCAAs as well as macromolecular degradation through autophagy and macropinocytosis to support cell viability.

some forms of cancer in mice (*90*, *91*). However, because autophagy supplies amino acids through protein degradation, it does not serve as a source of net protein synthesis. It is also potently suppressed by mTORC1. Macropinocytosis allows cells to internalize proteins and other components of the extracellular milieu and deliver them for degradation via the endocytic pathway. Under conditions of nutrient depletion, macropinocytosis supplies both nitrogen and carbon to central metabolic pathways (*92*). Evidence indicates that extracellular protein degradation, like autophagy, is suppressed by mTORC1 (*93*). Suppressing pathways of protein degradation may help maximize rates of net protein synthesis when extracellular amino acids are available and mTORC1 is active.

Tumor cells rapidly produce fatty acids for membrane biosynthesis, lipidation reactions, and cellular signaling. Fatty acid synthesis requires sources of acetyl-CoA and reducing power in the form of cytosolic NADPH; effective fatty acid synthesis therefore requires integration with other pathways of carbon and redox metabolism. In most cultured cells, glucose is the most prominent acetyl-CoA source for fatty acid synthesis (*94*, *95*). Glutamine and acetate have been demonstrated to provide alternative carbon sources when access to glucose-derived acetyl-CoA is impaired by hypoxia or mitochondrial dysfunction (*69*, *78*, *79*, *96*). Leucine degradation can also supply acetyl-CoA in some cell lines (*97*). The relative importance of these nutrients for fatty acid synthesis in vivo is unknown, although early studies suggested that most fatty acyl carbon in experimental tumors is derived from glucose (*98*, *99*). Isotopic tracing experiments designed to assess the cytosolic NADPH pool have recently suggested that most NADPH used for fatty acid synthesis arises from the PPP (*100*, *101*).

Transcription of genes involved in fatty acid synthesis is regulated by the SREBP-1 transcription factor (*102*). SREBP-1 regulates not only the enzymes needed to convert acetyl-CoA into fatty acids but also the enzymes of the PPP and pathways required to convert acetate and glutamine into acetyl-CoA (*103*). This transcription factor therefore regulates genes encoding proteins that catalyze or facilitate fatty acid synthesis. In lipid-replete conditions, SREBP-1's transcriptional activity is suppressed by its sequestration in the endoplasmic reticulum. Under conditions of sterol depletion, proteolytic cleavage releases the transcriptionally active domain, which travels to the nucleus and binds to sterol response elements in the promoters of lipogenic genes (*104*).

In cancer cells with constitutively high rates of fatty acid synthesis, additional mechanisms help keep SREBP-1 in a transcriptionally active state. mTORC1 signaling, via its effector S6 kinase (S6K), activates a transcriptional program that includes both SREBP-1 and the related protein SREBP-2, which regulates transcription of genes in sterol biosynthesis

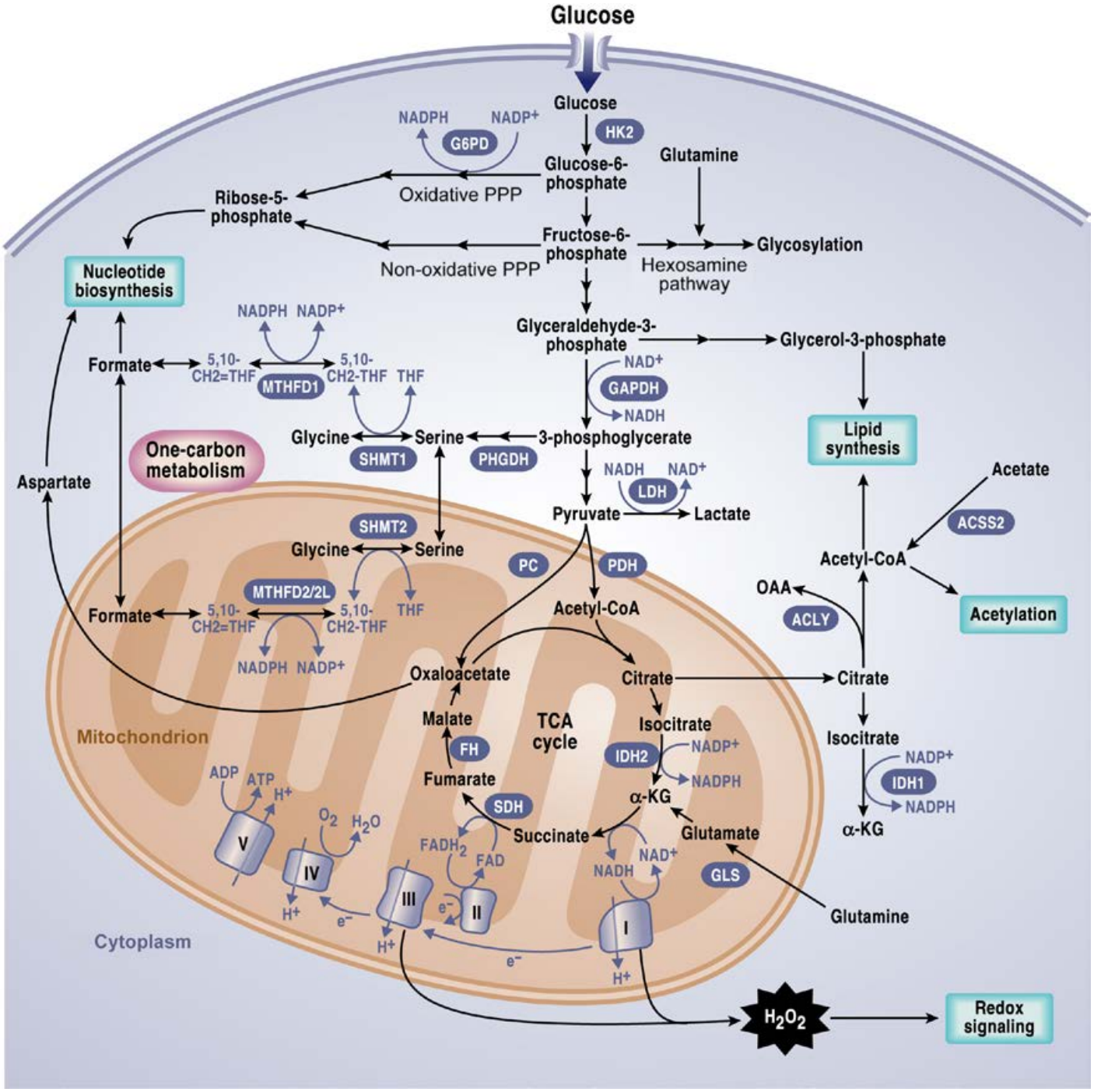

Fig. 3. Anabolic pathways that promote growth. Glucose metabolism generates glycolytic intermediates that can supply subsidiary pathways including the hexosamine pathway, PPP, and one-carbon metabolism, all of which support cell growth. Mitochondrial TCA cycle intermediates such as oxaloacetate (OAA) and citrate are used to generate cytosolic aspartate and acetyl-CoA for nucleotide and lipid synthesis, respectively. Mitochondria also generate H_2O_2 and acetyl-CoA for redox signaling and acetylation, respectively. NADPH is used to drive anabolic reactions and to maintain antioxidant capacity. Cytosolic sources of NADPH include the oxidative PPP, IDH1, and enzymes from one-carbon metabolism including MTHFD1. Mitochondrial sources of NADPH include MTHFD2, MTHF2L, and IDH2. HK2, hexokinase 2; G6PDH, glucose-6-phosphate dehydrogenase; GAPDH, glyceraldehyde-3-phosphate dehydrogenase; LDH, lactate dehydrogenase; ACLY, ATP citrate lyase; GLS, glutaminase; SHMT, serine hydroxymethyltransferase; MTHFD2, methylenetetrahydrofolate dehydrogenase 2; MTHFD2L, MTHFD2-like; ACSS2, acyl-CoA synthetase short-chain family member 2; THF, tetrahydrofolate.

(*103*). Both SREBP-1 and SREBP-2 are required for mTORC1-mediated cell proliferation. The mechanism of SREBP activation by mTORC1 is incompletely understood but involves nuclear entry of the phosphatidic acid phosphatase Lipin-1, which enhances nuclear SREBP abundance and activity on the promoters of lipogenic genes (*105*).

Both fatty acids and lipids can also be acquired from the extracellular space to supply membrane biosynthesis. PI3K signaling activates fatty acid uptake and suppresses fatty acid oxidation, thereby maximizing lipogenesis in proliferating cells under the control of growth factors (*106*). Lipid uptake may acquire further importance during conditions of metabolic stress, when the ability to meet oncogene-driven demands for biosynthesis is compromised. The ability to scavenge lysophospholipids (lipid intermediates containing a glycerophosphate backbone with one acyl chain) is required for maximal cancer cell growth during hypoxia, which suppresses de novo fatty acid synthesis from glucose (*85*). Furthermore, in cancer cells with constitutive mTORC1 signaling, hypoxia induces a state of dependence on access to extracellular desaturated fatty acids to maintain endoplasmic reticulum integrity in support of protein biosynthesis (*107*). Notably, SREBP-1 was first identified as the transcription factor responsible for expression of the low-density lipoprotein receptor (LDLR) (*108*), implying that enhanced de novo lipogenesis occurs concomitantly with enhanced import of lipids from the extracellular space. These parallel pathways appear to be essential in glioma, where oncogenic activation of epidermal growth factor receptor (EGFR) signaling stimulates SREBP-1 and expression of LDLR (*109*). These cancer cells are highly sensitive to inhibitors of fatty acid and cholesterol biosynthesis. Inhibition of the EGFR-PI3K signaling axis but not of mTORC1 suppresses nuclear translocation of SREBP-1 in glioma cells with oncogenic EGFR, suggesting an alternate, mTORC1-independent mode of SREBP-1 activation in glioma cells (*109*). This transcriptional program includes LDLR expression and induces reliance on cholesterol uptake to maintain the intracellular pool (*110*). Impairing intracellular cholesterol availability by activating liver X receptor induced cell death both in culture and in vivo, suggesting a pharmacological approach to silence lipogenic programs in glioma (*110*).

Purine and pyrimidine nucleotides are required for synthesis of RNA and DNA. De novo biosynthesis of nucleotides is complex, requiring input from several pathways in a coordinated fashion. The phosphoribosylamine backbone of these molecules is produced from ribose-5-phosphate, an intermediate of the PPP, and an amide donation reaction using glutamine as a substrate (*111*). The purine and pyrimidine bases are constructed from various nonessential amino acids and methyl groups donated from the one-carbon/folate pool. The TCA cycle contributes oxaloacetate, which is transaminated to aspartate, an intermediate required to synthesize both purine and pyrimidine bases. Conversion of ribonucleotides to deoxynucleotides by ribonucleotide reductase requires a source of NADPH. Well-characterized mechanisms of feedback inhibition exist to prevent excessive accumulation of nucleotides, and mutations interrupting these mechanisms can produce pathological accumulation of nucleotide intermediates (for example, precipitation of uric acid crystals in gout).

Clearly, nucleotide biosynthesis is a targetable vulnerability in cancer cells because nucleoside analogs and antifolates have been a mainstay of chemotherapeutic regimens for decades (*112*). However, relatively little is known about how oncogenic signaling interfaces with nucleotide biosynthesis. It is likely that the effects of numerous signaling pathways on glucose and amino acid metabolism influence the availability of precursors for purines and pyrimidines. In the case of mTORC1, evidence points to a distinct mechanism by which activation of the signaling pathway enables nucleotide biosynthesis. The mTORC1 effector ribosomal S6K1 phosphorylates the trifunctional enzyme CAD (carbamoylphosphate synthetase 2, aspartate transcarbamoylase, dihydroorotase), which catalyzes the first three steps of pyrimidine synthesis (*113*). Phosphorylation on CAD S1859 is required for mTORC1-dependent stimulation of pyrimidine biosynthesis (*113*). Additional work is needed to determine how other aspects of de novo nucleotide synthesis, purine and pyrimidine salvage pathways, and accessory activities like folate metabolism are regulated in cancer cells in support of cell proliferation.

REDOX BALANCE

ROS are intracellular chemical species that contain oxygen and include the superoxide anion (O_2^-), hydrogen peroxide (H_2O_2), and the hydroxyl radical (OH·) (*114*). The mitochondria and cytosolic NADPH oxidases (NOXs) produce O_2^- from the one-electron reduction of oxygen (*115*). O_2^- is converted into H_2O_2 by the enzymatic activity of superoxide dismutase 1 or 2, which are localized to the cytosol or mitochondrial matrix, respectively. H_2O_2 is subsequently detoxified to water by the enzymatic activity of mitochondrial and cytosolic peroxiredoxins (PRXs), which, as a consequence, undergo H_2O_2-mediated oxidation of their active-site cysteines (*116*). Thioredoxin (TXN), thioredoxin reductase (TrxR), and the reducing equivalent NADPH reduce oxidized PRXs to complete the catalytic cycle (*117*). Glutathione peroxidases (GPXs) can also convert H_2O_2 to water in the mitochondrial matrix and cytosol through H_2O_2-mediated oxidation of reduced glutathione (GSH) (*118*). Glutathione reductase (GR) and NADPH reduce oxidized glutathione (GSSG) back to GSH. Additionally, catalase, an abundant antioxidant in peroxisomes, can detoxify H_2O_2 to water without any cofactors. However, in the presence of ferrous or cuprous ions, H_2O_2 can become OH· and quickly cause the oxidation of lipids, proteins, and DNA, resulting in cellular damage. NADPH is required to maintain multiple antioxidant defense systems. The cytosol has multiple sources of NADPH generation, including the oxidative PPP, malic enzyme 1, IDH1, and one-carbon metabolism. NADPH generation in the mitochondria, in part, is controlled by one-carbon metabolism and IDH2.

Historically, ROS have been thought of as lethal metabolic byproducts of cellular respiration and protein folding. However, studies over the past two decades have unveiled a previously underappreciated role of ROS in cellular signaling. Low levels of ROS, particularly H_2O_2, can reversibly oxidize the cysteine residues of proteins to positively regulate cell proliferation and cellular adaptation to metabolic stress (*119*). As H_2O_2 levels increase, however, cell death signaling pathways are initiated, and H_2O_2 is converted to OH·, which can directly damage DNA, proteins, and lipids. Cancer cells have an increased rate of spatially localized mitochondria- and NOX-dependent ROS production compared to normal cells. This allows for the proximal activation of signaling pathways [PI3K and mitogen-activated protein kinase/extracellular signal–regulated kinase (MAPK/ERK)] and transcription factors [HIF and nuclear factor κB (NF-κB)] necessary for tumorigenesis. The cancer cell–specific increased rate of spatially localized ROS production is due to a combination of oncogenic lesions and the tumor microenvironment. For example, the activation of oncogenes, PI3K signaling pathway induction, and hypoxia (low-oxygen levels) stimulate the increased rate of ROS production from the mitochondria and NOXs in cancer cells (*120*–*122*). Thus, mitochondria-targeted antioxidants

and NOX inhibitors can prevent cancer cell proliferation, hypoxic activation of HIF, tumorigenesis, and metastasis (*64*, *123*–*125*).

The increased localized ROS in cancer cells, which activates signaling pathways and transcription factors to promote tumorigenesis, needs to be buffered from reaching levels of ROS that incur cellular damage by the increased expression of antioxidant proteins (*126*). Thus, cancer cells have higher levels of ROS scavenging enzymes than normal cells, preventing ROS-mediated activation of death-inducing pathways like c-Jun N-terminal kinase (JNK) and p38 MAPK and oxidation of lipids, proteins, and DNA, resulting in irreversible damage and cell death. One mechanism by which cancer cells increase their antioxidant capacity is by activating the transcription factor nuclear factor (erythroid-derived 2)–related factor-2 (NRF2) (*127*). Specifically, NRF2 is activated following disruption of the interaction of NRF2 with its binding partner Kelch-like ECH-associated protein 1 (KEAP1). Critical cysteine residues within KEAP1 can undergo oxidation, succination, and glutathionylation, thereby inhibiting the KEAP1-NRF2 interaction, leading to the proteasomal degradation of NRF2. Additionally, NRF2 activation can occur independently of KEAP1 (*128*). Once activated, NRF2 induces the transcription of many antioxidant proteins including GPXs and TXNs as well as enzymes involved in GSH synthesis and cysteine import through the cystine/glutamate antiporter. Furthermore, to maintain the antioxidant capacity of GPXs and TXNs, NADPH is required. NRF2 plays an important role in activating enzymes that increase cytosolic NADPH levels. NRF2 also regulates the serine biosynthesis pathway, generating NADPH in the mitochondria, which is critical for redox balance under hypoxic conditions (*129*, *130*). Therefore, inactivating NRF2 or disabling antioxidant proteins in cancer cells would allow for the accumulation of excessive amounts of ROS to levels that initiate toxicity and reduce tumorigenesis (*128*, *131*, *132*).

During tumorigenesis and metastasis, redox homeostasis is required (Fig. 4). An emerging model of redox balance is that as a tumor initiates, the metabolic activity of cancer cells is increased, resulting in an increase in ROS production and subsequent activation of signaling pathways that support cancer cell proliferation, survival, and metabolic adaptation (*126*). Accordingly, to prevent toxic levels of ROS, tumor cells increase their antioxidant capacity to allow for cancer progression (*133*). The harsh tumor microenvironment increases ROS levels due to hypoxia, and the low glucose levels limit flux through the cytosolic oxidative PPP, thus decreasing cytosolic NADPH levels. Cells in these nutrient-deprived conditions activate AMPK to increase NADPH levels by stimulating PPP-dependent NADPH and diminishing anabolic pathways, such as lipid synthesis, that require high levels of NADPH (*134*, *135*). ROS-dependent signaling and increased mitochondrial respiration are also necessary for tumor metastasis (*124*, *136*). However, when tumor cells detach from a matrix, they encounter high levels of ROS that incur cellular damage and require activation of adaptive ROS-mitigating pathways to survive and grow (*137*, *138*). The ability to up-regulate antioxidant proteins and increase flux through NADPH-producing metabolic pathways enables distant metastasis to occur (*8*). These findings suggest that perhaps disabling antioxidant capacity in cancer cells to raise ROS levels might be beneficial in preventing metastasis.

TARGETING METABOLISM FOR CANCER THERAPY

There are a few things to consider when determining what makes a good metabolic target for cancer therapy. First, inhibition of some metabolic enzymes is likely to be systemically toxic because of their physiological functions in normal tissues (*139*). The feasibility of targeting these pathways therapeutically depends on whether systemic blockade of the pathway can be tolerated. Normal proliferating cells, such as immune cells and stem cells, also reprogram their metabolism in a manner similar to cancer cells (*140*, *141*). Metabolic inhibitors should likely not interfere with the adaptive immune system. Nevertheless, there are excellent examples of pathways whose reprogramming does provide an adequate therapeutic window in cancer. Enhanced nucleotide and DNA synthesis in tumor cells is targeted by antifolates (methotrexate, pemetrexed, and others) (*112*). Although these drugs do produce toxicity in normal proliferative tissues like the intestinal epithelium and bone marrow, they are essential components of highly successful chemotherapeutic regimens. Thus, it is critical to elucidate in normal cells any toxic effects of metabolic enzyme inhibition. To circumvent this challenge, one approach is to target a metabolic enzyme in a deregulated pathway specific to cancer cells. To date, many of the genetic and pharmacologic interventions on metabolic enzymes have been conducted using human cancer cells subcutaneously injected into athymic mice. Therefore, it will be important for future experiments to not only use patient-derived xenograft (PDX) models but also make use of genetically engineered mouse cancer models and syngeneic mouse models that have intact immune systems, especially given the promising results from immunotherapy. An emerging theme is that cancer cells display metabolic plasticity and can alter their metabolic profile during the course of tumorigenesis and metastasis. Thus, it is conceivable that cancer cells could develop resistance to inhibition of a particular metabolic pathway by expressing alternate protein isoforms or up-regulating compensatory pathways. Therefore, a rational cancer therapeutic strategy should involve targeting multiple metabolic pathways simultaneously or targeting a particular metabolic pathway in combination with therapies against oncogenic or signaling pathways. Here, we highlight a few promising metabolic targets in glycolytic, one-carbon, mitochondrial, and redox metabolism.

Glycolysis was an early attractive target for cancer therapy given the clinical observation that many tumors exhibit a significant increase in glucose uptake compared with adjacent normal tissue (*112*). LDH-A, a metabolic enzyme that converts pyruvate (the final product of glycolysis) to lactate, was identified as the first metabolic target of the oncogene MYC (*142*). Genetic or pharmacologic inhibition of LDH-A has been shown to diminish MYC-driven tumors in xenograft models (*143*, *144*). Furthermore, recent studies indicate that inhibition of LDH-A leads to the regression of established tumors in genetically engineered mouse models of NSCLC without systemic toxicity (*145*). Genetic ablation of LDH-A also delays the progression of myeloid leukemia (*146*). Thus, the increased expression of LDH-A, specifically in MYC-mutant cancer cells, may prove to be an attractive target. Another potential therapeutic target is the glycolytic protein HK2. Many tumor cells overexpress HK2, and preclinical mouse models of genetically engineered NSCLC and breast cancer demonstrate that HK2 inhibition delays tumor progression (*3*). Furthermore, systemic HK2 deletion in mice does not cause adverse physiological consequences. However, the effect of LDH-A and HK2 on the adaptive immune system is currently unknown. Lactate has been shown to inhibit cytotoxic T cells; thus, LDH-A inhibition may cooperate with immune checkpoint inhibitors to unleash host inflammatory T cells that will specifically attack tumor cells (*147*). Lactate can also reprogram macrophages to promote tumorigenesis (*148*). Thus, it may be efficacious to target LDH-A or HK2 in highly glycolytic tumors that overexpress these proteins.

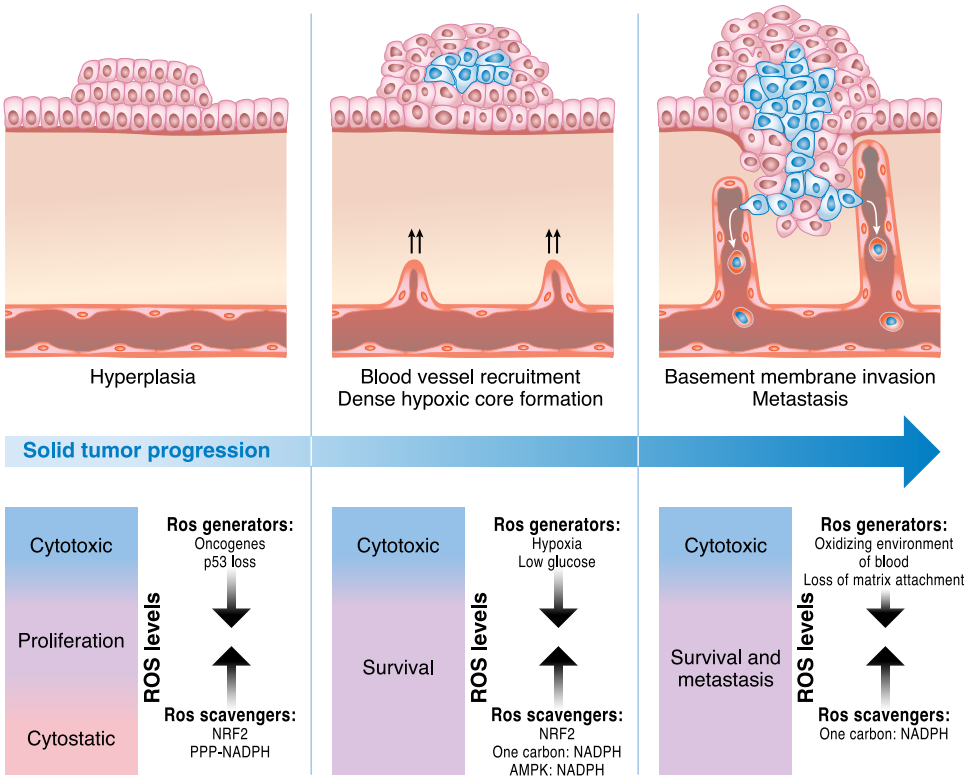

Fig. 4. Cancer cells maintain redox balance. Cancer cells have increased rates of ROS production due to activation of oncogenes and loss of tumor suppressors that promote signaling pathways supporting proliferation and survival. However, cancer cells prevent the buildup of ROS to levels that incur damage by increasing antioxidant capacity through induction of NRF2-dependent genes and, in glucose replete conditions, the use of PPP to generate NADPH. As cells encounter hypoxia and low glucose due to limited vasculature accessibility, the levels of ROS further increase, requiring AMPK and one-carbon metabolism to enhance NADPH production to raise antioxidant capacity. Loss of matrix attachment and escape of cancer cells into the blood for dissemination to distant sites incur further increases in ROS levels, which require additional enhancements of antioxidant defenses to avoid cell death. It is important to note that too little ROS or too high steady-state ROS levels within cancer cells result in failure for solid tumor progression and metastasis.

Another potential glucose-dependent target is PHGDH, an enzyme in the de novo serine synthesis pathway. High levels of PHGDH have been found in a subset of human melanoma and breast cancers, and these cancer cells require PHGDH for their growth in vitro (*25*, *26*). Serine starvation in mice diminishes tumorigenicity of p53-null cancers (*149*). De novo synthesis or exogenous uptake of serine can enter the mitochondria where SHMT2 converts it into glycine to generate folate intermediates (*101*, *150*). In many cancer types, SHMT2 expression is elevated and correlates with a poor prognosis. Furthermore, the transcription factors MYC and HIF induce SHMT2 under hypoxia to promote survival (*130*, *151*). Currently, it is not known whether targeting PHGDH, SHMT2, or other enzymes in the one-carbon metabolism pathway would be effective in delaying or regressing tumor progression in genetically engineered, PDX, or syngeneic mouse models of cancer without incurring systemic toxicity. However, given the importance of one-carbon metabolism in supporting the anabolic needs of cancer cells and its up-regulation in cancer cells, it is likely that this pathway is needed for in vivo tumor progression (*152*).

Mitochondrial metabolism has also emerged as a key target for cancer therapy, in part, due to the revelation that the antidiabetic drug metformin is an anticancer agent (*153*). Numerous epidemiological studies first suggested that diabetic patients taking metformin, to control their blood glucose levels, were less likely to develop cancer and had an improved survival rate if cancer was already present (*154*). Laboratory-based studies have also provided evidence that metformin may serve as an anticancer agent (*155*–*157*). Biochemists recognized that metformin reversibly inhibits mitochondrial complex I (*158*–*160*). Recent studies indicate that metformin acts as an anticancer agent by inhibiting mitochondrial ETC complex I (*161*). Specifically, metformin inhibits mitochondrial ATP production, inducing cancer cell death when glycolytic ATP levels diminish as a result of limited glucose availability. Metformin also inhibits the biosynthetic capacity of the mitochondria to generate macromolecules (lipids, amino acids, and nucleotides) within cancer cells (*162*). The remarkable safety profile of metformin is due to its uptake by organic cation transporters (OCTs), which are only present in a few tissues, such as the liver and kidney (*163*). Certain tumor cells also express OCTs to allow the uptake of metformin (*164*). However, in the absence of OCTs, tumors would not accumulate metformin to inhibit mitochondrial complex I. Ongoing clinical trials using metformin as an anticancer agent should assess the expression levels of OCTs to identify the tumors with highest expression, which are likely to be susceptible to metformin. Moreover, it is not clear whether the current antidiabetic dosing of metformin used in clinical trials allows for metformin accumulation to levels necessary to inhibit mitochondrial complex I in tumors. Thus, it is possible that metformin at doses higher than those currently used for diabetes might be more efficacious

without causing toxicity. Like metformin, the biguanide phenformin exhibits anticancer properties by inhibiting mitochondrial complex I (*165*). In contrast to metformin, phenformin is readily transported into tumor cells and has been withdrawn from human use in most parts of the world due to its clinical increase in the incidence of lactic acidosis. However, it is worth considering phenformin as a possible cancer therapy because lactic acidosis can be monitored. Biguanide sensitivity can be improved in mice starved for serine or in tumors that have lost p53 or LKB1 (*155*, *166*, *167*). Thus, biguanides, and possibly other mitochondrial complex I inhibitors, may be effective anticancer agents.

Another potential therapeutic strategy to inhibit mitochondrial metabolism in certain tumors would be to use autophagy or glutaminase inhibitors. Autophagy provides amino acids, such as glutamine, that fuel the TCA cycle in NSCLC and pancreatic cancers, and short-term autophagy inhibition has been shown to decrease tumor progression without incurring systemic toxicity in mouse models of NSCLC (*168*, *169*). Some tumors are addicted to using glutamine to support TCA cycle metabolism even in the absence of autophagy; thus, glutaminase inhibitors can reduce tumor burden in these models (*4*, *75*, *170*). An alternative approach is to target acetate metabolism. Although a major function of the mitochondria is to provide acetyl-CoA to the cell, cancer cells can also use acetate to support cell growth and survival during metabolic stress (hypoxia or nutrient deprivation) (*96*, *171*). The cytosolic enzyme acetyl-CoA synthase 2 (ACCS2), which converts acetate to acetyl-CoA, is dispensable for normal development; thus, ACCS2 is a promising target of acetate metabolism. ACCS2 knockout mice do not display overt pathologies, but genetic loss of ACCS2 reduces tumor burden in models of hepatocellular carcinoma (*171*). Human glioblastomas can oxidize acetate and may be sensitive to inhibitors of this process (*172*). Thus, targeting metabolism with inhibitors of autophagy, acetate metabolism, and other pathways that supply key metabolic intermediates may be efficacious in some contexts.

Because mitochondrial inhibitors are unlikely to be effective cancer therapies as single agents, combination therapy is likely the best approach. For example, the use of metformin with the current clinical PI3K inhibitors, which reduce glucose uptake and glycolysis (*173*), is one approach that would impair both sources of ATP within cells. Targeted therapies against oncogenes such as KRAS, BRAF, and NOTCH1 kill a large majority of cancer cells but ultimately yield resistant cells that exhibit an increased sensitivity to inhibitors that impair mitochondrial metabolism (*174*–*176*). Cancer-initiating cells also have increased sensitivity to mitochondrial inhibitors, adding further evidence that inhibiting mitochondrial metabolism may suppress tumor recurrence (*177*, *178*).

Furthermore, to counterbalance the increased production of ROS encountered during tumorigenesis and metastasis, cancer cells increase their antioxidant capacity (*126*). Thus, an additional therapeutic approach is to target redox metabolism, that is, selectively disable the antioxidant capacity of cancer cells causing ROS levels to rise and induce cancer cell death (*133*). The reducing equivalent NADPH is required to maintain multiple antioxidant defense systems. The cytosol has multiple sources of NADPH generation, including the oxidative PPP, malic enzyme 1, IDH1, and one-carbon metabolism. By contrast, NADPH generation in the mitochondria is controlled in part by one-carbon metabolism and IDH2. Many of these NADPH-generating systems are critical for normal cell survival and function. Nevertheless, there are two NADPH-generating systems that may serve as potential therapeutic targets. It is estimated that 400 million people worldwide are deficient in G6PDH, an enzyme in the oxidative PPP that converts $NADP^+$ to NADPH. However, certain tumors rely on this pathway as a major source of cytosolic NADPH; therefore, it may be therapeutic to disable this pathway and induce oxidative stress and diminish tumor growth. Moreover, RNA profiling of metabolic enzymes identified the mitochondrial one-carbon metabolism protein MTHFD2, which can generate NADPH, as being highly expressed in 19 different cancer types but not in normal adult proliferating cells (*152*). Loss of MTHFD2 in cancer cells increases ROS levels and sensitizes the cells to oxidant-induced cell death in vitro. An interesting approach to depleting NADPH levels and increasing ROS is to administer high doses of vitamin C (ascorbate). Vitamin C is imported into cells through sodium-dependent vitamin C transporters, whereas the oxidized form of vitamin C, dehydroascorbate (DHA), is imported into cells through glucose transporters such as GLUT1 (*179*). When the cell takes up DHA, it is reduced back to vitamin C by glutathione (GSH), which consequently becomes GSSG. Subsequently, GSSG is converted back to GSH by NADPH-dependent GR. Because the blood is an oxidizing environment, vitamin C becomes oxidized to DHA before being taken up by the cell. Thus, high doses of vitamin C diminish the tumorigenesis of colorectal tumors that harbor oncogenic KRAS mutations and express high levels of GLUT1 by depleting the NADPH and GSH pools and consequently increasing ROS levels to induce cancer cell death (*179*, *180*). Vitamin C administered at high doses intravenously is safe in humans and, in conjunction with conventional paclitaxel-carboplatin therapy, demonstrated a benefit in a small number of patients (*181*). Additional strategies to diminish GSH include the administration of buthionine sulfoximine, an irreversible inhibitor of γ-glutamylcysteine synthetase, which can be safely administered to humans and is efficacious in preclinical tumor models (*182*). Moreover, glutathione is a tripeptide consisting of cysteine, glutamate, and glycine. Thus, decreasing glutamate levels using glutaminase inhibitors or diminishing cysteine levels by preventing extracellular cystine (two linked cysteine molecules) uptake can also raise ROS levels in cancer cells to induce cell death.

An important consideration is that normal stem cells are sensitive to ROS levels; thus, it is important to stratify patients on the basis of their expression levels of a particular antioxidant protein or antioxidant pathway. It is critical to determine which antioxidant pathways are likely up-regulated as a result of the high rate of ROS production within cancer cells. Many cancer types use the NRF2 pathway to maintain redox balance; therefore, targeting this pathway may provide a viable therapeutic opportunity (*128*). Additionally, superoxide dismutase 1 (SOD1) is overexpressed in NSCLC, and its inhibition kills human NSCLC cells and decreases the tumor burden in mouse models of NSCLC (*183*). Because NRF2 and SOD1 knockout mice develop normally, short-term inhibition of these pathways might be an effective way to kill cancer cells.

TECHNOLOGIES ENABLING DISCOVERY IN CANCER METABOLISM

Many recent advances in our understanding of cancer metabolism have been propelled by advanced technologies to detect metabolites and metabolic activities (*184*). A key concept is that quantifying metabolites (that is, metabolomics) is a more distinct form of metabolic analysis than measuring the activities of metabolic pathways [that is, metabolic flux analysis (*185*)]. Although these two approaches can provide complementary types of information, they are not interchangeable. One cannot infer metabolic activity from changes in metabolite levels, and

altered metabolic fluxes may or may not cause changes in metabolite levels (*186*). Both of these approaches have provided important recent insights into cancer metabolism, and using the two techniques together provides the most complete assessment of metabolic phenotypes.

Metabolomics experiments seek to characterize and quantify the metabolites in a biological sample, usually by nuclear magnetic resonance (NMR) or, more commonly, mass spectrometry. Depending on the methods of extraction, separation, and detection, metabolomics experiments may focus on particular classes of metabolites or provide a comprehensive analysis of as many metabolites as possible. Targeted approaches typically detect a few dozen to a few hundred molecules, whereas untargeted analyses may detect more than 1000. Detecting alterations of metabolite levels in cancer can be extremely valuable. The massive accumulation of D2HG in IDH1-mutant gliomas was initially discovered through a metabolomics approach (*33*). Because altered metabolite levels can be detected noninvasively using ^{1}H magnetic resonance spectroscopy (MRS), perturbed metabolite levels discovered through metabolomics can sometimes be translated into clinical diagnostic techniques. Elevated levels of lactate, choline, glycine, and other metabolites are detected by MRS in glioma. More recently, MRS techniques have been developed to monitor specific metabolic states programmed by tumor-specific mutations in metabolic enzymes. Applications include elevated 2HG in IDH1/IDH2-mutated gliomas (*187*) and elevated succinate in SDH-deficient paragangliomas (*188*).

Metabolic flux studies use isotope tracers like ^{13}C, ^{15}N, and ^{2}H to track flow through metabolic pathways. Typically, a nutrient of interest is labeled by an isotope (for example, ^{13}C-glucose) and supplied to cancer cells in the culture medium. Metabolites extracted from the culture are analyzed for isotope enrichment using mass spectrometry or NMR. The extent and distribution of labeling within informative metabolites encode information about which pathways are active in the cells. Incorporating additional data (for example, definitive rates of nutrient consumption, waste secretion, and biomass production) allows quantitative fluxes to be determined across a metabolic network.

Isotope tracing studies provide information about metabolic alterations in cancer cells that cannot be detected by metabolite levels alone. For example, hypoxia and mutations in the ETC induce a restructuring of the TCA cycle in which many of the intermediates are produced in the reverse order from the conventional form of the cycle. The key reaction in this pathway involves the reductive carboxylation of α-ketoglutarate to isocitrate in a NADPH-dependent carboxylation reaction catalyzed by IDH1 and/or IDH2. Although metabolomics experiments can detect altered levels of TCA cycle metabolites in cells using the reductive carboxylation pathway or in cells with deficiencies in pyruvate import into mitochondria, the marked restructuring of the cycle is apparent only through isotope tracing experiments, particularly experiments using ^{13}C-glutamine as the tracer (*69*, *78*, *79*, *189*–*191*). An example of the use of isotope tracers to identify metabolic liabilities involves the surprising discovery that a significant fraction of cellular NADPH, particularly in the mitochondria, is produced through folate metabolism (*100*, *101*). These studies involved a sophisticated combination of ^{13}C and ^{2}H tracers, coupled with quantitative measurements of metabolic flux.

Several recent studies have begun to use stable isotopes to investigate metabolism in intact tumors. Because these isotopes do not undergo radioactive decay, they are safe for administration to animals and human subjects. Systemic administration of ^{13}C-labeled nutrients through either boluses or continuous infusions has been shown to generate substantial labeling of glycolytic and TCA cycle intermediates in tumors. In mice bearing orthotopic transplants of high-grade human gliomas, continuous infusion of ^{13}C-glucose was demonstrated to produce steady-state labeling of metabolites from the TCA cycle within the tumor, enabling the assessment of several metabolic pathways (*192*). Here, tumors with diverse oncogenotypes oxidized glucose-derived pyruvate in the mitochondria and synthesized glutamine from glucose carbon. In contrast to most cultured glioma cell lines, these tumors did not demonstrate significant levels of ^{13}C-glutamine oxidation in vivo, and primary cell lines derived from the tumors did not require glutamine for survival or proliferation. In another study, metabolism of ^{13}C-glucose and ^{13}C-glutamine in autochthonous models of *MYC*- or *MET*-driven tumorigenesis revealed that metabolic phenotypes depend not only on the tumor's genetic driver but also on the tissue or origin. *MYC* but not *MET* stimulated glutamine catabolism in liver tumors, whereas *MYC*-driven lung tumors expressed glutamine synthetase and accumulated glutamine (*193*). Thus, in vivo isotope tracing can detect metabolic activities of intact tumors and characterize some of the factors that specify the metabolic phenotype.

Administration of ^{13}C-labeled nutrients has also proven to be valuable in human cancer (*172*, *194*–*197*). Fan *et al.* (*196*) used ^{13}C-glucose to demonstrate that human non–small cell lung tumors metabolize glucose through glycolysis and the TCA cycle concurrently, with metabolites from both pathways demonstrating higher levels of labeling in tumors relative to adjacent lung tissue. In a subsequent study, these investigators demonstrated that the anaplerotic enzyme pyruvate carboxylase (PC) was highly expressed in lung tumors and contributed to ^{13}C labeling in TCA cycle intermediates (*195*). Enhanced glucose oxidation involving both PC and pyruvate dehydrogenase (PDH) was demonstrated in a separate cohort of non–small cell lung tumors, in which formal analysis of metabolic fluxes was used to complement measurements of ^{13}C labeling (*197*). An important conclusion from these studies, and from a similar study in mice bearing *KRAS*-driven tumors (*198*), is that non–small cell lung tumors demonstrate higher levels of both glycolysis and glucose oxidation relative to adjacent, benign lung. This finding sharply contrasts with the frequently invoked "switch" from oxidative metabolism to glycolysis in malignant tissue, commonly used to explain the Warburg effect (Fig. 5A). Rather, the data support a model in which the amplitude of both pathways is increased simultaneously, perhaps through increased substrate delivery and enzyme expression in tumor cells (Fig. 5B). It is also significant that human tumors exhibit substantial heterogeneity of metabolic phenotypes, both between tumors and even within distinct regions of the same tumor (*197*). The extent of glucose-dependent labeling of TCA cycle intermediates is predicted by noninvasive assessment of tumor perfusion by magnetic resonance imaging, providing an approach to identify areas of regional metabolic heterogeneity in human cancer (*197*).

Metabolomics and metabolic flux analysis can be integrated with functional genomics to identify and understand metabolic vulnerabilities in cancer cells. This approach has produced several good examples of screens that identified potential therapeutic targets while stimulating entirely new lines of investigation in cancer cell biology. For example, the serine biosynthetic enzyme PHGDH was first identified as a metabolic vulnerability in breast cancer cells through a large-scale in vivo short hairpin RNA screen targeting thousands of metabolic enzymes (*25*). *PHGDH* is frequently amplified at the genomic level in breast tumors and melanomas and exhibits oncogene-like features in cell culture (*25*, *26*). Subsequent work on serine biosynthesis, much of it involving

metabolomics and metabolic flux analysis, has uncovered novel functions and liabilities of this pathway in cancer cell growth and stress resistance (*129*, *150*, *151*). Combining functional screens with metabolic analysis can also identify context-specific vulnerabilities that may be therapeutically actionable. A CRISPR (clustered regularly interspaced short palindromic repeats)–based loss-of-function screen identified GOT1, the cytosolic aspartate aminotransferase, as conditionally essential for survival during treatment with the ETC inhibitor phenformin (*199*). Isotope labeling then demonstrated that ETC blockade caused the direction of this enzyme to reverse from aspartate consumption in untreated cells to aspartate synthesis during ETC blockade (*200*). In addition to the discovery of synthetic lethality between ETC and GOT1 inhibition, these studies led to the novel biological concept that a major function of the ETC in proliferating cells is to support the synthesis of aspartate for nucleotide and protein synthesis (*199*, *200*).

CONCLUSIONS AND CURRENT CHALLENGES

Substantial progress has been made in the past decade toward understanding the mechanisms, biological consequences, and liabilities associated with metabolic reprogramming in cancer. Several common themes have emerged from this research (Box 1). First, metabolic reprogramming is essential for the biology of malignant cells, particularly their ability to survive and grow by using conventional metabolic pathways to produce energy, synthesize biosynthetic precursors, and maintain redox balance. Second, metabolic reprogramming is the result of mutations in oncogenes and tumor suppressors, leading to activation of PI3K and mTORC1 signaling pathways and transcriptional networks involving HIFs, MYC, and SREBP-1. Third, alterations in metabolite levels can affect cellular signaling, epigenetics, and gene expression through posttranslational modifications such as acetylation, methylation, and thiol oxidation. Fourth, taken together, studies on cultured cells have demonstrated a remarkable diversity of anabolic and catabolic pathways in cancer, with induction of autophagy and utilization of extracellular lipids and proteins complementing the classical pathways like glycolysis and glutaminolysis. We have exited the period when cancer metabolism could be considered synonymous with the Warburg effect.

Several challenges will likely shape research over the next decade. First, the studies cited above were performed primarily in cancer cell lines rather than intact tumors. These straightforward experimental models have been highly informative about the molecular mechanisms of metabolic reprogramming, particularly those linking aberrant

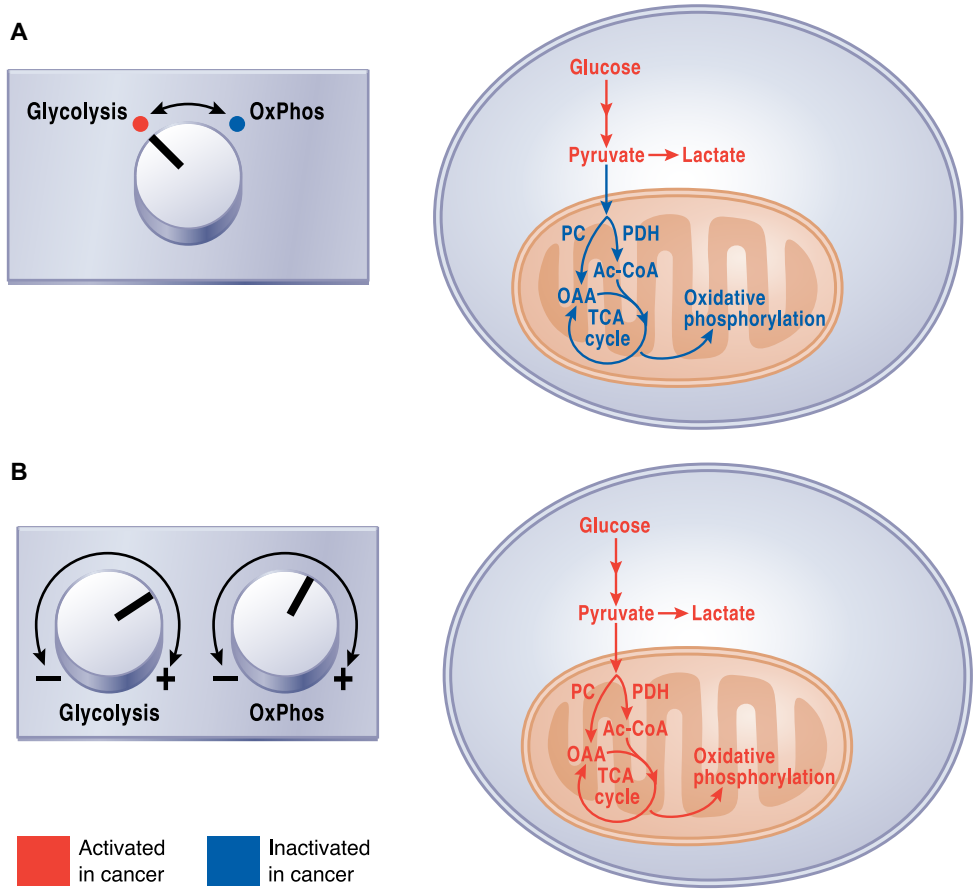

Fig. 5. Relationship between glycolysis and oxidative phosphorylation in cancer cells. (**A**) A common view of cancer cell metabolism invokes a switch from glucose oxidation in normal tissues toward glycolysis and suppressed oxidative phosphorylation (OxPhos) in cancer. (**B**) Analysis of metabolic activity in intact tumors from humans and mice argues against a switch. Rather, tumors appear to enhance both glycolysis and glucose oxidation simultaneously relative to surrounding tissue.

signaling to altered metabolic fluxes. But it is challenging (perhaps impossible) to model an accurate tumor microenvironment in culture. Direct analysis of metabolic fluxes in intact tumors should begin to play a more prominent role in the field and may prove essential in determining precisely how to deploy metabolic inhibitors in clinical trials. Along these lines, it is remarkable that some tumor cell metabolic vulnerabilities observed in vivo are absent from cultured cell models (*198*) and that metabolic phenotypes are inconsistent even across single solid tumors in patients (*197*). Developing rational therapeutic strategies will be aided by learning how to derive metabolic information efficiently and comprehensively from both preclinical and clinical models of intact tumor growth. A further challenge for these in vivo studies will be to develop analytical or computational approaches to deconvolute the distinct metabolic phenotypes of discrete cell types (cancer cells, cancer-associated fibroblasts, lymphocytes, and endothelial cells) within solid tumors. This may allow us to understand the metabolic cooperativity among populations of cells within a tumor and whether metabolic reprogramming of stromal cells provides therapeutic opportunities. Second, by far the best recent candidate for a targetable, tumor-specific metabolic activity is the neomorphic function of mutant IDH1/IDH2. This has stimulated intense interest in finding other metabolic alterations for which the therapeutic window may be wide enough for real clinical opportunities. Third, although we have learned a great deal about the metabolic pathways that support cancer cell proliferation, we know much less about the metabolism that supports survival of nonproliferating tumor cells, which constitute the bulk of the malignant cells in most solid tumors. Along these lines, the metabolism of tumor-initiating cells/cancer stem cells is just now beginning to be investigated, and it will be of major interest to devise strategies to target metabolism in these cells. Finally, we still know relatively little about metabolic interactions between tumor and host. This area has the potential for enormous impact on public health. It is clear that obesity and diabetes, both of which are reaching epidemic proportions in the developed world, increase cancer risk, but we lack insight into how to break these links.

Box 1: Key Principles and Lessons Learned

- Reprogrammed metabolic pathways are essential for cancer cell survival and growth.
- Frequently reprogrammed activities include those that allow tumor cells to take up abundant nutrients and use them to produce ATP, generate biosynthetic precursors and macromolecules, and tolerate stresses associated with malignancy (for example, redox stress and hypoxia).
- An emerging class of reprogrammed pathways includes those allowing cancer cells to tolerate nutrient depletion by catabolizing macromolecules from inside or outside the cell (for example, autophagy, macropinocytosis, and lipid scavenging).
- Reprogramming may be regulated intrinsically by tumorigenic mutations in cancer cells or extrinsically by influences of the microenvironment.
- Oncometabolites (for example, D2HG) accumulate as a consequence of genetic changes within a tumor and contribute to the molecular process of malignant transformation.
- Many metabolites exert their biological effects outside of the classical metabolic network, affecting signal transduction, epigenetics, and other functions.
- New approaches to assess metabolism in living tumors in humans and mice may improve our ability to understand how metabolic reprogramming is regulated and which altered pathways hold opportunities to improve care of cancer patients.

REFERENCES AND NOTES

1. D. Hanahan, R. A. Weinberg, Hallmarks of cancer: The next generation. *Cell* **144**, 646–674 (2011).
2. N. N. Pavlova, C. B. Thompson, The emerging hallmarks of cancer metabolism. *Cell Metab.* **23**, 27–47 (2016).
3. K. C. Patra, Q. Wang, P. T. Bhaskar, L. Miller, Z. Wang, W. Wheaton, N. Chandel, M. Laakso, W. J. Muller, E. L. Allen, A. K. Jha, G. A. Smolen, M. F. Clasquin, R. B. Robey, N. Hay, Hexokinase 2 is required for tumor initiation and maintenance and its systemic deletion is therapeutic in mouse models of cancer. *Cancer Cell* **24**, 213–228 (2013).
4. E. H. Shroff, L. S. Eberlin, V. M. Dang, A. M. Gouw, M. Gabay, S. J. Adam, D. I. Bellovin, P. T. Tran, W. M. Philbrick, A. Garcia-Ocana, S. C. Casey, Y. Li, C. V. Dang, R. N. Zare, D. W. Felshera, MYC oncogene overexpression drives renal cell carcinoma in a mouse model through glutamine metabolism. *Proc. Natl. Acad. Sci. U.S.A.* **112**, 6539–6544 (2015).
5. L. A. Clavell, R. D. Gelber, H. J. Cohen, S. Hitchcock-Bryan, J. R. Cassady, N. J. Tarbell, S. R. Blattner, R. Tantravahi, P. Leavitt, S. E. Sallan, Four-agent induction and intensive asparaginase therapy for treatment of childhood acute lymphoblastic leukemia. *N. Engl. J. Med.* **315**, 657–663 (1986).
6. J. Yun, C. Rago, I. Cheong, R. Pagliarini, P. Angenendt, H. Rajagopalan, K. Schmidt, J. K. Willson, S. Markowitz, S. Zhou, L. A. Diaz Jr., V. E. Velculescu, C. Lengauer, K. W. Kinzler, B. Vogelstein, N. Papadopoulos, Glucose deprivation contributes to the development of *KRAS* pathway mutations in tumor cells. *Science* **325**, 1555–1559 (2009).
7. J. M. Loo, A. Scherl, A. Nguyen, F. Y. Man, E. Weinberg, Z. Zeng, L. Saltz, P. B. Paty, S. F. Tavazoie, Extracellular metabolic energetics can promote cancer progression. *Cell* **160**, 393–406 (2015).
8. E. Piskounova, M. Agathocleous, M. M. Murphy, Z. Hu, S. E. Huddlestun, Z. Zhao, A. M. Leitch, T. M. Johnson, R. J. DeBerardinis, S. J. Morrison, Oxidative stress inhibits distant metastasis by human melanoma cells. *Nature* **527**, 186–191 (2015).
9. L. K. Boroughs, R. J. DeBerardinis, Metabolic pathways promoting cancer cell survival and growth. *Nat. Cell Biol.* **17**, 351–359 (2015).
10. P. S. Ward, C. B. Thompson, Metabolic reprogramming: A cancer hallmark even Warburg did not anticipate. *Cancer Cell* **21**, 297–308 (2012).
11. S. Y. Lunt, M. G. Vander Heiden, Aerobic glycolysis: Meeting the metabolic requirements of cell proliferation. *Annu. Rev. Cell Dev. Biol.* **27**, 441–464 (2011).
12. W. H. Koppenol, P. L. Bounds, C. V. Dang, Otto Warburg's contributions to current concepts of cancer metabolism. *Nat. Rev. Cancer* **11**, 325–337 (2011).
13. C. S. Ahn, C. M. Metallo, Mitochondria as biosynthetic factories for cancer proliferation. *Cancer Metab.* **3**, 1 (2015).
14. O. E. Owen, S. C. Kalhan, R. W. Hanson, The key role of anaplerosis and cataplerosis for citric acid cycle function. *J. Biol. Chem.* **277**, 30409–30412 (2002).
15. J. R. Cantor, D. M. Sabatini, Cancer cell metabolism: One hallmark, many faces. *Cancer Discov.* **2**, 881–898 (2012).
16. C. C. Dibble, B. D. Manning, Signal integration by mTORC1 coordinates nutrient input with biosynthetic output. *Nat. Cell Biol.* **15**, 555–564 (2013).
17. T. L. Yuan, L. C. Cantley, PI3K pathway alterations in cancer: Variations on a theme. *Oncogene* **27**, 5497–5510 (2008).
18. Z. E. Stine, Z. E. Walton, B. J. Altman, A. L. Hsieh, C. V. Dang, MYC, metabolism, and cancer. *Cancer Discov.* **5**, 1024–1039 (2015).
19. F. Kruiswijk, C. F. Labuschagne, K. H. Vousden, p53 in survival, death and metabolic health: A lifeguard with a licence to kill. *Nat. Rev. Mol. Cell Biol.* **16**, 393–405 (2015).
20. L. Jiang, N. Kon, T. Li, S. J. Wang, T. Su, H. Hibshoosh, R. Baer, W. Gu, Ferroptosis as a p53-mediated activity during tumour suppression. *Nature* **520**, 57–62 (2015).
21. T. Li, N. Kon, L. Jiang, M. Tan, T. Ludwig, Y. Zhao, R. Baer, W. Gu, Tumor suppression in the absence of p53-mediated cell-cycle arrest, apoptosis, and senescence. *Cell* **149**, 1269–1283 (2012).
22. R. K. Jain, L. L. Munn, D. Fukumura, Dissecting tumour pathophysiology using intravital microscopy. *Nat. Rev. Cancer* **2**, 266–276 (2002).
23. G.L. Semenza, Hypoxia-inducible factors in physiology and medicine. *Cell* **148**, 399–408 (2012).
24. W. G. Kaelin Jr., P. J. Ratcliffe, Oxygen sensing by metazoans: The central role of the HIF hydroxylase pathway. *Mol. Cell* **30**, 393–402 (2008).
25. R. Possemato, K. M. Marks, Y. D. Shaul, M. E. Pacold, D. Kim, K. Birsoy, S. Sethumadhavan, H.-K. Woo, H. G. Jang, A. K. Jha, W. W. Chen, F. G. Barrett, N. Stransky, Z.-Y. Tsun, G. S. Cowley, J. Barretina, N. Y. Kalaany, P. P. Hsu, K. Ottina, A. M. Chan, B. Yuan, L. A. Garraway, D. E. Root, M. Mino-Kenudson, E. F. Brachtel, E. M. Driggers, D. M. Sabatini, Functional genomics reveal that the serine synthesis pathway is essential in breast cancer. *Nature* **476**, 346–350 (2011).

26. J. W. Locasale, A. R. Grassian, T. Melman, C. A. Lyssiotis, K. R. Mattaini, A. J. Bass, G. Heffron, C. M. Metallo, T. Muranen, H. Sharfi, A. T. Sasaki, D. Anastasiou, E. Mullarky, N. I. Vokes, M. Sasaki, R. Beroukhim, G. Stephanopoulos, A. H. Ligon, M. Meyerson, A. L. Richardson, L. Chin, G. Wagner, J. M. Asara, J. S. Brugge, L. C. Cantley, M. G. Vander Heiden, Phosphoglycerate dehydrogenase diverts glycolytic flux and contributes to oncogenesis. *Nat. Genet.* **43**, 869–874 (2011).
27. J. W. Locasale, Serine, glycine and one-carbon units: Cancer metabolism in full circle. *Nat. Rev. Cancer* **13**, 572–583 (2013).
28. M. Yang, T. Soga, P. J. Pollard, Oncometabolites: Linking altered metabolism with cancer. *J. Clin. Invest.* **123**, 3652–3658 (2013).
29. H. Yan, D. W. Parsons, G. Jin, R. McLendon, B. A. Rasheed, W. Yuan, I. Kos, I. Batinic-Haberle, S. Jones, G. J. Riggins, H. Friedman, A. Friedman, D. Reardon, J. Herndon, K. W. Kinzler, V. E. Velculescu, B. Vogelstein, D. D. Bigner, *IDH1* and *IDH2* mutations in gliomas. *N. Engl. J. Med.* **360**, 765–773 (2009).
30. E. R. Mardis, L. Ding, D. J. Dooling, D. E. Larson, M. D. McLellan, K. Chen, D. C. Koboldt, R. S. Fulton, K. D. Delehaunty, S. D. McGrath, L. A. Fulton, D. P. Locke, V. J. Magrini, R. M. Abbott, T. L. Vickery, J. S. Reed, J. S. Robinson, T. Wylie, S. M. Smith, L. Carmichael, J. M. Eldred, C. C. Harris, J. Walker, J. B. Peck, F. Du, A. F. Dukes, G. E. Sanderson, A. M. Brummett, E. Clark, J. F. McMichael, R. J. Meyer, J. K. Schindler, C. S. Pohl, J. W. Wallis, X. Shi, L. Lin, H. Schmidt, Y. Tang, C. Haipek, M. E. Wiechert, J. V. Ivy, J. Kalicki, G. Elliott, R. E. Ries, J. E. Payton, P. Westervelt, M. H. Tomasson, M. A. Watson, J. Baty, S. Heath, W. D. Shannon, R. Nagarajan, D. C. Link, M. J. Walter, T. A. Graubert, J. F. DiPersio, R. K. Wilson, T. J. Ley, Recurring mutations found by sequencing an acute myeloid leukemia genome. *N. Engl. J. Med.* **361**, 1058–1066 (2009).
31. M. R. Kang, M. S. Kim, J. E. Oh, Y. R. Kim, S. Y. Song, S. I. Seo, J. Y. Lee, N. J. Yoo, S. H. Lee, Mutational analysis of IDH1 codon 132 in glioblastomas and other common cancers. *Int. J. Cancer* **125**, 353–355 (2009).
32. J.-A. Losman, W. G. Kaelin Jr., What a difference a hydroxyl makes: Mutant IDH, (*R*)-2-hydroxyglutarate, and cancer. *Genes Dev.* **27**, 836–852 (2013).
33. L. Dang, D. W. White, S. Gross, B. D. Bennett, M. A. Bittinger, E. M. Driggers, V. R. Fantin, H. G. Jang, S. Jin, M. C. Keenan, K. M. Marks, R. M. Prins, P. S. Ward, K. E. Yen, L. M. Liau, J. D. Rabinowitz, L. C. Cantley, C. B. Thompson, M. G. Vander Heiden, S. M. Su, Cancer-associated IDH1 mutations produce 2-hydroxyglutarate. *Nature* **465**, 966 (2010).
34. P. S. Ward, J. Patel, D. R. Wise, O. Abdel-Wahab, B. D. Bennett, H. A. Coller, J. R. Cross, V. R. Fantin, C. V. Hedvat, A. E. Perl, J. D. Rabinowitz, M. Carroll, S. M. Su, K. A. Sharp, R. L. Levine, C. B. Thompson, The common feature of leukemia-associated IDH1 and IDH2 mutations is a neomorphic enzyme activity converting α-ketoglutarate to 2-hydroxyglutarate. *Cancer Cell* **17**, 225–234 (2010).
35. M. E. Figueroa, O. Abdel-Wahab, C. Lu, P. S. Ward, J. Patel, A. Shih, Y. Li, N. Bhagwat, A. Vasanthakumar, H. F. Fernandez, M. S. Tallman, Z. Sun, K. Wolniak, J. K. Peeters, W. Liu, S. E. Choe, V. R. Fantin, E. Paietta, B. Löwenberg, J. D. Licht, L. A. Godley, R. Delwel, P. J. Valk, C. B. Thompson, R. L. Levine, A. Melnick, Leukemic IDH1 and IDH2 mutations result in a hypermethylation phenotype, disrupt TET2 function, and impair hematopoietic differentiation. *Cancer Cell* **18**, 553–567 (2010).
36. C. Lu, P. S. Ward, G. S. Kapoor, D. Rohle, S. Turcan, O. Abdel-Wahab, C. R. Edwards, R. Khanin, M. E. Figueroa, A. Melnick, K. E. Wellen, D. M. O'Rourke, S. L. Berger, T. A. Chan, R. L. Levine, I. K. Mellinghoff, C. B. Thompson, IDH mutation impairs histone demethylation and results in a block to cell differentiation. *Nature* **483**, 474–478 (2012).
37. J.-A. Losman, R. E. Looper, P. Koivunen, S. Lee, R. K. Schneider, C. McMahon, G. S. Cowley, D. E. Root, B. L. Ebert, W. G. Kaelin Jr., (*R*)-2-hydroxyglutarate is sufficient to promote leukemogenesis and its effects are reversible. *Science* **339**, 1621–1625 (2013).
38. P. Koivunen, S. Lee, C. G. Duncan, G. Lopez, G. Lu, S. Ramkissoon, J. A. Losman, P. Joensuu, U. Bergmann, S. Gross, J. Travins, S. Weiss, R. Looper, K. L. Ligon, R. G. W. Verhaak, H. Yan, W. G. Kaelin Jr., Transformation by the (*R*)-enantiomer of 2-hydroxyglutarate linked to EGLN activation. *Nature* **483**, 484–488 (2012).
39. S. Turcan, D. Rohle, A. Goenka, L. A. Walsh, F. Fang, E. Yilmaz, C. Campos, A. W. M. Fabius, C. Lu, P. S. Ward, C. B. Thompson, A. Kaufman, O. Guryanova, R. Levine, A. Heguy, A. Viale, L. G. T. Morris, J. T. Huse, I. K. Mellinghoff, T. A. Chan, IDH1 mutation is sufficient to establish the glioma hypermethylator phenotype. *Nature* **483**, 479–483 (2012).
40. R. Chowdhury, K. K. Yeoh, Y.-M. Tian, L. Hillringhaus, E. A. Bagg, N. R. Rose, I. K. H. Leung, X. S. Li, E. C. Y. Woon, M. Yang, M. A. McDonough, O. N. King, I. J. Clifton, R. J. Klose, T. D. W. Claridge, P. J. Ratcliffe, C. J. Schofield, A. Kawamura, The oncometabolite 2-hydroxyglutarate inhibits histone lysine demethylases. *EMBO Rep.* **12**, 463–469 (2011).
41. W. Xu, H. Yang, Y. Liu, Y. Yang, P. Wang, S.-H. Kim, S. Ito, C. Yang, P. Wang, M.-T. Xiao, L.-X. Liu, W.-. Jiang, J. Liu, J.-. Zhang, B. Wang, S. Frye, Y. Zhang, Y.-. Xu, Q.-. Lei, K.-L. Guan, S.-. Zhao, Y. Xiong, Oncometabolite 2-hydroxyglutarate is a competitive inhibitor of α-ketoglutarate-dependent dioxygenases. *Cancer Cell* **19**, 17–30 (2011).
42. A. M. Intlekofer, R. G. Dematteo, S. Venneti, L. W. S. Finley, C. Lu, A. R. Judkins, A. S. Rustenburg, P. B. Grinaway, J. D. Chodera, J. R. Cross, C. B. Thompson, Hypoxia induces production of L-2-hydroxyglutarate. *Cell Metab.* **22**, 304–311 (2015).
43. R. Rzem, M.-F. Vincent, E. Van Schaftingen, M. Veiga-da-Cunha, L-2-hydroxyglutaric aciduria, a defect of metabolite repair. *J. Inherit. Metab. Dis.* **30**, 681–689 (2007).
44. W. M. Oldham, C. B. Clish, Y. Yang, J. Loscalzo, Hypoxia-mediated increases in L-2-hydroxyglutarate coordinate the metabolic response to reductive stress. *Cell Metab.* **22**, 291–303 (2015).
45. M. Topçu, F. Jobard, S. Halliez, T. Coskun, C. Yalçinkayal, F. O. Gerceker, R. J. A. Wanders, J.-F. Prud'homme, M. Lathrop, M. Özguc, J. Fischer, L-2-Hydroxyglutaric aciduria: Identification of a mutant gene *C14orf160*, localized on chromosome 14q22.1. *Hum. Mol. Genet.* **13**, 2803–2811 (2004).
46. M. Aghili, F. Zahedi, E. Rafiee, Hydroxyglutaric aciduria and malignant brain tumor: A case report and literature review. *J. Neurooncol* **91**, 233–236 (2009).
47. A. R. Mullen, Z. Hu, X. Shi, L. Jiang, L. K. Boroughs, Z. Kovacs, R. Boriack, D. Rakheja, L. B. Sullivan, W. M. Linehan, N. S. Chandel, R. J. DeBerardinis, Oxidation of alpha-ketoglutarate is required for reductive carboxylation in cancer cells with mitochondrial defects. *Cell Rep.* **7**, 1679–1690 (2014).
48. E.-H. Shim, C. B. Livi, D. Rakheja, J. Tan, D. Benson, V. Parekh, E.-Y. Kho, A. P. Ghosh, R. Kirkman, S. Velu, S. Dutta, B. Chenna, S. L. Rea, R. J. Mishur, Q. Li, T. L. Johnson-Pais, L. Guo, S. Bae, S. Wei, K. Block, S. Sudarshan, L-2-Hydroxyglutarate: An epigenetic modifier and putative oncometabolite in renal cancer. *Cancer Discov.* **4**, 1290–1298 (2014).
49. I. P. M. Tomlinson, N. A. Alam, A. J. Rowan, E. Barclay, E. E. M. Jaeger, D. Kelsell, I. Leigh, P. Gorman, H. Lamlum, S. Rahman, R. R. Roylance, S. Olpin, S. Bevan, K. Barker, N. Hearle, R. S. Houlston, M. Kiuru, R. Lehtonen, A. Karhu, S. Vilkki, P. Laiho, C. Eklund, O. Vierimaa, K. Aittomäki, M. Hietala, P. Sistonen, A. Paetau, R. Salovaara, R. Herva, V. Launonen, L. A. Aaltonen; Multiple Leiomyoma Consortium, Germline mutations in *FH* predispose to dominantly inherited uterine fibroids, skin leiomyomata and papillary renal cell cancer. *Nat. Genet.* **30**, 406–410 (2002).
50. E. Gottlieb, I. P. M. Tomlinson, Mitochondrial tumour suppressors: A genetic and biochemical update. *Nat. Rev. Cancer* **5**, 857–866 (2005).
51. B. E. Baysal, R. E. Ferrell, J. E. Willett-Brozick, E. C. Lawrence, D. Myssiorek, A. Bosch, A. van der Mey, P. E. M. Taschner, W. S. Rubinstein, E. N. Myers, C. W. Richard III, C. J. Cornelisse, P. Devilee, B. Devlin, Mutations in *SDHD*, a mitochondrial complex II gene, in hereditary paraganglioma. *Science* **287**, 848–851 (2000).
52. T. Laukka, C. J. Mariani, T. Ihantola, J. Z. Cao, J. Hokkanen, W. G. Kaelin Jr., L. A. Godley, P. Koivunen, Fumarate and succinate regulate expression of hypoxia-inducible genes via TET enzymes. *J. Biol. Chem.* **291**, 4256–4265 (2016).
53. M. Xiao, H. Yang, W. Xu, S. Ma, H. Lin, H. Zhu, L. Liu, Y. Liu, C. Yang, Y. Xu, S. Zhao, D. Ye, Y. Xiong, K.-L. Guan, Inhibition of α-KG-dependent histone and DNA demethylases by fumarate and succinate that are accumulated in mutations of FH and SDH tumor suppressors. *Genes Dev.* **26**, 1326–1338 (2012).
54. W. G. Kaelin Jr., S. L. McKnight, Influence of metabolism on epigenetics and disease. *Cell* **153**, 56–69 (2013).
55. L. B. Sullivan, E. Martinez-Garcia, H. Nguyen, A. R. Mullen, E. Dufour, S. Sudarshan, J. D. Licht, R. J. Deberardinis, N. S. Chandel, The proto-oncometabolite fumarate binds glutathione to amplify ROS-dependent signaling. *Mol. Cell* **51**, 236–248 (2013).
56. J. Adam, E. Hatipoglu, L. O'Flaherty, N. Ternette, N. Sahgal, H. Lockstone, D. Baban, E. Nye, G. W. Stamp, K. Wolhuter, M. Stevens, R. Fischer, P. Carmeliet, P. H. Maxwell, C. W. Pugh, N. Frizzell, T. Soga, B. M. Kessler, M. El-Bahrawy, P. J. Ratcliffe, P. J. Pollard, Renal cyst formation in Fh1-deficient mice is independent of the Hif/Phd pathway: Roles for fumarate in KEAP1 succination and Nrf2 signaling. *Cancer Cell* **20**, 524–537 (2011).
57. C. Bardella, M. El-Bahrawy, N. Frizzell, J. Adam, N. Ternette, E. Hatipoglu, K. Howarth, L. O'Flaherty, I. Roberts, G. Turner, J. Taylor, K. Giaslakiotis, V. M. Macaulay, A. L. Harris, A. Chandra, H. J. Lehtonen, V. Launonen, L. A. Aaltonen, C. W. Pugh, R. Mihai, D. Trudgian, B. Kessler, J. W. Baynes, P. J. Ratcliffe, I. P. Tomlinson, P. J. Pollard, Aberrant succination of proteins in fumarate hydratase-deficient mice and HLRCC patients is a robust biomarker of mutation status. *J. Pathol.* **225**, 4–11 (2011).
58. A. Ooi, J.-C. Wong, D. Petillo, D. Roossien, V. Perrier-Trudova, D. Whitten, B. W. H. Min, M.-H. Tan, Z. Zhang, X. J. Yang, M. Zhou, B. Gardie, V. Molinié, S. Richard, P. H. Tan, B. T. Teh, K. A. Furge, An antioxidant response phenotype shared between hereditary and sporadic type 2 papillary renal cell carcinoma. *Cancer Cell* **20**, 511–523 (2011).
59. O. Warburg, On respiratory impairment in cancer cells. *Science* **124**, 269–270 (1956).
60. O. Warburg, On the origin of cancer cells. *Science* **123**, 309–314 (1956).
61. C. V. Dang, Links between metabolism and cancer. *Genes Dev.* **26**, 877–890 (2012).
62. W. J. Israelsen, T. L. Dayton, S. M. Davidson, B. P. Fiske, A. M. Hosios, G. Bellinger, J. Li, Y. Yu, M. Sasaki, J. W. Horner, L. N. Burga, J. Xie, M. J. Jurczak, R. A. DePinho, C. B. Clish, T. Jacks, R. G. Kibbey, G. M. Wulf, D. Di Vizio, G. B. Mills, L. C. Cantley, M. G. Vander Heiden, PKM2 isoform-specific deletion reveals a differential requirement for pyruvate kinase in tumor cells. *Cell* **155**, 397–409 (2013).
63. S. Joshi, D. Tolkunov, H. Aviv, A. A. Hakimi, M. Yao, J. J. Hsieh, S. Ganesan, C. S. Chan, E. White, The genomic landscape of renal oncocytoma identifies a metabolic barrier to tumorigenesis. *Cell Rep.* **13**, 1895–1908 (2015).

64. F. Weinberg, R. Hamanaka, W. W. Wheaton, S. Weinberg, J. Joseph, M. Lopez, B. Kalyanaraman, G. M. Mutlu, G. R. S. Budinger, N. S. Chandel, Mitochondrial metabolism and ROS generation are essential for Kras-mediated tumorigenicity. *Proc. Natl. Acad. Sci. U.S.A.* **107**, 8788–8793 (2010).
65. I. Martinez-Reyes, L. P. Diebold, H. Kong, M. Schieber, H. Huang, C. T. Hensley, M. M. Mehta, T. Wang, J. H. Santos, R. Woychik, E. Dufour, J. N. Spelbrink, S. E. Weinberg, Y. Zhao, R. J. DeBerardinis, N. S. Chandel, TCA cycle and mitochondrial membrane potential are necessary for diverse biological functions. *Mol. Cell* **61**, 199–209 (2016).
66. X. L. Zu, M. Guppy, Cancer metabolism: Facts, fantasy, and fiction. *Biochem. Biophys. Res. Commun.* **313**, 459–465 (2004).
67. C. Lussey-Lepoutre, K. E. R. Hollinshead, C. Ludwig, M. Menara, A. Morin, L.-J. Castro-Vega, S. J. Parker, M. Janin, C. Martinelli, C. Ottolenghi, C. Metallo, A.-P. Gimenez-Roqueplo, J. Favier, D. A. Tennant, Loss of succinate dehydrogenase activity results in dependency on pyruvate carboxylation for cellular anabolism. *Nat. Commun.* **6**, 8784 (2015).
68. S. Cardaci, L. Zheng, G. MacKay, N. J. F. van den Broek, E. D. MacKenzie, C. Nixon, D. Stevenson, S. Tumanov, V. Bulusu, J. J. Kamphorst, A. Vazquez, S. Fleming, F. Schiavi, G. Kalna, K. Blyth, D. Strathdee, E. Gottlieb, Pyruvate carboxylation enables growth of SDH-deficient cells by supporting aspartate biosynthesis. *Nat. Cell Biol.* **17**, 1317–1326 (2015).
69. A. R. Mullen, W. W. Wheaton, E. S. Jin, P.-H. Chen, L. B. Sullivan, T. Cheng, Y. Yang, W. M. Linehan, N. S. Chandel, R. J. DeBerardinis, Reductive carboxylation supports growth in tumour cells with defective mitochondria. *Nature* **481**, 385–388 (2012).
70. R. Guzy, B. Sharma, E. Bell, N. Chandel, P. Schumacker, Loss of the SdhB, but Not the SdhA, subunit of complex II triggers reactive oxygen species-dependent hypoxia-inducible factor activation and tumorigenesis. *Mol. Cell. Biol.* **28**, 718–731 (2008).
71. C. T. Hensley, A. T. Wasti, R. J. DeBerardinis, Glutamine and cancer: Cell biology, physiology, and clinical opportunities. *J. Clin. Invest.* **123**, 3678–3684 (2013).
72. J. R. Mayers, C. Wu, C. B. Clish, P. Kraft, M. E. Torrence, B. P. Fiske, C. Yuan, Y. Bao, M. K. Townsend, S. S. Tworoger, S. M. Davidson, T. Papagiannakopoulos, A. Yang, T. L. Dayton, S. Ogino, M. J. Stampfer, E. L. Giovannucci, Z. R. Qian, D. A. Rubinson, J. Ma, H. D. Sesso, J. M. Gaziano, B. B. Cochrane, S. Liu, J. Wactawski-Wende, J. E. Manson, M. N. Pollak, A. C. Kimmelman, A. Souza, K. Pierce, T. J. Wang, R. E. Gerszten, C. S. Fuchs, M. G. Vander Heiden, B. M. Wolpin, Elevation of circulating branched-chain amino acids is an early event in human pancreatic adenocarcinoma development. *Nat. Med.* **20**, 1193–1198 (2014).
73. N. Chandel, G. R. S. Budinger, S. H. Choe, P. T. Schumacker, Cellular respiration during hypoxia. Role of cytochrome oxidase as the oxygen sensor in hepatocytes. *J. Biol. Chem.* **272**, 18808–18816 (1997).
74. J. Fan, J. J. Kamphorst, R. Mathew, M. K. Chung, E. White, T. Shlomi, J. D. Rabinowitz, Glutamine-driven oxidative phosphorylation is a major ATP source in transformed mammalian cells in both normoxia and hypoxia. *Mol. Syst. Biol.* **9**, 712 (2013).
75. A. Le, A. N. Lane, M. Hamaker, S. Bose, A. Gouw, J. Barbi, T. Tsukamoto, C. J. Rojas, B. S. Slusher, H. Zhang, L. J. Zimmerman, D. C. Liebler, R. J. C. Slebos, P. K. Lorkiewicz, R. M. Higashi, T. W. M. Fan, C. V. Dang, Glucose-independent glutamine metabolism via TCA cycling for proliferation and survival in B cells. *Cell Metab.* **15**, 110–121 (2012).
76. A. Le, Z. E. Stine, C. Nguyen, J. Afzal, P. Sun, M. Hamaker, N. M. Siegel, A. M. Gouw, B.-h. Kang, S.-H. Yu, R. L. Cochran, K. A. Sailor, H. Song, C. V. Dang, Tumorigenicity of hypoxic respiring cancer cells revealed by a hypoxia–cell cycle dual reporter. *Proc. Natl. Acad. Sci. U.S.A.* **111**, 12486–12491 (2014).
77. J. J. Kamphorst, M. Nofal, C. Commisso, S. R. Hackett, W. Lu, E. Grabocka, M. G. Vander Heiden, G. Miller, J. A. Drebin, D. Bar-Sagi, C. B. Thompson, J. D. Rabinowitz, Human pancreatic cancer tumors are nutrient poor and tumor cells actively scavenge extracellular protein. *Cancer Res.* **75**, 544–553 (2015).
78. C. M. Metallo, P. A. Gameiro, E. L. Bell, K. R. Mattaini, J. Yang, K. Hiller, C. M. Jewell, Z. R. Johnson, D. J. Irvine, L. Guarente, J. K. Kelleher, M. G. Vander Heiden, O. Iliopoulos, G. Stephanopoulos, Reductive glutamine metabolism by IDH1 mediates lipogenesis under hypoxia. *Nature* **481**, 380–384 (2012).
79. D. R. Wise, P. S. Ward, J. E. S. Shay, J. R. Cross, J. J. Gruber, U. M. Sachdeva, J. M. Platt, R. G. DeMatteo, M. C. Simon, C. B. Thompson, Hypoxia promotes isocitrate dehydrogenase-dependent carboxylation of α-ketoglutarate to citrate to support cell growth and viability. *Proc. Natl. Acad. Sci. U.S.A.* **108**, 19611–19616 (2011).
80. M. Laplante, D. M. Sabatini, mTOR signaling in growth control and disease. *Cell* **149**, 274–293 (2012).
81. J. Y. Guo, H.-Y. Chen, R. Mathew, J. Fan, A. M. Strohecker, G. Karsli-Uzunbas, J. J. Kamphorst, G. Chen, J. M. S. Lemons, V. Karantza, H. A. Coller, R. S. DiPaola, C. Gelinas, J. D. Rabinowitz, E. White, Activated Ras requires autophagy to maintain oxidative metabolism and tumorigenesis. *Genes Dev.* **25**, 460–470 (2011).
82. A. M. Strohecker, E. White, Autophagy promotes $Braf^{V600E}$-driven lung tumorigenesis by preserving mitochondrial metabolism. *Autophagy* **10**, 384–385 (2014).
83. N. J. Lanning, B. D. Looyenga, A. L. Kauffman, N. M. Niemi, J. Sudderth, R. J. DeBerardinis, J. P. MacKeigan, A mitochondrial RNAi screen defines cellular bioenergetic determinants and identifies an adenylate kinase as a key regulator of ATP levels. *Cell Rep.* **7**, 907–917 (2014).
84. D. G. Hardie, B. E. Schaffer, A. Brunet, AMPK: An energy-sensing pathway with multiple inputs and outputs. *Trends Cell Biol.* **26**, 190–201 (2016).
85. J. J. Kamphorst, J. R. Cross, J. Fan, E. de Stanchina, R. Mathew, E. P. White, C. B. Thompson, J. D. Rabinowitz, Hypoxic and Ras-transformed cells support growth by scavenging unsaturated fatty acids from lysophospholipids. *Proc. Natl. Acad. Sci. U.S.A.* **110**, 8882–8887 (2013).
86. K. M. Nieman, H. A. Kenny, C. V. Penicka, A. Ladanyi, R. Buell-Gutbrod, M. R. Zillhardt, I. L. Romero, M. S. Carey, G. B. Mills, G. S. Hotamisligil, S. D. Yamada, M. E. Peter, K. Gwin, E. Lengyel, Adipocytes promote ovarian cancer metastasis and provide energy for rapid tumor growth. *Nat. Med.* **17**, 1498–1503 (2011).
87. A. N. McCracken, A. L. Edinger, Nutrient transporters: The Achilles' heel of anabolism. *Trends Endocrinol. Metab.* **24**, 200–208 (2013).
88. P. Nicklin, P. Bergman, B. Zhang, E. Triantafellow, H. Wang, B. Nyfeler, H. Yang, M. Hild, C. Kung, C. Wilson, V. E. Myer, J. P. MacKeigan, J. A. Porter, Y. K. Wang, L. C. Cantley, P. M. Finan, L. O. Murphy, Bidirectional transport of amino acids regulates mTOR and autophagy. *Cell* **136**, 521–534 (2009).
89. L. Galluzzi, F. Pietrocola, B. Levine, G. Kroemer, Metabolic control of autophagy. *Cell* **159**, 1263–1276 (2014).
90. E. White, The role for autophagy in cancer. *J. Clin. Invest.* **125**, 42–46 (2015).
91. L. Galluzzi, F. Pietrocola, J. M. Bravo-San Pedro, R. K. Amaravadi, E. H. Baehrecke, F. Cecconi, P. Codogno, J. Debnath, D. A. Gewirtz, V. Karantza, A. Kimmelman, S. Kumar, B. Levine, M. C. Maiuri, S. J. Martin, J. Penninger, M. Piacentini, D. C. Rubinsztein, H.-U. Simon, A. Simonsen, A. M. Thorburn, G. Velasco, K. M. Ryan, G. Kroemer, Autophagy in malignant transformation and cancer progression. *EMBO J.* **34**, 856–880 (2015).
92. C. Commisso, S. M. Davidson, R. G. Soydaner-Azeloglu, S. J. Parker, J. J. Kamphorst, S. Hackett, E. Grabocka, M. Nofal, J. A. Drebin, C. B. Thompson, J. D. Rabinowitz, C. M. Metallo, M. G. Vander Heiden, D. Bar-Sagi, Macropinocytosis of protein is an amino acid supply route in Ras-transformed cells. *Nature* **497**, 633–637 (2013).
93. W. Palm, Y. Park, K. Wright, N. N. Pavlova, D. A. Tuveson, C. B. Thompson, The utilization of extracellular proteins as nutrients is suppressed by mTORC1. *Cell* **162**, 259–270 (2015).
94. H. Yoo, G. Stephanopoulos, J. K. Kelleher, Quantifying carbon sources for de novo lipogenesis in wild-type and IRS-1 knockout brown adipocytes. *J. Lipid Res.* **45**, 1324–1332 (2004).
95. R. J. DeBerardinis, A. Mancuso, E. Daikhin, I. Nissim, M. Yudkoff, S. Wehrli, C. B. Thompson, Beyond aerobic glycolysis: Transformed cells can engage in glutamine metabolism that exceeds the requirement for protein and nucleotide synthesis. *Proc. Natl. Acad. Sci. U.S.A.* **104**, 19345–19350 (2007).
96. Z. T. Schug, B. Peck, D. T. Jones, Q. Zhang, S. Grosskurth, I. S. Alam, L. M. Goodwin, E. Smethurst, S. Mason, K. Blyth, L. McGarry, D. James, E. Shanks, G. Kalna, R. E. Saunders, M. Jiang, M. Howell, F. Lassailly, M. Z. Thin, B. Spencer-Dene, G. Stamp, N. J. F. van den Broek, G. Mackay, V. Bulusu, J. J. Kamphorst, S. Tardito, D. Strachan, A. L. Harris, E. O. Aboagye, S. E. Critchlow, M. J. O. Wakelam, A. Schulze, E. Gottlieb, Acetyl-CoA synthetase 2 promotes acetate utilization and maintains cancer cell growth under metabolic stress. *Cancer Cell* **27**, 57–71 (2015).
97. C. R. Green, M. Wallace, A. S. Divakaruni, S. A. Phillips, A. N. Murphy, T. P. Ciaraldi, C. M. Metallo, Branched-chain amino acid catabolism fuels adipocyte differentiation and lipogenesis. *Nat. Chem. Biol.* **12**, 15–21 (2016).
98. R. Kannan, I. Lyon, N. Baker, Dietary control of lipogenesis in vivo in host tissues and tumors of mice bearing Ehrlich ascites carcinoma. *Cancer Res.* **40**, 4606–4611 (1980).
99. M. Ookhtens, R. Kannan, I. Lyon, N. Baker, Liver and adipose tissue contributions to newly formed fatty acids in an ascites tumor. *Am. J. Physiol.* **247**, R146–R153 (1984).
100. J. Fan, J. Ye, J. J. Kamphorst, T. Shlomi, C. B. Thompson, J. D. Rabinowitz, Quantitative flux analysis reveals folate-dependent NADPH production. *Nature* **510**, 298–302 (2014).
101. C. A. Lewis, S. J. Parker, B. P. Fiske, D. McCloskey, D. Y. Gui, C. R. Green, N. I. Vokes, A. M. Feist, M. G. Vander Heiden, C. M. Metallo, Tracing compartmentalized NADPH metabolism in the cytosol and mitochondria of mammalian cells. *Mol. Cell* **55**, 253–263 (2014).
102. J. D. Horton, J. L. Goldstein, M. S. Brown, SREBPs: Activators of the complete program of cholesterol and fatty acid synthesis in the liver. *J. Clin. Invest.* **109**, 1125–1131 (2002).
103. K. Düvel, J. L. Yecies, S. Menon, P. Raman, A. I. Lipovsky, A. L. Souza, E. Triantafellow, Q. Ma, R. Gorski, S. Cleaver, M. G. Vander Heiden, J. P. MacKeigan, P. M. Finan, C. B. Clish, L. O. Murphy, B. D. Manning, Activation of a metabolic gene regulatory network downstream of mTOR complex 1. *Mol. Cell* **39**, 171–183 (2010).
104. J. L. Goldstein, R. A. DeBose-Boyd, M. S. Brown, Protein sensors for membrane sterols. *Cell* **124**, 35–46 (2006).
105. T. R. Peterson, S. S. Sengupta, T. E. Harris, A. E. Carmack, S. A. Kang, E. Balderas, D. A. Guertin, K. L. Madden, A. E. Carpenter, B. N. Finck, D. M. Sabatini, mTOR complex 1 regulates lipin 1 localization to control the SREBP pathway. *Cell* **146**, 408–420 (2011).

106. R. J. Deberardinis, J. J. Lum, C. B. Thompson, Phosphatidylinositol 3-kinase-dependent modulation of carnitine palmitoyltransferase 1A expression regulates lipid metabolism during hematopoietic cell growth. *J. Biol. Chem.* **281**, 37372–37380 (2006).
107. R. M. Young, D. Ackerman, Z. L. Quinn, A. Mancuso, M. Gruber, L. Liu, D. N. Giannoukos, E. Bobrovnikova-Marjon, J. A. Diehl, B. Keith, M. C. Simon, Dysregulated mTORC1 renders cells critically dependent on desaturated lipids for survival under tumor-like stress. *Genes Dev.* **27**, 1115–1131 (2013).
108. C. Yokoyama, X. Wang, M. R. Briggs, A. Admon, J. Wu, X. Hua, J. L. Goldstein, M. S. Brown, SREBP-1, a basic-helix-loop-helix-leucine zipper protein that controls transcription of the low density lipoprotein receptor gene. *Cell* **75**, 187–197 (1993).
109. D. Guo, R. M. Prins, J. Dang, D. Kuga, A. Iwanami, H. Soto, K. Y. Lin, T. T. Huang, D. Akhavan, M. B. Hock, S. Zhu, A. A. Kofman, S. J. Bensinger, W. H. Yong, H. V. Vinters, S. Horvath, A. D. Watson, J. G. Kuhn, H. I. Robins, M. P. Mehta, P. Y. Wen, L. M. DeAngelis, M. D. Prados, I. K. Mellinghoff, T. F. Cloughesy, P. S. Mischel, EGFR signaling through an Akt-SREBP-1–dependent, rapamycin-resistant pathway sensitizes glioblastomas to antilipogenic therapy. *Sci. Signal.* **2**, ra82 (2009).
110. D. Guo, F. Reinitz, M. Youssef, C. Hong, D. Nathanson, D. Akhavan, D. Kuga, A. N. Amzajerdi, H. Soto, S. Zhu, I. Babic, K. Tanaka, J. Dang, A. Iwanami, B. Gini, J. DeJesus, D. D. Lisiero, T. T. Huang, R. M. Prins, P. Y. Wen, H. I. Robins, M. D. Prados, L. M. DeAngelis, I. K. Mellinghoff, M. P. Mehta, C. D. James, A. Chakravarti, T. F. Cloughesy, P. Tontonoz, P. S. Mischel, An LXR agonist promotes glioblastoma cell death through inhibition of an EGFR/AKT/SREBP-1/LDLR–dependent pathway. *Cancer Discov.* **1**, 442–456 (2011).
111. A. Stincone, A. Prigione, T. Cramer, M. M. C. Wamelink, K. Campbell, E. Cheung, V. Olin-Sandoval, N.-M. Grüning, A. Krüger, M. Tauqeer Alam, M. A. Keller, M. Breitenbach, K. M. Brindle, J. D. Rabinowitz, M. Ralser, The return of metabolism: Biochemistry and physiology of the pentose phosphate pathway. *Biol. Rev. Camb. Philos. Soc.* **90**, 927–963 (2014).
112. M. G. Vander Heiden, Targeting cancer metabolism: A therapeutic window opens. *Nat. Rev. Drug Discov.* **10**, 671–684 (2011).
113. I. Ben-Sahra, J. J. Howell, J. M. Asara, B. D. Manning, Stimulation of de novo pyrimidine synthesis by growth signaling through mTOR and S6K1. *Science* **339**, 1323–1328 (2013).
114. M. P. Murphy, How mitochondria produce reactive oxygen species. *Biochem. J.* **417**, 1–13 (2009).
115. M. D. Brand, The sites and topology of mitochondrial superoxide production. *Exp. Gerontol.* **45**, 466–472 (2010).
116. S. G. Rhee, H. A. Woo, I. S. Kil, S. H. Bae, Peroxiredoxin functions as a peroxidase and a regulator and sensor of local peroxides. *J. Biol. Chem.* **287**, 4403–4410 (2012).
117. A. G. Cox, C. C. Winterbourn, M. B. Hampton, Mitochondrial peroxiredoxin involvement in antioxidant defence and redox signalling. *Biochem. J.* **425**, 313–325 (2010).
118. M. P. Murphy, Mitochondrial thiols in antioxidant protection and redox signaling: Distinct roles for glutathionylation and other thiol modifications. *Antioxid. Redox Signal.* **16**, 476–495 (2012).
119. T. Finkel, From sulfenylation to sulfhydration: What a thiolate needs to tolerate. *Sci. Signal.* **5**, pe10 (2012).
120. E. C. Cheung, P. Lee, F. Ceteci, C. Nixon, K. Blyth, O. J. Sansom, K. H. Vousden, Opposing effects of TIGAR- and RAC1-derived ROS on Wnt-driven proliferation in the mouse intestine. *Genes Dev.* **30**, 52–63 (2016).
121. K. Irani, Y. Xia, J. L. Zweier, S. J. Sollott, C. J. Der, E. R. Fearon, M. Sundaresan, T. Finkel, P. J. Goldschmidt-Clermont, Mitogenic signaling mediated by oxidants in Ras-transformed fibroblasts. *Science* **275**, 1649–1652 (1997).
122. N. S. Chandel, E. Maltepe, E. Goldwasser, C. E. Mathieu, M. C. Simon, P. T. Schumacker, Mitochondrial reactive oxygen species trigger hypoxia-induced transcription. *Proc. Natl. Acad. Sci. U.S.A.* **95**, 11715–11720 (1998).
123. A. L. Orr, L. Vargas, C. N. Turk, J. E. Baaten, J. T. Matzen, V. J. Dardov, S. J. Attle, J. Li, D. C. Quackenbush, R. L. S. Goncalves, I. V. Perevoshchikova, H. M. Petrassi, S. L. Meeusen, E. K. Ainscow, M. D. Brand, Suppressors of superoxide production from mitochondrial complex III. *Nat. Chem. Biol.* **11**, 834–836 (2015).
124. P. E. Porporato, V. L. Payen, J. Pérez-Escuredo, C. J. De Saedeleer, P. Danhier, T. Copetti, S. Dhup, M. Tardy, T. Vazeille, C. Bouzin, O. Feron, C. Michiels, B. Gallez, P. Sonveaux, A mitochondrial switch promotes tumor metastasis. *Cell Rep.* **8**, 754–766 (2014).
125. J. M. Munson, L. Fried, S. A. Rowson, M. Y. Bonner, L. Karumbaiah, B. Diaz, S. A. Courtneidge, U. G. Knaus, D. J. Brat, J. L. Arbiser, R. V. Bellamkonda, Anti-invasive adjuvant therapy with imipramine blue enhances chemotherapeutic efficacy against glioma. *Sci. Transl. Med.* **4**, 127ra36 (2012).
126. N. S. Chandel, D. A. Tuveson, The promise and perils of antioxidants for cancer patients. *N. Engl. J. Med.* **371**, 177–178 (2014).
127. M. C. Jaramillo, D. D. Zhang, The emerging role of the Nrf2–Keap1 signaling pathway in cancer. *Genes Dev.* **27**, 2179–2191 (2013).
128. G. M. DeNicola, F. A. Karreth, T. J. Humpton, A. Gopinathan, C. Wei, K. Frese, D. Mangal, K. H. Yu, C. J. Yeo, E. S. Calhoun, F. Scrimieri, J. M. Winter, R. H. Hruban, C. Iacobuzio-Donahue, S. E. Kern, I. A. Blair, D. A. Tuveson, Oncogene-induced Nrf2 transcription promotes ROS detoxification and tumorigenesis. *Nature* **475**, 106–109 (2011).
129. G. M. DeNicola, P.-H. Chen, E. Mullarky, J. A. Sudderth, Z. Hu, D. Wu, H. Tang, Y. Xie, J. M. Asara, K. E. Huffman, I. I. Wistuba, J. D. Minna, R. J. DeBerardinis, L. C. Cantley, NRF2 regulates serine biosynthesis in non–small cell lung cancer. *Nat. Genet.* **47**, 1475–1481 (2015).
130. J. Ye, J. Fan, S. Venneti, Y.-W. Wan, B. R. Pawel, J. Zhang, L. W. S. Finley, C. Lu, T. Lindsten, J. R. Cross, G. Qing, Z. Liu, M. C. Simon, J. D. Rabinowitz, C. B. Thompson, Serine catabolism regulates mitochondrial redox control during hypoxia. *Cancer Discov.* **4**, 1406–1417 (2014).
131. I. S. Harris, A. E. Treloar, S. Inoue, M. Sasaki, C. Gorrini, K. C. Lee, K. Y. Yung, D. Brenner, C. B. Knobbe-Thomsen, M. A. Cox, A. Elia, T. Berger, D. W. Cescon, A. Adeoye, A. Brüstle, S. D. Molyneux, J. M. Mason, W. Y. Li, K. Yamamoto, A. Wakeham, H. K. Berman, R. Khokha, S. J. Done, T. J. Kavanagh, C.-W. Lam, T. W. Mak, Glutathione and thioredoxin antioxidant pathways synergize to drive cancer initiation and progression. *Cancer Cell* **27**, 211–222 (2015).
132. D. J. Garama, T. J. Harris, C. L. White, F. J. Rossello, M. Abdul-Hay, D. J. Gough, D. E. Levy, A synthetic lethal interaction between glutathione synthesis and mitochondrial reactive oxygen species provides a tumor-specific vulnerability dependent on STAT3. *Mol. Cell. Biol.* **35**, 3646–3656 (2015).
133. C. Gorrini, I. S. Harris, T. W. Mak, Modulation of oxidative stress as an anticancer strategy. *Nat. Rev. Drug Discov.* **12**, 931–947 (2013).
134. Y. Saito, R. H. Chapple, A. Lin, A. Kitano, D. Nakada, AMPK protects leukemia-initiating cells in myeloid leukemias from metabolic stress in the bone marrow. *Cell Stem Cell* **17**, 585–596 (2015).
135. S.-M. Jeon, N. S. Chandel, N. Hay, AMPK regulates NADPH homeostasis to promote tumour cell survival during energy stress. *Nature* **485**, 661–665 (2012).
136. V. S. LeBleu, J. T. O'Connell, K. N. Gonzalez Herrera, H. Wikman, K. Pantel, M. C. Haigis, F. M. de Carvalho, A. Damascena, L. T. Domingos Chinen, R. M. Rocha, J. M. Asara, R. Kalluri, PGC-1α mediates mitochondrial biogenesis and oxidative phosphorylation in cancer cells to promote metastasis. *Nat. Cell Biol.* **16**, 992–1003 (2014).
137. Z. T. Schafer, A. R. Grassian, L. Song, Z. Jiang, Z. Gerhart-Hines, H. Y. Irie, S. Gao, P. Puigserver, J. S. Brugge, Antioxidant and oncogene rescue of metabolic defects caused by loss of matrix attachment. *Nature* **461**, 109–113 (2009).
138. L. Jiang, A. A. Shestov, P. Swain, C. Yang, S. J. Parker, Q. A. Wang, L. S. Terada, N. D. Adams, M. T. McCabe, B. Pietrak, S. Schmidt, C. M. Metallo, B. P. Dranka, B. Schwartz, R. J. DeBerardinis, Reductive carboxylation supports redox homeostasis during anchorage-independent growth. *Nature* **532**, 255–258 (2016).
139. A. Erez, R. J. DeBerardinis, Metabolic dysregulation in monogenic disorders and cancer—Finding method in madness. *Nat. Rev. Cancer* **15**, 440–448 (2015).
140. E. L. Pearce, M. C. Poffenberger, C.-H. Chang, R. G. Jones, Fueling immunity: Insights into metabolism and lymphocyte function. *Science* **342**, 1242454 (2013).
141. K. Ito, T. Suda, Metabolic requirements for the maintenance of self-renewing stem cells. *Nat. Rev. Mol. Cell Biol.* **15**, 243–256 (2014).
142. H. Shim, C. Dolde, B. C. Lewis, C.-S. Wu, G. Dang, R. A. Jungmann, R. Dalla-Favera, C. V. Dang, c-Myc transactivation of *LDH-A*: Implications for tumor metabolism and growth. *Proc. Natl. Acad. Sci. U.S.A.* **94**, 6658–6663 (1997).
143. V. R. Fantin, J. St-Pierre, P. Leder, Attenuation of LDH-A expression uncovers a link between glycolysis, mitochondrial physiology, and tumor maintenance. *Cancer Cell* **9**, 425–434 (2006).
144. A. Le, C. R. Cooper, A. M. Gouw, R. Dinavahi, A. Maitra, L. M. Deck, R. E. Royer, D. L. Vander Jagt, G. L. Semenza, C. V. Dang, Inhibition of lactate dehydrogenase A induces oxidative stress and inhibits tumor progression. *Proc. Natl. Acad. Sci. U.S.A.* **107**, 2037–2042 (2010).
145. H. Xie, J.-. Hanai, J.-G. Ren, L. Kats, K. Burgess, P. Bhargava, S. Signoretti, J. Billiard, K. J. Duffy, A. Grant, X. Wang, P. K. Lorkiewicz, S. Schatzman, M. Bousamra II, A. N. Lane, R. M. Higashi, T. W. M. Fan, P. P. Pandolfi, V. P. Sukhatme, P. Seth, Targeting lactate dehydrogenase-a inhibits tumorigenesis and tumor progression in mouse models of lung cancer and impacts tumor-initiating cells. *Cell Metab.* **19**, 795–809 (2014).
146. Y.-H. Wang, W. J. Israelsen, D. Lee, V. W. C. Yu, N. T. Jeanson, C. B. Clish, L. C. Cantley, M. G. Vander Heiden, D. T. Scadden, Cell-state-specific metabolic dependency in hematopoiesis and leukemogenesis. *Cell* **158**, 1309–1323 (2014).
147. R. Haas, J. Smith, V. Rocher-Ros, S. Nadkarni, T. Montero-Melendez, F. D'Acquisto, E. J. Bland, M. Bombardieri, C. Pitzalis, M. Perretti, F. M. Marelli-Berg, C. Mauro, Lactate regulates metabolic and pro-inflammatory circuits in control of T cell migration and effector functions. *PLOS Biol.* **13**, e1002202 (2015).
148. O. R. Colegio, N.-Q. Chu, A. L. Szabo, T. Chu, A. M. Rhebergen, V. Jairam, N. Cyrus, C. E. Brokowski, S. C. Eisenbarth, G. M. Phillips, G. W. Cline, A. J. Phillips, R. Medzhitov, Functional polarization of tumour-associated macrophages by tumour-derived lactic acid. *Nature* **513**, 559–563 (2014).
149. O. D. K. Maddocks, C. R. Berkers, S. M. Mason, L. Zheng, K. Blyth, E. Gottlieb, K. H. Vousden, Serine starvation induces stress and p53-dependent metabolic remodelling in cancer cells. *Nature* **493**, 542–546 (2013).
150. C. F. Labuschagne, N. J. F. van den Broek, G. M. Mackay, K. H. Vousden, O. D. K. Maddocks, Serine, but not glycine, supports one-carbon metabolism and proliferation of cancer cells. *Cell Rep.* **7**, 1248–1258 (2014).

151. D. Kim, B. P. Fiske, K. Birsoy, E. Freinkman, K. Kami, R. L. Possemato, Y. Chudnovsky, M. E. Pacold, W. W. Chen, J. R. Cantor, L. M. Shelton, D. Y. Gui, M. Kwon, S. H. Ramkissoon, K. L. Ligon, S. W. Kang, M. Snuderl, M. G. Vander Heiden, D. M. Sabatini, SHMT2 drives glioma cell survival in ischaemia but imposes a dependence on glycine clearance. *Nature* **520**, 363–367 (2015).
152. R. Nilsson, M. Jain, N. Madhusudhan, N. G. Sheppard, L. Strittmatter, C. Kampf, J. Huang, A. Asplund, V. K. Mootha, Metabolic enzyme expression highlights a key role for MTHFD2 and the mitochondrial folate pathway in cancer. *Nat. Commun.* **5**, 3128 (2014).
153. S. E. Weinberg, N. S. Chandel, Targeting mitochondria metabolism for cancer therapy. *Nat. Chem. Biol.* **11**, 9–15 (2015).
154. J. M. M. Evans, L. A. Donnelly, A. M. Emslie-Smith, D. R. Alessi, A. D. Morris, Metformin and reduced risk of cancer in diabetic patients. *BMJ* **330**, 1304–1305 (2005).
155. M. Buzzai, R. G. Jones, R. K. Amaravadi, J. J. Lum, R. J. DeBerardinis, F. Zhao, B. Viollet, C. B. Thompson, Systemic treatment with the antidiabetic drug metformin selectively impairs p53-deficient tumor cell growth. *Cancer Res.* **67**, 6745–6752 (2007).
156. R. M. Memmott, J. R. Mercado, C. R. Maier, S. Kawabata, S. D. Fox, P. A. Dennis, Metformin prevents tobacco carcinogen–induced lung tumorigenesis. *Cancer Prev. Res.* **3**, 1066–1076 (2010).
157. A. Tomimoto, H. Endo, M. Sugiyama, T. Fujisawa, K. Hosono, H. Takahashi, N. Nakajima, Y. Nagashima, K. Wada, H. Nakagama, A. Nakajima, Metformin suppresses intestinal polyp growth in $Apc^{Min/+}$ mice. *Cancer Sci.* **99**, 2136–2141 (2008).
158. H. R. Bridges, A. J. Y. Jones, M. N. Pollak, J. Hirst, Effects of metformin and other biguanides on oxidative phosphorylation in mitochondria. *Biochem. J.* **462**, 475–487 (2014).
159. M.-Y. El-Mir, V. Nogueira, E. Fontaine, N. Avéret, M. Rigoulet, X. Leverve, Dimethylbiguanide inhibits cell respiration via an indirect effect targeted on the respiratory chain complex I. *J. Biol. Chem.* **275**, 223–228 (2000).
160. M. R. Owen, E. Doran, A. P. Halestrap, Evidence that metformin exerts its anti-diabetic effects through inhibition of complex 1 of the mitochondrial respiratory chain. *Biochem. J.* **348** (Pt. 3), 607–614 (2000).
161. W. W. Wheaton, S. E. Weinberg, R. B. Hamanaka, S. Soberanes, L. B. Sullivan, E. Anso, A. Glasauer, E. Dufour, G. M. Mutlu, G. R. S. Budigner, N. S. Chandel, Metformin inhibits mitochondrial complex I of cancer cells to reduce tumorigenesis. *Elife* **3**, e02242 (2014).
162. T. Griss, E. E. Vincent, R. Egnatchik, J. Chen, E. H. Ma, B. Faubert, B. Viollet, R. J. DeBerardinis, R. G. Jones, Metformin antagonizes cancer cell proliferation by suppressing mitochondrial-dependent biosynthesis. *PLOS Biol.* **13**, e1002309 (2015).
163. A. Emami Riedmaier, P. Fisel, A. T. Nies, E. Schaeffeler, M. Schwab, Metformin and cancer: From the old medicine cabinet to pharmacological pitfalls and prospects. *Trends Pharmacol. Sci.* **34**, 126–135 (2013).
164. M. Pollak, Overcoming drug development bottlenecks with repurposing: Repurposing biguanides to target energy metabolism for cancer treatment. *Nat. Med.* **20**, 591–593 (2014).
165. K. Birsoy, R. Possemato, F. K. Lorbeer, E. C. Bayraktar, P. Thiru, B. Yucel, T. Wang, W. W. Chen, C. B. Clish, D. M. Sabatini, Metabolic determinants of cancer cell sensitivity to glucose limitation and biguanides. *Nature* **508**, 108–112 (2014).
166. D. B. Shackelford, E. Abt, L. Gerken, D. S. Vasquez, A. Seki, M. Leblanc, L. Wei, M. C. Fishbein, J. Czernin, P. S. Mischel, R. J. Shaw, LKB1 inactivation dictates therapeutic response of non-small cell lung cancer to the metabolism drug phenformin. *Cancer Cell* **23**, 143–158 (2013).
167. S.-P. Gravel, L. Hulea, N. Toban, E. Birman, M.-J. Blouin, M. Zakikhani, Y. Zhao, I. Topisirovic, J. St-Pierre, M. Pollak, Serine deprivation enhances antineoplastic activity of biguanides. *Cancer Res.* **74**, 7521–7533 (2014).
168. G. Karsli-Uzunbas, J. Y. Guo, S. Price, X. Teng, S. V. Laddha, S. Khor, N. Y. Kalaany, T. Jacks, C. S. Chan, J. D. Rabinowitz, E. White, Autophagy is required for glucose homeostasis and lung tumor maintenance. *Cancer Discov.* **4**, 914–927 (2014).
169. J. Son, C. A. Lyssiotis, H. Ying, X. Wang, S. Hua, M. Ligorio, R. M. Perera, C. R. Ferrone, E. Mullarky, N. Shyh-Chang, Y. Kang, J. B. Fleming, N. Bardeesy, J. M. Asara, M. C. Haigis, R. A. DePinho, L. C. Cantley, A. C. Kimmelman, Glutamine supports pancreatic cancer growth through a KRAS-regulated metabolic pathway. *Nature* **496**, 101–105 (2013).
170. Y. Xiang, Z. E. Stine, J. Xia, Y. Lu, R. S. O'Connor, B. J. Altman, A. L. Hsieh, A. M. Gouw, A. G. Thomas, P. Gao, L. Sun, L. Song, B. Yan, B. S. Slusher, J. Zhuo, L. L. Ooi, C. G. L. Lee, A. Mancuso, A. S. McCallion, A. Le, M. C. Milone, S. Rayport, D. W. Felsher, C. V. Dang, Targeted inhibition of tumor-specific glutaminase diminishes cell-autonomous tumorigenesis. *J. Clin. Invest.* **125**, 2293–2306 (2015).
171. S. A. Comerford, Z. Huang, X. Du, Y. Wang, L. Cai, A. K. Witkiewicz, H. Walters, M. N. Tantawy, A. Fu, H. C. Manning, J. D. Horton, R. E. Hammer, S. L. McKnight, B. P. Tu, Acetate dependence of tumors. *Cell* **159**, 1591–1602 (2014).
172. T. Mashimo, K. Pichumani, V. Vemireddy, K. J. Hatanpaa, D. K. Singh, S. Sirasanagandla, S. Nannepaga, S. G. Piccirillo, Z. Kovacs, C. Foong, Z. Huang, S. Barnett, B. E. Mickey, R. J. DeBerardinis, B. P. Tu, E. A. Maher, R. M. Bachoo, Acetate is a bioenergetic substrate for human glioblastoma and brain metastases. *Cell* **159**, 1603–1614 (2014).
173. J. A. Engelman, L. Chen, X. Tan, K. Crosby, A. R. Guimaraes, R. Upadhyay, M. Maira, K. McNamara, S. A. Perera, Y. Song, L. R. Chirieac, R. Kaur, A. Lightbown, J. Simendinger, T. Li, R. F. Padera, C. García-Echeverría, R. Weissleder, U. Mahmood, L. C. Cantley, K.-K. Wong, Effective use of PI3K and MEK inhibitors to treat mutant *Kras* G12D and *PIK3CA* H1047R murine lung cancers. *Nat. Med.* **14**, 1351–1356 (2008).
174. D. Herranz, A. Ambesi-Impiombato, J. Sudderth, M. Sánchez-Martín, L. Belver, V. Tosello, L. Xu, A. A. Wendorff, M. Castillo, J. E. Haydu, J. Márquez, J. M. Matés, A. L. Kung, S. Rayport, C. Cordon-Cardo, R. J. DeBerardinis, A. A. Ferrando, Metabolic reprogramming induces resistance to anti-NOTCH1 therapies in T cell acute lymphoblastic leukemia. *Nat. Med.* **21**, 1182–1189 (2015).
175. A. Viale, P. Pettazzoni, C. A. Lyssiotis, H. Ying, N. Sánchez, M. Marchesini, A. Carugo, T. Green, S. Seth, V. Giuliani, M. Kost-Alimova, F. Muller, S. Colla, L. Nezi, G. Genovese, A. K. Deem, A. Kapoor, W. Yao, E. Brunetto, Y. Kang, M. Yuan, J. M. Asara, Y. A. Wang, T. P. Heffernan, A. C. Kimmelman, H. Wang, J. B. Fleming, L. C. Cantley, R. A. DePinho, G. F. Draetta, Oncogene ablation-resistant pancreatic cancer cells depend on mitochondrial function. *Nature* **514**, 628–632 (2014).
176. P. Yuan, K. Ito, R. Perez-Lorenzo, C. Del Guzzo, J. H. Lee, C.-H. Shen, M. W. Bosenberg, M. McMahon, L. C. Cantley, B. Zheng, Phenformin enhances the therapeutic benefit of $BRAF^{V600E}$ inhibition in melanoma. *Proc. Natl. Acad. Sci. U.S.A.* **110**, 18226–18231 (2013).
177. A. Roesch, A. Vultur, I. Bogeski, H. Wang, K. M. Zimmermann, D. Speicher, C. Körbel, M. W. Laschke, P. A. Gimotty, S. E. Philipp, E. Krause, S. Pätzold, J. Villanueva, C. Krepler, M. Fukunaga-Kalabis, M. Hoth, B. C. Bastian, T. Vogt, M. Herlyn, Overcoming intrinsic multidrug resistance in melanoma by blocking the mitochondrial respiratory chain of slow-cycling $JARID1B^{high}$ cells. *Cancer Cell* **23**, 811–825 (2013).
178. A. Janzer, N. J. German, K. N. Gonzalez-Herrera, J. M. Asara, M. C. Haigis, K. Struhl, Metformin and phenformin deplete tricarboxylic acid cycle and glycolytic intermediates during cell transformation and NTPs in cancer stem cells. *Proc. Natl. Acad. Sci. U.S.A.* **111**, 10574–10579 (2014).
179. J. Yun, E. Mullarky, C. Lu, K. N. Bosch, A. Kavalier, K. Rivera, J. Roper, I. I. C. Chio, E. G. Giannopoulou, C. Rago, A. Muley, J. M. Asara, J. Paik, O. Elemento, Z. Chen, D. J. Pappin, L. E. Dow, N. Papadopoulos, S. S. Gross, L. C. Cantley, Vitamin C selectively kills *KRAS* and *BRAF* mutant colorectal cancer cells by targeting GAPDH. *Science* **350**, 1391–1396 (2015).
180. Q. Chen, M. G. Espey, A. Y. Sun, C. Pooput, K. L. Kirk, M. C. Krishna, D. B. Khosh, J. Drisko, M. Levine, Pharmacologic doses of ascorbate act as a prooxidant and decrease growth of aggressive tumor xenografts in mice. *Proc. Natl. Acad. Sci. U.S.A.* **105**, 11105–11109 (2008).
181. Y. Ma, J. Chapman, M. Levine, K. Polireddy, J. Drisko, Q. Chen, High-dose parenteral ascorbate enhanced chemosensitivity of ovarian cancer and reduced toxicity of chemotherapy. *Sci. Transl. Med.* **6**, 222ra18 (2014).
182. A. Tagde, H. Singh, M. H. Kang, C. P. Reynolds, The glutathione synthesis inhibitor buthionine sulfoximine synergistically enhanced melphalan activity against preclinical models of multiple myeloma. *Blood Cancer J.* **4**, e229 (2014).
183. A. Glasauer, L. A. Sena, L. P. Diebold, A. P. Mazar, N. S. Chandel, Targeting SOD1 reduces experimental non-small-cell lung cancer. *J. Clin. Invest.* **124**, 117–128 (2014).
184. O. Oivares, J. H. M. Däbritz, A. King, E. Gottlieb, C. Halsey, Research into cancer metabolomics: Towards a clinical metamorphosis. *Semin. Cell Dev. Biol.* **43**, 52–64 (2015).
185. J. M. Buescher, M. R. Antoniewicz, L. G. Boros, S. C. Burgess, H. Brunengraber, C. B. Clish, R. J. DeBerardinis, O. Feron, C. Frezza, B. Ghesquiere, E. Gottlieb, K. Hiller, R. G. Jones, J. J. Kamphorst, R. G. Kibbey, A. C. Kimmelman, J. W. Locasale, S. Y. Lunt, O. D. K. Maddocks, C. Malloy, C. M. Metallo, E. J. Meuillet, J. Munger, A roadmap for interpreting ^{13}C metabolite labeling patterns from cells. *Curr. Opin. Biotechnol.* **34**, 189–201 (2015).
186. R. J. DeBerardinis, C. B. Thompson, Cellular metabolism and disease: What do metabolic outliers teach us? *Cell* **148**, 1132–1144 (2012).
187. O. C. Andronesi, O. Rapalino, E. Gerstner, A. Chi, T. T. Batchelor, D. P. Cahill, A. G. Sorensen, B. R. Rosen, Detection of oncogenic IDH1 mutations using magnetic resonance spectroscopy of 2-hydroxyglutarate. *J. Clin. Invest.* **123**, 3659–3663 (2013).
188. C. Lussey-Lepoutre, A. Bellucci, A. Morin, A. Buffet, L. Amar, M. Janin, C. Ottolenghi, F. Zinzindohoué, G. Autret, N. Burnichon, E. Robidel, B. Banting, S. Fontaine, C.-A. Cuenod, P. Benit, P. Rustin, P. Halimi, L. Fournier, A.-P. Gimenez-Roqueplo, J. Favier, B. Tavitian, In vivo detection of succinate by magnetic resonance spectroscopy as a hallmark of *SDHx* mutations in paraganglioma. *Clin. Cancer Res.* **22**, 1120–1129 (2016).
189. N. M. Vacanti, A. S. Divakaruni, C. R. Green, S. J. Parker, R. R. Henry, T. P. Ciaraldi, A. N. Murphy, C. M. Metallo, Regulation of substrate utilization by the mitochondrial pyruvate carrier. *Mol. Cell* **56**, 425–435 (2014).
190. C. Yang, B. Ko, C. T. Hensley, L. Jiang, A. T. Wasti, J. Kim, J. Sudderth, M. A. Calvaruso, L. Lumata, M. Mitsche, J. Rutter, M. E. Merritt, R. J. DeBerardinis, Glutamine oxidation maintains the TCA cycle and cell survival during impaired mitochondrial pyruvate transport. *Mol. Cell* **56**, 414–424 (2014).
191. J. C. Schell, K. A. Olson, L. Jiang, A. J. Hawkins, J. G. Van Vranken, J. Xie, R. A. Egnatchik, E. G. Earl, R. J. DeBerardinis, J. Rutter, A role for the mitochondrial pyruvate carrier as a repressor of the Warburg effect and colon cancer cell growth. *Mol. Cell* **56**, 400–413 (2014).

192. I. Marin-Valencia, C. Yang, T. Mashimo, S. Cho, H. Baek, X.-L. Yang, K. N. Rajagopalan, M. Maddie, V. Vemireddy, Z. Zhao, L. Cai, L. Good, B. P. Tu, K. J. Hatanpaa, B. E. Mickey, J. M. Matés, J. M. Pascual, E. A. Maher, C. R. Malloy, R. J. DeBerardinis, Robert M. Bachoo, Analysis of tumor metabolism reveals mitochondrial glucose oxidation in genetically diverse human glioblastomas in the mouse brain in vivo. *Cell Metab*. **15**, 827–837 (2012).
193. M. O. Yuneva, T. W. M. Fan, T. D. Allen, R. M. Higashi, D. V. Ferraris, T. Tsukamoto, J. M. Matés, F. J. Alonso, C. Wang, Y. Seo, X. Chen, J. M. Bishop, The metabolic profile of tumors depends on both the responsible genetic lesion and tissue type. *Cell Metab.* **15**, 157–170 (2012).
194. E. A. Maher, I. Marin-Valencia, R. M. Bachoo, T. Mashimo, J. Raisanen, K. J. Hatanpaa, A. Jindal, F. M. Jeffrey, C. Choi, C. Madden, D. Mathews, J. M. Pascual, B. E. Mickey, C. R. Malloy, R. J. DeBerardinis, Metabolism of [U-^{13} C]glucose in human brain tumors *in vivo*. *NMR Biomed.* **25**, 1234–1244 2012).
195. K. Sellers, M. P. Fox, M. Bousamra II, S. P. Slone, R. M. Higashi, D. M. Miller, Y. Wang, J. Yan, M. O. Yuneva, R. Deshpande, A. N. Lane, T. W.-M. Fan, Pyruvate carboxylase is critical for non-small-cell lung cancer proliferation. *J. Clin. Invest.* **125**, 687–698 (2015).
196. T. W. M. Fan, A. N. Lane, R. M. Higashi, M. A. Farag, H. Gao, M. Bousamra, D. M. Miller, Altered regulation of metabolic pathways in human lung cancer discerned by ^{13}C stable isotope-resolved metabolomics (SIRM). *Mol. Cancer* **8**, 41 (2009).
197. C. T. Hensley, B. Faubert, Q. Yuan, N. Lev-Cohain, E. Jin, J. Kim, L. Jiang, B. Ko, R. Skelton, L. Loudat, M. Wodzak, C. Klimko, E. McMillan, Y. Butt, M. Ni, D. Oliver, J. Torrealba, C. R. Malloy, K. Kernstine, R. E. Lenkinski, R. J. DeBerardinis, Metabolic heterogeneity in human lung tumors. *Cell* **164**, 681–694 (2016).
198. S. M. Davidson, T. Papagiannakopoulos, B. A. Olenchock, J. E. Heyman, M. A. Keibler, A. Luengo, M. R. Bauer, A. K. Jha, J. P. O'Brien, K. A. Pierce, D. Y. Gui, L. B. Sullivan, T. M. Wasylenko, L. Subbaraj, C. R. Chin, G. Stephanopolous, B. T. Mott, T. Jacks, C. B. Clish, M. G. Vander Heiden, Environment impacts the metabolic dependencies of ras-driven non-small cell lung cancer. *Cell Metab.* **23**, 517–528 (2016).
199. K. Birsoy, T. Wang, W. W. Chen, E. Freikman, M. Abu-Remaileh, D. M. Sabatini, An essential role of the mitochondrial electron transport chain in cell proliferation is to enable aspartate synthesis. *Cell* **162**, 540–551 (2015).
200. L. B. Sullivan, D. Y. Gui, A. M. Hosios, L. N. Bush, E. Freinkman, M. G. Vander Hediden, Supporting aspartate biosynthesis is an essential function of respiration in proliferating cells. *Cell* **162**, 552–563 (2015).

Acknowledgments: We are grateful to J. Schaffer for illustrating the figures. **Funding:** This work was supported by NIH grants RO1 CA12306708 (to N.S.C.) and RO1 CA157996 to (R.J.D.). **Author contributions:** N.S.C. wrote the abstract, bioenergetics, redox, and targeting metabolism for cancer therapy sections. R.J.D. wrote the introduction, biosynthesis, technology, Box 1, and conclusion sections. N.S.C. and R.J.D. both wrote the metabolic reprogramming and oncometabolites sections. **Competing interests:** R.J.D. is on the Advisory Boards of Agios Pharmaceuticals and Peloton Therapeutics. N.S.C. declares no competing interests. **Data and materials availability:** All data needed to evaluate the conclusions in the paper are present in the paper and/or the Supplementary Materials. Additional data related to this paper may be requested from the authors.

Submitted 1 February 2016
Accepted 29 April 2016
Published 27 May 2016
10.1126/sciadv.1600200

Citation: R. J. DeBerardinis, N. S. Chandel, Fundamentals of cancer metabolism. *Sci. Adv.* **2**, e1600200 (2016).

ScienceAdvances

HEALTH AND MEDICINE

The DNA cytosine deaminase APOBEC3B promotes tamoxifen resistance in ER-positive breast cancer

Emily K. Law,[1,2,3,4]* Anieta M. Sieuwerts,[5]* Kelly LaPara,[2] Brandon Leonard,[2,3,4] Gabriel J. Starrett,[2,3,4] Amy M. Molan,[2,3,4] Nuri A. Temiz,[2,3,4] Rachel Isaksson Vogel,[2,6] Marion E. Meijer-van Gelder,[5] Fred C. G. J. Sweep,[7] Paul N. Span,[8] John A. Foekens,[5] John W. M. Martens,[5] Douglas Yee,[2] Reuben S. Harris[1,2,3,4]†

2016 © The Authors, some rights reserved; exclusive licensee American Association for the Advancement of Science. Distributed under a Creative Commons Attribution NonCommercial License 4.0 (CC BY-NC).

Breast tumors often display extreme genetic heterogeneity characterized by hundreds of gross chromosomal aberrations and tens of thousands of somatic mutations. Tumor evolution is thought to be ongoing and driven by multiple mutagenic processes. A major outstanding question is whether primary tumors have preexisting mutations for therapy resistance or whether additional DNA damage and mutagenesis are necessary. Drug resistance is a key measure of tumor evolvability. If a resistance mutation preexists at the time of primary tumor presentation, then the intended therapy is likely to fail. However, if resistance does not preexist, then ongoing mutational processes still have the potential to undermine therapeutic efficacy. The antiviral enzyme APOBEC3B (apolipoprotein B mRNA-editing enzyme, catalytic polypeptide-like 3B) preferentially deaminates DNA C-to-U, which results in signature C-to-T and C-to-G mutations commonly observed in breast tumors. We use clinical data and xenograft experiments to ask whether APOBEC3B contributes to ongoing breast tumor evolution and resistance to the selective estrogen receptor modulator, tamoxifen. First, APOBEC3B levels in primary estrogen receptor–positive (ER^+) breast tumors inversely correlate with the clinical benefit of tamoxifen in the treatment of metastatic ER^+ disease. Second, APOBEC3B depletion in an ER^+ breast cancer cell line results in prolonged tamoxifen responses in murine xenograft experiments. Third, APOBEC3B overexpression accelerates the development of tamoxifen resistance in murine xenograft experiments by a mechanism that requires the enzyme's catalytic activity. These studies combine to indicate that APOBEC3B promotes drug resistance in breast cancer and that inhibiting APOBEC3B-dependent tumor evolvability may be an effective strategy to improve efficacies of targeted cancer therapies.

INTRODUCTION

Improvements in the detection and therapy of operable breast tumors have contributed to a steady decline in mortality (*1*, *2*). Essentially all breast cancer deaths are caused by metastatic outgrowths that compromise vital organs, such as the brain, liver, or lungs. Adjuvant systemic therapies effectively reduce the risk of recurrence at these distant metastatic sites by treating preexisting, clinically undetectable, micrometastatic deposits. In estrogen receptor–positive (ER^+) breast cancer, a propensity for late recurrence more than 5 years after surgery is well documented and has resulted in recommendations to extend adjuvant endocrine therapy for a total of 10 years (*3*, *4*). Although endocrine therapy may be extended, it is evident that late recurrences occur even while the patient is taking appropriate therapy (*5*). The late recurrence of these apparently dormant metastatic breast cancer cells may be due to ongoing tumor evolution and acquisition of additional genetic aberrations.

Mutations are thought to be the major drivers of recurrence, metastasis, and therapeutic resistance. Recent studies on the molecular origins of mutations in breast cancer have implicated several molecular mechanisms, including both spontaneous and enzyme-catalyzed deamination of DNA cytosine bases (*6*–*10*) [reviewed by Swanton *et al.* (*11*), Roberts and Gordenin (*12*), and Helleday *et al.* (*13*)]. The former process correlates with aging and is mostly due to hydrolytic conversion of 5-methyl cytosine (mC) bases within 5′ NmCG motifs into thymines, which escape base excision repair and are converted into C-to-T transition mutations by DNA replication (N = A, C, G, or T). The latter process is attributable to single-stranded DNA cytosine-to-uracil (C-to-U) deamination catalyzed by one or more members of the APOBEC3 (apolipoprotein B mRNA-editing enzyme, catalytic polypeptide-like 3) family of enzymes, characterized by C-to-T transitions and C-to-G transversions in 5′TCW motifs (W = A or T).

Human cells have the capacity to express up to seven distinct APOBEC3 enzymes, which function normally as overlapping innate immune defenses against a wide variety of DNA-based viruses and transposons [reviewed by Malim and Bieniasz (*14*), Stavrou and Ross (*15*), and Simon *et al.* (*16*)]. APOBEC3A (A3A) and APOBEC3B (A3B) are leading candidates for explaining APOBEC signature mutations in breast tumors because overexpression of these enzymes triggers DNA damage responses and inflicts chromosomal mutations in hallmark trinucleotide contexts (*7*, *17*–*21*). However, endogenous *A3A* is not expressed significantly, nor is its activity detectable in breast cancer cell lines (*7*, *22*) (see Results). The molecular relevance of A3A is therefore difficult to assess because the impact of the endogenous protein cannot be quantified. In comparison, endogenous A3B is predominantly nuclear and has been shown to be responsible for elevated levels of genomic uracil and mutation in multiple breast cancer cell lines (*7*, *22*). A3B is overexpressed in approximately 50%

[1]Howard Hughes Medical Institute, University of Minnesota, Minneapolis, MN 55455, USA. [2]Masonic Cancer Center, University of Minnesota, Minneapolis, MN 55455, USA. [3]Institute for Molecular Virology, University of Minnesota, Minneapolis, MN 55455, USA. [4]Department of Biochemistry, Molecular Biology and Biophysics, University of Minnesota, Minneapolis, MN 55455, USA. [5]Department of Medical Oncology and Cancer Genomics Netherlands, Erasmus MC Cancer Institute, 3015 GE Rotterdam, Netherlands. [6]Division of Gynecologic Oncology, Department of Obstetrics, Gynecology and Women's Health, University of Minnesota, Minneapolis, MN 55455, USA. [7]Department of Laboratory Medicine, Radboud University Medical Center, Nijmegen, Netherlands. [8]Department of Radiation Oncology, Radboud University Medical Center, Nijmegen, Netherlands.
*These authors contributed equally to this work.
†Corresponding author. Email: rsh@umn.edu

of primary breast tumors (*7*, *8*), and retrospective studies have associated elevated *A3B* mRNA levels with poor outcomes for adjuvant treatment–naïve ER$^+$ breast cancer cohorts (*23*, *24*). Our original studies relied on a retrospective prognostic analysis of a treatment-naïve ER$^+$ breast cancer cohort (*23*); therefore, the observed correlation between elevated *A3B* mRNA levels and poor clinical outcomes is consistent with a variety of therapy-independent intrinsic molecular mechanisms ranging from indirect models (such as A3B promoting tumor cell growth) to direct models (such as A3B causing the genomic DNA damage that results in mutations that fuel ongoing tumor evolution).

A current debate in the cancer field is whether the mutations that cause therapy resistance preexist in primary tumors (that is, exist even before diagnosis) or continually accumulate (even after treatment initiation). In support of the former view, primary tumors are often composed of billions of cells that are highly heterogeneous, and deep-sequencing studies have found known drug resistance mutations before therapy initiation [for example, (*25*–*27*)]. However, many studies also support the latter view of ongoing tumor evolution. For instance, primary tumor deep-sequencing studies often fail to find evidence for preexisting resistance mutations [for example, (*26*, *28*)]. Recurrent breast tumors also often have many more somatic mutations compared to corresponding primary tumors, suggesting ongoing and cumulative mutational processes (*29*, *30*). In addition, the subclonal nature of most mutations in breast cancer, as well as many other cancer types, provides strong evidence for ongoing tumor evolution, including significant proportions of APOBEC signature mutations (*28*, *31*, *32*). Moreover, at the clinical level, the fact that remission periods in breast cancer can last for many years strongly suggests that additional genetic changes are required for at least one remaining tumor cell to manifest as recurrent disease (*3*, *4*). Here, we test the hypothesis that A3B contributes to ongoing tumor evolution and to the development of drug resistance mutations in ER$^+$ breast cancer.

RESULTS

Primary breast tumor *A3B* mRNA levels predict therapeutic failure upon tumor recurrence

To determine whether A3B contributes to endocrine therapy resistance, we evaluated the predictive potential of *A3B* expression in primary breast tumors from a total of 285 hormone therapy–naïve breast cancer patients who received tamoxifen as a first-line therapy for recurrent disease (*33*). A schematic of the study timeline is shown in Fig. 1A, and detailed patient characteristics are shown in table S1. Archived fresh-frozen primary tumor specimens were used to prepare total RNA, and reverse transcription quantitative polymerase chain reaction (RT-qPCR) was used to quantify *A3B* mRNA levels. These gene expression results were divided into four quartiles for subsequent clinical data analysis, with primary tumors of the upper quartile expressing an average of fourfold to sixfold more *A3B* mRNA than those in the lower quartile (dark blue versus red histogram bars, respectively, in Fig. 1B).

The progression-free survival (PFS) durations following recurrence and subsequent first-line tamoxifen therapy were compared for each of the four *A3B* expression groups. This analysis revealed a dose-response relationship, with the highest *A3B*-expressing group associating with the shortest PFS and with the lowest *A3B*-expressing group associating with the longest PFS (Fig. 1C; log-rank, $P < 0.0001$). The median PFS was 6.2 months for the highest *A3B*-expressing group and 14.5 months for the lowest *A3B*-expressing group [hazard ratio (HR) 2.40 (1.69 to 3.41); log-rank, $P < 0.0001$]. This result remained significant for high versus low A3B levels in

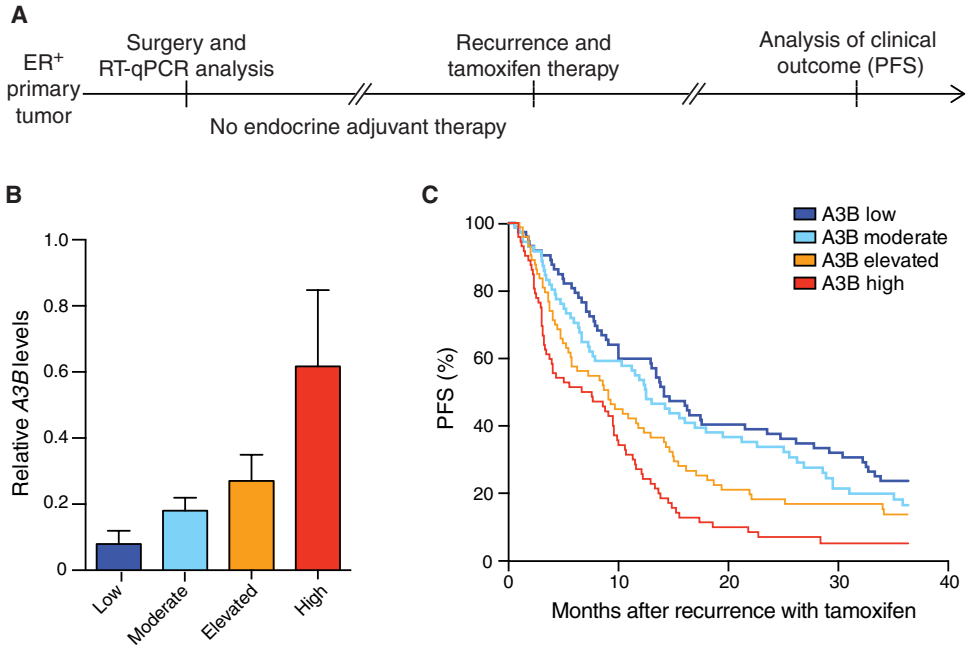

Fig. 1. High *A3B* levels in primary ER$^+$ breast tumors predict poor response to tamoxifen therapy after tumor recurrence. (**A**) Schematic of the clinical time course. Timeline breaks depict variable intervals between clinical milestones. (**B**) Relative *A3B* expression levels in each observation group [mean ± SD of $n = 72$ (quartiles 1 and 3), $n = 70$ (quartile 2), and $n = 71$ (quartile 4)]. (**C**) Kaplan-Meier curves showing the periods of PFS after initiating tamoxifen therapy for patients whose primary tumors expressed *A3B* at low (dark blue line), intermediate (light blue and orange lines), or high levels [red line; patient groups and color scheme match those in (B)].

a multivariate analysis after including the known clinical pathological predictors of age, disease-free interval, dominant site of relapse, adjuvant chemotherapy, and ER and progesterone receptor mRNA levels measured in the primary tumor [HR 2.19 (1.51 to 3.20); log-rank, $P < 0.0001$; table S2]. These data indicate that primary tumor *A3B* mRNA levels are strong and independent predictors of PFS for recurrent ER$^+$ breast cancer treated with tamoxifen. These observations do not support models in which resistance-conferring mutations preexist in primary tumors—or disease outcomes would have had no correlation with *A3B* expression levels and the data for each quartile group would have superimposed. Rather, the data support a model in which A3B promotes the ongoing diversification of residual primary tumor cells (micrometastatic deposits) that ultimately manifest in the recurrent setting as acquired resistance, failed tamoxifen therapy, and disease progression.

Endogenous *A3B* depletion does not alter the phenotype of MCF-7L ER$^+$ breast cancer cells in culture

MCF-7 has been used for decades as a unique cell-based model for ER$^+$ breast cancer research [reviewed by Lee *et al.* (*34*)]. Engrafted MCF-7 tumors are dependent on ER function and therefore are sensitive to selective ER modulators, including tamoxifen. Furthermore, tamoxifen-induced tumor dormancy (indolence) in this model system, which can last for several months, frequently leads to drug-resistant and highly proliferative cell masses. For further studies, including animal experiments below, we elected to use the derivative line MCF-7L because it is tumorigenic in immunodeficient mice [Ibrahim *et al.* (*35*), Sachdev *et al.* (*36*), and references therein] and expresses endogenous *A3B* mRNA at levels approximating those found in many primary breast tumors (*7*). Like most other breast cancer cell lines, MCF-7L cells have very low levels of *A3A* and variable levels of other *APOBEC3* mRNAs, which have not been implicated in breast cancer mutagenesis (fig. S1).

We initially asked whether endogenous *A3B* depletion alters molecular or cellular characteristics of MCF-7L. Cells were transduced with an *A3B*-specific short hairpin RNA (shRNA) construct (shA3B) or a nonspecific shRNA construct as a control (shCON) (*7*), and uniform shRNA-expressing pools were selected using the linked puromycin resistance gene. In all shA3B-transduced pools, a robust >25-fold depletion of endogenous *A3B* mRNA was achieved (Fig. 2A). Moreover, the depletion of *A3B* mRNA was mirrored by a corresponding ablation of all measurable DNA cytosine deaminase activities from whole-cell and nuclear extracts (Fig. 2B). Although several other *APOBEC* family member genes are expressed in MCF-7L, their protein levels are likely too low to detect using this assay (A3A, A3D, A3G, and A1), the enzyme is not active on DNA (A2), and/or their single-stranded DNA cytosine deaminase activity is not evident in cellular extracts (A3C and A3F) (*7*, *22*). At the microscopic level, shA3B- and shCON-expressing cells were visibly indistinguishable (Fig. 2C). The two cell populations showed nearly identical growth rates and doubling times in cell culture (Fig. 2, D and E). These results are consistent with *A3B* knockdown data using the same shRNA construct in other breast cancer cell lines (*7*, *22*) and with the observation that *A3B* is a nonessential human gene (*37*).

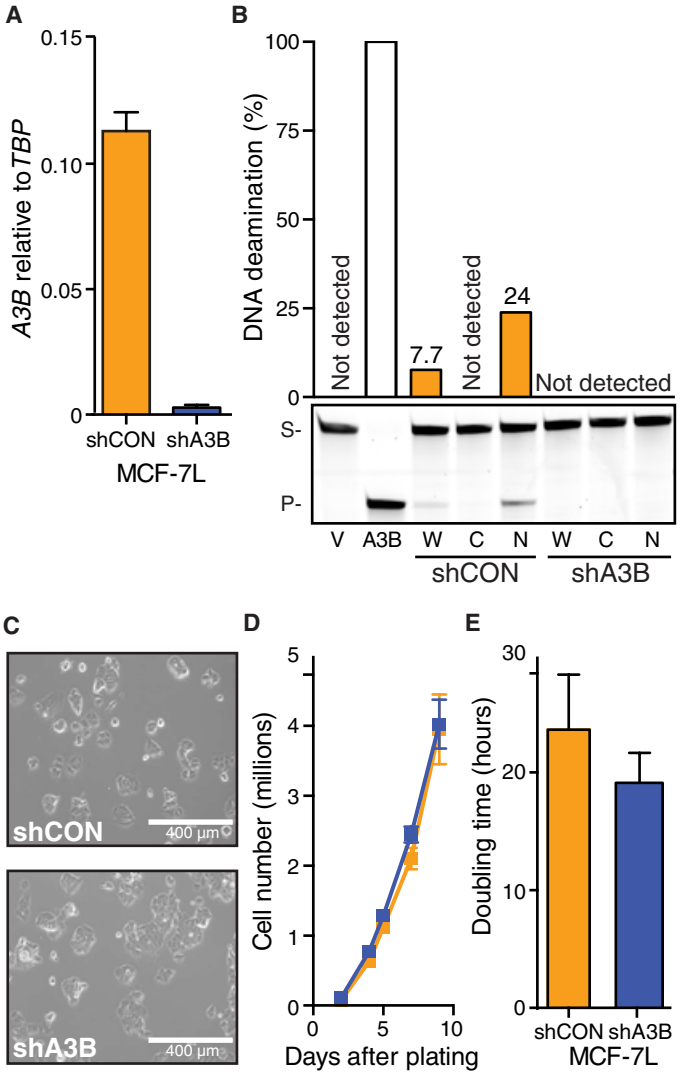

Fig. 2. Endogenous *A3B* depletion does not alter MCF-7L ER$^+$ breast cancer cells in culture. (**A**) *A3B* mRNA levels in MCF-7L cells expressing shA3B or shCON constructs (*TBP*, TATA-binding protein mRNA; each bar represents the mean ± SD of three RT-qPCR assays). (**B**) A3B DNA cytosine deaminase activity in soluble whole-cell (W), cytoplasmic (C), and nuclear (N) extracts of MCF-7L cells expressing shA3B or shCON constructs. Vector (V) and A3B-transfected 293T cell lysates were used as controls (S, substrate; P, product). (**C**) Light microscopy images of shA3B and shCON expressing MCF-7L pools. (**D** and **E**) Growth kinetics and doubling times of cultured MCF-7L cells expressing shA3B versus shCON constructs (mean ± SD of $n = 6$ cultures per condition).

A3B is required for the development of tamoxifen-resistant tumors in mice

The clinical data reported in Fig. 1 support a model in which A3B is responsible for precipitating the mutations that promote tamoxifen resistance. To directly test this model, we performed a series of xenograft experiments using MCF-7L pools in which endogenous *A3B* was left intact (shCON) or was depleted with the specific shRNA described above (shA3B). For each condition, 5 million cells were injected subcutaneously into the flank regions of a cohort of 5-week-old immunodeficient mice, and tumors were allowed to reach a volume of approximately 150 mm^3. At this point, typically 40 to 50 days after engraftment, the mice in each experimental group were randomly assigned into two subcohorts, one to receive daily tamoxifen injections and the other to be observed in parallel as a control (schematic of experimental design in Fig. 3A).

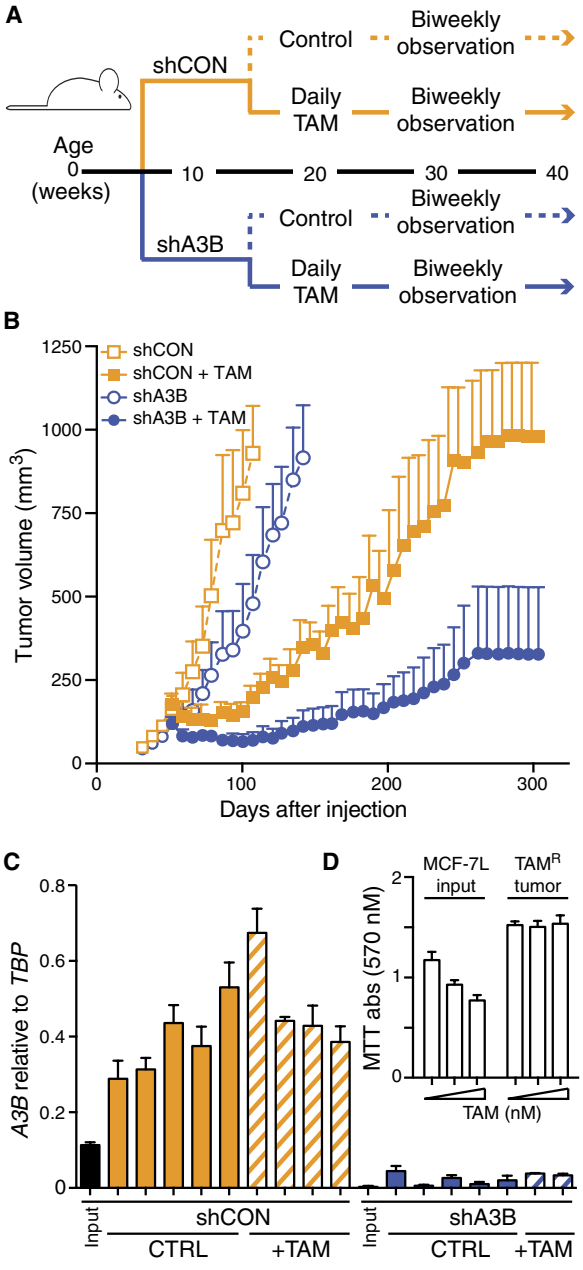

Fig. 3. A3B is required for the development of tamoxifen-resistant tumors in mice. (**A**) Schematic of the *A3B* knockdown xenograft study design and time course (see text for details). (**B**) Growth kinetics of engrafted MCF-7L cells expressing shA3B or shCON in the absence or presence of tamoxifen (TAM) treatment. Tumor volumes were measured weekly (mean + SEM shown for clarity of data presentation). (**C**) *A3B* mRNA levels in xenografted tumors recovered from the experiment shown in (B) (*TBP* mRNA; each bar represents the mean ± SD of three RT-qPCR assays). (**D**) MTT [3-(4,5-dimethylthiazol-2-yl)-2,5-diphenyltetrazolium bromide] data comparing tamoxifen susceptibility of input MCF-7L cells versus tamoxifen resistance of a representative MCF-7L shCON tumor [tamoxifen (10, 100, and 1000 ng/ml)].

Control-transduced MCF-7L cells formed large 1000-mm^3 tumors within 100 days after engraftment and, interestingly, *A3B* knockdown caused a modest delay in tumor growth (open blue versus open orange symbols in Fig. 3B; linear mixed model, *F* test, $P = 0.002$). This result differed from the near-identical growth rates in cell culture (Fig. 2, D and E) and may be due to the likelihood that additional adaptations/mutations are required for monolayer/plastic-conditioned cells to be able to grow optimally as tumors in mice. As expected, tamoxifen treatment attenuated the growth of both engineered pools (filled orange and blue symbols in Fig. 3B). However, control-transduced cells rapidly developed resistance to tamoxifen and grew into large tumors, whereas the growth of the *A3B*-depleted cell masses was mostly suppressed by tamoxifen over the year-long duration of this representative experiment (filled orange versus blue symbols in Fig. 3B; linear mixed model, *F* test, $P < 0.0001$). Similar outcomes were observed in additional experiments (for example, fig. S2).

Xenograft tumor *A3B* mRNA levels were analyzed by RT-qPCR, and, in all instances, the intended knockdown or control mRNA level was found to be durable and maintained through the entire duration of the experiment (Fig. 3C). This series of control experiments also revealed that endogenous *A3B* mRNA levels increase in control shRNA–transduced tumor masses in comparison to the same cells before engraftment (Fig. 3C). The mechanism for *A3B* induction in immunodeficient mice is not known but is unlikely to be due to estrogen (figs. S3 and S4), as suggested by a recent report (*38*). Representative xenografts were recovered in culture, and the tamoxifen-resistant phenotype was reconfirmed (for example, Fig. 3D). These results are fully supportive of a mechanism in which endogenous A3B causes an inheritable drug resistance phenotype (addressed further below). It is notable that endogenous *A3B* mRNA levels in this system are comparable to those observed in a large proportion of primary tumors [approximately 0.1 to 0.2 relative to *TBP* mRNA levels in cultured MCF-7L cells (Fig. 2B), 0.4 relative to *TBP* in animal tumors described here (Fig. 3C and fig. S3), and a range of 0 to 1.25 and a median of 0.25 relative to *TBP* in primary breast tumors previously documented using the same RT-qPCR assay (*7*)].

A novel lentivirus-based system enables A3B overexpression in any cell type

We next developed a conditional A3B overexpression system to further test the A3B mutagenesis model. A conditional approach is required because A3B expression in virus-producing cells causes lethal mutagenesis of retroviral complementary DNA intermediates during reverse transcription (*39*–*42*), and excessive levels of cellular A3B have the potential to inflict genomic DNA damage that ultimately leads to cytotoxicity (*7*, *18*, *19*). We therefore developed a novel lentiviral construct that will only express A3B upon transduction into susceptible target cells (Fig. 4A). This construct mitigates viral toxicity issues because it is inactive in virus-producing cells as a result of disruption of the antisense *A3B* open reading frame with a sense strand intron, and it is only expressed after intron removal by splicing in the virus-producing cells and reverse transcription and integration of the full proviral DNA in susceptible target cells. It also mitigates toxicity issues for target cell populations because expression levels are not excessive (see below). In parallel, an A3B catalytic mutant derivative (E255Q) was created by site-directed mutagenesis to serve as a negative control.

Transducing viruses were made by plasmid transfection into 293T cells with appropriate retroviral helper plasmids encoding Gag, Pol, and Env (vesicular stomatitis virus glycoprotein). As anticipated, no producer cell toxicity was observed, and A3B and A3B-E255Q viral titers were equivalent by RT-qPCR. MCF-7L cells were transduced

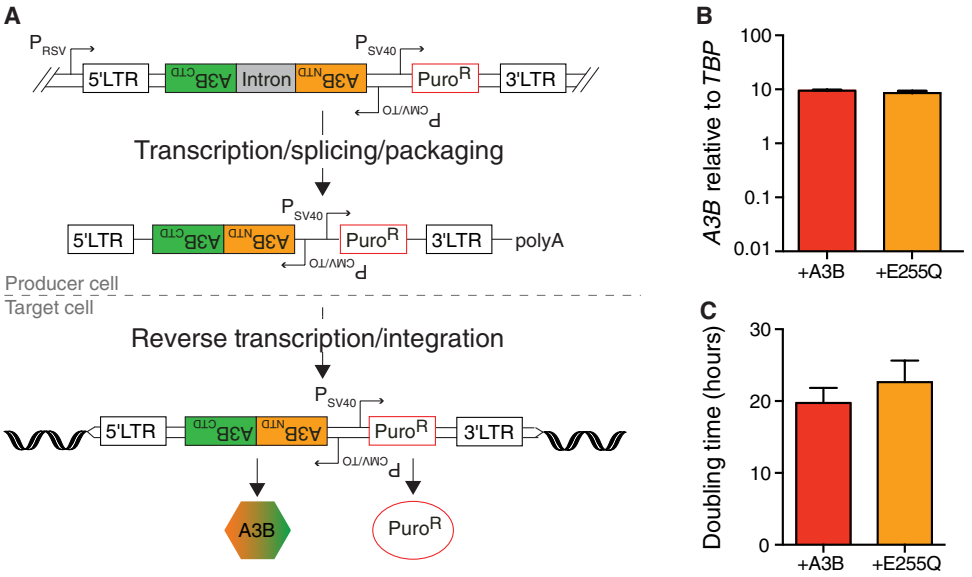

Fig. 4. Novel lentivirus-based system for conditional A3B overexpression. (**A**) Schematic of the lentiviral construct for conditional *A3B* overexpression (see text for details). LTR, long terminal repeat; RSV, Rous sarcoma virus; CTD, C-terminal domain; NTD, N-terminal domain; CMV, cytomegalovirus; SV40, simian virus 40. (**B**) *A3B* mRNA levels relative to *TBP* in MCF-7L cells expressing lentivirus-delivered *A3B* or a catalytic mutant derivative (E255Q) as well as endogenous *A3B* (mean ± SD of three RT-qPCR assays). (**C**) Doubling times of cultured MCF-7L cells overexpressing A3B or A3B-E255Q (mean ± SD of four replicates).

with each virus stock, and puromycin selection was used to eliminate nontransduced cells and to ensure 100% transduction efficiencies. *A3B* quantification by RT-qPCR showed that each construct elevates mRNA expression to levels approximately 10-fold higher than those of the reference gene *TBP* (Fig. 4B), which equate to levels approximately 50-fold higher than those of the endogenous *A3B* expressed in this system. These *A3B* mRNA levels are similar to those found in the top fraction of breast tumors and cancer cell lines [Burns *et al.* (*7*), Leonard *et al.* (*22*), Sieuwerts *et al.* (*23*), and this study]. As for the *A3B* knockdown experiments above, A3B- and A3B-E255Q–overexpressing MCF-7L populations showed no overt signs of toxicity and indistinguishable growth rates (Fig. 4C).

Overexpression of catalytically active A3B accelerates the development of tamoxifen-resistant tumors

To further test the model in which A3B provides mutagenic fuel for tumor evolution and drug resistance, we performed a series of xenograft experiments using MCF-7L cells transduced with the aforementioned constructs and thereby overexpressing wild-type A3B or the catalytic mutant derivative A3B-E255Q (Fig. 5A). Immunodeficient animals were injected subcutaneously with 5 million cells and, upon palpable tumor growth (150 mm^3), randomly divided into groups for tamoxifen injections or control observation. Remarkably, most of the cell masses overexpressing *A3B* developed rapid resistance to tamoxifen (filled red symbols in Fig. 5B). In comparison, MCF-7L cells expressing equivalent levels of *A3B-E255Q* mutant mRNA showed resistance kinetics similar to those of the shCON engraftments described above (filled orange symbols in Fig. 5B; linear mixed model, *F* test, $P = 0.015$). An independent experiment yielded similar results (fig. S5). These data demonstrate that A3B overexpression accelerates the kinetics of the development of tamoxifen resistance and, notably, that this phenotype requires catalytic activity.

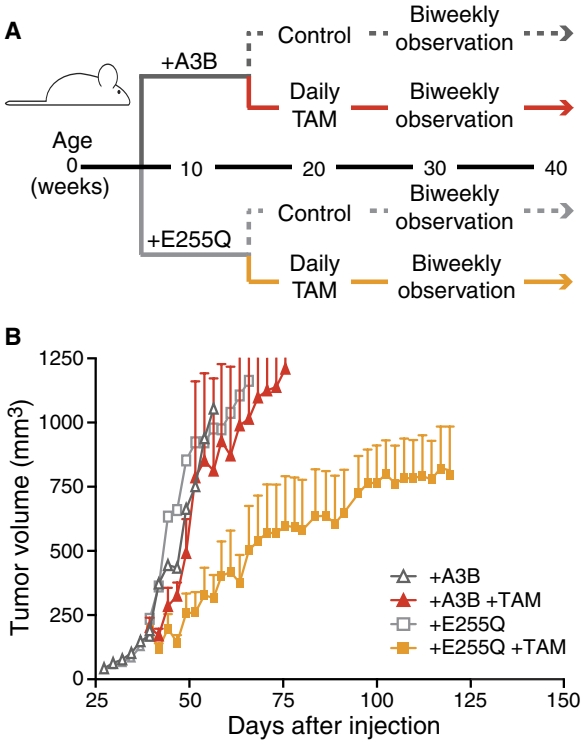

Fig. 5. Overexpression of catalytically active A3B accelerates the development of tamoxifen-resistant tumors in mice. (**A**) Schematic of the *A3B* overexpression xenograft study design and time course (see text for details). (**B**) Growth kinetics of engrafted MCF-7L cells overexpressing A3B or A3B-E255Q in the absence or presence of tamoxifen treatment. The graph reports tumor volumes measured weekly (mean + SEM shown for clarity of data presentation). Average tumor volumes from the untreated control arms are shown by gray symbols, and overlapping error bars are omitted for clarity of presentation.

ESR1 mutations are not responsible for tamoxifen resistance in the MCF-7L model for ER$^+$ breast cancer

Although the development of tamoxifen-resistant breast tumors is a major clinical problem, in most cases the molecular basis for resistance is unknown. A small fraction of treated patients develop tumors with *ESR1* exonic mutations that cause amino acid changes in the hormone-binding domain of the ER. These mutations have been seen mostly in tumors resistant to aromatase inhibitors and not as frequently in tumors resistant to tamoxifen [reviewed by Clarke *et al.* (*43*) and Jeselsohn *et al.* (*44*)]. To determine whether *ESR1* mutations are also part of the tamoxifen resistance mechanism in MCF-7L cells, we performed DNA exome sequencing on 9 independent tamoxifen-resistant xenografts and 10 independent control tumor masses. The *ESR1* gene contained no mutations under either condition (see table S3 for a full list of base substitution mutations). Resistant tumor *ESR1* mRNA levels were somewhat variable but still similar to those present in the original MCF-7L cell populations (fig. S6). Together with the data presented above indicating heritable resistance to tamoxifen (Fig. 3D), these results suggest that at least one other resistance mechanism occurs in the MCF-7 model system for ER$^+$ breast cancer.

DISCUSSION

The clinical and xenograft results presented here strongly support a model in which A3B drives tamoxifen resistance in ER$^+$ breast cancer. Clinically, resistance to endocrine therapies has been defined as primary or secondary, depending on the length of time a patient benefits from ER-targeted therapy. Our data suggest that A3B may have a role in both kinds of resistance and particularly in the development of secondary, acquired resistance. Suppression of endogenous levels of A3B enhances tamoxifen benefit (Fig. 3), whereas overexpression of A3B eliminates almost all benefits from tamoxifen therapy (Fig. 5). Because the only known biochemical activity of A3B is single-stranded DNA cytosine deamination [for example, (*7*, *42*, *45*)] and the tamoxifen resistance phenotype is heritable (Fig. 3D), the most likely mechanism is A3B-catalyzed DNA C-to-U editing coupled to the processing of these uracil lesions into somatic mutations by normal DNA repair processes [reviewed by Swanton *et al.* (*11*), Roberts and Gordenin (*12*), and Helleday *et al.* (*13*)]. In further support of this mechanism, the catalytic glutamate of A3B (E255) is required for accelerated tamoxifen resistance kinetics upon enzyme overexpression.

Because *ESR1* mutations were not observed in MCF-7L tamoxifen-resistant tumors, the identity of the resistance-conferring mutations in this system will require significant future studies and possibly even whole-genome sequencing if the predominant causal lesions lie outside the exomic fraction of the genome. The intrinsic signature of A3B may help to identify candidate (frequently mutated) sites for mechanistic follow-up. Then, for instance, genetic knock-in experiments could be used to unambiguously establish a cause-effect relationship. However, the resistance-conferring mutations (such as gene translocations, amplifications, or deletions) could also be complex and difficult to recapitulate precisely because DNA repair enzymes can readily process genomic uracil lesions into single- and double-stranded breaks (*46*, *47*).

A3B has been implicated as a dominant source of mutation in breast, head/neck, lung, bladder, and cervical cancers and—to a lesser but still significant extent—in many other tumor types (*7*–*10*, *28*, *32*, *48*, *49*). The fundamental nature of the DNA deamination mechanism, together with the data presented here, strongly suggests that A3B may be a general mechanism of therapeutic resistance to cancer therapy. At this point, potential mutagenic contributions from other APOBEC3 family members, such as A3A, cannot be excluded fully, but they do not appear to manifest in the MCF-7L system, nor are these potential contributions large enough to prevent the significant association between *A3B* expression levels and clinical outcomes for ER$^+$ breast cancer patients [treatment-naïve data in the studies by Sieuwerts *et al.* (*23*) and Cescon *et al.* (*24*) and post-recurrence tamoxifen resistance data in Fig. 1]. Thus, strategies to down-regulate A3B activity or expression, as reported here using a specific shRNA knockdown construct in a model system for ER$^+$ breast cancer, may be beneficial as chemotherapeutic adjuvants to "turn down" the mutation rate, decrease the likelihood of evolving drug resistance, and prolong the clinical benefit of therapy for the many cancers that are likely to be driven by this ongoing mutational process.

MATERIALS AND METHODS

Clinical studies

The clinical characteristics of the 285 patients [225 from Rotterdam (Erasmus University Medical Center) and 60 from Nijmegen (Radboud University Medical Center)] whose primary tumor specimens and data were used here have been described previously by Sieuwerts *et al.* (*33*). The protocol to study biological markers associated with disease outcome was approved by the medical ethics committee of the Erasmus University Medical Center (Rotterdam, Netherlands) (MEC 02.953); for Nijmegen, coded primary tumor tissues were used in accordance with the Codes of Conduct of the Federation of Medical Scientific Societies in the Netherlands (www.federa.org/codes-conduct). Thirty-two patients presented with distant metastasis at diagnosis or developed distant metastasis (including supraclavicular lymph node metastasis) within 1 month following primary surgery (M1 patients). These 32 patients and the 253 patients who developed a first recurrence during follow-up (25 patients with local-regional relapse and 228 patients with distant metastasis) were treated with first-line tamoxifen. All patients were ER$^+$ and anti–hormonal therapy–naïve, but 38 patients received adjuvant chemotherapy. The median time between the primary surgery and the start of therapy was 24 months (range, 0 to 120 months). The median follow-up of patients alive at the end of follow-up was 98 months (range, 9 to 240 months) after the primary surgery and 45 months (range, 3 to 178 months) after the start of first-line tamoxifen therapy. For 182 patients (64%), disease progression occurred within 6 months of the start of the first-line therapy being controlled by tamoxifen. At the end of the follow-up period, 268 (94%) patients had developed tumor progression, and 222 (78%) patients had died.

Total RNA was extracted with RNA Bee (Tel Test, Thermo Fisher Scientific Inc.) from 30-μm fresh-frozen primary tumor tissue sections containing at least 30% invasive tumor cell nuclei, and mRNA transcripts were quantified by RT-qPCR as described previously by Sieuwerts *et al.* (*23*). The median *A3B* expression level in the group of 285 breast cancers was 0.22 relative to the normalized average of three reference genes [*HPRT1*, *HMBS*, and *TBP* (*23*)].

DNA constructs

A3B knockdown and control shRNA constructs were described and validated previously by Burns *et al.* (*7*) and Leonard *et al.* (*50*). The A3B and A3B-E255Q lentiviral expression constructs were based

on the pLenti4TO backbone (Life Technologies). Overlapping PCR was used to place a sense-encoded intron between an antisense-encoded A3B open reading frame (primers available on request). A cytomegalovirus promoter drove A3B expression, and a simian virus 40 early promoter drove puromycin resistance. Constructs were verified by DNA sequencing.

Cell culture studies

MCF-7L cells were cultured at 37°C under 5% CO_2 and maintained in improved minimum essential medium (Richter's modification medium) containing 5% fetal bovine serum, penicillin (100 U/ml), streptomycin (100 μg/ml), and 11.25 nM recombinant human insulin. These cells were originally obtained from C. Kent Osborne (Baylor College of Medicine, Houston, TX) and are subject to short tandem repeat analysis yearly to confirm their identity with the original MCF-7 cell line. Cells were transduced with the lentivirus-based shRNA or conditional expression constructs described above and selected with puromycin (1 μg/ml; United States Biological) for 72 hours to generate uniformly transduced pools. Cell growth experiments were performed by plating 100,000 cells per six-well plate and incubating them at 37°C for the indicated days. Cells were trypsinized, diluted 1:2 in trypan blue (Invitrogen), and counted via a hemocytometer (six biological replicates per day per condition). Cell proliferation rates were determined using the xCELLigence real-time cell analyzer dual-plate instrument according to the manufacturer's instructions (ACEA Biosciences).

The mRNA level of each *APOBEC* family member gene was quantified using previously described RT-qPCR protocols and primer/probe combinations and presented relative to the housekeeping gene *TBP* (*7*, *51*, *52*). *ESR1* and *C-MYC* RNA were quantified by RT-qPCR using intron-spanning primers 5′-ATGACCATGACCCTCCACACC and 5′-TCAGACCGTGGCAGGGAAACC (UPL24) and 5′-GCTGCTTAGACGCTGGATTT and 5′-TAACGTTGAGGGGCATCG (UPL66), respectively, and manufacturer-recommended protocols (LightCycler 480, Roche). *C-MYC* is an established estrogen-responsive gene (*53*).

DNA deaminase activity was measured in soluble whole-cell, nuclear, and cytoplasmic fractions of MCF-7L cultures using established protocols (*7*, *54*). The single-stranded DNA substrate contained a single target cytosine (5′-ATTATTATTATTCGAATGGATTTATTTATTTATTTATTTATTT-fluorescein); deamination, uracil excision, and backbone cleavage resulted in a single faster-migrating product on SDS–polyacrylamide gel electrophoresis and image analysis (Typhoon FLA 7000 and ImageQuant software, GE Healthcare Life Sciences).

Xenograft studies

The University of Minnesota Institutional Animal Care and Use Committee approved the animal protocols used here (1305-30638A). MCF-7L cells were harvested at 70% confluence, counted, and resuspended in serum-free medium (without phenol red) at a concentration of 5 million cells per 50 μl of final volume. Ovariectomized, athymic mice (Harlan) were injected subcutaneously in the left flank with 50 μl of cell suspension at approximately 5 weeks of age. Each experiment was initiated with 5 or 10 mice per experimental condition. One week before injection and at all times following, the mice were provided with drinking water supplemented with 1 μM β-estradiol (Sigma-Aldrich) (except for the subset of mice used in the experiment shown in fig. S3). Tumors were measured bidirectionally twice weekly, and tamoxifen treatment began when the average tumor volume reached 150 mm^3. Tamoxifen citrate (500 μg; Sigma-Aldrich) emulsified in 50 μl of peanut oil was administered subcutaneously 5 of 7 days each week. Tumor volumes were calculated using the following formula: length × $breadth^2/2$.

MCF-7L exome sequencing

Genomic DNA was prepared from tumor cell masses (~20 mg per sample) via the Gentra Puregene Tissue DNA isolation protocols (Qiagen). Samples were diluted to 100 ng/μl and assessed further for quality and purity by SYBR Green PCR on a 197-bp fragment of *A3H* using primers 5′-CATGGGACTGGACGAAGCGCA and 5′-TGGGATCCACACAGAAGCCGCA. Samples with no amplification were excluded from the analysis. One microgram of total genomic DNA per sample was subjected to whole-exome sequencing on the Complete Genomics platform to an average target depth of 100× (BGI). Reads were aligned by BGI using its in-house pipeline, and the alignments in bam format were used for variant calling. Somatic variants were called for each tumor alignment by VarScan 2 (*55*) using an estrogen-treated shA3B sample as the normal control. The variants were filtered with a minimum overall coverage depth of 20 reads and a minimum coverage depth of 4 reads for the alternate allele. Any variant occurring at any frequency above 0 at the same position in more than one sample was considered a common mutation in the input pool and was removed. A full list of base substitution mutations is provided in table S3.

Statistics

Comparisons of the PFS of hormone-naïve breast cancer patients following treatment for first recurrence with tamoxifen, by *A3B* expression level (divided into quartiles), were conducted using log-rank tests; HRs and 95% confidence intervals are presented for pairwise comparisons. Clinical data were analyzed using SPSS Statistics version 23.0 (IBM). In the xenograft studies, repeated measures of tumor volume over time were compared by treatment group using linear mixed models with fixed effects for treatment, days, and interaction between treatment and days and with random intercept and slope effects for each mouse. P values <0.05 were considered statistically significant. Xenograft data were analyzed using Prism 6 and SAS 9.3.

SUPPLEMENTARY MATERIALS

Supplementary material for this article is available at http://advances.sciencemag.org/cgi/content/full/2/10/e1601737/DC1

fig. S1. APOBEC family member expression in MCF-7L cells.
fig. S2. Replica *A3B* knockdown xenograft experiment.
fig. S3. Estrogen does not affect *A3B* mRNA levels in engrafted MCF-7L cells.
fig. S4. *A3B* is not estrogen-inducible.
fig. S5. Replica *A3B* overexpression xenograft experiment.
fig. S6. *ESR1* mRNA levels in tamoxifen-resistant MCF-7L cells.
table S1. Patient characteristics and median and interquartile range of *APOBEC3B* mRNA levels.
table S2. Cox univariate and multivariate analyses for PFS after initiating first-line tamoxifen.
table S3. Single-base substitution mutations in tamoxifen-resistant tumors (separate Microsoft Excel file).

REFERENCES AND NOTES

1. E. B. Elkin, C. A. Hudis, Parsing progress in breast cancer. *J. Clin. Oncol.* **33**, 2837–2838 (2015).
2. J. H. Park, W. F. Anderson, M. H. Gail, Improvements in US breast cancer survival and proportion explained by tumor size and estrogen-receptor status. *J. Clin. Oncol.* **33**, 2870–2876 (2015).

3. T. Saphner, D. C. Tormey, R. Gray, Annual hazard rates of recurrence for breast cancer after primary therapy. *J. Clin. Oncol.* **14**, 2738–2746 (1996).
4. H. J. Burstein, S. Temin, H. Anderson, T. A. Buchholz, N. E. Davidson, K. E. Gelmon, S. H. Giordano, C. A. Hudis, D. Rowden, A. J. Solky, V. Stearns, E. P. Winer, J. J. Griggs, Adjuvant endocrine therapy for women with hormone receptor–positive breast cancer: American Society of Clinical Oncology clinical practice guideline focused update. *J. Clin. Oncol.* **32**, 2255–2269 (2014).
5. C. Davies, H. Pan, J. Godwin, R. Gray, R. Arriagada, V. Raina, M. Abraham, V. H. Medeiros Alencar, A. Badran, X. Bonfill, J. Bradbury, M. Clarke, R. Collins, S. R. Davis, A. Delmestri, J. F. Forbes, P. Haddad, M.-F. Hou, M. Inbar, H. Khaled, J. Kielanowska, W. H. Kwan, B. S. Mathew, I. Mittra, B. Müller, A. Nicolucci, O. Peralta, F. Pernas, L. Petruzelka, T. Pienkowski, R. Radhika, B. Rajan, M. T. Rubach, S. Tort, G. Urrútia, M. Valentini, Y. Wang, R. Peto; Adjuvant Tamoxifen: Longer Against Shorter Collaborative, Long-term effects of continuing adjuvant tamoxifen to 10 years versus stopping at 5 years after diagnosis of oestrogen receptor-positive breast cancer: ATLAS, a randomised trial. *Lancet* **381**, 805–816 (2013).
6. S. Nik-Zainal, L. B. Alexandrov, D. C. Wedge, P. Van Loo, C. D. Greenman, K. Raine, D. Jones, J. Hinton, J. Marshall, L. A. Stebbings, A. Menzies, S. Martin, K. Leung, L. Chen, C. Leroy, M. Ramakrishna, R. Rance, K. W. Lau, L. J. Mudie, I. Varela, D. J. McBride, G. R. Bignell, S. L. Cooke, A. Shlien, J. Gamble, I. Whitmore, M. Maddison, P. S. Tarpey, H. R. Davies, E. Papaemmanuil, P. J. Stephens, S. McLaren, A. P. Butler, J. W. Teague, G. Jönsson, J. E. Garber, D. Silver, P. Miron, A. Fatima, S. Boyault, A. Langerød, A. Tutt, J. W. M. Martens, S. A. J. R. Aparicio, Å. Borg, A. V. Salomon, G. Thomas, A.-L. Børresen-Dale, A. L. Richardson, M. S. Neuberger, P. A. Futreal, P. J. Campbell, M. R. Stratton; Breast Cancer Working Group of the International Cancer Genome Consortium, Mutational processes molding the genomes of 21 breast cancers. *Cell* **149**, 979–993 (2012).
7. M. B. Burns, L. Lackey, M. A. Carpenter, A. Rathore, A. M. Land, B. Leonard, E. W. Refsland, D. Kotandeniya, N. Tretyakova, J. B. Nikas, D. Yee, N. A. Temiz, D. E. Donohue, R. M. McDougle, W. L. Brown, E. K. Law, R. S. Harris, APOBEC3B is an enzymatic source of mutation in breast cancer. *Nature* **494**, 366–370 (2013).
8. M. B. Burns, N. A. Temiz, R. S. Harris, Evidence for APOBEC3B mutagenesis in multiple human cancers. *Nat. Genet.* **45**, 977–983 (2013).
9. S. A. Roberts, M. S. Lawrence, L. J. Klimczak, S. A. Grimm, D. Fargo, P. Stojanov, A. Kiezun, G. V. Kryukov, S. L. Carter, G. Saksena, S. Harris, R. R. Shah, M. A. Resnick, G. Getz, D. A. Gordenin, An APOBEC cytidine deaminase mutagenesis pattern is widespread in human cancers. *Nat. Genet.* **45**, 970–976 (2013).
10. L. B. Alexandrov, S. Nik-Zainal, D. C. Wedge, S. A. J. R. Aparicio, S. Behjati, A. V. Biankin, G. R. Bignell, N. Bolli, A. Borg, A.-L. Børresen-Dale, S. Boyault, B. Burkhardt, A. P. Butler, C. Caldas, H. R. Davies, C. Desmedt, R. Eils, J. E. Eyfjörd, J. A. Foekens, M. Greaves, F. Hosoda, B. Hutter, T. Ilicic, S. Imbeaud, M. Imielinsk, N. Jäger, D. T. W. Jones, D. Jones, S. Knappskog, M. Kool, S. R. Lakhani, C. López-Otín, S. Martin, N. C. Munshi, H. Nakamura, P. A. Northcott, M. Pajic, E. Papaemmanuil, A. Paradiso, J. V. Pearson, X. S. Puente, K. Raine, M. Ramakrishna, A. L. Richardson, J. Richter, P. Rosenstiel, M. Schlesner, T. N. Schumacher, P. N. Span, J. W. Teague, Y. Totoki, A. N. J. Tutt, R. Valdés-Mas, M. M. van Buuren, L. van't Veer, A. Vincent-Salomon, N. Waddell, L. R. Yates; Australian Pancreatic Cancer Genome Initiative, ICGC Breast Cancer Consortium, ICGC MMML-Seq Consortium, ICGC PedBrain, J. Zucman-Rossi, P. A. Futreal, U. McDermott, P. Lichter, M. Meyerson, S. M. Grimmond, R. Siebert, E. Campo, T. Shibata, S. M. Pfister, P. J. Campbell, M. R. Stratton, Signatures of mutational processes in human cancer. *Nature* **500**, 415–421 (2013).
11. C. Swanton, N. McGranahan, G. J. Starrett, R. S. Harris, APOBEC enzymes: Mutagenic fuel for cancer evolution and heterogeneity. *Cancer Discov.* **5**, 704–712 (2015).
12. S. A. Roberts, D. A. Gordenin, Hypermutation in human cancer genomes: Footprints and mechanisms. *Nat. Rev. Cancer* **14**, 786–800 (2014).
13. T. Helleday, S. Eshtad, S. Nik-Zainal, Mechanisms underlying mutational signatures in human cancers. *Nat. Rev. Genet.* **15**, 585–598 (2014).
14. M. H. Malim, P. D. Bieniasz, HIV restriction factors and mechanisms of evasion. *Cold Spring Harb. Perspect. Med.* **2**, a006940 (2012).
15. S. Stavrou, S. R. Ross, APOBEC3 proteins in viral immunity. *J. Immunol.* **195**, 4565–4570 (2015).
16. V. Simon, N. Bloch, N. R. Landau, Intrinsic host restrictions to HIV-1 and mechanisms of viral escape. *Nat. Immunol.* **16**, 546–553 (2015).
17. S. Landry, I. Narvaiza, D. C. Linfesty, M. D. Weitzman, APOBEC3A can activate the DNA damage response and cause cell-cycle arrest. *EMBO Rep.* **12**, 444–450 (2011).
18. M. Shinohara, K. Io, K. Shindo, M. Matsui, T. Sakamoto, K. Tada, M. Kobayashi, N. Kadowaki, A. Takaori-Kondo, APOBEC3B can impair genomic stability by inducing base substitutions in genomic DNA in human cells. *Sci. Rep.* **2**, 806 (2012).
19. B. J. M. Taylor, S. Nik-Zainal, Y. L. Wu, L. A. Stebbings, K. Raine, P. J. Campbell, C. Rada, M. R. Stratton, M. S. Neuberger, DNA deaminases induce break-associated mutation showers with implication of APOBEC3B and 3A in breast cancer kataegis. *ELife* **2**, e00534 (2013).
20. B. Mussil, R. Suspène, M.-M. Aynaud, A. Gauvrit, J.-P. Vartanian, S. Wain-Hobson, Human APOBEC3A isoforms translocate to the nucleus and induce DNA double strand breaks leading to cell stress and death. *PLOS One* **8**, e73641 (2013).
21. V. Caval, R. Suspène, M. Shapira, J.-P. Vartanian, S. Wain-Hobson, A prevalent cancer susceptibility APOBEC3A hybrid allele bearing APOBEC3B 3'UTR enhances chromosomal DNA damage. *Nat. Commun.* **5**, 5129 (2014).
22. B. Leonard, J. L. McCann, G. J. Starrett, L. Kosyakovsky, E. M. Luengas, A. M. Molan, M. B. Burns, R. M. McDougle, P. J. Parker, W. L. Brown, R. S. Harris, The PKC/NF-kB signaling pathway induces APOBEC3B expression in multiple human cancers. *Cancer Res.* **75**, 4538–4547 (2015).
23. A. M. Sieuwerts, S. Willis, M. B. Burns, M. P. Look, M. E. Meijer-Van Gelder, A. Schlicker, M. R. Heideman, H. Jacobs, L. Wessels, B. Leyland-Jones, K. P. Gray, J. A. Foekens, R. S. Harris, J. W. M. Martens, Elevated *APOBEC3B* correlates with poor outcomes for estrogen-receptor-positive breast cancers. *Horm. Cancer* **5**, 405–413 (2014).
24. D. W. Cescon, B. Haibe-Kains, T. W. Mak, *APOBEC3B* expression in breast cancer reflects cellular proliferation, while a deletion polymorphism is associated with immune activation. *Proc. Natl. Acad. Sci. U.S.A.* **112**, 2841–2846 (2015).
25. L. R. Yates, M. Gerstung, S. Knappskog, C. Desmedt, G. Gundem, P. Van Loo, T. Aas, L. B. Alexandrov, D. Larsimont, H. Davies, Y. Li, Y. S. Ju, M. Ramakrishna, H. K. Haugland, P. K. Lilleng, S. Nik-Zainal, S. McLaren, A. Butler, S. Martin, D. Glodzik, A. Menzies, K. Raine, J. Hinton, D. Jones, L. J. Mudie, B. Jiang, D. Vincent, A. Greene-Colozzi, P.-Y. Adnet, A. Fatima, M. Maetens, M. Ignatiadis, M. R. Stratton, C. Sotiriou, A. L. Richardson, P. E. Lønning, D. C. Wedge, P. J. Campbell, Subclonal diversification of primary breast cancer revealed by multiregion sequencing. *Nat. Med.* **21**, 751–759 (2015).
26. A. N. Hata, M. J. Niederst, H. L. Archibald, M. Gomez-Caraballo, F. M. Siddiqui, H. E. Mulvey, Y. E. Maruvka, F. Ji, H. E. Bhang, V. Krishnamurthy Radhakrishna, G. Siravegna, H. Hu, S. Raoof, E. Lockerman, A. Kalsy, D. Lee, C. L. Keating, D. A. Ruddy, L. J. Damon, A. S. Crystal, C. Costa, Z. Piotrowska, A. Bardelli, A. J. Iafrate, R. I. Sadreyev, F. Stegmeier, G. Getz, L. V. Sequist, A. C. Faber, J. A. Engelman, Tumor cells can follow distinct evolutionary paths to become resistant to epidermal growth factor receptor inhibition. *Nat. Med.* **22**, 262–269 (2016).
27. K. Kemper, O. Krijgsman, P. Cornelissen-Steijger, A. Shahrabi, F. Weeber, J.-Y. Song, T. Kuilman, D. J. Vis, L. F. Wessels, E. E. Voest, T. N. M. Schumacher, C. U. Blank, D. J. Adams, J. B. Haanen, D. S. Peeper, Intra- and inter-tumor heterogeneity in a vemurafenib-resistant melanoma patient and derived xenografts. *EMBO Mol. Med.* **7**, 1104–1118 (2015).
28. S. Nik-Zainal, H. Davies, J. Staaf, M. Ramakrishna, D. Glodzik, X. Zou, I. Martincorena, L. B. Alexandrov, S. Martin, D. C. Wedge, P. Van Loo, Y. S. Ju, M. Smid, A. B. Brinkman, S. Morganella, M. R. Aure, O. C. Lingjærde, A. Langerød, M. Ringnér, S.-M. Ahn, S. Boyault, J. E. Brock, A. Broeks, A. Butler, C. Desmedt, L. Dirix, S. Dronov, A. Fatima, J. A. Foekens, M. Gerstung, G. K. J. Hooijer, S. J. Jang, D. R. Jones, H.-Y. Kim, T. A. King, S. Krishnamurthy, H.-J. Lee, J. Y. Lee, Y. Li, S. McLaren, A. Menzies, V. Mustonen, S. O'Meara, I. Pauporté, X. Pivot, C. A. Purdie, K. Raine, K. Ramakrishnan, F. G. Rodríguez-González, G. Romieu, A. M. Sieuwerts, P. T. Simpson, R. Shepherd, L. Stebbings, O. A. Stefansson, J. Teague, S. Tommasi, I. Treilleux, G. G. Van den Eynden, P. Vermeulen, A. Vincent-Salomon, L. Yates, C. Caldas, L. van't Veer, A. Tutt, S. Knappskog, B. K. T. Tan, J. Jonkers, Å. Borg, N. T. Ueno, C. Sotiriou, A. Viari, P. A. Futreal, P. J. Campbell, P. N. Span, S. Van Laere, S. R. Lakhani, J. E. Eyfjord, A. M. Thompson, E. Birney, H. G. Stunnenberg, M. J. van de Vijver, J. W. M. Martens, A.-L. Børresen-Dale, A. L. Richardson, G. Kong, G. Thomas, M. R. Stratton, Landscape of somatic mutations in 560 breast cancer whole-genome sequences. *Nature* **534**, 47–54 (2016).
29. D. Juric, P. Castel, M. Griffith, O. L. Griffith, H. H. Won, H. Ellis, S. H. Ebbesen, B. J. Ainscough, A. Ramu, G. Iyer, R. H. Shah, T. Huynh, M. Mino-Kenudson, D. Sgroi, S. Isakoff, A. Thabet, L. Elamine, D. B. Solit, S. W. Lowe, C. Quadt, M. Peters, A. Derti, R. Schegel, A. Huang, E. R. Mardis, M. F. Berger, J. Baselga, M. Scaltriti, Convergent loss of PTEN leads to clinical resistance to a PI(3)Kα inhibitor. *Nature* **518**, 240–244 (2015).
30. S. P. Shah, A. Roth, R. Goya, A. Oloumi, G. Ha, Y. Zhao, G. Turashvili, J. Ding, K. Tse, G. Haffari, A. Bashashati, L. M. Prentice, J. Khattra, A. Burleigh, D. Yap, V. Bernard, A. McPherson, K. Shumansky, A. Crisan, R. Giuliany, A. Heravi-Moussavi, J. Rosner, D. Lai, I. Birol, R. Varhol, A. Tam, N. Dhalla, T. Zeng, K. Ma, S. K. Chan, M. Griffith, A. Moradian, S.-W. G. Cheng, G. B. Morin, P. Watson, K. Gelmon, S. Chia, S.-F. Chin, C. Curtis, O. M. Rueda, P. D. Pharoah, S. Damaraju, J. Mackey, K. Hoon, T. Harkins, V. Tadigotla, M. Sigaroudinia, P. Gascard, T. Tlsty, J. F. Costello, I. M. Meyer, C. J. Eaves, W. W. Wasserman, S. Jones, D. Huntsman, M. Hirst, C. Caldas, M. A. Marra, S. Aparicio, The clonal and mutational evolution spectrum of primary triple-negative breast cancers. *Nature* **486**, 395–399 (2012).
31. S. Nik-Zainal, P. Van Loo, D. C. Wedge, L. B. Alexandrov, C. D. Greenman, K. W. Lau, K. Raine, D. Jones, J. Marshall, M. Ramakrishna, A. Shlien, S. L. Cooke, J. Hinton, A. Menzies, L. A. Stebbings, C. Leroy, M. Jia, R. Rance, L. J. Mudie, S. J. Gamble, P. J. Stephens, S. McLaren, P. S. Tarpey, E. Papaemmanuil, H. R. Davies, I. Varela, D. J. McBride, G. R. Bignell, K. Leung, A. P. Butler, J. W. Teague, S. Martin, G. Jönsson, O. Mariani, S. Boyault, P. Miron, A. Fatima, A. Langerød, S. A. J. R. Aparicio, A. Tutt, A. M. Sieuwerts, Å. Borg, G. Thomas, A. V. Salomon, A. L. Richardson, A.-L. Børresen-Dale, P. A. Futreal, M. R. Stratton, P. J. Campbell, The life history of 21 breast cancers. *Cell* **149**, 994–1007 (2012).
32. E. C. de Bruin, N. McGranahan, R. Mitter, M. Salm, D. C. Wedge, L. Yates, M. Jamal-Hanjani, S. Shafi, N. Murugaesu, A. J. Rowan, E. Grönroos, M. A. Muhammad, S. Horswell,

M. Gerlinger, I. Varela, D. Jones, J. Marshall, T. Voet, P. Van Loo, D. M. Rassl, R. C. Rintoul, S. M. Janes, S.-M. Lee, M. Forster, T. Ahmad, D. Lawrence, M. Falzon, A. Capitanio, T. T. Harkins, C. C. Lee, W. Tom, E. Teefe, S.-C. Chen, S. Begum, A. Rabinowitz, B. Phillimore, B. Spencer-Dene, G. Stamp, Z. Szallasi, N. Matthews, A. Stewart, P. Campbell, C. Swanton, Spatial and temporal diversity in genomic instability processes defines lung cancer evolution. *Science* **346**, 251–256 (2014).
33. A. M. Sieuwerts, M. B. Lyng, M. E. Meijer-van Gelder, V. de Weerd, F. C. Sweep, J. A. Foekens, P. N. Span, J. W. Martens, H. J. Ditzel, Evaluation of the ability of adjuvant tamoxifen-benefit gene signatures to predict outcome of hormone-naive estrogen receptor-positive breast cancer patients treated with tamoxifen in the advanced setting. *Mol. Oncol.* **8**, 1679–1689 (2014).
34. A. V. Lee, S. Oesterreich, N. E. Davidson, MCF-7 cells—Changing the course of breast cancer research and care for 45 years. *J. Natl. Cancer Inst.* **107**, djv073 (2015).
35. Y. H. Ibrahim, S. A. Byron, X. Cui, A. V. Lee, D. Yee, Progesterone receptor-B regulation of insulin-like growth factor—Stimulated cell migration in breast cancer cells via insulin receptor substrate-2. *Mol. Cancer Res.* **6**, 1491–1498 (2008).
36. D. Sachdev, X. Zhang, I. Matise, M. Gaillard-Kelly, D. Yee, The type I insulin-like growth factor receptor regulates cancer metastasis independently of primary tumor growth by promoting invasion and survival. *Oncogene* **29**, 251–262 (2010).
37. J. M. Kidd, T. L. Newman, E. Tuzun, R. Kaul, E. E. Eichler, Population stratification of a common *APOBEC* gene deletion polymorphism. *PLOS Genet.* **3**, e63 (2007).
38. M. Periyasamy, H. Patel, C.-F. Lai, V. T. M. Nguyen, E. Nevedomskaya, A. Harrod, R. Russell, J. Remenyi, A. M. Ochocka, R. S. Thomas, F. Fuller-Pace, B. Győrffy, C. Caldas, N. Navaratnam, J. S. Carroll, W. Zwart, R. C. Coombes, L. Magnani, L. Buluwela, S. Ali, APOBEC3B-mediated cytidine deamination is required for estrogen receptor action in breast cancer. *Cell Rep.* **13**, 108–121 (2015).
39. K. N. Bishop, R. K. Holmes, A. M. Sheehy, N. O. Davidson, S.-J. Cho, M. H. Malim, Cytidine deamination of retroviral DNA by diverse APOBEC proteins. *Curr. Biol.* **14**, 1392–1396 (2004).
40. Q. Yu, D. Chen, R. König, R. Mariani, D. Unutmaz, N. R. Landau, APOBEC3B and APOBEC3C are potent inhibitors of simian immunodeficiency virus replication. *J. Biol. Chem.* **279**, 53379–53386 (2004).
41. B. P. Doehle, A. Schäfer, B. R. Cullen, Human APOBEC3B is a potent inhibitor of HIV-1 infectivity and is resistant to HIV-1 Vif. *Virology* **339**, 281–288 (2005).
42. J. F. Hultquist, J. A. Lengyel, E. W. Refsland, R. S. LaRue, L. Lackey, W. L. Brown, R. S. Harris, Human and rhesus APOBEC3D, APOBEC3F, APOBEC3G, and APOBEC3H demonstrate a conserved capacity to restrict Vif-deficient HIV-1. *J. Virol.* **85**, 11220–11234 (2011).
43. R. Clarke, J. J. Tyson, J. M. Dixon, Endocrine resistance in breast cancer—An overview and update. *Mol. Cell. Endocrinol.* **418**, 220–234 (2015).
44. R. Jeselsohn, G. Buchwalter, C. De Angelis, M. Brown, R. Schiff, *ESR1* mutations—A mechanism for acquired endocrine resistance in breast cancer. *Nat. Rev. Clin. Oncol.* **12**, 573–583 (2015).
45. K. Shi, M. A. Carpenter, K. Kurahashi, R. S. Harris, H. Aihara, Crystal structure of the DNA deaminase APOBEC3B catalytic domain. *J. Biol. Chem.* **290**, 28120–28130 (2015).
46. H. E. Krokan, F. Drabløs, G. Slupphaug, Uracil in DNA—Occurrence, consequences and repair. *Oncogene* **21**, 8935–8948 (2002).
47. J. M. Di Noia, M. S. Neuberger, Molecular mechanisms of antibody somatic hypermutation. *Annu. Rev. Biochem.* **76**, 1–22 (2007).
48. S. Henderson, A. Chakravarthy, X. Su, C. Boshoff, T. R. Fenton, APOBEC-mediated cytosine deamination links *PIK3CA* helical domain mutations to human papillomavirus-driven tumor development. *Cell Rep.* **7**, 1833–1841 (2014).
49. N. McGranahan, C. Swanton, Biological and therapeutic impact of intratumor heterogeneity in cancer evolution. *Cancer Cell* **27**, 15–26 (2015).
50. B. Leonard, S. N. Hart, M. B. Burns, M. A. Carpenter, N. A. Temiz, A. Rathore, R. I. Vogel, J. B. Nikas, E. K. Law, W. L. Brown, Y. Li, Y. Zhang, M. J. Maurer, A. L. Oberg, J. M. Cunningham, V. Shridhar, D. A. Bell, C. April, D. Bentley, M. Bibikova, R. K. Cheetham, J.-B. Fan, R. Grocock, S. Humphray, Z. Kingsbury, J. Peden, J. Chien, E. M. Swisher, L. C. Hartmann, K. R. Kalli, E. L. Goode, H. Sicotte, S. H. Kaufmann, R. S. Harris, APOBEC3B upregulation and genomic mutation patterns in serous ovarian carcinoma. *Cancer Res.* **73**, 7222–7231 (2013).
51. E. W. Refsland, M. D. Stenglein, K. Shindo, J. S. Albin, W. L. Brown, R. S. Harris, Quantitative profiling of the full *APOBEC3* mRNA repertoire in lymphocytes and tissues: Implications for HIV-1 restriction. *Nucleic Acids Res.* **38**, 4274–4284 (2010).
52. M. D. Stenglein, M. B. Burns, M. Li, J. Lengyel, R. S. Harris, APOBEC3 proteins mediate the clearance of foreign DNA from human cells. *Nat. Struct. Mol. Biol.* **17**, 222–229 (2010).
53. C. S. Ross-Innes, R. Stark, A. E. Teschendorff, K. A. Holmes, H. R. Ali, M. J. Dunning, G. D. Brown, O. Gojis, I. O. Ellis, A. R. Green, S. Ali, S.-F. Chin, C. Palmieri, C. Caldas, J. S. Carroll, Differential oestrogen receptor binding is associated with clinical outcome in breast cancer. *Nature* **481**, 389–393 (2012).
54. L. Lackey, E. K. Law, W. L. Brown, R. S. Harris, Subcellular localization of the APOBEC3 proteins during mitosis and implications for genomic DNA deamination. *Cell Cycle* **12**, 762–772 (2013).
55. D. C. Koboldt, Q. Zhang, D. E. Larson, D. Shen, M. D. McLellan, L. Lin, C. A. Miller, E. R. Mardis, L. Ding, R. K. Wilson, VarScan 2: Somatic mutation and copy number alteration discovery in cancer by exome sequencing. *Genome Res.* **22**, 568–576 (2012).

Acknowledgments: We thank several laboratory members for thoughtful comments. **Funding:** Animal studies were supported by the Department of Defense Breast Cancer Research Program (BC121347), the Jimmy V Foundation for Cancer Research, and the Prospect Creek Foundation. Additional support for cancer research in the Harris laboratory was provided by the Howard Hughes Medical Institute, Norwegian Centennial Chair Program, and Minnesota Ovarian Cancer Alliance. An NSF Graduate Research Fellowship provided salary support for G.J.S. NIH grant T32 CA009138 provided partial salary support for B.L. Clinical studies were supported by Cancer Genomics Netherlands (A.M.S. and J.W.M.M.), Netherlands Organisation for Scientific Research (NWO) (J.W.M.M.), and European Research Council Advanced Grant no. 322737 (J.A.F.). Statistical analyses were supported by NIH grant P30 CA77598 using the Biostatistics and Bioinformatics Core shared resource of the Masonic Cancer Center, University of Minnesota (R.I.V.). R.S.H. is an investigator of the Howard Hughes Medical Institute. **Author contributions:** R.S.H. and D.Y. designed the xenograft studies. A.M.S., J.A.F., and J.W.M.M. designed the clinical experiments. E.K.L. performed the xenograft experiments with assistance from B.L., whereas G.J.S., N.A.T., and R.I.V. contributed to bioinformatics and statistical analyses. K.L., E.K.L., and A.M.M. performed cell culture studies. M.E.M.-v.G. supplied the clinical data. F.C.G.J.S., P.N.S., J.W.M.M., and J.A.F. provided the clinical samples. A.M.S. quantified gene expression in primary tumors and performed statistical analyses. R.S.H. drafted the manuscript. All authors contributed revisions and approved the submitted version. **Competing interests:** R.S.H. is a cofounder of ApoGen Biotechnologies Inc. D.Y. is a scientific advisory board member of ApoGen Biotechnologies Inc. All other authors declare that they have no competing interests. **Data and materials availability:** All data needed to evaluate the conclusions in the paper are present in the paper and/or the Supplementary Materials. All the reagents and primary data sets reported here are available upon written request to R.S.H.

Submitted 26 July 2016
Accepted 31 August 2016
Published 7 October 2016
10.1126/sciadv.1601737

Citation: E. K. Law, A. M. Sieuwerts, K. LaPara, B. Leonard, G. J. Starrett, A. M. Molan, N. A. Temiz, R. I. Vogel, M. E. Meijer-van Gelder, F. C. G. J. Sweep, P. N. Span, J. A. Foekens, J. W. M. Martens, D. Yee, R. S. Harris, The DNA cytosine deaminase APOBEC3B promotes tamoxifen resistance in ER-positive breast cancer. *Sci. Adv.* **2**, e1601737 (2016).

TUMOR IMMUNOLOGY

A melanin-mediated cancer immunotherapy patch

Yanqi Ye,[1,2]* Chao Wang,[1,2]* Xudong Zhang,[1,2] Quanyin Hu,[1,2] Yuqi Zhang,[1,2] Qi Liu,[1,2] Di Wen,[1,2] Joshua Milligan,[1] Adriano Bellotti,[1,3] Leaf Huang,[1,2] Gianpietro Dotti,[4] Zhen Gu[1,2,3]†

Copyright © 2017 The Authors, some rights reserved; exclusive licensee American Association for the Advancement of Science. No claim to original U.S. Government Works

Melanin is capable of transforming 99.9% of the absorbed sunlight energy into heat, reducing the risk of skin cancer. We here develop a melanin-mediated cancer immunotherapy strategy through a transdermal microneedle patch. B16F10 whole tumor lysate containing melanin is loaded into polymeric microneedles that allow sustained release of the lysate upon insertion into the skin. In combination with the near-infrared light irradiation, melanin in the patch mediates the generation of heat, which further promotes tumor-antigen uptake by dendritic cells, and leads to enhanced antitumor vaccination. We found that the spatiotemporal photoresponsive immunotherapy increases infiltration of polarized T cells and local cytokine release. These immunological effects increase the survival of mice after tumor challenge and elicited antitumor effects toward established primary tumor and distant tumor. Collectively, melanin generates local heat, boosts T cell activities by transdermal vaccines, and promotes antitumor immune responses.

INTRODUCTION

Emerging technologies associated with immunotherapy hold tremendous promise in cancer therapy (*1*). Micro- or nanoformulations or engineered immune cells can be used to deliver a variety of immunomodulators (*2*, *3*). Scaffolds, such as hydrogel, have also been developed to generate an immunogenic microenvironment that recruits and activates immune cells in situ (*4*–*7*). Moreover, T cell engineering that incorporates antibodies or therapeutics facilitates immune targeting and treatment (*8*–*11*). Also, dendritic cell (DC)–based vaccination can effectively capture antigens to improve the effectiveness of the immune response and is a powerful tool for cancer therapy (*12*–*16*). However, engineering of DCs often involves complex and expensive ex vivo manipulation (*4*, *17*). In addition, the limited lymph node–homing capability of ex vivo manipulated DCs is, at least in part, responsible for the limited anticancer efficacy (*18*). Vaccination with whole tumor antigens provides a broad source of tumor-associated antigens that elicit substantially enhanced immune responses compared with narrowly defined tumor antigens (*19*). Moreover, presenting a broad spectrum of immunogenic epitopes not only augments the immunity mediated by the DC antigen uptake and processing but also improves the direct activation of $CD4^+$ T helper and $CD8^+$ cytotoxic T lymphocytes (*7*, *20*).

Here, we describe a B16F10 melanoma vaccine patch that targets antigen-presenting cells (APCs) directly via transdermal delivery of tumor lysates combined with melanin (Fig. 1A). This vaccine involves the encapsulation of inactive whole tumor lysate that is gradually released by an intradermal microneedle (MN) patch inserted into the skin. MNs facilitate the uptake and presentation of antigens by DCs and, in turn, promote immune activation through the extensive network of lymphatic vessels in the dermis (*21*–*23*). At the same time, the presence of melanin, the existing natural biological pigment in the whole tumor lysate, allows the local release of heat via remotely controllable near-infrared (NIR) light emission. Local heat causes the release of inflammatory cytokines that attract immune cells, generation of immunogenic substrates such as extracellular heat shock proteins (HSPs), reactive oxygen species (ROS), antigen adjuvants, and some other danger signals that activate the immune system (*24*, *25*). The mild increase in the local temperature of the interstitial tissues also contributes to the increased blood and lymphatic flow that facilitates the migration of APCs and T cells (*24*) and finally initiates B16F10-specific immune responses (*23*, *26*). The increased blood flow may also allow the recruitment of other cell subsets such as natural killer (NK) cells (*7*, *27*, *28*). We found that the administration of the vaccine MN patch generated robust innate and adaptive immune responses and induced tumor regression in the B16F10 melanoma model. Moreover, the NIR-enhanced transdermal vaccination delayed the growth of distant tumor and improved long-term survival, paving a strong rationale for pursuing this strategy in clinical studies.

RESULTS

Preparation and characterization of the cancer immunotherapy patch

We first investigated whether the tumor lysate can be loaded and released from transdermal MN patches in a sustained manner. We fabricated the MN patch within a micromold to form hyaluronic acid–based MNs that encapsulate the whole tumor lysate (with melanin) and adjuvants, such as granulocyte-macrophage colony-stimulating factor (GM-CSF) (*29*, *30*). Patches with and without tumor lysate were illustrated from the axial and transverse perspectives, respectively (Fig. 1B). An array of 15 × 15 MNs was assembled on a 9 mm by 9 mm patch with a center-to-center interval of 600 μm. The detailed dimensions of the MNs were visualized by the scanning electron microscopy (Fig. 1C). Each MN had a conical construction with a diameter of 300 μm at the base, a height of 800 μm, and a sharp tip tapering to a 5-μm radius of curvature. Upon loading with the tumor lysate, MNs appeared notably darker than the blank hyaluronic acid–based MNs because of the presence of melanin in the patch (*31*, *32*). The amount of melanin was around 50 μg per patch, which is within the safe dosage range of a single administration (*33*). A

[1]Joint Department of Biomedical Engineering, University of North Carolina at Chapel Hill and North Carolina State University, Raleigh, NC 27695, USA. [2]Division of Pharmacoengineering and Molecular Pharmaceutics, Eshelman School of Pharmacy, University of North Carolina at Chapel Hill, Chapel Hill, NC 27599, USA. [3]Department of Medicine, University of North Carolina School of Medicine, Chapel Hill, NC 27599, USA. [4]Department of Microbiology and Immunology, Lineberger Comprehensive Cancer Center, University of North Carolina at Chapel Hill, Chapel Hill, NC 27599, USA.
*These authors contributed equally to this work.
†Corresponding author. Email: zgu@email.unc.edu

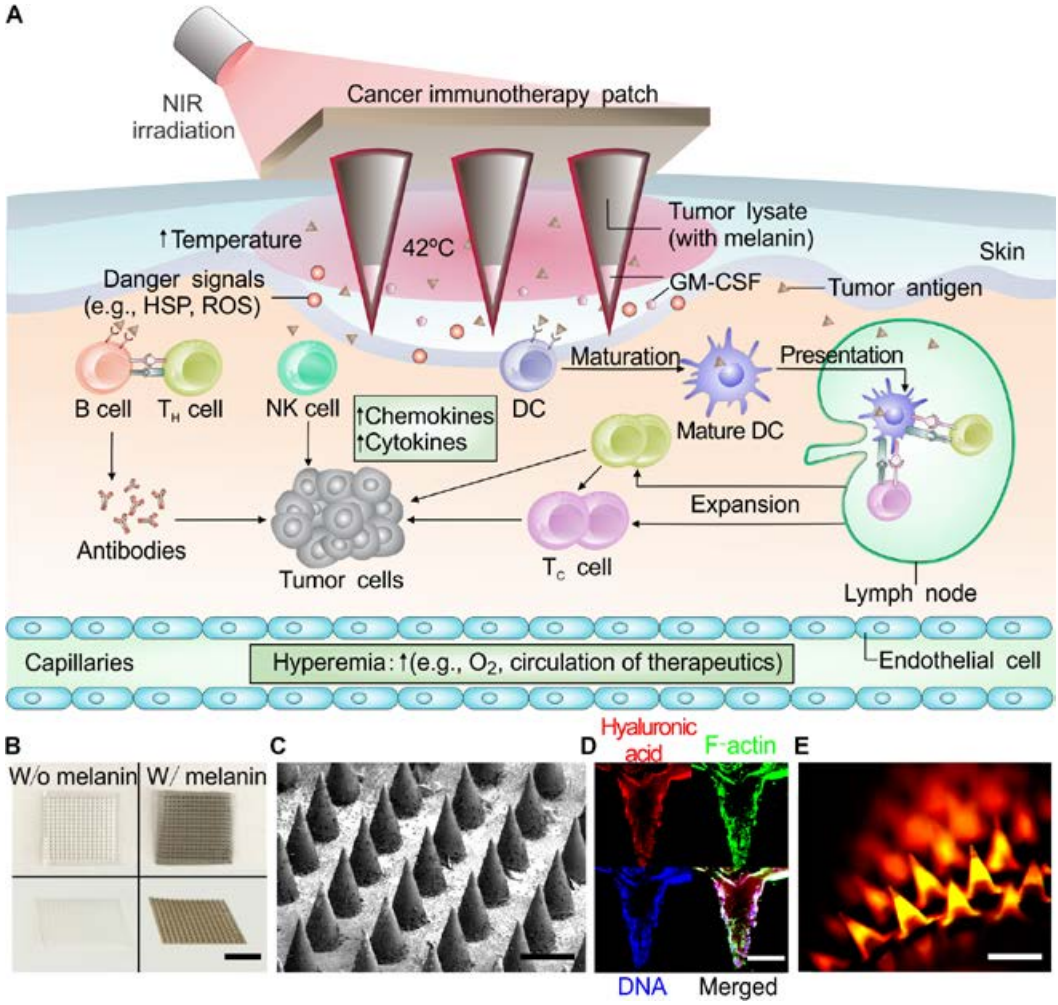

Fig. 1. Schematic of melanin-mediated cancer immunotherapy through a transdermal MN-based vaccine patch. (**A**) Schematic illustration of MN-based transdermal vaccination. T_H cell, T helper cell; T_C cell, cytotoxic T cell. (**B**) Photograph of representative MN patches without (W/o) melanin and with (W/) melanin (scale bar, 4 mm). (**C**) Scanning electron microscopy image of the MN patch (scale bar, 400 μm). (**D**) Fluorescence cross-sectional images of a representative MN. Actin filaments in cells were visualized by Alexa Fluor 488 phalloidin (green), cell DNA fragments were stained with Hoechst (blue), and hyaluronic acid polymer matrix was labeled with rhodamine B (red) (scale bar, 200 μm). (**E**) Fluorescence imaging of a representative MN patch that contained the Alexa Fluor 488 phalloidin–labeled tumor lysate and rhodamine B–labeled hyaluronic acid (scale bar, 400 μm).

representative MN was constructed with rhodamine B–labeled hyaluronic acid encapsulating tumor lysate with actin filaments and DNA stained with phalloidin and Hoechst, respectively (Fig. 1D). A fluorescent view of the array further showed the uniform loading of tumor lysate and alignment of the MNs (Fig. 1E). The MN underwent failure at 0.39 N in strain testing while being compressed to a quarter of its height (fig. S1), demonstrating sufficient strength for potential skin insertion without buckling (*34*).

Next, we evaluated the effects of the NIR laser irradiation on melanin-induced heat generation. The temperature variations of the MNs were recorded in real time using an infrared thermal camera (Fig. 2A). Compared with the transparent hyaluronic acid–based MNs, the surface temperature of the MNs loaded with tumor lysate increased dramatically within 1 min because of the melanin-induced light-to-heat transduction (Fig. 2B). NIR irradiation at 808 nm could be absorbed by the melanin contained in the tumor lysate as demonstrated by the melanin's absorption spectrum (fig. S2A). The absorption coefficient of the melanin content in the tumor lysate was also comparable with that of the synthetic melanin (fig. S2A and table S1). Despite the temperature increase, the morphology of the MNs remained unchanged, and the photothermal property of melanin was stable during the treatment (fig. S2B) (*35*). The heating behavior of the MN patch was also maintained when repeated NIR light exposures were performed (fig. S3). Furthermore, the steady state of the patch's surface temperature was lysate concentration– and NIR light intensity–dependent, whereas the thickness of the MN backing had a minimum effect (fig. S4 and Fig. 2C). The surface temperature of the patch could be controlled under hyperthermia (42°C) to minimize the potential thermal-induced denaturation of the tumor antigen and other biomolecules.

In vitro activation of DCs in response to vaccine MN

GM-CSF that serves as a potent cytokine for DC recruitment and activation was physically encapsulated into MN tips by cross-linking

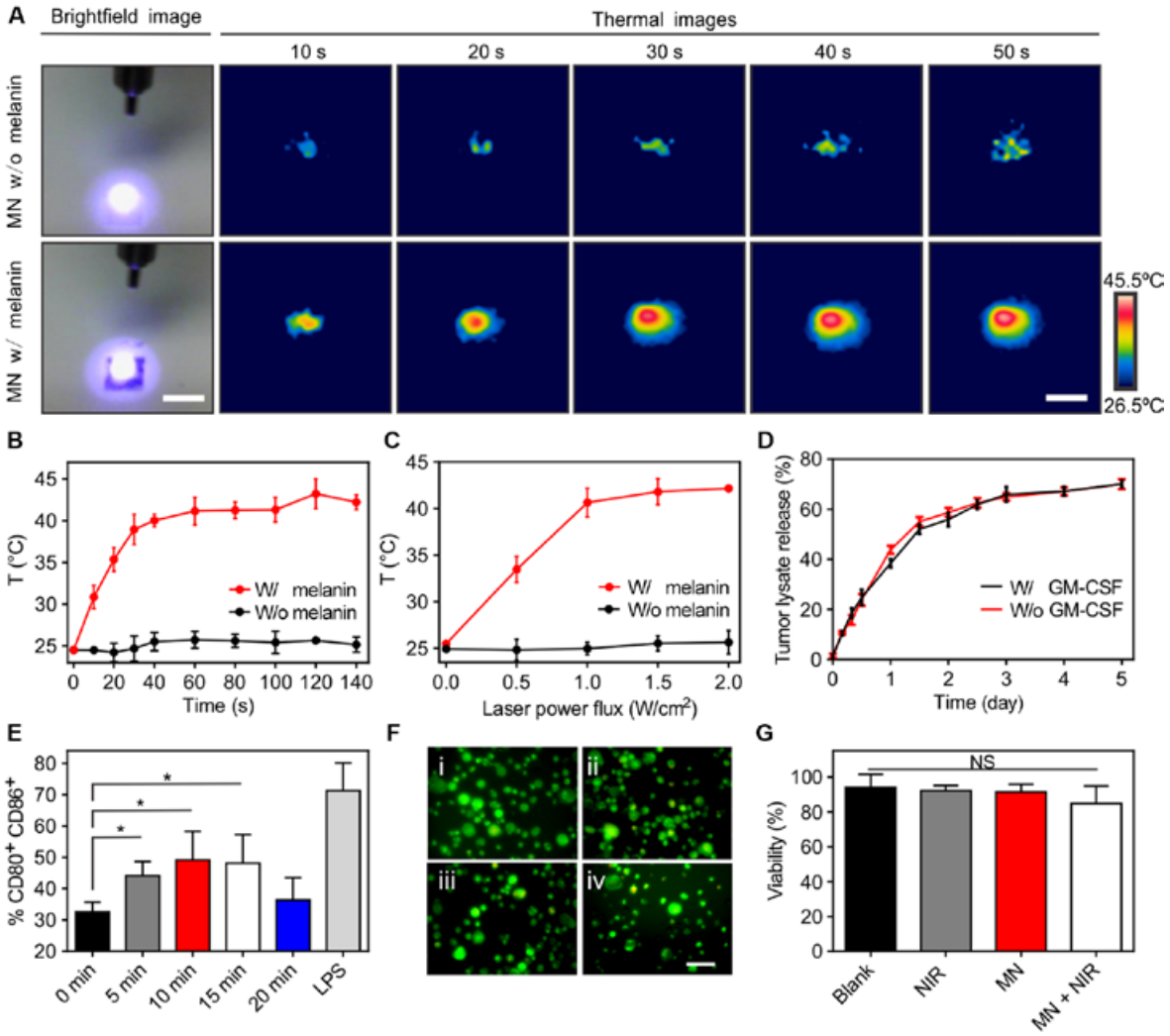

Fig. 2. Characterization of the light-responsive transdermal MNs. (**A**) Surface temperature changes of the MNs with or without tumor lysate in real time with continuous 808-nm NIR irradiation at 1.0 W/cm^2, characterized by an infrared thermal camera (scale bars, 1 mm). (**B**) Quantitative surface temperature changes of representative MNs with continuous NIR irradiation at 1.0 W/cm^2 ($n = 3$). (**C**) Quantitative temperature changes of representative MN patch with increasing laser power flux ($n = 3$). (**D**) In vitro collective release of tumor lysate proteins from the MN patch ($n = 3$). (**E**) In vitro activation of DCs in response to MNs loaded with tumor lysate and GM-CSF or LPS and exposed to NIR irradiation for different time ($n = 3$). (**F**) LIVE/DEAD assay of DCs after treatments with (i) blank MN, (ii) 10 min of NIR, (iii) MN, and (iv) MN and 10 min of NIR. Live cell (green), dead cell (red). (**G**) Quantification of DC viability after treatments. Data points represent mean ± SD ($n = 3$). Error bars indicate SD. Statistical significance was calculated by Student's *t* test [not significant (NS), $P > 0.05$; $^*P < 0.05$].

methacrylated hyaluronic acid upon ultraviolet irradiation. We found that 60% of the bioactive GM-CSF was released from MN within 48 hours (fig. S5, A and B), whereas sustained release of the tumor lysate protein was observed over 5 days (Fig. 2D). Incorporation of the NIR treatment did not alter the release profiles of GM-CSF and tumor lysate (fig. S5, C and D). Scanning electron microscopy images of vaccine MNs showed a gradual dissociation of tips over time (fig. S6).

To evaluate whether GM-CSF in MNs provided signaling cues that could efficiently promote DC maturation, we exposed bone marrow–derived DCs to the dissolved MN suspension. The percentage of matured DCs (CD80$^+$ and CD86$^+$) substantially increased from 36.7 ± 2.3% to 48.9 ± 3.1% after treatment with tumor lysate– and GM-CSF–loaded MNs with 10 min of NIR laser irradiation (Fig. 2E) (*36*). The effect of varying NIR laser irradiation time on the activation of DCs was also measured. Ten minutes of NIR irradiation allowed optimal DC activation as compared with samples treated with 5 or 15 min (Fig. 2E). Only 20 min of NIR exposure slightly impaired DC viability and functionality (fig. S7). DCs in all other experimental conditions of either MN suspension or 10 min of NIR irradiation exhibited high viability (Fig. 2, F and G, and fig. S8).

In vivo efficacy of MN-mediated immunization upon NIR

To characterize the in vivo efficacy of MN-based immunization, we transdermally treated C57BL/6J mice with vaccine MN patch loaded with B16F10 whole tumor lysate containing 1.5 mg of extracted protein. We measured the magnitude and duration of the immune response after NIR irradiation and subsequent tumor challenge (Fig. 3A). MN patches were applied on the mice skin of the caudal-dorsal area for about 10 min and further affixed using the Skin Affix surgical

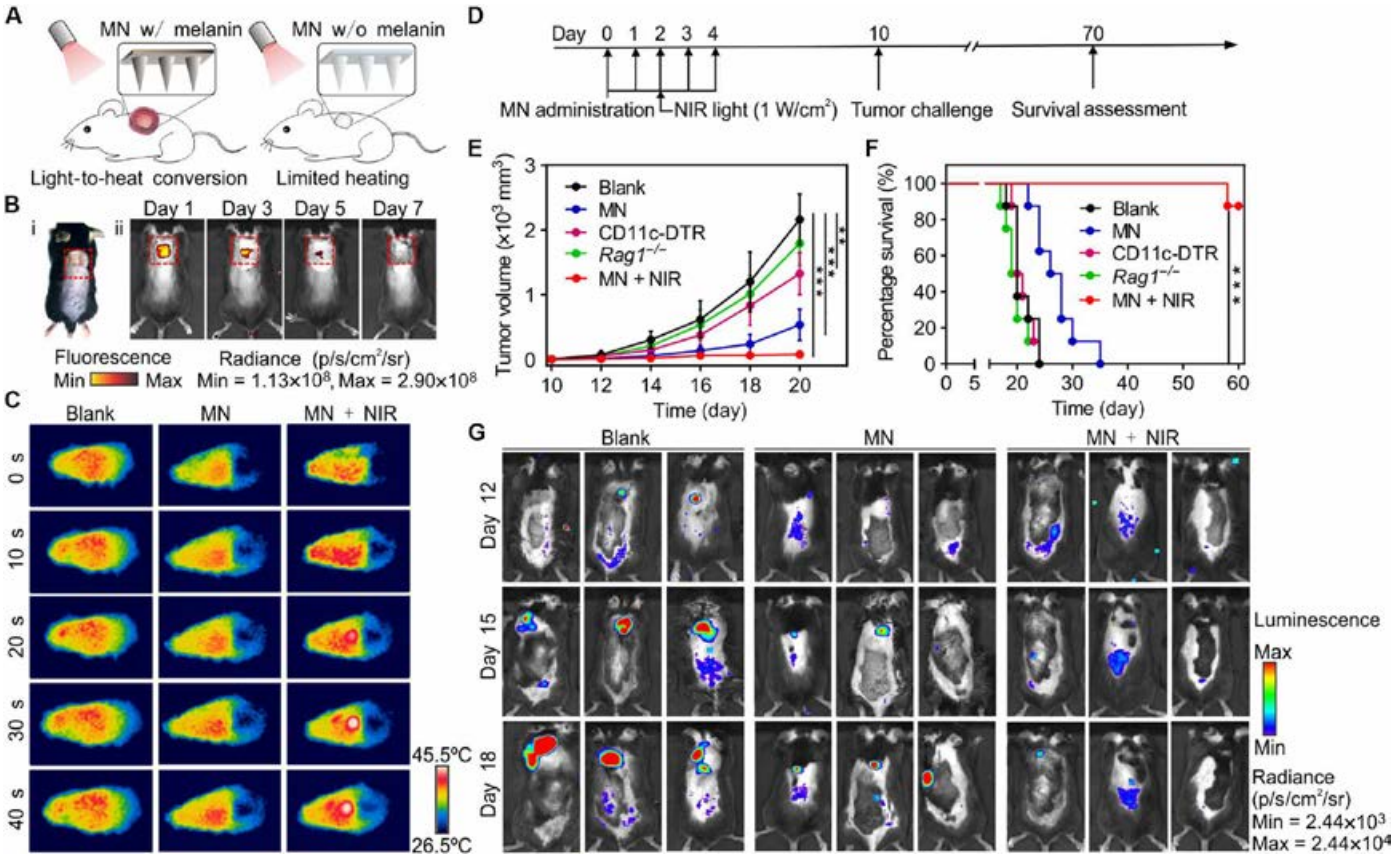

Fig. 3. Vaccine MN confer protective innate and adaptive immunity. (**A**) Schematic illustration of MN cancer immunotherapy. (**B**) Characterization of the MNs after insertion. (i) Photo of mouse dorsal skin (the area within the red line) that was treated transdermally with one MN patch and (ii) fluorescence signals of Cy5.5-labeled MN patch over time. (**C**) Surface temperature changes of individual animal after MN insertion into the skin measured by an infrared thermal camera. (**D**) Schematic representation of the B16F10 vaccine tumor model. (**E**) Average tumor volumes in treated mice after tumor challenge. (**F**) Kaplan-Meier survival curves for treated and control mice. Data points represent mean ± SD ($n = 8$). Error bars indicate SD. Statistical significance was calculated by Student's test and log-rank test (**$P < 0.01$; ***$P < 0.001$). (**G**) In vivo bioluminescence imaging of the B16F10 melanoma in different experimental groups and at different time points after tumor challenge. Three representative mice per treatment group are shown. The tumor growth in (E) to (G) was measured 10 days after tumor cell inoculation.

adhesive. Staining with trypan blue and hematoxylin and eosin (H&E) indicated successful penetration of MNs in the excised skin (fig. S9). The transdermal patch remained in the skin for at least 5 days (Fig. 3B). We then performed localized NIR irradiation on the MN region for 10 min daily for 5 days (MN + NIR). Control mice were treated with either vaccine MN patch without NIR irradiation (MN), MN patch loaded only with melanin (melanin), or MNs containing only hyaluronic acid with NIR irradiation (blank).

Temperature changes in the regional skin surface after vaccine MN insertion were recorded in real time using an infrared thermal camera. Light-to-heat transduction upon NIR irradiation caused a local heating effect observed in mice treated with vaccine MNs (Fig. 3C). The melanin in the vaccine patch mediated the transdermal heating at temperatures between 38° and 42°C within 30 s. Mild hyperthermia at the local treated site was similarly observed in mice treated with synthetic melanin–loaded MNs (fig. S10A). In contrast, mice treated with blank MNs and NIR and mice implanted with loaded MNs but without NIR showed limited variations in skin surface temperature within the normal range of 33° to 36°C (Fig. 3C).

In a prophylactic mouse model, mice were implanted with B16F10 melanoma cells 10 days after vaccination (Fig. 3D). All mice treated with the blank MNs had appreciable tumor growth within 15 days after tumor cell inoculation and required euthanasia by day 25. MNs loaded with melanin and treated with NIR irradiation slightly improved the survival of the mice because some mice survived to day 25 (fig. S10, B and C). Similarly, MNs loaded with tumor lysate and melanin but without NIR irradiation caused tumor protection in 13% of the mice until day 30 (Fig. 3, E and F). In sharp contrast, mice receiving the combined vaccination (MNs loaded with tumor lysate and GM-CSF and NIR irradiation) showed long-term survival with complete tumor rejection in 87% of the treated mice (Fig. 3, E and F, and fig. S11). Bioluminescence imaging of the B16F10 melanoma–bearing mice confirmed significant inhibition of tumor growth (Fig. 3G and fig. S12). This was further evidenced by the measurement of tumor weight (fig. S13) and histologic analysis (fig. S14A).

We next assessed the requirement of immune cells for the antitumor effects observed by combined vaccination–based treatments. Depletion of $CD11c^+$ DCs in diphtheria toxin receptor (DTR) mice was sufficient to abrogate the antitumor effect of the vaccine MN (Fig. 3, E and F). A study in $Rag1^{-/-}$ mice deficient in T cells and B cells showed a significant loss of tumor growth suppression during treatment with combined vaccination (fig. S11). Selective depletions of $CD8^+$ and $CD4^+$ T cells before combined MN vaccination were also studied. Eliminating $CD8^+$ T lymphocytes showed no significant

tumor regression compared with blank control (fig. S15). When anti-CD4 antibody was given to the mice, there was a decrease ($P < 0.01$) in tumor size in contrast to the control, suggesting the benefit of CD4 T cells to a lesser extent than CD8 T cells for the antitumor response (fig. S15). The depletion of B cells and NK cells also had deleterious impact on the immune response while not diminishing the vaccination effect toward tumor challenge (fig. S15). Together, these results showed that the MN vaccination was associated with $CD11c^+$ DCs and other immune cells such as T cells, B cells, and NK cells.

Loading of GM-CSF in the MNs played an important role in the local recruitment of DCs [$CD11c^+$, paired immunoglobulin (Ig)–like receptors (PIRs) of activating-A/B^+] (Fig. 4, A and C). Three days after combined vaccination, a 5.9-fold increase in accumulated DCs was observed in the skin section compared with mice treated with blank MN. NIR further augmented the effect of GM-CSF–loaded MNs on recruiting DCs (Fig. 4C). Increased localization of NK cells was also observed (Fig. 4, B and D). In addition, the elevated local microcirculatory blood perfusion observed after NIR and MN treatment could contribute in enhancing the migration of immune cells (table S2 and fig. S16). Tumor infiltration by T cells upon treatment was analyzed by flow cytometry on day 15 after tumor inoculation. About 9.8-fold increase in $CD8^+$ T cells was observed in mice receiving the combined vaccination compared with control mice, whereas MN-only group showed a 5.8-fold increase (Fig. 5A). Furthermore, staining with H-$2D^b$ gp100 tetramers identified B16F10-specific $CD8^+$ T cells in tumors of treated mice (*37*). The percentage of tetramer-positive $CD8^+$ T cells was found to be greater in the MN-treated mice compared with control mice lacking immunization (fig. S17). Mice with combined treatment or MN-only treatment exhibited 1.5- and 1.3-fold increases in activated DCs ($CD80^+$ and $CD86^+$), respectively, in regional skin as compared with control mice (Fig. 5B). Immunofluorescence staining and in situ cell apoptosis confirmed the results obtained with flow cytometry (Fig. 5C and fig. S14B). Local immune activation was associated with systemic immune responses. We measured an eightfold increase in IgG titers in the serum of immunized mice as compared with mice treated with blank control (Fig. 5D). NIR treatment promoted further increase in IgG titers by day 15 and prolonged immune responses compared with

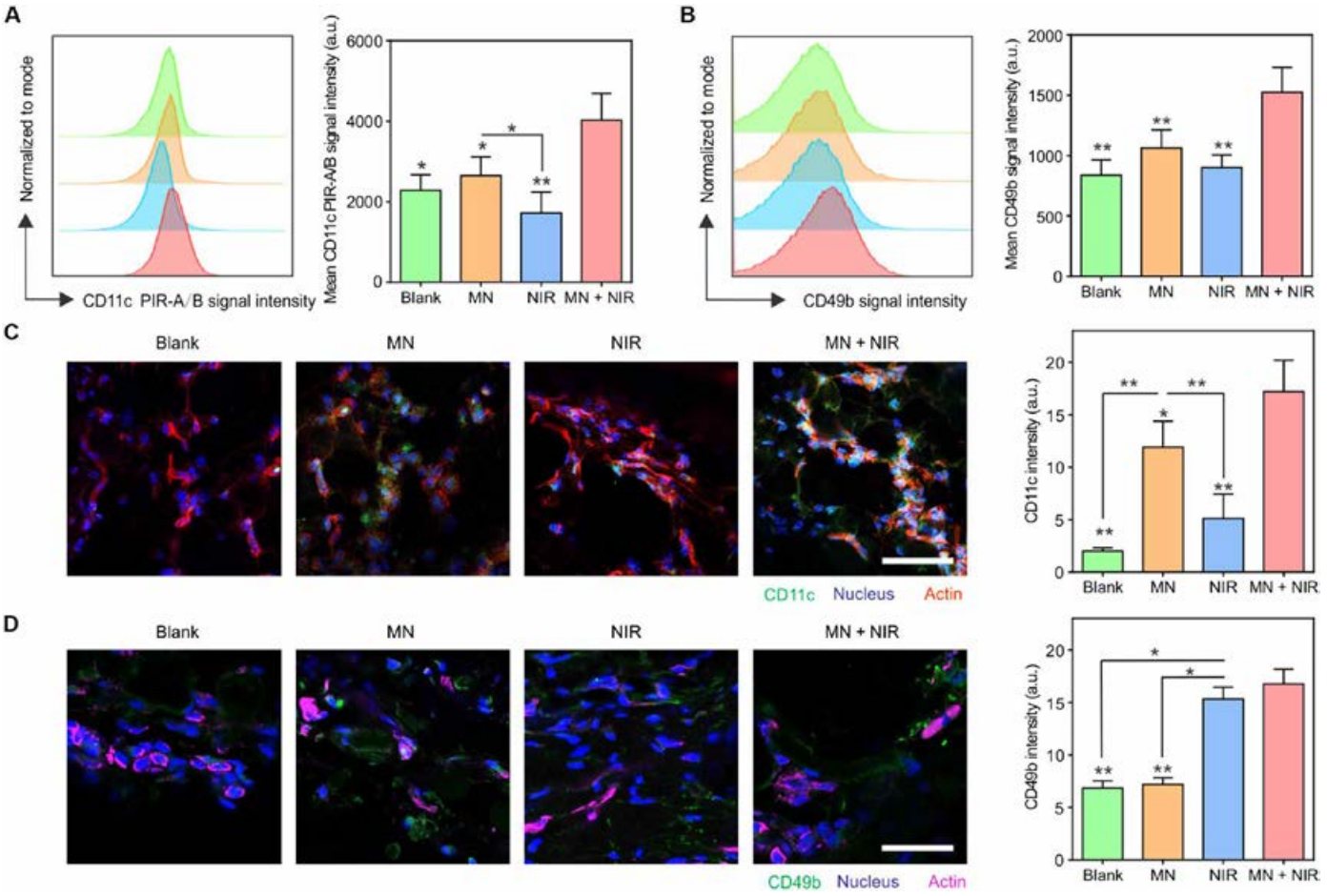

Fig. 4. Immune cell recruitment after the NIR-boosted and MN-mediated cancer immunotherapy. (**A**) Representative quantitative analysis of DCs ($CD11c^+$ and PIR-A/B^+) infiltrated in the skin 3 days after treatments as assessed by flow cytometry. The indicated samples were treated with blank MN (blank), vaccine MN (MN), MN loaded with tumor lysate without GM-CSF and treated with NIR (NIR), and vaccine MN and treated with NIR (MN + NIR). a.u., arbitrary units. (**B**) Representative quantitative analysis of NK cells ($CD49b^+$) in the skin upon transdermal cancer immunotherapy as assessed by flow cytometry. (**C** and **D**) Immunofluorescence staining and quantitative analysis of (C) $CD11c^+$ DCs (scale bar, 100 μm) and (D) $CD49b^+$ NK cells (scale bar, 100 μm). Statistical significance was calculated by Student's *t* test (*$P < 0.05$; **$P < 0.01$). Asterisks indicate significant differences between the MN + NIR group and all other treatment groups. Data points represent mean ± SD ($n = 3$). Error bars indicate SD.

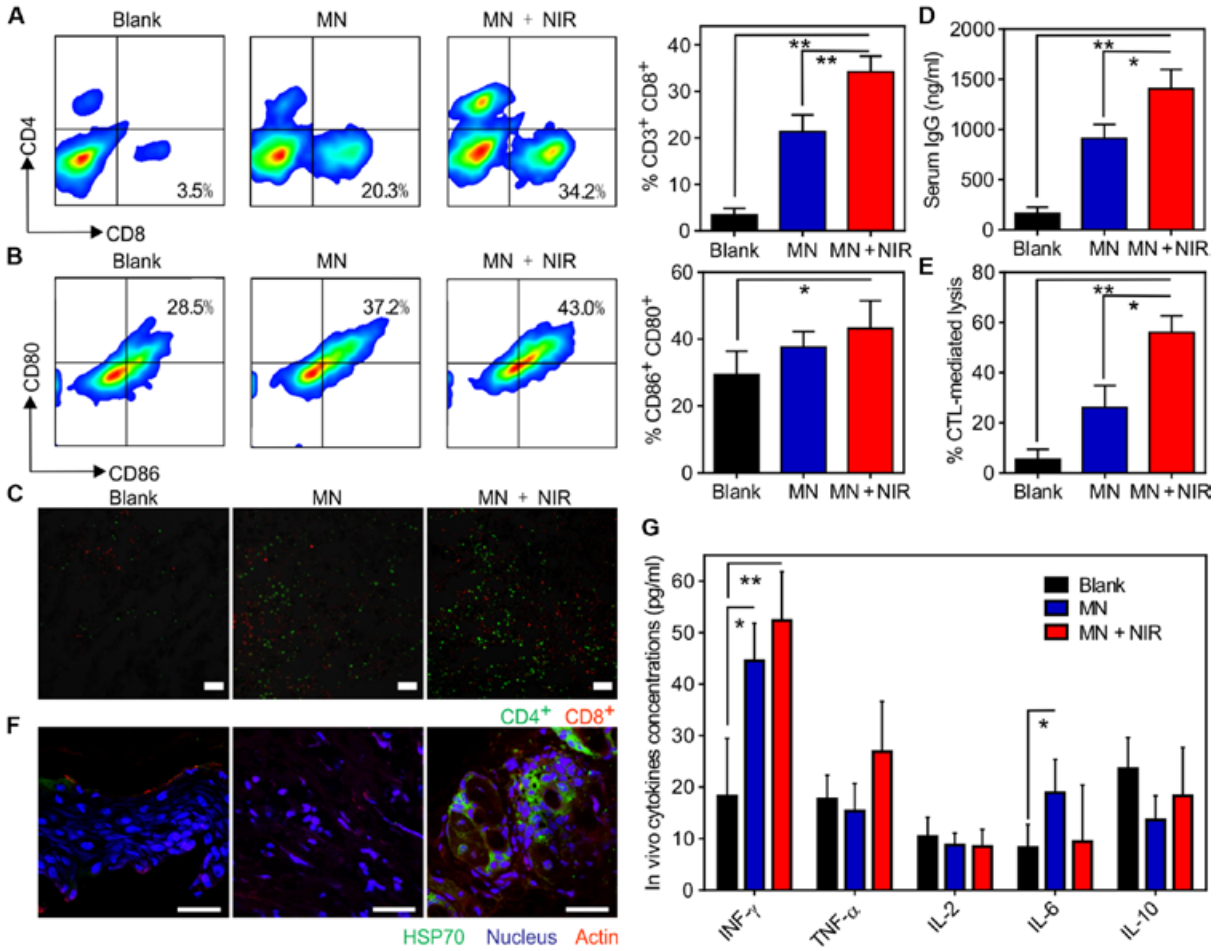

Fig. 5. Immunologic responses after the MN-mediated cancer immunotherapy. (**A**) Representative quantitative analysis of T cells (gated on $CD3^+$ T cells) in treated tumors analyzed by flow cytometry. (**B**) Representative quantitative analysis of activated DCs ($CD86^+$ and $CD80^+$) in the draining lymph nodes analyzed by flow cytometry. Data points represent mean ± SD ($n = 8$). (**C**) Immunofluorescence staining of the tumors showing $CD4^+$ T cell and $CD8^+$ T cell infiltration (scale bars, 100 μm). (**D**) Quantification of IgG1 subtypes in serum collected at day 10. Data points represent mean ± SD ($n = 8$). (**E**) Cytotoxic responses of splenocytes against B16F10 cells in vitro. Data points represent mean ± SD ($n = 6$). (**F**) Immunofluorescence staining of HSP70 (green) in the regional skin with actin filaments visualized by Alexa Fluor 660 phalloidin (red) and cell nuclei stained with Hoechst (blue) (scale bars, 100 μm). (**G**) In vivo local detection of cytokines from extracted patches at day 3. Statistical significance was calculated by Student's *t* test (*$P < 0.05$; **$P < 0.01$). Data points represent mean ± SD ($n = 8$). Error bars indicate SD. CTL, cytotoxic T lypmphocyte.

control groups (fig. S18). The in vitro analysis of splenocytes revealed 10-fold higher frequency of T cells responding to B16F10 tumor lysate in mice receiving the combined vaccination (Fig. 5E).

To examine that the light-to-heat transduction induced the production of danger signals and proinflammatory cytokines, we first measured local levels of ROS in the MN-treated surrounding tissue by flow cytometry. Samples from mice receiving the combined treatment showed about fourfold increase in ROS levels compared with the untreated group, whereas 1.5-fold increase was observed compared with the MN control without the NIR irradiation (fig. S19). In line with the elicitation of danger signals, combined vaccination caused the expression of HSP70 and HSP90 (Fig. 5F and fig. S20) (*38*). Danger signals from the local tissue and the antigenic molecules promote proinflammatory cytokine production (*39*). Consistent with this effect, we found local increases of interferon-γ (IFN-γ), tumor necrosis factor–α (TNF-α), and interleukin-6 (IL-6) in mice treated with the combined vaccination compared with MN controls (Fig. 5G and fig. S21).

Efficacy of MN patch in distant tumors

We further analyzed whether the local vaccination confers protection toward secondary tumors distant from the NIR- and MN-treated site (Fig. 6A). Local NIR irradiation and MN treatment were performed only on the left-side tumor in B16F10 mice bearing bilateral tumors. Right-side tumor was not injected and was shielded from light (Fig. 6B). We observed that the tumor sizes and bioluminescence signals decreased significantly on both sides of the mice that had the combined vaccination (Fig. 6, C to G). Meanwhile, substantial increase of activated DCs in the regional lymph node (Fig. 5B) and enhanced cytotoxic responses to B16F10 cells of the splenocytes in vitro (Fig. 5E) indicated that systemic antitumor effect could be achieved by the transdermal immunotherapy. This effect was parallel by fivefold increases in $CD8^+$ T cell infiltration compared with control, which was consistent with the role of immune cells for antitumor efficacy (Fig. 6D). Distant metastases were not observed in the lungs of the mice with combinational treatment (fig. S22).

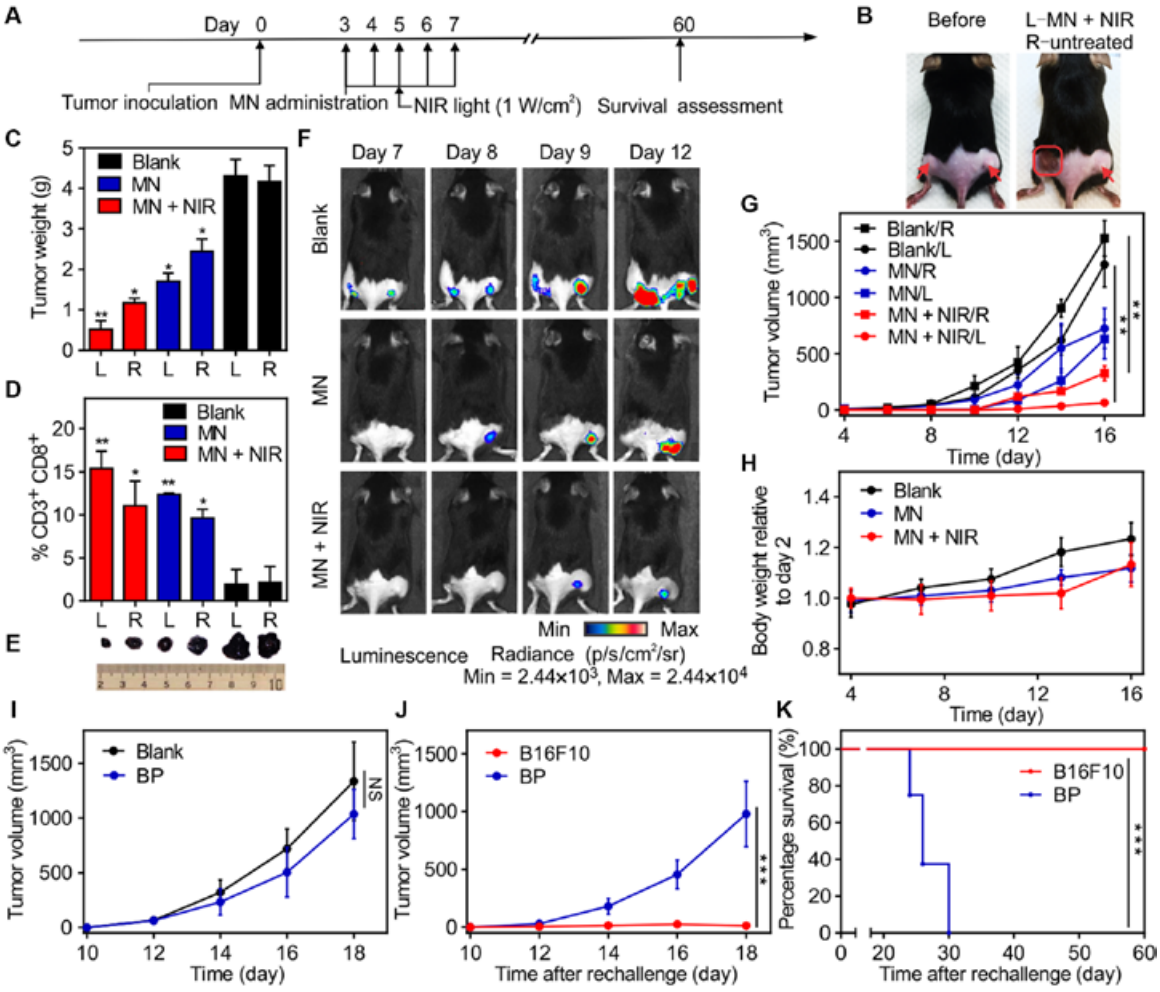

Fig. 6. Antitumor effect of local cancer immunotherapy treatment toward distant B16F10 tumors. (**A**) Schematic representation of the B16F10 tumor model. (**B**) Photograph of a mouse before and after MN administration. Red arrows indicate established tumors on both sides. L, left; R, right.The red line indicates the MN injection site. (**C**) Tumor weights in different experimental groups ($n = 3$). (**D**) Tumor-infiltrating $CD8^+$ T cells after treatments in different experimental groups ($n = 6$). Asterisks in (C) and (D) indicate statistically significant differences between blank MN and other groups. (**E**) Images of tumors extracted from treated mice indicated by the labels in (D). (**F**) In vivo bioluminescence imaging of treated B16F10 melanoma at different time points after treatment. One representative mouse per treatment group is shown. (**G**) Average tumor volumes in treated mice. (**H**) Body weights of treated mice ($n = 6$). (**I**) Average B16F10 tumor volumes in mice treated with MNs loaded with BP lysate with melanin and blank MN ($n = 8$). (**J**) Average tumor volumes in vaccinated mice rechallenged with either B16F10 cells or BP cells on day 80. (**K**) Kaplan-Meier survival curves for rechallenged mice. Data points represent mean ± SD ($n = 8$). Error bars indicate SD. Statistical significance was calculated by Student's *t* test and log-rank test (NS, $P > 0.05$; *$P < 0.05$; **$P < 0.01$; ***$P < 0.001$).

Body weight measurements indicated that the treated mice gained weight within the normal ranges (Fig. 6H). When the mice were vaccinated with tumor lysate of a different melanoma cell type [$BRAF^{V600E}PTEN^{-/-}$ Duke-clone 6 cell line (BPD6 or BP), syngeneic with C57BL/6J] (*40*, *41*), minimal changes in the B16F10 tumor growth were observed (Fig. 6I), indicating the specificity of the immunological memory. Similarly, when vaccinated mice were rechallenged with B16F10 cells or BP cells, tumor protection was observed only in mice challenged with B16F10 (Fig. 6, J and K, and fig. S23).

Efficacy of MN patch in other tumor models

To demonstrate that the potency of proposed vaccination is not limited to the B16 melanoma model in which there is an up-regulation of the melanogenesis, we used a $BRAF^{V600E}$-mutated BP melanoma in C57BL/6J mice and a triple-negative breast cancer 4T1 carcinoma tumor in BALB/cJ mice. Studies of MN loaded with synthetic melanin (with the same amount of pigment as quantified by spectrophotometry; table S1) and tumor lysate showed similar hyperthermic effect and enhanced immune responses with combined vaccination (fig. S24). Tumor regression and long-term survival were also achieved. Vaccination with the combined approach rendered 75 and 87% of mice resistant to BP and 4T1 engraftment, respectively (Fig. 7, A and B, and fig. S25). In the tumor-bearing mice, MN and NIR treatments induced complete remissions in 87 and 37% of mice engrafted with BP and 4T1 cells, respectively (Fig. 7, C and D, and fig. S25). Analysis of the local HSP70 expression showed a 2.5-fold increase in BP and a 4-fold increase in 4T1 models upon combined vaccination compared with the MN alone (fig. S26). Production of proinflammatory cytokines was also induced with the combined treatment, resulting in enhanced DC activation (figs. S27 and S28). Treatments were well

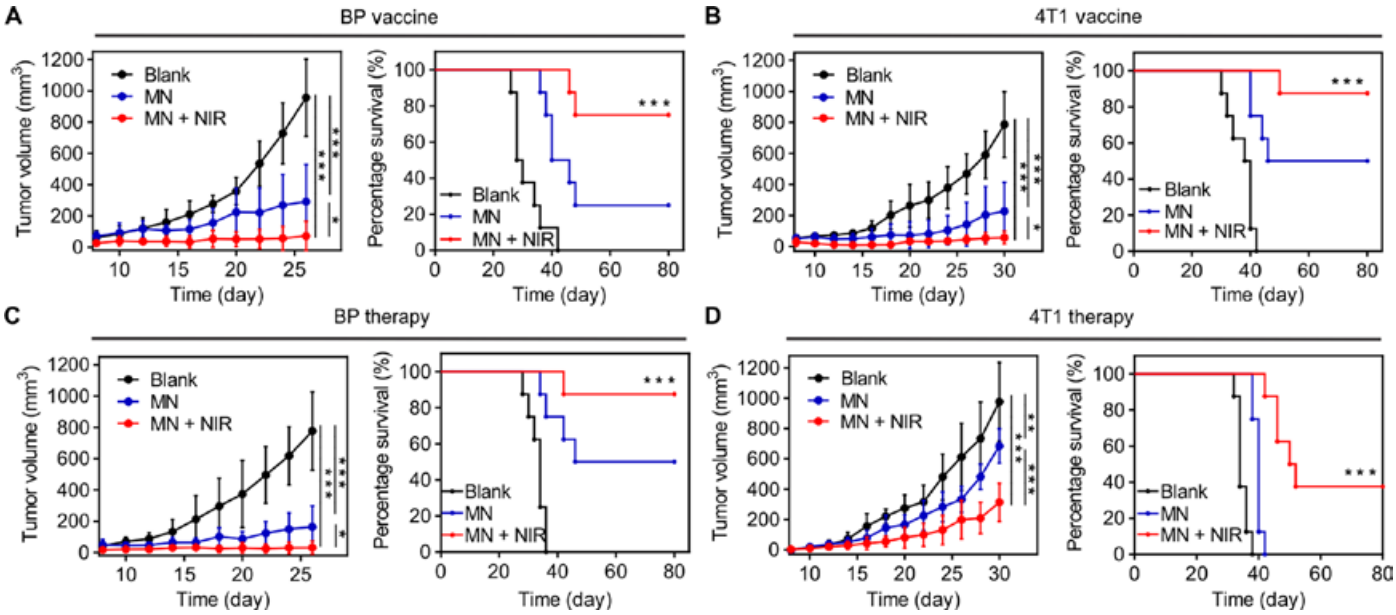

Fig. 7. Antitumor effect of local cancer immunotherapy treatment in various tumor models. (**A**) Average tumor growth and Kaplan-Meier survival rate of vaccinated C57BL/6J mice after BP tumor cell challenge. Mice were pretreated with blank MN (blank), MN loaded with BP tumor lysate and melanin (MN), or loaded MN combined with NIR irradiation (MN + NIR). (**B**) Average tumor growth and Kaplan-Meier survival rate of vaccinated BALB/cJ mice after 4T1 tumor cell challenge. Mice were pretreated with blank MN, MN loaded with 4T1 tumor lysate and melanin, or loaded MN combined with NIR irradiation. (**C**) Average tumor growth and Kaplan-Meier survival rate of C57BL/6J mice bearing established BP tumors. Mice were treated with blank MN, MN loaded with BP tumor lysate and melanin, or loaded MN combined with NIR irradiation. (**D**) Average tumor growth and Kaplan-Meier survival rate of BALB/cJ mice bearing established 4T1 tumors. Mice were treated with blank MN, MN loaded with 4T1 tumor lysate and melanin, or loaded MN combined with NIR irradiation. Data points represent mean ± SD ($n = 8$). Error bars indicate SD. Statistical significance was calculated by Student's *t* test and log-rank test (*$P < 0.05$; **$P < 0.01$; ***$P < 0.001$).

tolerated and did not cause weight loss or clinical signs of distant metastasis (figs. S29 and S30).

DISCUSSION

In the current study, we have integrated the B16F10 whole tumor lysate and GM-CSF into a transdermal MN patch to sustain the delivery of the cancer vaccine and target immune cell populations in the epidermis. By incorporating the melanin, we have demonstrated that the combined vaccine facilitated local immune activation upon NIR irradiation through the recruitment of DCs and other immune cells. Compared with other photosensitizing agents (*42*, *43*), melanin is a natural pigment with high biocompatibility and broad absorption spectrum. The efficient light-to-heat transduction mediated by melanin contributed to the rapid increase in skin temperature toward 42°C.

The combined treatment caused long-term survival with tumor rejection in 87% of vaccinated C57BL/6J mice. Complete tumor protection was further observed in mice rechallenged with B16F10 tumor cells. After NIR treatment, the elevated local microcirculatory blood perfusion was associated with the migration of local DCs and NK cells. Depletion of B cells, NK cells, and T cells attenuated the treatment efficacy in vaccinated mice, highlighting the relevance of the immune control in the tumor development. In accordance, the production of danger signals and proinflammatory cytokines triggered the immune activation. We have identified the elevated HSP70 and HSP90 expression and ROS levels in the surrounding tissues. This effect was also associated with local enrichment of IFN-γ, TNF-α, and IL-6. Characterization of other relevant danger signals and antigen adjuvants needs to be further examined.

In summary, the whole tumor lysate with melanin in a light-irradiated MN patch generates a hyperthermic-mimicking microenvironment that effectively recruits and activates immune cells at the vaccination site. As a result, the melanin-mediated patch prevents tumor engraftment in prophylactic models and causes sustained tumor regression in tumor-bearing mice. In addition, the natural melanin used in this treatment can also be extended to other biological pigments, such as carotenoid, xanthophylls, and bilirubin, for photomediated therapy. This method is also adaptable to deep-tissue photoacoustic imaging, biological labeling, and targeting a variety of diseases in a photo-/thermoresponsive manner (*44*–*46*). Nevertheless, the parameters associated with this immune activation need further optimization, for instance, the duration of NIR irradiation and the selection of light wavelength, as well as the treatment site. For the future study of the proposed approach, personal neoantigens and checkpoint inhibitors could be incorporated into the MNs to further enhance treatment specificity and efficacy (*47*). For the potential translation of the vaccine patch, it relies profoundly on a prolonged safety evaluation of the local and systemic toxicity, as well as other potential side effects.

MATERIALS AND METHODS

Study design

The objective of this study was to assess the effect of a melanin-mediated transdermal patch on cancer vaccine–based immunotherapy. The B16F10 whole tumor lysate containing melanin was integrated into an MN patch that allows controlled release of the cancer vaccine.

Upon NIR light irradiation on the patch, the local heating effect on boosting immune responses was evaluated. Mice subjects were purchased from the Jackson Laboratory, weighed, and randomly divided into different experimental groups. The numbers of sampling and experimental replicates were included in each figure legend.

Preparation and characterization of MNs

All MNs were prepared using silicone molds with arrays of conical holes machined by laser ablation (Blueacre Technology Ltd.). Each MN had a 300 μm by 300 μm round base tapering to a height of 800 μm with a tip radius of around 5 μm. MNs were arranged in a 15 × 15 array with a 600-μm center-to-center spacing. GM-CSF solution (0.1 mg/ml, 10-μl final volume) was directly deposited by pipetting onto each silicone micromold surface, followed by vacuum (600 mmHg) condition for 5 min to allow the solution to flow into the cavities. After that, 0.2 ml of 4.0 weight % (wt %) methacrylated hyaluronic acid solution mixed with *N*,*N*′-methylenebisacrylamide (2.0 wt %) and photoinitiator (Irgacure 2959; 0.05 wt %) were directly deposited by pipetting onto each silicone micromold surface, followed by vacuum (600 mmHg) condition for 5 min and centrifugation at 2000 rpm for 5 min (Hettich Universal 32R centrifuge). GM-CSF layer was cross-linked via ultraviolet irradiation (wavelength, 365 nm) for 10 s, and a piece of 4 cm by 9 cm silver adhesive tape was applied around the 2 cm by 2 cm micromold baseplate. Three milliliters of homogenized B16F10 tumor lysate (containing 1.5 mg of extracted tumor lysate proteins) in 4.0 wt % mixed methacrylated hyaluronic acid solution was added to the prepared micromold reservoir. We also used hyaluronic acid solution with different concentrations of tumor protein from 0.25 to 0.5 to 1.0 mg/ml. Protein concentration was quantified by measuring extracted protein content in the tumor lysate supernatant using T-PER (tissue protein extraction reagent) and Bradford assay before the MN fabrication. For the BP or 4T1 tumor lysate–loaded MNs, 50-μg melanin was dissolved in 4.0 wt % mixed methacrylated hyaluronic acid solution with tumor lysate (containing 1.5 mg of extract tumor lysate proteins, 3.0-ml final volume) to fabricate the MN matrix. For the blank MNs without tumor lysate, mixed methacrylated hyaluronic acid solution was used without the tumor lysate. For the melanin-loaded MNs, 50-μg melanin was dissolved in 4.0 wt % mixed methacrylated hyaluronic acid solution to fabricate the MN matrix. The stock melanin solution (100 mg/ml) was prepared by dissolving melanin in 1.0 M sodium hydroxide and heating to 99°C for 10 min. Final formulation was dried at 25°C in a vacuum desiccator overnight. After desiccation was completed, needle arrays were carefully separated from the silicone molds and cross-linked via ultraviolet irradiation. The needle base was tailored into a square shape. Fluorescent MNs were fabricated with phalloidin-labeled tumor lysate and rhodamine B– or Cy5.5-labeled hyaluronic acid. The preparation and storage of MNs were under sterilized condition. Morphology of MNs was characterized on a FEI Verios 460L field-emission scanning electron microscope operating at 20 kV after sputter coating with gold/palladium at the Analytical Instrumentation Facility. Cross sections of MNs were obtained by cutting 5-μm slides using Thermo Fisher Scientific HM525 NX Cryostat and stained with Alexa Fluor 488 phalloidin and Hoechst. Fluorescence images of MNs were taken by the Olympus IX70 multiparameter fluorescence microscope.

NIR-responsive property of MN

To evaluate the property of the MN patch in response to NIR light irradiation, we irradiated samples with 808-nm NIR laser light. The diode infrared laser module (Opto Engine LLC, MDL-N-808) was approved by a laser safety officer of the North Carolina State University (NC State) Environmental Health and Safety Center. The MN patches were placed on a piece of white paper with the needle tips facing down. The laser wire was fixed in place using a plate stand with a support rod and a clamp. The distance between the patch and spotlight was fixed at 10 cm, and the spot size was ~1 cm^2. The output energy of the diode infrared laser module was adjusted within 1.0 W and led to the intensity per unit area ($E = I/d^2$) of 1.0 W/cm^2 (at 808 nm). The NIR light was irradiated continuously or intermittently as needed. Surface temperature changes of the MN patch backing were recorded, and the highest temperature was controlled below 42°C in real time using a thermal imager (FLIR E4) and a noncontact infrared thermometer gun (Leegoal). For intermittent irradiation, the MNs were repeatedly exposed to the laser (1.0 W/cm^2), and the local temperature reached about 42°C for 1 min. Subsequently, the laser was turned off for 1 min. This cycle was repeated four times to assess the responsive behavior of MN patch under repeated NIR irradiation. For the continuous irradiation, samples with different parameters were tested. The effect of melanin content on the light-responsive behavior was tested on MNs loaded with tumor lysate of different protein concentration or blank MN with hyaluronic acid. Quantitative surface temperature changes of the representative MNs were recorded under continuous NIR irradiation at 1.0 W/cm^2. In a separate experiment, the laser power flux was controlled. During continuous NIR exposure for 2 min, the maximal temperature of the MN surface was recorded and plotted. The effect of MN backing thickness on the light-responsive behavior was tested on MNs with continuous NIR irradiation at 1.0 W/cm^2. The thickness of the MN patch was measured with an average value of 181 μm and an SD of 12.5 μm using a digimatic indicator (Mitutoyo Corp. ID-C112E Series 543). MN patch samples with different backing thicknesses (169, 175, 179, 181, and 202 μm) were used.

In vitro DC activation

Bone marrow was collected by flushing the femur and tibia with complete RPMI 1640 containing 10% fetal bovine growth serum. After lysis of red blood cells (lysate solution, Cwbiotech), 1 × 10^6 bone marrow cells were seeded in six-well culture dishes with 3.0 ml of the culture medium containing GM-CSF (20 ng/ml) and 50 μM β-mercaptoethanol (Bio-Rad, Hercules, CA, USA). On day 3, an additional 4.0 ml of the same medium with GM-CSF was added into the plates. On day 6, half of the culture supernatant was collected and centrifuged. Cells were resuspended in RPMI 1640 and added back into the original plates. On day 7, nonadherent cells were collected and used as bone marrow–derived DCs for further research use. Another murine DC line JAWS II cells were cultured in minimum essential medium Eagle alpha modification (Sigma-Aldrich) supplemented with GM-CSF (5 ng/ml). DCs were left unstimulated or stimulated for 12 hours with blank MN (100 μg/ml) or tumor lysate–loaded MN release medium or lipopolysaccharide (LPS; 100 ng/ml). After the stimulation, the cells were exposed to NIR irradiation (1.0 W/cm^2) at a distance of 10 cm for 0, 5, 10, 15, and 20 min, respectively. After cell incubation for 4 hours, the supernatants were collected and measured by IL-12 p70 mouse ELISA kit (Thermo Fisher Scientific, MC0121). The cells were washed and stained with LIVE/DEAD assay (Thermo Fisher Scientific, L3224) and $CD80^+$, and $CD86^+$ maturation marker-specific antibodies and subsequently analyzed by the confocal microscopy and flow cytometer. Both bone marrow–derived DCs and JAWS II cell line were used for characterization of DC activation. The LIVE/DEAD assay imaging data were obtained from the JAWS II cell line.

Mice and in vivo tumor models

Female C57BL/6J mice, BALB/cJ mice, CD11c-DTR transgenic mice [B6.FVB-Tg(Itgax-DTR/EGFP)57Lan/J; stock no. 004509], and *Rag1*$^{-/-}$ knockout mice (B6.129S7-*Rag1*^{tm1Mom}/J; stock no. 002216) were purchased from the Jackson Laboratory. Mice were weighed and randomly divided into different groups. On day 0, healthy mice were treated with MNs loaded with tumor lysates and GM-CSF, blank MNs loaded with synthetic melanin without tumor lysates, or blank MNs containing hyaluronic acid only (blank). MN patches were applied into the skin of the caudal-dorsal area for about 10 min and further fixed using Skin Affix surgical adhesive (Medline Industries Inc.). After injection of the MNs, NIR irradiation was performed on the localized MN region for 10 min each day for five successive days after immunization (MN + NIR). The diode infrared laser module at 808 nm (Opto Engine LLC, MDL-N-808) was approved by a laser safety officer of the NC State University Environmental Health and Safety Center. Mice in the control groups were treated with either vaccine MNs without NIR irradiation (MN), blank MNs loaded with synthetic melanin without tumor lysate with NIR irradiation (melanin), or blank MNs containing hyaluronic acid only with NIR irradiation (blank). Surface temperature changes of the regional skin were recorded and controlled below 42°C in real time using a thermal imager (FLIR E4) and a noncontact infrared thermometer gun (Leegoal). On day 10, 1×10^6 B16F10 tumor cell lines in 25 μl of phosphate-buffered saline (PBS) were subcutaneously transplanted into the flank of the C57BL/6J mice, CD11c-DTR transgenic mice, and *Rag1*$^{-/-}$ knockout mice. Tumor-free mice were rechallenged with 1×10^6 B16F10 tumor cells in 25 μl of PBS 80 days after the first tumor inoculation. For the depletion antibody study, we depleted specific T cell, B cell, and NK cell populations in mouse models. Mice were intraperitoneally given 200 μg of antibody purified from mouse thymus or spleen dissolved in 200 μl of PBS. Antibodies against CD4 (BioLegend, LEAF 100435), CD8 (BioLegend, LEAF 100735), CD19 (BioLegend, LEAF 152402), and NK-1.1 (BioLegend, LEAF 108712) were administered twice weekly for 3 weeks, starting 1 week before the tumor inoculation. Depletions were confirmed by flow cytometry of splenic suspension. For another melanoma model, 1×10^6 BP tumor cells in 25 μl of PBS were subcutaneously transplanted into the flank of the C57BL/6J mice. For the carcinoma tumor model, 1×10^6 4T1 tumor cells in 25 μl of PBS were subcutaneously transplanted into the flank of the BALB/cJ mice. For experimental metastasis model, 1×10^5 tumor cells were intravenously infused into mice via the tail vein. In another set of experiments, tumor cells were subcutaneously transplanted into the flank of the mice on day 0. The tumor-bearing mice were weighed and randomly divided into four groups when the tumor volume reached around 50 mm^3 on day 3. After that, the mice were peritumorally administrated with sterile MN loaded with tumor lysate and GM-CSF (MN) or blank MN containing hyaluronic acid only (blank). After that, NIR light was irradiated on the MN patch for 10 min during the following 5 days from days 3 to 7. Tumor growth was measured by a digital caliper or monitored by bioluminescence signals of luciferase-tagged cells. The tumor volume (cubic millimeter) was calculated as 1/2 × long diameter × (short diameter)^2.

To assess potential toxicity, we monitored mice daily for weight loss. H&E staining was performed on the organs collected from the mice following the standard procedure (Histology Laboratory at NC State College of Veterinary Medicine). Lungs were excised, and macroscopically visible metastases were counted. The resected primary tumors were stored at −20°C for immunofluorescence staining or fixed in 4% paraformaldehyde for subsequent analysis.

Identification of DC subsets, T cells, and cytokines

Antibodies used were purchased from Thermo Fisher Scientific and BioLegend Inc. Staining antibodies, including CD3 (Thermo Fisher Scientific, A18644), CD4 (Thermo Fisher Scientific, A18667), CD8 (Thermo Fisher Scientific, A18609), CD11c (BioLegend, 117309), CD49b (BioLegend, 108909), CD80 (BioLegend, 104707), CD86 (BioLegend, 105007), PIR-A/B (gp91, BioLegend, 144103), tetramer (MBL International, H-2D^b gp100, EGSRNQDWL-P), and fluorogenic CellROX Deep Red reagent (BioLegend, C10422) were used for fluorescence-activated cell sorting (FACS) and were analyzed following the manufacturers' instructions. Organs (skin, tumor, lymph node, and spleen) were harvested and minced into 2- to 4-mm pieces using scissors or scalpel blade. A single-cell suspension was prepared in the cell staining buffer (BioLegend, 420201). CellROX reagents at predetermined optimum concentrations were added to the cells and incubated on ice for 20 to 30 min in the dark for ROS detection. The relevant tetramer phycoerythrin (PE) was stained at room temperature for 30 min in the dark before additional staining with appropriately conjugated fluorescent antibodies. Stained cells were analyzed on a FACSCalibur instrument (BD) and using FlowJo software. To determine the concentration of different cytokines at the vaccine MN site, patch and adjacent tissues were excised and digested with T-PER (Pierce). Cytokine concentrations in the extracted patch were analyzed with a BioLegend's LEGENDplex bead-based immunoassays, according to the manufacturer's instructions.

Statistical analysis

Statistical analysis was evaluated using GraphPad Prism (6.0). Statistical analysis was performed with paired Student's *t* test and analysis of variance (ANOVA). *P* values for Kaplan-Meier curves were calculated with log-rank test. *P* values of 0.05 or less were considered significant.

Study approval

All mouse studies were performed following animal protocols approved by the Institutional Animal Care and Use Committee at the NC State University and the University of North Carolina at Chapel Hill (UNC-CH).

SUPPLEMENTARY MATERIALS

immunology.sciencemag.org/cgi/content/full/2/17/eaan5692/DC1

Materials and Methods

Fig. S1. Mechanical property of the MN.

Fig. S2. Characteristics of tumor lysate solution and synthetic melanin.

Fig. S3. Heating behavior of MN patches by repetitive NIR irradiation.

Fig. S4. Surface temperature of MN patches with various loadings of tumor lysates upon NIR irradiation.

Fig. S5. In vitro release profiles of GM-CSF and tumor lysate proteins.

Fig. S6. Scanning electron microscopy images of MN patch after insertion into the mouse skin over time.

Fig. S7. DC function evaluation after in vitro activation.

Fig. S8. Cytotoxicity study of the blank MNs.

Fig. S9. Characterization of the skin after MN insertion.

Fig. S10. Melanin-loaded MNs confer protective immunity in vivo.

Fig. S11. Tumor growth in control and treated mice.

Fig. S12. Quantified B16F10 bioluminescent tumor signals in control and treated mice.

Fig. S13. Tumor weights in control and treated mice.

Fig. S14. Histology and apoptosis analysis of the tumor sections.

Fig. S15. Tumor growth of mice receiving the transdermal cancer immunotherapy.

Fig. S16. Measurement of local microcirculatory blood perfusion of mice.

Fig. S17. Immunologic responses after the transdermal cancer immunotherapy.

Fig. S18. Quantification of IgG1 subtypes in serum after treatment with blank, MN, or MN + NIR.

Fig. S19. ROS detection by flow cytometry in tumor sections.

Fig. S20. HSP90 expression after the transdermal cancer immunotherapy.

Fig. S21. Cytokine kinetics after the transdermal cancer immunotherapy.

Fig. S22. Histology analysis after the transdermal cancer immunotherapy.
Fig. S23. Antitumor effect of the transdermal cancer immunotherapy toward different tumor models.
Fig. S24. Surface temperature changes of the melanin-loaded MNs.
Fig. S25. Antitumor effect of the transdermal cancer immunotherapy.
Fig. S26. HSP70 expression after the transdermal cancer immunotherapy.
Fig. S27. Representative quantitative analysis of the DC activation.
Fig. S28. Cytokine kinetics after the transdermal cancer immunotherapy.
Fig. S29. Average weights of mice after the transdermal cancer immunotherapy in control and treated mice.
Fig. S30. H&E staining of organs collected after the transdermal cancer immunotherapy.
Table S1. Melanin content of tumors excised from tumor-bearing mice.
Table S2. Measurement of total local microcirculatory blood perfusion of mice receiving different treatments using the laser Doppler flowmetry.
Excel file 1.
Excel file 2.

REFERENCES AND NOTES

1. J. Couzin-Frankel, Cancer immunotherapy. *Science* 342, 1432–1433 (2013).
2. D. Ricklin, G. Hajishengallis, K. Yang, J. D. Lambris, Complement: A key system for immune surveillance and homeostasis. *Nat. Immunol.* **11**, 785–797 (2010).
3. J. B. Swann, M. J. Smyth, Immune surveillance of tumors. *J. Clin. Invest.* **117**, 1137–1146 (2007).
4. L. Gu, D. J. Mooney, Biomaterials and emerging anticancer therapeutics: Engineering the microenvironment. *Nat. Rev. Cancer* **16**, 56–66 (2015).
5. L. E. Klevorn, R. M. Teague, Adapting cancer immunotherapy models for the real world. *Trends Immunol.* **37**, 354–363 (2016).
6. D. R. Littman, Releasing the brakes on cancer immunotherapy. *Cell* **162**, 1186–1190 (2015).
7. C. G. Drake, E. J. Lipson, J. R. Brahmer, Breathing new life into immunotherapy: Review of melanoma, lung and kidney cancer. *Nat. Rev. Clin. Oncol.* **11**, 24–37 (2013).
8. M. E. Dudley, S. A. Rosenberg, Adoptive-cell-transfer therapy for the treatment of patients with cancer. *Nat. Rev. Cancer* **3**, 666–675 (2003).
9. S. A. Rosenberg, N. P. Restifo, J. C. Yang, R. A. Morgan, M. E. Dudley, Adoptive cell transfer: A clinical path to effective cancer immunotherapy. *Nat. Rev. Cancer* **8**, 299–308 (2008).
10. M. T. Stephan, J. J. Moon, S. H. Um, A. Bershteyn, D. J. Irvine, Therapeutic cell engineering with surface-conjugated synthetic nanoparticles. *Nat. Med.* **16**, 1035–1041 (2010).
11. B. Huang, W. D. Abraham, Y. Zheng, S. C. Bustamante López, S. S. Luo, D. J. Irvine, Active targeting of chemotherapy to disseminated tumors using nanoparticle-carrying T cells. *Sci. Transl. Med.* **7**, 291ra94 (2015).
12. D. J. Irvine, M. A. Swartz, G. L. Szeto, Engineering synthetic vaccines using cues from natural immunity. *Nat. Mater.* **12**, 978–990 (2013).
13. M. F. Bachmann, G. T. Jennings, Vaccine delivery: A matter of size, geometry, kinetics and molecular patterns. *Nat. Rev. Immunol.* **10**, 787–796 (2010).
14. J. Banchereau, A. K. Palucka, Dendritic cells as therapeutic vaccines against cancer. *Nat. Rev. Immunol.* **5**, 296–306 (2005).
15. M. V. Dhodapkar, M. Sznol, B. Zhao, D. Wang, R. D. Carvajal, M. L. Keohan, E. Chuang, R. E. Sanborn, J. Lutzky, J. Powderly, H. Kluger, S. Tejwani, J. Green, V. Ramakrishna, A. Crocker, L. Vitale, M. Yellin, T. Davis, T. Keler, Induction of antigen-specific immunity with a vaccine targeting NY-ESO-1 to the dendritic cell receptor DEC-205. *Sci. Transl. Med.* **6**, 232ra51 (2014).
16. A. D. Garg, L. Vandenberk, C. Koks, T. Verschuere, L. Boon, S. W. Van Gool, P. Agostinis, Dendritic cell vaccines based on immunogenic cell death elicit danger signals and T cell–driven rejection of high-grade glioma. *Sci. Transl. Med.* **8**, 328ra27 (2016).
17. T. R. Fadel, F. A. Sharp, N. Vudattu, R. Ragheb, J. Garyu, D. Kim, E. P. Hong, N. Li, G. L. Haller, L. D. Pfefferle, S. Justesen, K. C. Herold, T. M. Fahmy, Corrigendum: A carbon nanotube-polymer composite for T-cell therapy. *Nat. Nanotechnol.* **9**, 723 (2014).
18. J. V. Kim, J.-B. Latouche, I. Rivière, M. Sadelain, The ABCs of artificial antigen presentation. *Nat. Biotechnol.* **22**, 403–410 (2004).
19. C. L.-L. Chiang, G. Coukos, L. Kandalaft, Whole tumor antigen vaccines: Where are we? *Vaccines* **3**, 344–372 (2015).
20. W. Kratky, C. Reis e Sousa, A. Oxenius, R. Spörri, Direct activation of antigen-presenting cells is required for $CD8^+$ T-cell priming and tumor vaccination. *Proc. Natl. Acad. Sci. U.S.A.* **108**, 17414–17419 (2011).
21. S. B. Stephan, A. M. Taber, I. Jileaeva, E. P. Pegues, C. L. Sentman, M. T. Stephan, Biopolymer implants enhance the efficacy of adoptive T-cell therapy. *Nat. Biotechnol.* **33**, 97–101 (2015).
22. J. Kim, W. A. Li, Y. Choi, S. A. Lewin, C. S. Verbeke, G. Dranoff, D. J. Mooney, Injectable, spontaneously assembling, inorganic scaffolds modulate immune cells in vivo and increase vaccine efficacy. *Nat. Biotechnol.* **33**, 64–72 (2015).
23. O. A. Ali, D. Emerich, G. Dranoff, D. J. Mooney, In situ regulation of DC subsets and T cells mediates tumor regression in mice. *Sci. Transl. Med.* **1**, 8ra19 (2009).
24. S. S. Evans, E. A. Repasky, D. T. Fisher, Fever and the thermal regulation of immunity: The immune system feels the heat. *Nat. Rev. Immunol.* **15**, 335–349 (2015).
25. K. Sato, N. Sato, B. Xu, Y. Nakamura, T. Nagaya, P. L. Choyke, Y. Hasegawa, H. Kobayashi, Spatially selective depletion of tumor-associated regulatory T cells with near-infrared photoimmunotherapy. *Sci. Transl. Med.* **8**, 352ra110 (2016).
26. J. Fu, D. B. Kanne, M. Leong, L. H. Glickman, S. M. McWhirter, E. Lemmens, K. Mechette, J. J. Leong, P. Lauer, W. Liu, K. E. Sivick, Q. Zeng, K. C. Soares, L. Zheng, D. A. Portnoy, J. J. Woodward, D. M. Pardoll, T. W. Dubensky Jr., Y. Kim, STING agonist formulated cancer vaccines can cure established tumors resistant to PD-1 blockade. *Sci. Transl. Med.* **7**, 283ra52 (2015).
27. T. S. Kupper, R. C. Fuhlbrigge, Immune surveillance in the skin: Mechanisms and clinical consequences. *Nat. Rev. Immunol.* **4**, 211–222 (2004).
28. K. Nagao, F. Ginhoux, W. W. Leitner, S.-I. Motegi, C. L. Bennett, B. E. Clausen, M. Merad, M. C. Udey, Murine epidermal Langerhans cells and langerin-expressing dermal dendritic cells are unrelated and exhibit distinct functions. *Proc. Natl. Acad. Sci. U.S.A.* **106**, 3312–3317 (2009).
29. C. Wang, Y. Ye, G. M. Hochu, H. Sadeghifar, Z. Gu, Enhanced cancer immunotherapy by microneedle patch-assisted delivery of anti-PD1 antibody. *Nano Lett.* **16**, 2334–2340 (2016).
30. J. Yu, Y. Zhang, Y. Ye, R. DiSanto, W. Sun, D. Ranson, F. S. Ligler, J. B. Buse, Z. Gu, Microneedle-array patches loaded with hypoxia-sensitive vesicles provide fast glucose-responsive insulin delivery. *Proc. Natl. Acad. Sci. U.S.A.* **112**, 8260–8265 (2015).
31. A. Filson, J. Hope, Isolation of melanin granules. *Nature* **179**, 211 (1957).
32. A. J. Lea, Solubility of melanins. *Nature* **170**, 709 (1952).
33. R. Zhang, Q. Fan, M. Yang, K. Cheng, X. Lu, L. Zhang, W. Huang, Z. Cheng, Engineering melanin nanoparticles as an efficient drug-delivery system for imaging-guided chemotherapy. *Adv. Mater.* **27**, 5063–5069 (2015).
34. S. P. Sullivan, D. G. Koutsonanos, M. del Pilar Martin, J. W. Lee, V. Zarnitsyn, S.-O. Choi, N. Murthy, R. W. Compans, I. Skountzou, M. R. Prausnitz, Dissolving polymer microneedle patches for influenza vaccination. *Nat. Med.* **16**, 915–920 (2010).
35. M. L. Moraes, P. J. Gomes, P. A. Ribeiro, P. Vieira, A. A. Freitas, R. Kohler, O. N. Oliveira Jr., M. Raposo, Polymeric scaffolds for enhanced stability of melanin incorporated in liposomes. *J. Colloid Interface Sci.* **350**, 268–274 (2010).
36. B. M. Carreno, V. Magrini, M. Becker-Hapak, S. Kaabinejadian, J. Hundal, A. A. Petti, A. Ly, W. R. Lie, W. H. Hildebrand, E. R. Mardis, G. P. Linette, A dendritic cell vaccine increases the breadth and diversity of melanoma neoantigen-specific T cells. *Science* **348**, 803–808 (2015).
37. J. C. Castle, S. Kreiter, J. Diekmann, M. Löwer, N. van de Roemer, J. de Graaf, A. Selmi, M. Diken, S. Boegel, C. Paret, M. Koslowski, A. N. Kuhn, C. M. Britten, C. Huber, Ö. Türeci, U. Sahin, Exploiting the mutanome for tumor vaccination. *Cancer Res.* **72**, 1081–1091 (2012).
38. A. Murshid, J. Gong, S. K. Calderwood, The role of heat shock proteins in antigen cross presentation. *Front. Immunol.* **3**, 63 (2012).
39. M. M. Hoffmann, C. Molina-Mendiola, A. D. Nelson, C. A. Parks, E. E. Reyes, M. J. Hansen, G. Rajagopalan, L. R. Pease, A. G. Schrum, D. Gil, Co-potentiation of antigen recognition: A mechanism to boost weak T cell responses and provide immunotherapy in vivo. *Sci. Adv.* **1**, e1500415 (2015).
40. D. Dankort, D. P. Curley, R. A. Cartlidge, B. Nelson, A. N. Karnezis, W. E. Damsky Jr., M. J. You, R. A. DePinho, M. McMahon, M. Bosenberg, *Braf*^{V600E} cooperates with *Pten* loss to induce metastatic melanoma. *Nat. Genet.* **41**, 544–552 (2009).
41. A. Holtzhausen, F. Zhao, K. S. Evans, M. Tsutsui, C. Orabona, D. S. Tyler, B. A. Hanks, Melanoma-derived Wnt5a promotes local dendritic-cell expression of IDO and immunotolerance: Opportunities for pharmacologic enhancement of immunotherapy. *Cancer Immunol. Res.* **3**, 1082–1095 (2015).
42. Q. Chen, L. Xu, C. Liang, C. Wang, R. Peng, Z. Liu, Photothermal therapy with immune-adjuvant nanoparticles together with checkpoint blockade for effective cancer immunotherapy. *Nat. Commun.* **7**, 13193 (2016).
43. J. Conde, N. Oliva, Y. Zhang, N. Artzi, Local triple-combination therapy results in tumour regression and prevents recurrence in a colon cancer model. *Nat. Mater.* **15**, 1128–1138 (2016).
44. W. Sun, Q. Hu, W. Ji, G. Wright, Z. Gu, Leveraging physiology for precision drug delivery. *Physiol. Rev.* **97**, 189–225 (2017).
45. Y. Zhang, J. Yu, A. Kahkoska, Z. Gu, Photoacoustic drug delivery. *Sensors* **17**, 1400 (2017).
46. L. Cheng, C. Wang, L. Feng, K. Yang, Z. Liu, Functional nanomaterials for phototherapies of cancer. *Chem. Rev.* **114**, 10869–10939 (2014).
47. C. Wang, Y. Ye, Q. Hu, A. Bellotti, Z. Gu, Tailoring biomaterials for cancer immunotherapy: Emerging trends and future outlook. *Adv. Mater.* **29**, 1606036 (2017).

Acknowledgments: We thank L. Huang at the UNC-CH for providing the B16F10-Luc cell line and *BRAF*^{V600E}*PTEN*$^{-/-}$ Duke-clone 6 cell line (generated in the laboratory of B. A. Hanks at Duke Cancer Institute), B. Andersen at the NC State University for Fourier transform infrared analysis,

and the UNC Research Opportunity Initiative for the strain tests. **Funding:** This work was supported by grants from the NC Translational and Clinical Sciences, the NIH Clinical and Translational Science Awards (NIH grant 1L1TR001111) at the UNC-CH, the Sloan Research Fellowship of the Alfred P. Sloan Foundation, and the pilot grant from the UNC Lineberger Comprehensive Cancer Center. **Author contributions:** Y.Y., C.W., L.H., G.D., and Z.G. designed the experiments. Y.Y., C.W., and X.Z. performed the experiments. Y.Y. and C.W. performed the statistical analyses. Y.Y., C.W., Q.H., Y.Z., Q.L., D.W., J.M., A.B., L.H., G.D., and Z.G. analyzed the data and wrote the paper. **Competing interests:** The authors declare that they have no competing interests.

Submitted 2 May 2017
Accepted 11 October 2017
Published 10 November 2017
10.1126/sciimmunol.aan5692

Citation: Y. Ye, C. Wang, X. Zhang, Q. Hu, Y. Zhang, Q. Liu, D. Wen, J. Milligan, A. Bellotti, L. Huang, G. Dotti, Z. Gu, A melanin-mediated cancer immunotherapy patch. *Sci. Immunol.* **2**, eaan5692 (2017).

IMMUNOTHERAPY

2017 © The Authors, some rights reserved; exclusive licensee American Association for the Advancement of Science.

Platelets subvert T cell immunity against cancer via GARP-TGFβ axis

Saleh Rachidi,[1,2]* Alessandra Metelli,[1,2]* Brian Riesenberg,[1,2] Bill X. Wu,[1,2] Michelle H. Nelson,[1,2] Caroline Wallace,[1,2] Chrystal M. Paulos,[1,2,3] Mark P. Rubinstein,[1,2,3] Elizabeth Garrett-Mayer,[2,4] Mirko Hennig,[5] Daniel W. Bearden,[6] Yi Yang,[1,2] Bei Liu,[1,2] Zihai Li[1,2,7†]

Cancer-associated thrombocytosis has long been linked to poor clinical outcome, but the underlying mechanism is enigmatic. We hypothesized that platelets promote malignancy and resistance to therapy by dampening host immunity. We show that genetic targeting of platelets enhances adoptive T cell therapy of cancer. An unbiased biochemical and structural biology approach established transforming growth factor β (TGFβ) and lactate as major platelet-derived soluble factors to obliterate $CD4^+$ and $CD8^+$ T cell functions. Moreover, we found that platelets are the dominant source of functional TGFβ systemically as well as in the tumor microenvironment through constitutive expression of the TGFβ-docking receptor glycoprotein A repetitions predominant (GARP) rather than secretion of TGFβ per se. Platelet-specific deletion of the GARP-encoding gene *Lrrc32* blunted TGFβ activity at the tumor site and potentiated protective immunity against both melanoma and colon cancer. Last, this study shows that T cell therapy of cancer can be substantially improved by concurrent treatment with readily available antiplatelet agents. We conclude that platelets constrain T cell immunity through a GARP-TGFβ axis and suggest a combination of immunotherapy and platelet inhibitors as a therapeutic strategy against cancer.

INTRODUCTION

Platelets, or thrombocytes, play essential roles in hemostasis (*1*). Increasingly, they have emerged to possess other regulatory functions in physiology such as angiogenesis, wound healing, and immunomodulation (*2*–*4*). Intriguingly, cancer-associated thrombocytosis is an independent poor prognostic factor in multiple cancer types (*5*, *6*), via enhancing invasiveness of cancer cells (*7*), promoting cancer motility (*4*, *8*), and inducing epithelial-mesenchymal cell transition (*9*). Despite knowledge of platelet cross-talk with natural killer cells (*10*), neutrophils (*11*), macrophages (*12*), dendritic cells (*13*–*15*), and T lymphocytes (*14*), the direct impact of thrombocytes on T cell immunity against cancer and the underlying molecular mechanisms have yet to be fully elucidated.

Platelets are bioactive, anuclear cellular fragments that are shed out of megakaryocytes in the bone marrow vasculature (*16*). They are the smallest cellular component of the hematopoietic system and are second only to red blood cells in number. Platelets express a number of cell surface receptors for adhesion and aggregation (*1*, *17*), such as glycoprotein (GP) Ib-IX-V complex, which serves as a receptor for von Willebrand factor, and GPIIb-IIIa integrin, which binds to fibrinogen and fibronectin. They also express other activation receptors, including the thromboxane A2 receptor, the adenosine diphosphate (ADP) receptors P2Y1 and P2Y12, and the protease-activated receptors PAR1 and PAR4, the latter of which can be activated by thrombin (*18*). Platelets have been found to constitutively express the nonsignaling transforming growth factor β (TGFβ)–docking receptor glycoprotein A repetitions predominant (GARP) (*19*), encoded by the *leucine-rich repeat-containing protein 32* (*Lrrc32*) gene. The role of GARP is to increase the activation of latent TGFβ (LTGFβ) and thus its biological function in the close proximity of GARP-expressing cells. The other cells that express GARP are regulatory T (T_{reg}) cells, which do so only after activation via T cell receptor (TCR) (*20*). Both GPIb-IX-V complex and GARP depend on the molecular chaperone gp96 for folding and cell surface expression (*21*, *22*). Genetic deletion of *Hsp90b1* (encoding gp96) from platelets results in significant thrombocytopenia and impaired platelet function (*21*). Last, there are cytoplasmic granules in platelets containing a variety of molecules such as TGFβ, ADP, serotonin, and proteases, which are released upon platelet activation and degranulation to exert their functions (*23*, *24*).

The key unresolved questions are how platelets affect the adaptive immunity in cancer and what are the underlying molecular mechanisms for such an action. With regard to TGFβ, it is completely unknown what the physiological function of platelet-specific cell surface GARP-TGFβ is in host immunity. In addition, GARP-TGFβ complex on platelets could be formed intracellularly, during the de novo biogenesis, or extracellularly, where GARP snatches LTGFβ in the extracellular matrix from nonplatelet sources and binds to it. However, it is unclear which source of the GARP-TGFβ complex is critical in regulating the host immunity against cancer in vivo. In this study, we systematically probed the effect of platelets on the effector function of antitumor T cells. We also took an unbiased approach to identify platelet-derived soluble immunoregulatory factors in blunting T cell function. This study not only uncovers mechanisms of platelet-mediated T cell suppression but also demonstrates the validity of the combination therapy of cancer with immunotherapeutics and antiplatelet (AP) agents in clinically relevant mouse models.

[1]Department of Microbiology and Immunology, Medical University of South Carolina, Charleston, SC 29425, USA. [2]Hollings Cancer Center, Medical University of South Carolina, Charleston, SC 29425, USA. [3]Department of Surgery, Medical University of South Carolina, Charleston, SC 29425, USA. [4]Department of Public Health Sciences, Medical University of South Carolina, Charleston, SC 29425, USA. [5]Department of Biochemistry and Molecular Biology, Medical University of South Carolina, Charleston, SC 29425, USA. [6]National Institutes of Standards and Technology, Hollings Marine Laboratory, Charleston, SC 29412, USA. [7]First Affiliated Hospital, Zhengzhou University School of Medicine, Zhengzhou 450052, Henan, China.
*These authors contributed equally to this work.
†Corresponding author. Email: zihai@musc.edu

RESULTS

Genetic inhibition of platelets enhances adoptive T cell therapy of cancer

Using bone marrow chimeric mice, we previously demonstrated that genetic deletion of *Hsp90b1* from the hematopoietic system resulted in macrothrombocytopenia coupled with dysfunctional platelets due to the loss of cell surface GPIb-IX-V, the receptor for von Willebrand factor (*21*). To probe the immunological function of platelets, we generated a megakaryocyte-specific *Hsp90b1* knockout (KO) mouse model in this study. As expected, KO mice had significantly lower platelet counts in the blood compared with wild-type (WT) mice (Fig. 1A). The dysfunction of platelets was evidenced by prolonged bleeding time (Fig. 1B). Extensive phenotypical analysis showed no obvious abnormalities in other cellular lineages, including T and B cells in the hematopoietic system of KO mice (fig. S1, A to D). The ability of $CD8^+$ and $CD4^+$ cells from the KO mice to produce interferon-γ (IFNγ) in response to polyclonal activation was also unaffected (fig. S1, E and F).

Adoptive T cell therapy (ACT) was next used to determine whether platelet dysfunction in the host affects the ability of transferred donor T cells to control cancer. ACT is a process of transferring preactivated antigen-specific T cells for the treatment of established cancers (*25*). Melanoma was chosen because (i) immunotherapy of unresectable melanoma has been increasingly implemented over the past few years with encouraging efficacies (*26*) and (ii) TCR transgenic mice of both $CD4^+$ (TRP1) and $CD8^+$ (Pmel) lineages (*27*, *28*) against melanoma antigens permit studying tumor-reactive T cells in our mouse models. B16-F1 melanomas were therefore established in C57BL/6 mice after subcutaneous injection on day 0, followed by infusion of ex vivo primed Pmel cells on day 11, along with interleukin-2 (IL-2)–anti–IL-2 antibody complex (*29*). Transferred Pmel cells had better antitumor activity in the *Hsp90b1* KO recipients compared with WT ones (Fig. 1C), whereas no difference in tumor growth was observed between the two groups without ACT (Fig. 1D). The improved ACT efficacy in the KO mice was associated with increased production of IFNγ (Fig. 1E) and tumor necrosis factor–α (TNFα) (Fig. 1F) by the donor T cells. These results suggest that platelet function in tumor-bearing mice constrains T cell–mediated cancer immunotherapy.

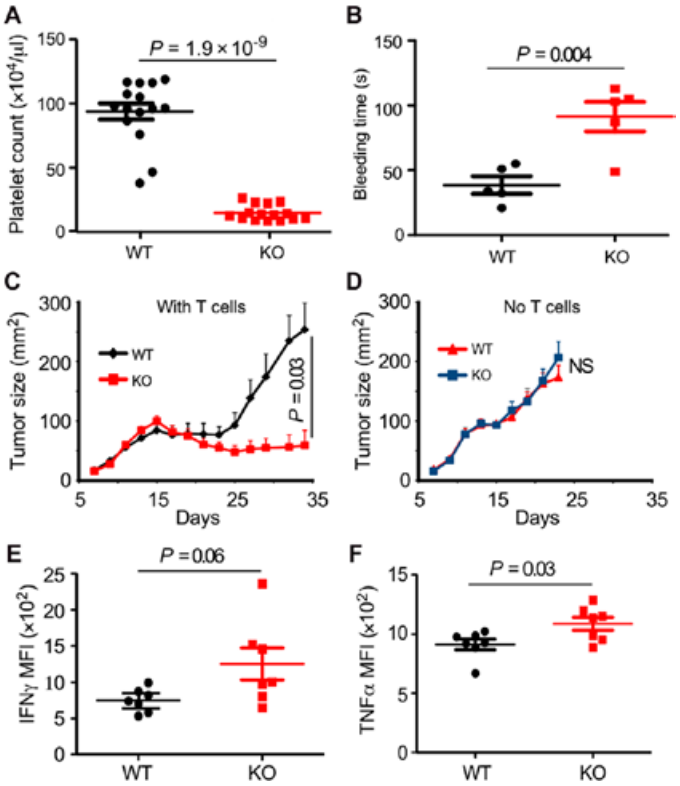

Fig. 1. Targeting platelets genetically potently enhances ACT of cancer. (**A**) Platelet counts from the peripheral blood of WT and *Pf4-cre-Hsp90b1*$^{flox/flox}$ (KO) mice (n = 15 per group). (**B**) Bleeding time was measured in WT and KO mice by pricking the lateral tail vein (n = 5 per group). (**C**) B16-F1 melanoma tumors were established in WT and *Pf4-cre-Hsp90b1*$^{flox/flox}$ mice, followed by adoptive transfer of activated Thy1.1$^+$ Pmel cells on day 11 plus IL-2–anti–IL-2 antibody complexes on days 11, 13, 15, and 17. Average tumor growth curves (n = 7 to 9 per group) are shown. (**D**) Same as in (C) except that mice did not receive T cells (n = 5 to 6 per group). (**E** and **F**) Pmel cells from the tumor-draining lymph nodes of the adoptively transferred mice in (D) were stimulated with hgp100 peptide for 4 hours, followed by intracellular staining for IFNγ (E) and TNFα (F). MFI, mean fluorescence intensity. Repeated-measures two-way ANOVA was used to compare the tumor growth curves. Two-tailed independent Student's t test was used in (A), (B), (E), and (F). Data are means ± SEM.

Platelet releasate suppresses T cell activation and function

We next focused on understanding the molecular mechanisms of T cell suppression by platelets. Given that platelets are not usually found in the lymphatic system and the T/B cell zone of the lymphoid organs, we reasoned that activated platelets exert their immunosuppressive function via releasing soluble factors. Purified platelets were suspended at 10^8 platelets/ml (several times lower than physiological platelet concentration) and activated with thrombin to generate platelet releasate (PR). The suppressive capacity was then measured in vitro using a standard polyclonal T cell activation assay (fig. S2A). Soluble factors in PR, but not platelet microvesicles (MVs), completely blocked T cell proliferation, blastogenesis, and IFNγ production (Fig. 2 and fig. S2, B to G). The activity of PR was not species-specific because both mouse (Fig. 2A) and human (Fig. 2B) PRs suppressed the activation and effector function of T cells from either source. Several parameters related to PR-mediated T cell suppression were also examined (fig. S3, A to J). The negative effect of PR could not be rescued by high-dose IL-2 (fig. S3A). Kinetic studies showed that the inhibitory effect was most pronounced during the first 2 days of T cell activation and was irreversible (fig. S3, B to G). Supernatant from unstimulated platelets had minimal effects (fig. S3H). PR had no direct effect on the proliferation of nonlymphocytes such as fibroblasts and B16-F1 melanoma (fig. S3, I and J). In addition, PR-treated T cells displayed a naïve phenotype expressing more CD62L and less CD44, programmed death–1 (PD-1), glucocorticoid-induced TNF receptor–related protein (GITR), and CD25 (Fig. 2, C and D). Moreover, the presence of PR during in vitro activation of $CD4^+$ TRP1 transgenic T helper 17 (T_H17) cells (*27*) abolished their activity upon adoptive transfer against B16-F10 melanoma (Fig. 3A) and reduced their persistence in the recipient mice (Fig. 3B). Similarly, $CD8^+$ Pmel cells also lost their antitumor activity in the adoptive transfer setting after exposure to PR during ex vivo activation (Fig. 3C), which correlated with poor donor cell persistence (Fig. 3D).

Platelet TGFβ and lactate mediate T cell suppression

Next, we took an unbiased approach to identify active T cell–suppressive molecule(s) in the PR. Human PR was fractionated by size exclusion chromatography, followed by quantifying individual fractions for their suppressive activity. Two major peaks with suppressive activity were resolved (Fig. 4A). Fraction A (>150 kDa) was further subfractionated

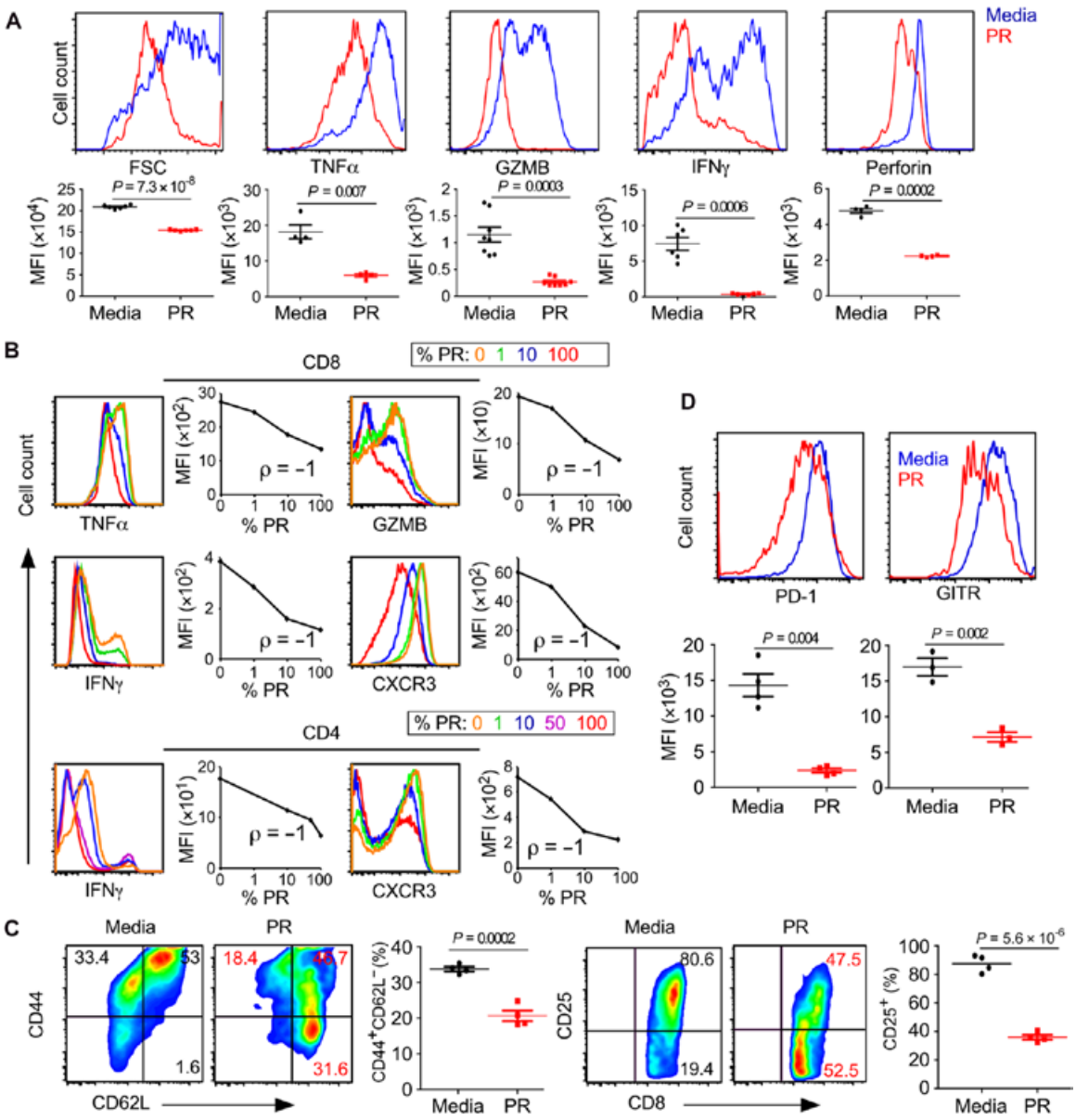

Fig. 2. Platelet-derived soluble factors suppress T cell function. (**A**) Naïve splenic CD8$^+$ T lymphocytes were activated polyclonally with or without mouse PR for 3 days, followed by measuring forward scatter profile (FSC) and multiple intracellular molecules. Data from multiple experiments (n > 5 times) were summarized at the bottom of the panel. GZMB, granzyme B. (**B**) Human peripheral blood CD4$^+$ or CD8$^+$ cells were activated polyclonally for 7 days with or without human PR, followed by measuring the indicated markers (representative of two experiments). Correlation between % PR and cytokine quantity was established using Spearman's correlation coefficient. (**C** and **D**) Naive CD8$^+$ T cells were polyclonally activated in the presence or absence of PR for 3 days, followed by flow cytometry. Numbers represent percentage of cells in the corresponding quadrants (n = 3 to 4 per group). Comparisons in (A), (C), and (D) were performed using two-tailed independent Student's t tests.

by anion exchange chromatography (Fig. 4B). Coomassie blue staining of a reducing SDS–polyacrylamide gel electrophoresis (SDS-PAGE) of the most active subfractions showed prominent bands corresponding to 150 to 250 kDa and 10 to 50 kDa (Fig. 4B). Mass spectrometry identified these proteins to be mature TGFβ (mTGFβ), latency-associated peptide (LAP), LTGFβ-binding protein 1 (LTBP1), and thrombospondin-1 (TSP1), indicating the presence of an mTGFβ-LAP-LTBP1-TSP1 complex (*30*). Immunoblot confirmed the existence of mature (12.5 kDa) and latent (44 kDa) TGFβ, LTBP1 (180 kDa), and TSP1 (110 to 180 kDa) in the whole PR, as well as in fraction A (Fig. 4B). Neutralizing TGFβ with the combination of an inhibitor for activin receptor–like kinase 5 (ALK5) (also known as type I TGFβ receptor) and anti-TGFβ antibody in fraction A completely rescued T cell function (Fig. 4C). We thus defined TGFβ as a major T cell–suppressive factor in the PR.

However, blocking TGFβ in the whole mouse PR only partially rescued T cell activity in vitro (fig. S4), indicating the presence of other TGFβ-independent factors. Furthermore, the activity of fraction B in both human and mouse PRs was heat-stable, proteinase K–resistant, and smaller than 1.0 kDa in size (fig. S5). Fraction B was then subfractionated by an anion exchange column to obtain subfractions B1 to B8 and used nuclear magnetic resonance (NMR) spectroscopy to delineate the metabolite composition (Fig. 4, D and E). Targeted

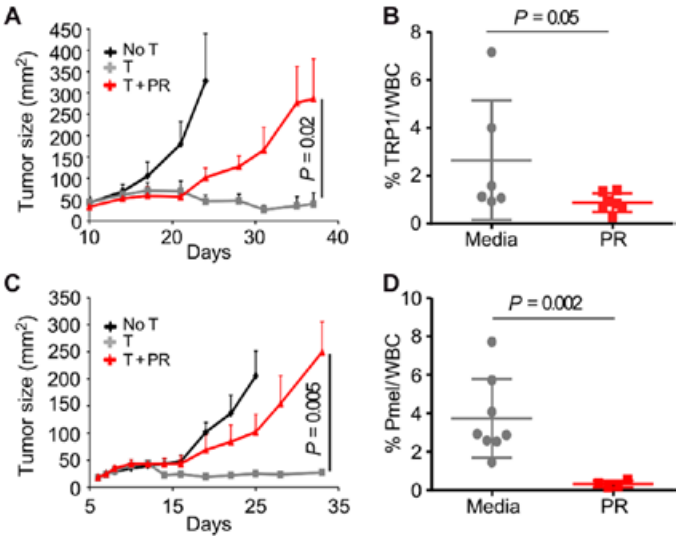

Fig. 3. Priming of antigen-specific T cells in the PR abrogates their antitumor immunity in vivo. (**A**) TRP1 transgenic CD4$^+$ T cells were primed under T_H17-differentiating conditions, in control media or human PR (n = 6 per group). They were then adoptively transferred on day +10 to B16-F10–bearing mice that also received sublethal dose of total body irradiation on day +9. (**B**) Percentages of TRP1 cells in the peripheral blood on day +37 (n = 6 to 7 per group). Mann-Whitney test for non-normal distribution was used to compare the two groups. WBC, white blood cell. (**C**) Pmel T cells were primed with IL-12 and hgp100 peptide, in control media or human PR. They were then adoptively transferred on day +8 to B16-F10–bearing mice that also received cyclophosphamide on day +7 (n = 4 to 8 per group). (**D**) Percentages of Pmel cells in the peripheral blood on day +33 (n = 4 to 8 per group). Tumor growth curves were compared using repeated-measures two-way ANOVA. Percentages of T cells were compared using two-tailed independent Student's t tests. Data are means ± SEM.

profiling using the Chenomx NMR Suite software identified lactate as the most abundant metabolite (~3.4 mM) in the most suppressive B3 and B4 subfractions (Fig. 4E). The immunoregulatory roles of lactate in T cells (*31*) and macrophages (*32*) have been reported. The concentration of lactate in the whole PR was ~5.7 mM. Lactate efficiently suppressed T cell activation with concentrations as low as 2.5 mM (Fig. 4F). Blocking both TGFβ (by a neutralizing antibody) and lactic acid (LA) (by inhibiting monocarboxylate transporter I with α-cyano-4-hydroxycinnamic acid) (*32*) in the whole human PR almost completely rescued IFNγ production, CD25 expression, and blastogenesis of CD8$^+$ T cells (fig. S6). Thus, we conclude that the suppressive activity of PR primarily resides in TGFβ and lactate.

To further address the suppressive components in the PR, we performed an in vitro T_{reg} induction assay. Splenocytes were activated with anti-CD3/28 antibody in the presence of PR, TGFβ, and lactate for 3 days. Consistent with earlier findings, PR attenuated T cell blastogenesis (fig. S7, A and D), and this was partially recapitulated by each of TGFβ and LA. A proportion of CD4$^+$ cells cultured with PR differentiated into the T_{reg} lineage (fig. S7, B and D), and this was accompanied by up-regulation of phosphorylated Smad2/3 (p-Smad2/3) (fig. S7, C and D). Expectedly, TGFβ, but not LA, also induced T_{reg} differentiation and p-Smad2/3.

We then investigated whether TGFβ and/or LA can independently recapitulate the inhibitory effects of PR on tumor-reactive T cells. B16-F1 melanoma tumors were established in C57BL/6 mice, which were subsequently treated with Pmel CD8 T cells, similar to the experiment described in Fig. 3C. T cells were primed ex vivo with human gp100 (hgp100) and IL-12 in control media (Pmel-12), PR, TGFβ, and/or LA (fig. S8). T cells primed in the presence of PR or TGFβ (650 pg/ml, the concentration of TGFβ present in PR from 1×10^8 platelets/ml) failed to control melanoma progression and to persist in peripheral blood (fig. S8, A to C). This poor in vivo persistence is likely explained by the failure of Pmel cells to up-regulate receptors of the homeostatic cytokines IL-2 and IL-7 under these conditions (fig. S8D). IL-7 is crucial for Pmel cell persistence in vivo in the Pmel tumor model (*33*). In turn, LA in the priming phase had no effect on the subsequent antitumor activity of Pmel T cells. This suggests that platelet-derived TGFβ is likely a more relevant target in immunotherapy.

Platelet-intrinsic GARP plays critical roles in generating active TGFβ

Platelets not only produce and store high levels of TGFβ intracellularly (*34*) but also are the only cellular entity known so far that constitutively expresses the cell surface–docking receptor GARP for TGFβ (*19*). Thus, platelets may contribute to the systemic levels of TGFβ via active secretion, as well as GARP-mediated capturing from other cells or the extracellular matrix (*9*, *35*–*37*). We next addressed to what extent and how platelets contribute to the physiological TGFβ pool. Baseline sera were obtained from WT mice followed by administration of a platelet-depleting antibody. These mice were sequentially bled, and serum TGFβ was quantified by enzyme-linked immunosorbent assay (ELISA). Depletion of platelets resulted in a complete loss of active and total TGFβ, which rebounded effectively as soon as platelet count recovered (Fig. 5A). These experiments demonstrate that platelets contribute dominantly to the circulating TGFβ level. By comparison, serum LA with or without depletion showed no significant changes (fig. S9), arguing that platelet-derived TGFβ, but not LA, is a more relevant platelet-derived immunosuppressive molecule in vivo.

The biology of platelet-derived TGFβ in cancer immunity was addressed next, focusing on the role of platelet GARP in the production of active TGFβ.In addition to platelet-specific *Hsp90b1* KO mice, two additional mouse models were generated: one with selective deletion of GARP in platelets (*Pf4-cre-Lrrc32*$^{flox/flox}$ or Plt-GARP^{KO}) and another with platelet-restricted KO of TGFβ1 (*Pf4-cre-Tgfb1*$^{flox/flox}$ or Plt-TGFβ1^{KO}) (Fig. 5B). Because gp96 is also an obligate chaperone for GARP (*22*), platelets from neither Plt-gp96^{KO} mice nor Plt-GARP^{KO} mice expressed cell surface GARP-TGFβ complex. However, platelets from Plt-TGFβ1^{KO} mice expressed similar levels of surface GARP-TGFβ1 complex when compared with WT platelets (Fig. 5, B to D), indicating that the GARP-TGFβ1 complex can be formed without autocrine TGFβ1.

The levels of active TGFβ and LTGFβ were then measured in the plasma and sera of WT and KO mice (Fig. 5, E and F). In WT mice, active TGFβ was elevated in serum compared with plasma, indicating a role for platelets and/or the coagulation cascade in TGFβ activation (Fig. 5E). Plt-gp96^{KO} and Plt-GARP^{KO} mice had very little active TGFβ in their sera, confirming the importance of platelet-intrinsic GARP in converting LTGFβ to the active form. In contrast, the serum level of active TGFβ in Plt-TGFβ1^{KO} mice was comparable with that of WT mice (Fig. 5E), indicating that platelets are capable of activating TGFβ from nonplatelet sources in a trans fashion. Significantly, the total LTGFβ level in the serum is only reduced in Plt-TGFβ1^{KO} mice but not Plt-gp96^{KO} or Plt-GARP^{KO} mice (Fig. 5F). Collectively, these data indicate that platelet-intrinsic GARP is the most important mechanism in the activation of TGFβ systemically. This experiment also categorically confirmed that serum but not plasma level of active TGFβ reflects platelet activation.

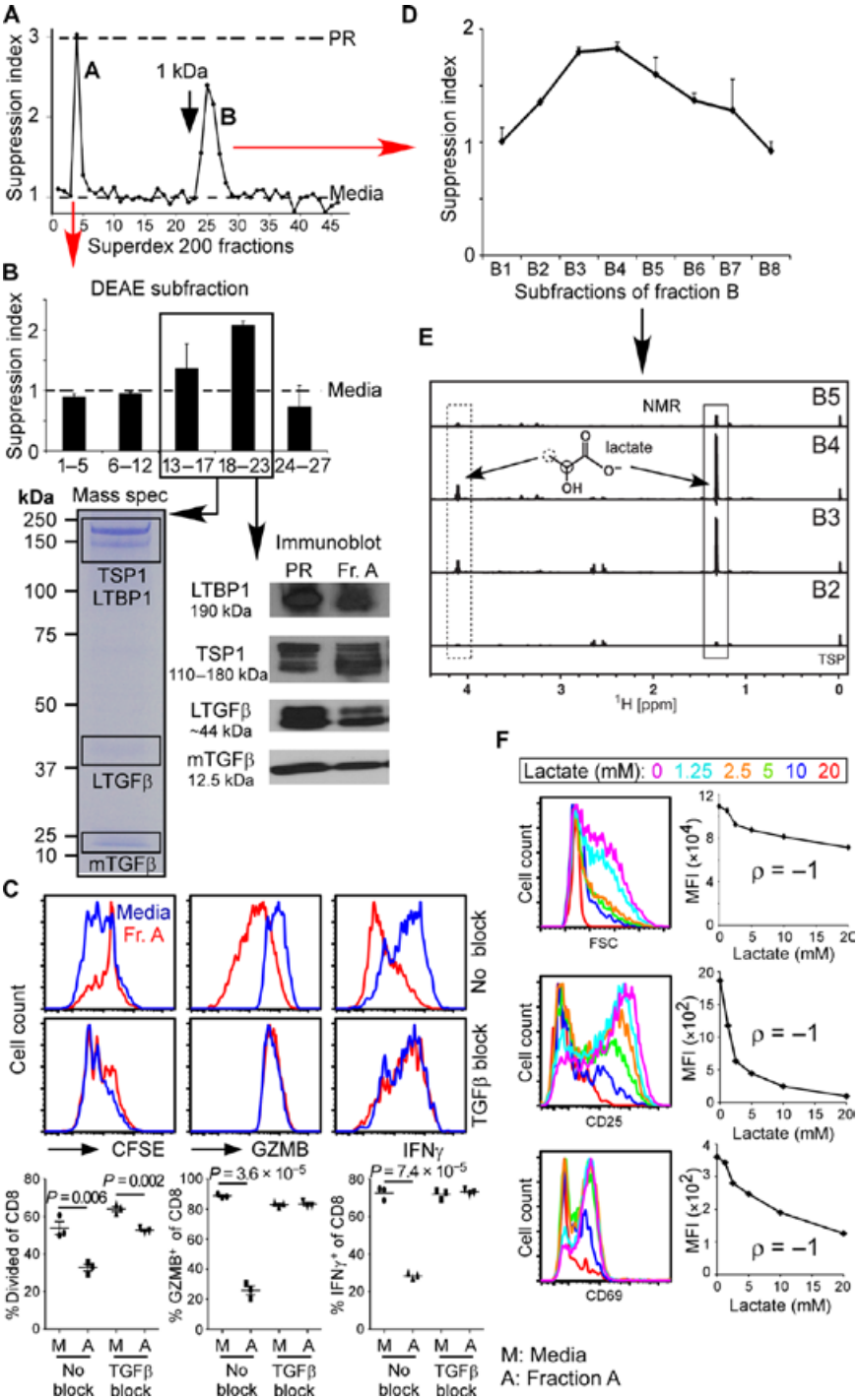

Fig. 4. TGFβ and lactate contribute to platelet-mediated T cell suppression. (**A**) Human PR was fractionated by size exclusion chromatography, followed by quantifying individual fractions for their suppressive activity. T cell suppression indices of all fractions are shown. Suppression index of media (percent of undivided CD8 T cells) was set as 1 and is indicated. (**B**) Fraction A was further resolved by DEAE column, and subfractions were assayed for T cell suppression. The most active fractions (boxed) were resolved by SDS-PAGE and Coomassie blue stain. The protein identities of the major bands were determined by mass spectrometry and immunoblot. (**C**) CFSE-labeled naïve $CD8^+$ T cells were stimulated with anti-CD3ε/CD28 antibodies and IL-2 for 3 days in media or fraction A (Fr. A) with or without TGFβ blockade. Cells were assayed for CFSE dilution, granzyme B, and IFNγ production by $CD8^+$ cells (n = 3 per group). Representative histograms are shown. Corresponding quantifications are displayed below the flow cytometry data. (**D**) Suppressive activity of various subfractions B1 to B8. (**E**) Upfield 600-MHz ^{1}H excitation sculpting NMR spectra of fractions B2 to B5 (bottom to top). Solid and dashed boxes highlight varying concentrations of lactate methyl and methine proton resonances, respectively. Spectra are normalized to the defined concentration of TSP. (**F**) Purified $CD8^+$ T cells were cultured for 3 days in the presence of agonistic CD3ε and CD28 antibodies and IL-2. Cell surface expression of CD25 and CD69 and blastogenesis (FSC) were assayed by flow cytometry. Correlation between LA concentration and cytokine production was established using Spearman's correlation coefficient. Difference between groups in (C) was tested by two-tailed independent Student's t test.

Platelet GARP-TGFβ complex blunts antitumor T cell immunity

So far, we have shown that TGFβ is a major T cell suppressor molecule from PR and that platelet-specific deletion of gp96 (which functionally deletes GARP) improves ACT of cancer. These fortuitous observations suggest that platelet-specific GARP plays critically negative roles in antitumor T cell immunity. This hypothesis was next addressed by comparing the efficacy of ACT of melanoma in WT, Plt-TGFβ1^{KO}, and Plt-GARP^{KO} recipient mice (Fig. 6). B16-F1 melanomas were established in either WT or KO mice, followed by lymphodepletion with cyclophosphamide (Cy) on day 9, and the infusion of ex vivo activated Pmel T cells on day 10 (Fig. 6A). Tumors were controlled much more efficiently in the Plt-GARP^{KO} mice compared with WT mice (Fig. 6A). This was associated with enhanced persistence (Fig. 6B) and functionality of Pmel cells in the peripheral blood of Plt-GARP^{KO} mice (Fig. 6, C and D). In contrast, Plt-TGFβ1^{KO} mice, whose platelets express GARP and remain capable of activating TGFβ, did not have improved control of tumors (Fig. 6D). The generality of these findings was next studied in the MC38 colon carcinoma system, given that the growth of this transplantable tumor in syngeneic mice undergoes both CD4- and CD8-mediated immune pressure (*38*, *39*). The growth of MC38 was significantly diminished in Plt-GARP^{KO} mice compared with WT mice (Fig. 7, A to C). The MC38-bearing Plt-GARP^{KO} mice had reduced serum levels of active TGFβ (Fig. 7D). Staining for p-Smad2/3 in MC38 tumor sections demonstrated a remarkable attenuation of TGFβ signaling in MC38 cells in Plt-GARP^{KO} mice (Fig. 7, E and F). This was associated with reduction of both systemic myeloid-derived suppressor cells (Fig. 7G) and tumor-infiltrating T_{reg} cells in Plt-GARP^{KO} mice (Fig. 7H). Together, this demonstrates that platelets are the commanding source of TGFβ activity in the tumor microenvironment and that they exert potent immunosuppressive effects on antitumor immunity via GARP-TGFβ.

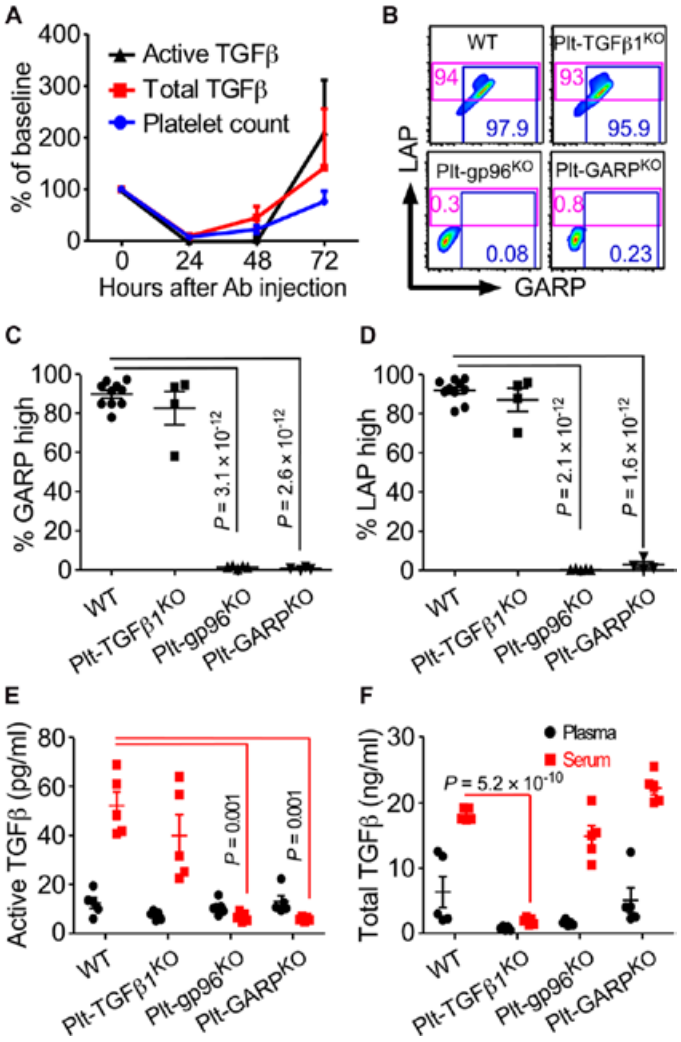

Fig. 5. Platelet-intrinsic GARP plays critical roles in generating active TGFβ. (**A**) Baseline serum was collected from WT C57BL/6 mice, followed by a single dose of anti-mouse thrombocyte sera ($n = 7$). Serum was collected 24, 48, and 72 hours after injection. Ab, antibody. (**B**) Representative flow cytometry plots. Platelet-specific marker CD41$^+$ population was gated on and analyzed for the expression of cell surface GARP and LTGFβ. Numbers represent percentages of the gated population over all CD41$^+$ events. (**C** and **D**) Graphical representation of flow cytometry data from (B) ($n = 4$ to 9 per group). (**E**) Serum and plasma levels of active TGFβ from indicated mice ($n = 5$ per group). (**F**) Serum and plasma levels of total TGFβ from indicated mice ($n = 5$ per group). Comparison was performed using two-tailed independent Student's *t* test. Data are means ± SEM.

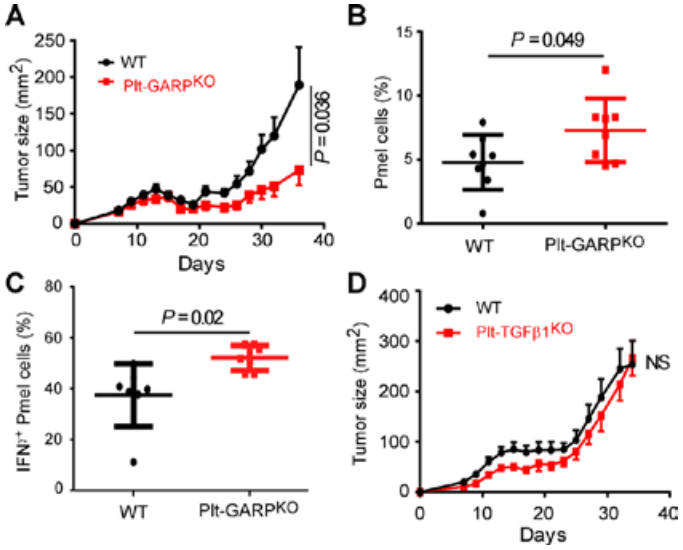

Fig. 6. Platelet-derived GARP-TGFβ complex blunts ACT of melanoma. (**A** to **C**) B16-F1–bearing WT and Plt-GARP^{KO} mice ($n = 7$ to 8 per group) expressing congenic marker Thy1.2 were given Cy on day 9, followed by adoptive transfer of activated Thy1.1$^+$ Pmel cells on day 10. (A) Tumor growth curves. (B) The frequency of Pmel cells in mice was enumerated 3 weeks after adoptive transfer of T cells by flow cytometry in the peripheral blood (CD8$^+$Thy1.1$^+$/total CD8$^+$). (C) IFNγ-producing ability of antigen-specific donor T cells (Pmel) from indicated mice 3 weeks after T cell transfer. (**D**) B16-F1 melanoma tumors were established in WT and *Plt-Tgfβ KO* mice, followed by adoptive transfer of activated Thy1.1$^+$ Pmel cells on day 11 plus IL-2–anti–IL-2 antibody complexes on days 11, 13, 15, and 17. Average tumor growth curves ($n = 4$ to 9 per group) are shown. Repeated-measures ANOVA was used in (A) and (D). Two-tailed independent Student's *t* test was used in (B) and (C). Data are means ± SEM.

Antiplatelet pharmacological agents potentiate ACT of cancer

To establish the clinical relevance of the suppressive effect of platelets on antitumor immunity, we sought to inhibit platelets pharmacologically. The results so far suggest that antiplatelet (AP) pharmacological agents can be exploited for enhancing cancer immunotherapy. This possibility was addressed using Pmel adoptive therapy of B16 melanoma (*40*–*42*). B16-F1 melanomas were established in C57BL/6 mice after subcutaneous injection on day 0, followed by lymphodepletion with Cy on day 7, and infusion of ex vivo primed Pmel cells on day 8 (*29*), along with AP agents: aspirin and clopidogrel (*43*). Aspirin and clopidogrel inhibit platelet activation by blocking cyclooxygenase and ADP receptors, respectively. Cy alone failed to control tumors, and the additional AP also had no antitumor effects in this model (Fig. 8A, left). Melanoma was controlled well with T cells plus Cy for about 1 month, but most mice eventually relapsed. In contrast, AP agents plus adoptive T cell transfer were highly effective against B16-F1, with relapse-free survival of most mice beyond 3 months (Fig. 8A, right). As a further proof, antigen-specific T cells were sustained at higher numbers in the blood, inguinal lymph nodes (ILNs), and spleens of mice receiving concurrent AP therapy and ACT (Fig. 8B). AP agents conferred no benefit when the transferred T cells lacked IFNγ (Fig. 8C) or when anti-IFNγ neutralization antibodies were administered (Fig. 8D).

DISCUSSION

The role of platelets in promoting cancer invasion has been previously observed (*44*, *45*). Multiple mechanisms have been attributed to this phenomenon including the promotion of angiogenesis (*46*) and stimulating epithelial-mesenchymal cell transition (*9*). However, the direct contribution of platelets to anticancer immunity has not been well described despite the emerging appreciation of the cross-talk between platelets and the host immunity. The current study uncovers that platelets directly dampen T cell function both in vitro and in vivo. Furthermore, we demonstrated that the PR suppresses both CD4$^+$ and CD8$^+$ T cells mostly via TGFβ and, to a lesser extent, through lactate. It is intriguing that both lactate and TGFβ are enriched in the

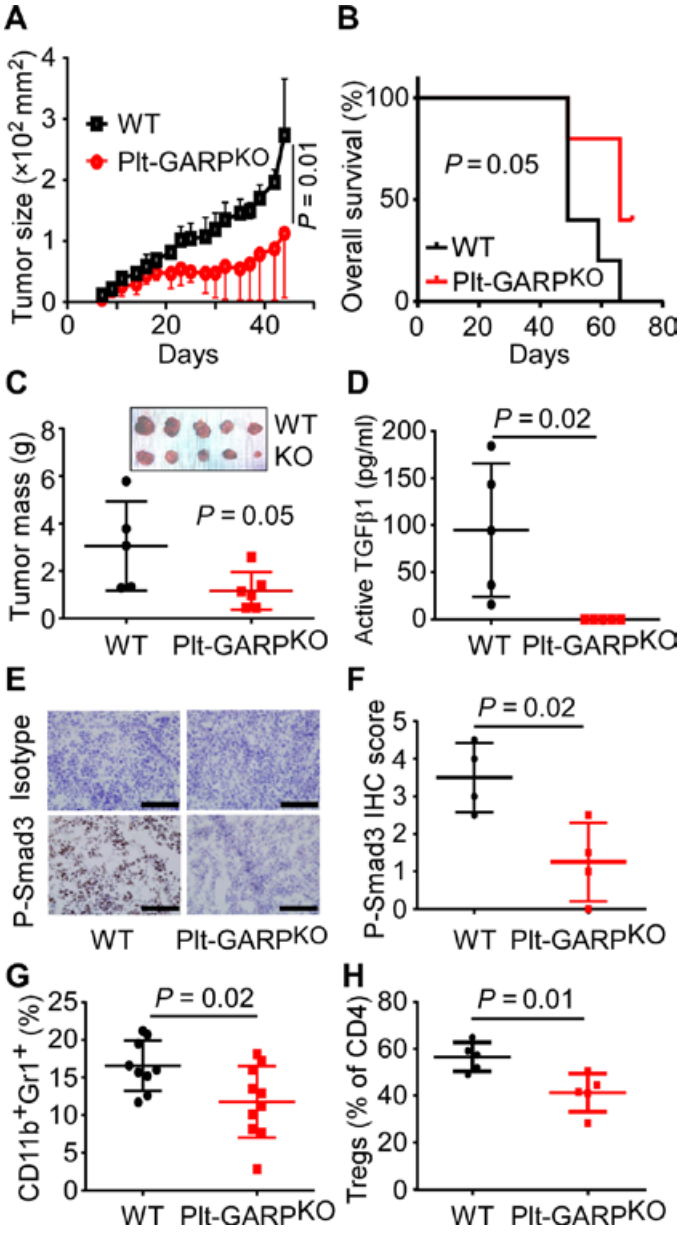

Fig. 7. Targeting platelet-derived GARP-TGFβ complex results in reduction of TGFβ activity in the tumor microenvironment and protection against colon cancer. (**A**) WT or Plt-GARP^{KO} mice ($n = 5$ per group) were injected in the right flank with 1×10^6 MC38 colon cancer cells. Tumor size was measured every 3 days with digital vernier caliper. (**B**) Kaplan-Meier survival curve in MC38-bearing mice ($n = 5$ per group). (**C**) In a separate experiment, 6 weeks after MC38 injection, mice were sacrificed and the primary tumors were resected and weighed. The inset shows the images of primary tumors resected from mice 6 weeks after injection. (**D**) Serum was obtained from mice 6 weeks after MC38 injection, and active TGFβ1 was measured by ELISA. (**E**) IHC for p-Smad2/3 in MC38 tumors from indicated mice; representative images are shown. Scale bar, 12.5 μm. (**F**) Independent histopathological quantification of p-Smad2/3 staining intensity from (E) ($n = 4$ per group). (**G**) Flow cytometric analysis of peripheral blood myeloid–derived suppressor cells. (**H**) Percentage of T_{reg} cells ($CD25^+$ $Foxp3^+$) in the $CD4^+$ tumor-infiltrating lymphocytes from the indicated mice. Repeated-measures two-way ANOVA was used in (A); Kaplan-Meier curves and log-rank tests were used in (B). Two-tailed independent Student's *t* test was used in (C), (D), (F), (G), and (H). Data are means ± SEM.

tumor microenvironment, whose source so far has been attributed mostly to cancer cells and other stromal cells (*32*, *47*). This study revealed that platelet-related TGFβ activation contributes dominantly to this immunosuppressive pool in cancer via cell surface TGFβ-docking receptor GARP. This conclusion is supported by enhanced tumor-specific T cell immunity in mice with platelet-specific deletion of GARP or its critical molecular chaperone gp96.

Platelets are known to respond to tissue injury and infection. Upon activation, platelets self-aggregate and release a variety of soluble factors to promote tissue homeostasis (*48*). Multiple molecules in the PR have immunomodulatory properties (*2*, *23*). We identified TGFβ and lactate to be the major mediators. Platelet contribution to extracellular TGFβ can be accomplished through the release of prestored TGFβ in the cytoplasmic granules or via the ability of surface GARP on platelets to snatch and bind TGFβ from nonplatelet sources. Our study demonstrates that platelet-intrinsic GARP plays the most dominant role in activating TGFβ and thus likely contributes significantly to the immunosuppressive molecular hallmarks in the cancer microenvironment. Platelets are known to express GARP constitutively and to up-regulate its expression upon activation. The other cells that are known to express GARP are T_{reg} cells. We found that conditional deletion of GARP from T_{reg} cells is not as effective as platelet-specific KO of GARP in supporting ACT (fig. S10). Future studies are necessary to understand the roles and mechanisms of platelets broadly and the GARP-TGFβ axis specifically in regulating the biology of endogenous T cells in the tumor microenvironment such as differentiation and functionality.

There have been inconsistent reports on the systemic TGFβ level as a reliable biomarker for cancer, inflammation, and other conditions (*49*–*51*). Consistent with the literature, we found that active TGFβ level is low in the plasma; however, after platelet activation and coagulation, serum active TGFβ level increased significantly. It has been unclear where active TGFβ in the serum comes from and what is the underlying mechanism of activation. The current study has resolved these long-standing puzzles. By genetically deleting GARP or TGFβ1 from platelets selectively, we have now reached several important conclusions: (i) Platelet-specific GARP is responsible for TGFβ activation because little active TGFβ can be detected in the sera of mice with platelet-specific deletion of either GARP or gp96; (ii) LTGFβ in the blood (both serum and plasma) is primarily supplied by platelets as revealed by platelet-specific TGFβ1 KO mice and platelet depletion studies; and (iii) the serum level of active TGFβ depends on the cell surface GARP-TGFβ complex, not the total level of soluble LTGFβ. Such evidence derived from the fact that, although platelet-specific TGFβ1 KO mice have drastically reduced soluble LTGFβ1 in the serum, they remain capable of making a comparable level of active TGFβ.

Consistent with the genetic studies, pharmacological platelet inhibitors were found to be effective in potentiating ACT of melanoma. It is also possible that platelet inhibitors may have other antitumor mechanisms, such as blocking angiogenesis and immunosuppressive prostaglandins (*52*), which contribute to their antitumor activity. Notwithstanding, our work demonstrated that the AP agents alone do not have significant antitumor activity in our model. In addition, the improved antitumor effect was abolished when IFNγ was removed from the system, demonstrating that platelet inhibition promotes antitumor efficacy via an immunologically based mechanism. Given the clinical availability of multiple platelet inhibitors targeting distinct pathways of platelet activation, we hope that our study will catalyze a

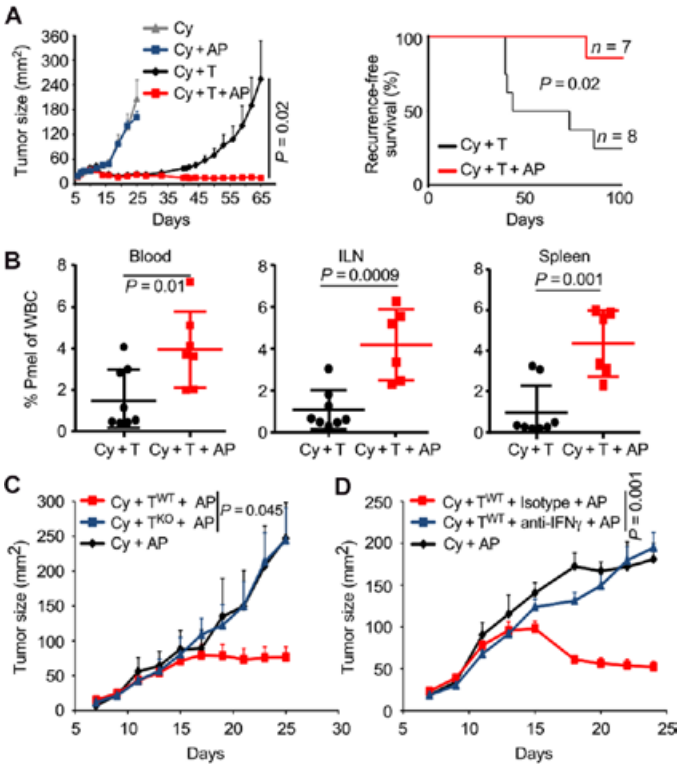

Fig. 8. Pharmacological inhibition of platelets enhances ACT of cancer. (**A**) C57BL/6 mice were inoculated with B16-F1 subcutaneously on day 0, given Cy on day 7, followed by adoptive therapy with activated Pmel cells on day 8 (Cy + T; $n = 7$ to 8 per group) or not (Cy; $n = 4$ to 5 per group). Each of the above groups of mice received concurrent aspirin and clopidogrel or water. Left: Average tumor growth curves. Right: Recurrence-free survival. (**B**) Pmel cells in the peripheral blood (day +62 after tumor inoculation), ILNs, and spleens (upon sacrifice) of mice in different treatment groups were enumerated by flow cytometry. (**C**) C57BL/6 mice were inoculated with B16-F1 subcutaneously on day 0. Mice were lymphodepleted with Cy on day 9, followed by adoptive transfer of either activated Pmel WT cells or IFNγ$^{-/-}$ Pmel cells on day 10. AP were given as described in (A) (T^{WT}, WT Pmel cells; T^{KO}, IFNγ KO Pmel cells; $n = 4$ to 10 per group). (**D**) C57BL/6 mice were inoculated with B16-F1 subcutaneously on day 0. Mice were lymphodepleted with Cy on day 9, followed by adoptive transfer of activated Pmel cells on day 10. IFNγ-neutralizing antibody (clone XMG1.2, BioXCell) was delivered intraperitoneally at 100 μg per mouse every other day starting on day 11 until sacrifice. AP were given as described in (A) ($n = 4$ to 8 per group). Repeated-measures two-way ANOVA was used to compare the tumor growth curves in (A), (C), and (D). Kaplan-Meier curves and log-rank tests were used for relapse-free survival analysis. Two-tailed independent Student's *t* test was used in (B). Data are means ± SEM.

systematic effort to optimize cancer immunotherapy by simultaneously blocking platelets and immune checkpoint molecules in prospective clinical trials.

Platelets have also been shown to play positive roles in the homing of T cells to sites of inflammation, to mediate a positive feedback loop of T cell recruitment through T cell activation via platelet CD40 (*14*), and to promote liver cancer induced by dysfunctional liver-directed T cell responses (*53*). The complexity of the roles of platelets in the tumor microenvironment is also illustrated by the finding that platelets can be extensively educated by tumor cells to uptake tumor-associated biomolecules such as RNAs (*54*). However, our work strongly indicates that the net effect of platelets in cancer patients is to promote immune evasion of cancer. Physiologically, cancer represents a chronic nonhealing wound, whose progression and metastasis are inevitably accompanied by vascular endothelial damage and local exposure to multiple platelet activators (*1*, *48*). Our study thus suggests that cancer hijacks the tissue-repairing and hemostatic functions of platelets to suppress antitumor T cell immunity. A combination therapy with AP agents and immunotherapeutical modalities may thus represent a new paradigm for rational treatment of cancer in the future.

Last, although this study uncovers major suppressive molecules in the PR in an unbiased approach, such molecules were identified using in vitro experiments and translated to in vivo models using a hypothesis-driven approach. For example, TGFβ was identified as a major suppressive molecule secreted by platelets and this was validated in tumor mouse models. Although TGFβ was shown to be of biological relevance, it remains possible that, in vivo, the PR has a different composition and molecules other than TGFβ could play stronger roles. Furthermore, standard-of-care immunological therapies for melanoma at this point in time are mostly based on checkpoint inhibition {PD ligand–1 [PD(L)-1] and cytotoxic T lymphocyte–associated antigen 4 (CTLA-4)}. Various forms of adoptive T cell transfer have shown very promising results in clinical trials but are still under investigation and not yet standard of care. Our mouse models are based on adoptive T cell transfer and not checkpoint inhibition, so understanding these differences in immunological therapies is important when designing future studies.

MATERIALS AND METHODS

Study design

In this study, an unbiased approach was used to identify the major T cell suppressors in the PR. This was achieved by fractionating the releasate as described below, screening for the active fractions, and subsequently identifying the active molecules. End points for in vitro experiments included T cell proliferation, blastogenesis, and cytokine production and activation markers. The clinical relevance of the in vitro findings was investigated in vivo. For in vivo experiments, each group contained between 4 and 10 mice; this provided enough power and validity to detect biologically relevant phenomena while ensuring the use of minimal numbers of mice necessary as per the guidelines of the Medical University of South Carolina (MUSC) Institutional Animal Care and Use Committee. Commercially obtained mice were randomly assigned to different groups in each experiment. For in house–bred, genetically engineered mice, littermates were assigned for comparison groups. Efficacy end points for in vivo experiments were tumor size, T cell engraftment, and cytokine secretion. Mice were sacrificed when they showed signs of severe moribund disease. Measurement techniques for in vitro and in vivo experiments are indicated accordingly for each experiment. All experiments were performed at least two times. Numbers of key experiments were indicated in the figure legend. Blinding was not feasible for most of the in vitro experiments and was not critical because data collection was mostly through objective measures such as flow cytometry. The surgical pathologist scoring immunohistochemical (IHC) stains was blinded to the identity of the samples. For in vivo experiments, researchers were blinded because genetically modified mice are not readily identifiable, as their outer appearances are comparable and they share the same cages. In Fig. 3, blinding was maintained for the CD4 T_H17 adoptive transfer experiment, but not the CD8 transfer one.

Mice

Platelet-specific *Hsp90b1* KO mice were generated by crossing *Pf4-cre* mice (*55*) with *Hsp90b1*$^{flox/flox}$ mice (*21*, *56*). *Lrrc32*$^{flox/flox}$ mice were obtained from Riken (Japan) (*20*). *Tgfb1*$^{flox/flox}$, *Foxp3*$^{eGFP\text{-}CreERT2}$, Pmel-1, and TRP1 mice were purchased from the Jackson Laboratory. *Ifng*$^{-/-}$ Pmel-1 mice were a gift from S. Mehrotra (MUSC). All animal experiments were conducted under approved protocols by the Institutional Animal Care and Use Committee at MUSC.

Ex vivo stimulation of tumor-draining lymph nodes

ILNs from tumor-bearing mice were isolated, mashed in cold phosphate-buffered saline (PBS), and filtered. One million cells per well were cultured in 96-well plates for 4 hours in the presence of phorbol 12-myristate 13-acetate (PMA) (500 ng/ml) and ionomycin (1.5 μg/ml), or hgp100 peptide (Lys-Val-Pro-Arg-Asn-Gln-Asp-Trp-Leu, 25–33) (5 μg/ml) for melanoma-draining lymph nodes. Brefeldin A (BD Biosciences) was added to the cells in all experiments.

Preparation of releasate from activated platelets

Mice were anesthetized, and blood was withdrawn to a 5-ml tube containing another 0.5 ml of acid citrate dextrose (ACD) buffer [39 mM citric acid, 75 mM sodium citrate, 135 mM dextrose, and prostaglandin E_1 (1 μg/ml) (pH 7.4)]. Samples were centrifuged for 10 min at 100*g*, and the upper layer of platelet-rich plasma was collected. Platelets were washed twice with citrate washing buffer [128 mM NaCl, 11 mM glucose, 7.5 mM Na_2HPO_4, 4.8 mM sodium citrate, 4.3 mM NaH_2PO_4, 2.4 mM citric acid, 0.35% bovine serum albumin, and prostaglandin E_1 (50 ng/ml) (pH 6.5)], then resuspended in RPMI 1640, enumerated by a blood cell counter, and diluted to a final concentration of 1×10^8/ml. Purified platelets were incubated with thrombin (1 IU/ml) for 45 min at 37°C (125 rpm). Stimulated platelets were sedimented by centrifugation at 3200*g* for 15 min, and supernatant was collected. Microvesicles (MVs) were collected by centrifugation at 25,000*g* and resuspension in PBS in the same volume as the original PR volume. For human platelet secretome, platelets from healthy donors were obtained from the blood bank at MUSC, resuspended in ACD buffer at room temperature, and then activated as above.

Size-based and anion exchange fractionation

PR fractionation was carried out using a Pharmacia Akta–fast performance liquid chromatography system, and columns were purchased from GE Healthcare. The first fractionation was based on size by loading PR onto a Superdex 200 column and eluting with PBS or RPMI 1640 (Gibco). The active fractions were pooled and dialyzed with phosphate buffer (20 mM; pH 7.2). The resulted material was then loaded onto a diethylaminoethyl (DEAE) column and eluted with a linear gradient of NaCl from 0 to 1 M.

NMR-based metabolite profiling

Human PR was prepared at concentrations of 2×10^9/ml and fractionated by size exclusion chromatography, followed by anion exchange chromatography. Fractions were eluted with sodium phosphate buffer (pH 7.0; 20 mM final concentration) containing sodium 3-trimethylsilyl-2,2,3,3-d_4-propionate (TSP; 0.1 mM final concentration) and 10% D_2O. NMR data were collected at 298 K on a Bruker Avance III 600 MHz NMR spectrometer (Bruker BioSpin Inc.) equipped with a 5-mm cryogenically cooled QCI-inverse probe. Solvent suppression was achieved using the excitation sculpting scheme (*57*). Typically, one-dimensional (1D) ^{1}H NMR spectra with a 7-s recycle delay were acquired with a total of 128 transients in addition to four dummy scans. Real data points (32,768) were collected across a spectral width of 12 parts per million (ppm) (acquisition time, 2.27 s). Data were zero-filled to twice the original data set size, manually phased, and automatically baseline-corrected using TopSpin 3.1 software (Bruker BioSpin Inc., Billerica, MA), and a 1.0-Hz line-broadening apodization was applied before spectral analysis. The singlet produced by the known quantity of the TSP methyl groups was used as an internal standard for chemical shift referencing (set to 0 ppm) and quantification.

Metabolite assignments were established after comparison of chemical shifts and spin-spin couplings with reference spectra as implemented in the Chenomx NMR Suite (Chenomx Inc., Edmonton, Alberta, Canada) profiling software (version 7.72). Specifically, quantification was achieved using the Chenomx 600 MHz metabolite library (version 8). Confirmatory 1D ^{31}P and 2D ^{1}H,^{13}C-multiplicity–edited heteronuclear single quantum correlation spectra with adiabatic ^{13}C inversion, refocusing, and decoupling were recorded for selected PR fractions to enhance metabolite identification by comparison of ^{13}C chemical shifts with the biological magnetic resonance data bank. Concentration of LA was then quantified by an L-lactate assay kit (Eton Bioscience).

In vitro T cell culture suppression assay of PR

$CD4^+$ and $CD8^+$ T cells were purified using magnetic beads to a purity of ≥95%. Cells (1×10^5) were cultured in 96-well plates precoated with anti-CD3ε antibody (3 μg/ml) in the presence of IL-2 (100 U/ml) and soluble anti-CD28 (2 μg/ml), together with either media or PR. On day 3 of culture, T cells were stimulated with PMA (500 ng/ml)/ionomycin (1.5 μg/ml) or hgp100 peptide 25–33 (5 μg/ml) for 4 hours in the presence of GolgiPlug (BD Biosciences), followed by staining for relevant markers. TGFβ receptor signaling was blocked using the combination of an ALK5 inhibitor (SB431542, Selleckchem) at 20 μM and anti-TGFβ antibody (clone MAB1835, R&D Systems) at 2 μg/ml. LA activity was inhibited by blocking the monocarboxylate transporter using α-cyano-4-hydroxycinnamic acid (C2020, Sigma-Aldrich). For carboxyfluorescein diacetate succinimidyl ester (CFSE) dilution assays, cells were labeled with 5 μM CFSE for 10 min at room temperature before culture on day 0. Flow cytometry was then performed, and the data were analyzed and displayed with FlowJo software. Suppression index by PR was calculated as percentage of undivided cells treated with a given fraction of PR/percentage of undivided cells in the control media.

Adoptive T cell therapy

Treatment of B16-F1 melanoma by adoptive transfer of ex vivo activated Pmel T cells was done as described previously (*29*). To test the effect of AP agents on ACT, we administered clopidogrel by oral gavage 3 days after T cell transfer and then every 48 hours until day 25. Aspirin was administered through drinking water (150 mg/liter) starting 2 days before T cell transfer and was replaced every 48 hours afterward. For TRP1 T_H17 T cell therapy, single-cell suspensions of splenocytes from *Rag1*$^{-/-}$ TRP1 mice (*27*) were seeded with irradiated C57BL/6 splenocytes pulsed with TRP1 106–130 peptide (SGHNCGTCRPGWRGAACNQKILTVR; American Peptide). To obtain T_H17-polarized cells, we added recombinant human IL-6 [100 ng/ml; National Institutes of Health (NIH)], TGFβ1 (30 ng/ml; BioLegend), IL-1β (10 ng/ml; Shenandoah), and anti–IL-4 and anti-IFNγ antibodies (10 μg/ml; BioXCell) to the cultures. On the second day of culture, complete medium containing recombinant human IL-2

and IL-23 (40 ng/ml; PeproTech) was added. Where appropriate, human PR was added at 100% on days 0, 2, and 4. Cells were cultured for 5 days before experimentation. C57BL/6 mice were injected subcutaneously with 4×10^5 B16-F10 melanoma cells and treated 10 days later with TRP1-specific $CD4^+$ T cells. Recipient mice were lymphodepleted using 5-gray total body irradiation on the day before cell transfer. Tumor growth was measured using calipers, and the products of the perpendicular diameters were recorded. In some experiments, IFNγ-neutralizing antibody (clone XMG1.2, BioXCell) or isotype control antibody was administered via intraperitoneal injection at 100 μg per mouse every other day starting on day 12 until sacrifice (*58*). The adoptive T cell transfer experiment with *Ifng* KO Pmel-1 cells was done identically as above except that Pmel cells were isolated from *Ifng* KO Pmel-1 mice (*59*). For some experiments, adoptive transfer was supplemented with exogenous IL-2–anti–IL-2 complexes on days 0, 2, 4, and 6 after transfer in the absence of lymphodepletion (*60*). Briefly, 1.5 μg of human IL-2 (National Cancer Institute Biological Resources Branch Preclinical Repository) was mixed with 7.5 μg of anti–IL-2 monoclonal antibody (clone 5355, R&D Systems) for 15 min at room temperature. Cytokine complexes were administered via intraperitoneal injections.

Platelet depletion and serum collection for TGFβ ELISA

WT mice were given one dose of rabbit anti-mouse thrombocyte polyclonal sera (1:40, Cedarlane) at 500 μl per mouse intraperitoneally in sterile-filtered PBS. Blood was collected at 0, 24, 48, and 72 hours. Serum was harvested via coagulation and centrifugation (12,000*g*).

Measurement of TGFβ via ELISA

Mouse serum or plasma samples were collected by pricking the lateral tail vein. Capture ELISA for TGFβ1 was performed according to the manufacturer's instructions (BioLegend). Total TGFβ1 was measured after acidic activation using 1 M HCl for 10 min at room temperature.

Activation of human T cells

Human samples were isolated from buffy coats (Pennsylvania Plasma). $CD8^+$ T cells were positively enriched from human peripheral blood mononuclear cells, followed by negative isolation of $CD4^+$ T cells using magnetic isolation kits (Invitrogen). Cells were then stimulated with anti-CD3/anti-ICOS beads (Dynal) at 10:1 T cell/bead ratio for 4 days. IL-2 (100 IU/ml; NIH) was added to the T cell cultures. Human PR was added on day 0 and every other day thereafter. Cells were assayed on day 7 for cytokine production and phenotype.

MC38 model

MC38 tumor cells were obtained from Y.-X. Fu (University of Texas Southwestern Medical Center). WT or Plt-$GARP^{KO}$ mice were injected in the right flank with 1×10^6 MC38 colon cancer cells. Tumor size was measured with digital caliper kinetically. Tumor-infiltrating lymphocytes were isolated from fresh primary tumors by density gradient after single-cell suspensions were made with mechanical dissociation and enzymatic digestion (deoxyribonuclease and collagenase).

Immunohistochemistry

For p-Smad2/3 stain on fresh-frozen MC38 tumors, 5-μm tumor sections were fixed with 4% paraformaldehyde followed by incubation with 3% H_2O_2. To minimize nonspecific staining, we incubated the sections with the appropriate animal serum for 20 min at room temperature, followed by incubation with primary anti–p-Smad2/3 antibody (EP823Y, Abcam) overnight at 4°C. Staining with secondary antibodies (Vectastain ABC Kit) was then performed before development using DAB substrate (SK-4100, Vector Labs). The staining intensity of p-Smad2/3 was graded as follows, with the sample identity blinded: 0, negative; 1, faint; 2, moderate; 3, strong but less intense than 4; 4, intense.

Statistical analysis

Two-sided, two-sample Student's *t* tests were used for all comparisons involving continuous dependent variables and categorical independent variables using Excel software. The variances were compared between groups using an *F* test. The Student's *t* test was then implemented assuming equal or unequal variances (i.e., if the *F* test *P* value was less than 0.05, then unequal variances were assumed). For tumor curves, two-way repeated-measures analysis of variance (ANOVA) was used. For dose-response correlations between continuous dependent and independent variables in Figs. 2 and 4, Spearman's rank-order correlation test was used to determine rho (ρ). Kaplan-Meier curves were compared using log-rank tests. Error bars represent SEM. NS denotes statistically nonsignificant difference.

SUPPLEMENTARY MATERIALS

immunology.sciencemag.org/cgi/content/full/2/11/eaai7911/DC1

Table S1. Source data for all the figure panels with small *n* ($n < 20$).
Fig. S1. *Pf4-cre-Hsp90b1*$^{flox/flox}$ (KO) mice show no noticeable immune dysfunction at baseline.
Fig. S2. PR, but not MVs, directly suppresses T cell proliferation and differentiation in vitro.
Fig. S3. Immune suppression by PR is independent of TCR signaling and specific to lymphocytes.
Fig. S4. T cell–suppressive function of the whole PR is significantly, but not completely, neutralized by blocking TGFβ pathway.
Fig. S5. A small–molecular weight, heat-stable, proteinase K–resistant T cell–suppressive fraction is shared between human and mouse PRs.
Fig. S6. TGFβ and LA in the PR are the major suppressors of $CD8^+$ T cell activation.
Fig. S7. TGFβ contained in the PR drives Foxp3 expression and up-regulates p-Smad2/3.
Fig. S8. TGFβ1, but not LA, abrogates CD8-mediated tumor control.
Fig. S9. Platelet depletion has no effect on serum LA concentration.
Fig. S10. Inducible deletion of GARP from $Foxp3^+$ T_{reg} cells does not improve ACT of melanoma.
Fig. S11. Sample staining and isotype controls for flow cytometry.

REFERENCES AND NOTES

1. K. Jurk, B. E. Kehrel, Platelets: Physiology and biochemistry. *Semin. Thromb. Hemost.* **31**, 381–392 (2005).
2. A. S. Weyrich, G. A. Zimmerman, Platelets: Signaling cells in the immune continuum. *Trends Immunol.* **25**, 489–495 (2004).
3. R. Möhle, D. Green, M. A. S. Moore, R. L. Nachman, S. Rafii, Constitutive production and thrombin-induced release of vascular endothelial growth factor by human megakaryocytes and platelets. *Proc. Natl. Acad. Sci. U.S.A.* **94**, 663–668 (1997).
4. L. J. Gay, B. Felding-Habermann, Contribution of platelets to tumour metastasis. *Nat. Rev. Cancer* **11**, 123–134 (2011).
5. E. Sierko, M. Z. Wojtukiewicz, Platelets and angiogenesis in malignancy. *Semin. Thromb. Hemost.* **30**, 95–108 (2004).
6. R. L. Stone, A. M. Nick, I. A. McNeish, F. Balkwill, H. D. Han, J. Bottsford-Miller, R. Rupairmoole, G. N. Armaiz-Pena, C. V. Pecot, J. Coward, M. T. Deavers, H. G. Vasquez, D. Urbauer, C. N. Landen, W. Hu, H. Gershenson, K. Matsuo, M. M. K. Shahzad, E. R. King, I. Tekedereli, B. Ozpolat, E. H. Ahn, V. K. Bond, R. Wang, A. F. Drew, F. Gushiken, D. Lamkin, K. Collins, K. DeGeest, S. K. Lutgendorf, W. Chiu, G. Lopez-Berestein, V. Afshar-Kharghan, A. K. Sood, Paraneoplastic thrombocytosis in ovarian cancer. *N. Engl. J. Med.* **366**, 610–618 (2012).
7. S. Karpatkin, E. Pearlstein, C. Ambrogio, B. S. Coller, Role of adhesive proteins in platelet tumor interaction in vitro and metastasis formation in vivo. *J. Clin. Invest.* **81**, 1012–1019 (1988).
8. D. Schumacher, B. Strilic, K. K. Sivaraj, N. Wettschureck, S. Offermanns, Platelet-derived nucleotides promote tumor-cell transendothelial migration and metastasis via $P2Y_2$ receptor. *Cancer Cell* **24**, 130–137 (2013).

9. M. Labelle, S. Begum, R. O. Hynes, Direct signaling between platelets and cancer cells induces an epithelial-mesenchymal-like transition and promotes metastasis. *Cancer Cell* **20**, 576–590 (2011).
10. H.-G. Kopp, T. Placke, H. R. Salih, Platelet-derived transforming growth factor-β down-regulates NKG2D thereby inhibiting natural killer cell antitumor reactivity. *Cancer Res.* **69**, 7775–7783 (2009).
11. P. Haselmayer, L. Grosse-Hovest, P. von Landenberg, H. Schild, M. P. Radsak, TREM-1 ligand expression on platelets enhances neutrophil activation. *Blood* **110**, 1029–1035 (2007).
12. B. Xiang, G. Zhang, L. Guo, X.-A. Li, A. J. Morris, A. Daugherty, S. W. Whiteheart, S. S. Smyth, Z. Li, Platelets protect from septic shock by inhibiting macrophage-dependent inflammation via the cyclooxygenase 1 signalling pathway. *Nat. Commun.* **4**, 2657 (2013).
13. P. Duffau, J. Seneschal, C. Nicco, C. Richez, E. Lazaro, I. Douchet, C. Bordes, J.-F. Viallard, C. Goulvestre, J.-L. Pellegrin, B. Weil, J.-F. Moreau, F. Batteux, P. Blanco, Platelet CD154 potentiates interferon-α secretion by plasmacytoid dendritic cells in systemic lupus erythematosus. *Sci. Transl. Med.* **2**, 47ra63 (2010).
14. B. D. Elzey, J. Tian, R. J. Jensen, A. K. Swanson, J. R. Lees, S. R. Lentz, C. S. Stein, B. Nieswandt, Y. Wang, B. L. Davidson, T. L. Ratliff, Platelet-mediated modulation of adaptive immunity. A communication link between innate and adaptive immune compartments. *Immunity* **19**, 9–19 (2003).
15. A. Verschoor, M. Neuenhahn, A. A. Navarini, P. Graef, A. Plaumann, A. Seidlmeier, B. Nieswandt, S. Massberg, R. M. Zinkernagel, H. Hengartner, D. H. Busch, A platelet-mediated system for shuttling blood-borne bacteria to CD8α$^+$ dendritic cells depends on glycoprotein GPIb and complement C3. *Nat. Immunol.* **12**, 1194–1201 (2011).
16. T. Junt, H. Schulze, Z. Chen, S. Massberg, T. Goerge, A. Krueger, D. D. Wagner, T. Graf, J. E. Italiano Jr., R. A. Shivdasani, U. H. von Andrian, Dynamic visualization of thrombopoiesis within bone marrow. *Science* **317**, 1767–1770 (2007).
17. S. P. Jackson, Arterial thrombosis—Insidious, unpredictable and deadly. *Nat. Med.* **17**, 1423–1436 (2011).
18. S. Offermanns, Activation of platelet function through G protein–coupled receptors. *Circ. Res.* **99**, 1293–1304 (2006).
19. D. Q. Tran, J. Andersson, R. Wang, H. Ramsey, D. Unutmaz, E. M. Shevach, GARP (LRRC32) is essential for the surface expression of latent TGF-β on platelets and activated FOXP3$^+$ regulatory T cells. *Proc. Natl. Acad. Sci. U.S.A.* **106**, 13445–13450 (2009).
20. J. P. Edwards, H. Fujii, A. X. Zhou, J. Creemers, D. Unutmaz, E. M. Shevach, Regulation of the expression of GARP/latent TGF-β1 complexes on mouse T cells and their role in regulatory T cell and Th17 differentiation. *J. Immunol.* **190**, 5506–5515 (2013).
21. M. Staron, S. Wu, H. Feng, A. Stojanovic, X. Du, R. Bona, B. Liu, Z. Li, Heat-shock protein gp96/grp94 is an essential chaperone for the platelet glycoprotein Ib-IX-V complex. *Blood* **117**, 7136–7144 (2011).
22. Y. Zhang, B. X. Wu, A. Metelli, J. E. Thaxton, F. Hong, S. Rachidi, E. Ansa-Addo, S. Sun, C. Vasu, Y. Yang, B. Liu, Z. Li, GP96 is a GARP chaperone and controls regulatory T cell functions. *J. Clin. Invest.* **125**, 859–869 (2015).
23. L. Senzel, D. V. Gnatenko, W. F. Bahou, The platelet proteome. *Curr. Opin. Hematol.* **16**, 329–333 (2009).
24. G. L. Reed, M. L. Fitzgerald, J. Polgár, Molecular mechanisms of platelet exocytosis: Insights into the "secrete" life of thrombocytes. *Blood* **96**, 3334–3342 (2000).
25. S. A. Rosenberg, N. P. Restifo, Adoptive cell transfer as personalized immunotherapy for human cancer. *Science* **348**, 62–68 (2015).
26. P. Sharma, J. P. Allison, Immune checkpoint targeting in cancer therapy: Toward combination strategies with curative potential. *Cell* **161**, 205–214 (2015).
27. P. Muranski, A. Boni, P. A. Antony, L. Cassard, K. R. Irvine, A. Kaiser, C. M. Paulos, D. C. Palmer, C. E. Touloukian, K. Ptak, L. Gattinoni, C. Wrzesinski, C. S. Hinrichs, K. W. Kerstann, L. Feigenbaum, C.-C. Chan, N. P. Restifo, Tumor-specific Th17–polarized cells eradicate large established melanoma. *Blood* **112**, 362–373 (2008).
28. W. W. Overwijk, M. R. Theoret, S. E. Finkelstein, D. R. Surman, L. A. de Jong, F. A. Vyth-Dreese, T. A. Dellemijn, P. A. Antony, P. J. Spiess, D. C. Palmer, D. M. Heimann, C. A. Klebanoff, Z. Yu, L. N. Hwang, L. Feigenbaum, A. M. Kruisbeek, S. A. Rosenberg, N. P. Restifo, Tumor regression and autoimmunity after reversal of a functionally tolerant state of self-reactive CD8$^+$ T cells. *J. Exp. Med.* **198**, 569–580 (2003).
29. M. P. Rubinstein, C. A. Cloud, T. E. Garrett, C. J. Moore, K. M. Schwartz, C. B. Johnson, D. H. Craig, M. L. Salem, C. M. Paulos, D. J. Cole, Ex vivo interleukin-12-priming during CD8$^+$ T cell activation dramatically improves adoptive T cell transfer antitumor efficacy in a lymphodepleted host. *J. Am. Coll. Surg.* **214**, 700–707 (2012).
30. J. E. Murphy-Ullrich, M. Poczatek, Activation of latent TGF-β by thrombospondin-1: Mechanisms and physiology. *Cytokine Growth Factor Rev.* **11**, 59–69 (2000).
31. K. Fischer, P. Hoffmann, S. Voelkl, N. Meidenbauer, J. Ammer, M. Edinger, E. Gottfried, S. Schwarz, G. Rothe, S. Hoves, K. Renner, B. Timischl, A. Mackensen, L. Kunz-Schughart, R. Andreesen, S. W. Krause, M. Kreutz, Inhibitory effect of tumor cell-derived lactic acid on human T cells. *Blood* **109**, 3812–3819 (2007).
32. O. R. Colegio, N.-Q. Chu, A. L. Szabo, T. Chu, A. M. Rhebergen, V. Jairam, N. Cyrus, C. E. Brokowski, S. C. Eisenbarth, G. M. Phillips, G. W. Cline, A. J. Phillips, R. Medzhitov, Functional polarization of tumour-associated macrophages by tumour-derived lactic acid. *Nature* **513**, 559–563 (2014).
33. C. B. Johnson, B. P. Riesenberg, B. R. May, S. C. Gilreath, G. Li, K. F. Staveley-O'Carroll, E. Garrett-Mayer, S. Mehrotra, D. J. Cole, M. P. Rubinstein, Effector CD8$^+$ T-cell engraftment and antitumor immunity in lymphodepleted hosts is IL7Rα dependent. *Cancer Immunol. Res.* **3**, 1364–1374 (2015).
34. R. K. Assoian, A. Komoriya, C. A. Meyers, D. M. Miller, M. B. Sporn, Transforming growth factor-β in human platelets. Identification of a major storage site, purification, and characterization. *J. Biol. Chem.* **258**, 7155–7160 (1983).
35. R. Wang, J. Zhu, X. Dong, M. Shi, C. Lu, T. A. Springer, GARP regulates the bioavailability and activation of TGFβ. *Mol. Biol. Cell* **23**, 1129–1139 (2012).
36. J. Cuende, S. Liénart, O. Dedobbeleer, B. van der Woning, G. De Boeck, J. Stockis, C. Huygens, D. Colau, J. Somja, P. Delvenne, M. Hannon, F. Baron, L. Dumoutier, J.-C. Renauld, H. De Haard, M. Saunders, P. G. Coulie, S. Lucas, Monoclonal antibodies against GARP/TGF-β1 complexes inhibit the immunosuppressive activity of human regulatory T cells in vivo. *Sci. Transl. Med.* **7**, 284ra56 (2015).
37. A. Meyer, W. Wang, J. Qu, L. Croft, J. L. Degen, B. S. Coller, J. Ahamed, Platelet TGF-β1 contributions to plasma TGF-β1, cardiac fibrosis, and systolic dysfunction in a mouse model of pressure overload. *Blood* **119**, 1064–1074 (2012).
38. S. F. Ngiow, A. Young, N. Jacquelot, T. Yamazaki, D. Enot, L. Zitvogel, M. J. Smyth, A threshold level of intratumor CD8$^+$ T-cell PD1 expression dictates therapeutic response to anti-PD1. *Cancer Res.* **75**, 3800–3811 (2015).
39. B. Homet Moreno, J. M. Zaretsky, A. Garcia-Diaz, J. Tsoi, G. Parisi, L. Robert, K. Meeth, A. Ndoye, M. Bosenberg, A. T. Weeraratna, T. G. Graeber, B. Comin-Anduix, S. Hu-Lieskovan, A. Ribas, Response to programmed cell death-1 blockade in a murine melanoma syngeneic model requires costimulation, CD4, and CD8 T cells. *Cancer Immunol. Res.* **4**, 845–857 (2016).
40. A. Wallace, V. Kapoor, J. Sun, P. Mrass, W. Weninger, D. F. Heitjan, C. June, L. R. Kaiser, L. E. Ling, S. M. Albelda, Transforming growth factor-β receptor blockade augments the effectiveness of adoptive T-cell therapy of established solid cancers. *Clin. Cancer Res.* **14**, 3966–3974 (2008).
41. J. G. Quatromoni, Y. Wang, D. D. Vo, L. F. Morris, A. R. Jazirehi, W. McBride, T. Chatila, R. C. Koya, J. S. Economou, T cell receptor (TCR)-transgenic CD8 lymphocytes rendered insensitive to transforming growth factor beta (TGFβ) signaling mediate superior tumor regression in an animal model of adoptive cell therapy. *J. Transl. Med.* **10**, 127 (2012).
42. L. Zhang, Z. Yu, P. Muranski, D. C. Palmer, N. P. Restifo, S. A. Rosenberg, R. A. Morgan, Inhibition of TGF-β signaling in genetically engineered tumor antigen-reactive T cells significantly enhances tumor treatment efficacy. *Gene Ther.* **20**, 575–580 (2013).
43. A. D. Michelson, Antiplatelet therapies for the treatment of cardiovascular disease. *Nat. Rev. Drug Discov.* **9**, 154–169 (2010).
44. H. Zhou, E. C. Gabazza, H. Takeya, H. Deguchi, H. Urano, Y. Adachi, K. Suzuki, Prothrombin and its derivatives stimulate motility of melanoma cells. *Thromb. Haemost.* **80**, 407–412 (1998).
45. L. Erpenbeck, M. P. Schön, Deadly allies: The fatal interplay between platelets and metastasizing cancer cells. *Blood* **115**, 3427–3436 (2010).
46. H. M. Pinedo, H. M. W. Verheul, R. J. D'Amato, J. Folkman, Involvement of platelets in tumour angiogenesis? *Lancet* **352**, 1775–1777 (1998).
47. J. Massagué, TGFβ in cancer. *Cell* **134**, 215–230 (2008).
48. G. de Gaetano, Historical overview of the role of platelets in hemostasis and thrombosis. *Haematologica* **86**, 349–356 (2001).
49. D. J. Grainger, P. R. Kemp, J. C. Metcalfe, A. C. Liu, R. M. Lawn, N. R. Williams, A. A. Grace, P. M. Schofield, A. Chauhan, The serum concentration of active transforming growth factor-β is severely depressed in advanced atherosclerosis. *Nat. Med.* **1**, 74–79 (1995).
50. T.-H. Lin, Y.-Y. Shao, S.-Y. Chan, C.-Y. Huang, C.-H. Hsu, A.-L. Cheng, High serum transforming growth factor-β1 levels predict outcome in hepatocellular carcinoma patients treated with sorafenib. *Clin. Cancer Res.* **21**, 3678–3684 (2015).
51. S. F. Shariat, M. Shalev, A. Menesses-Diaz, I. Y. Kim, M. W. Kattan, T. M. Wheeler, K. M. Slawin, Preoperative plasma levels of transforming growth factor beta$_1$ (TGF-β$_1$) strongly predict progression in patients undergoing radical prostatectomy. *J. Clin. Oncol.* **19**, 2856–2864 (2001).
52. S. Zelenay, A. G. van der Veen, J. P. Böttcher, K. J. Snelgrove, N. Rogers, S. E. Acton, P. Chakravarty, M. R. Girotti, R. Marais, S. A. Quezada, E. Sahai, C. Reis e Sousa, Cyclooxygenase-dependent tumor growth through evasion of immunity. *Cell* **162**, 1257–1270 (2015).
53. G. Sitia, R. Aiolfi, P. Di Lucia, M. Mainetti, A. Fiocchi, F. Mingozzi, A. Esposito, Z. M. Ruggeri, F. V. Chisari, M. Iannacone, L. G. Guidotti, Antiplatelet therapy prevents hepatocellular carcinoma and improves survival in a mouse model of chronic hepatitis B. *Proc. Natl. Acad. Sci. U.S.A.* **109**, E2165–E2172 (2012).
54. M. G. Best, N. Sol, I. Kooi, J. Tannous, B. A. Westerman, F. Rustenburg, P. Schellen, H. Verschueren, E. Post, J. Koster, B. Ylstra, N. Ameziane, J. Dorsman, E. F. Smit, H. M. Verheul, D. P. Noske, J. C. Reijneveld, R. J. A. Nilsson, B. A. Tannous, P. Wesseling, T. Wurdinger, RNA-seq of tumor-educated platelets enables blood-based

pan-cancer, multiclass, and molecular pathway cancer diagnostics. *Cancer Cell* **28**, 666–676 (2015).
55. R. Tiedt, T. Schomber, H. Hao-Shen, R. C. Skoda, *Pf4-Cre* transgenic mice allow the generation of lineage-restricted gene knockouts for studying megakaryocyte and platelet function in vivo. *Blood* **109**, 1503–1506 (2007).
56. Y. Yang, B. Liu, J. Dai, P. K. Srivastava, D. J. Zammit, L. Lefrançois, Z. Li, Heat shock protein gp96 is a master chaperone for Toll-like receptors and is important in the innate function of macrophages. *Immunity* **26**, 215–226 (2007).
57. T. L. Hwang, A. J. Shaka, Water suppression that works. Excitation sculpting using arbitrary wave-forms and pulsed-field gradients. *J. Magn. Reson.* **112**, 275–279 (1995).
58. H. Matsushita, A. Hosoi, S. Ueha, J. Abe, N. Fujieda, M. Tomura, R. Maekawa, K. Matsushima, O. Ohara, K. Kakimi, Cytotoxic T lymphocytes block tumor growth both by lytic activity and IFNγ-dependent cell-cycle arrest. *Cancer Immunol. Res.* **3**, 26–36 (2015).
59. D. C. Palmer, C.-C. Chan, L. Gattinoni, C. Wrzesinski, C. M. Paulos, C. S. Hinrichs, D. J. Powell Jr., C. A. Klebanoff, S. E. Finkelstein, R. N. Fariss, Z. Yu, R. B. Nussenblatt, S. A. Rosenberg, N. P. Restifo, Effective tumor treatment targeting a melanoma/melanocyte-associated antigen triggers severe ocular autoimmunity. *Proc. Natl. Acad. Sci. U.S.A.* **105**, 8061–8066 (2008).
60. E. W. Su, C. J. Moore, S. Suriano, C. B. Johnson, N. Songalia, A. Patterson, D. J. Neitzke, K. Andrijauskaite, E. Garrett-Mayer, S. Mehrotra, C. M. Paulos, A. L. Doedens, A. W. Goldrath, Z. Li, D. J. Cole, M. P. Rubinstein, IL-2Rα mediates temporal regulation of IL-2 signaling and enhances immunotherapy. *Sci. Transl. Med.* **7**, 311ra170 (2015).

Acknowledgments: We received technical help from Y. Zhang, F. Hong, E. Ansa-Addo, S. Mehrotra, J. Thaxton, C. Morales, J. Bowers, S. Suriano, C. Cloud, and T. Benton. We thank Y.-T. Hsu, L. Ball, R. Drake, and J. Bielawski for their initial assistance with PR fractionation. **Funding:** This work was supported by multiple NIH grants CA186866, CA188419, AI070603, and AI077283 (to Z.L.); CA175061 and CA208514 (to C.M.P.); UL1 TR001450 and NIH–National Center for Advancing Translational Sciences Grant TL1 TR001451 (to C.W. and B.R.); and Hollings Cancer Center Cancer Center Support Grant P30CA138313. **Author contributions:** Z.L. and S.R. conceived the idea, designed the study, and wrote the manuscript. S.R., A.M., B.R., B.X.W., M.H.N., C.W., C.M.P., M.P.R., M.H., and D.W.B. performed the experiments. Z.L., B.L., and Y.Y. supervised the study. E.G.-M. assisted in data analysis, statistics, and interpretation. All authors provided critical comments on the manuscript. **Competing interests:** A provisional patent application has been filed to target GARP and platelets for cancer immunotherapy. The authors declare no other competing interests.

Submitted 11 August 2016
Resubmitted 16 November 2016
Accepted 23 March 2017
Published 5 May 2017
10.1126/sciimmunol.aai7911

Citation: S. Rachidi, A. Metelli, B. Riesenberg, B. X. Wu, M. H. Nelson, C. Wallace, C. M. Paulos, M. P. Rubinstein, E. Garrett-Mayer, M. Hennig, D. W. Bearden, Y. Yang, B. Liu, Z. Li, Platelets subvert T cell immunity against cancer via GARP-TGFβ axis. *Sci. Immunol.* **2**, eaai7911 (2017).

CANCER IMMUNOTHERAPY

Blockade of TNFR2 signaling enhances the immunotherapeutic effect of CpG ODN in a mouse model of colon cancer

Yingjie Nie,[1,2] Jiang He,[3] Hidekazu Shirota,[1] Anna L. Trivett,[1] De Yang,[1] Dennis M. Klinman,[1] Joost J. Oppenheim,[1]* Xin Chen[3,1]*

Copyright © 2018 The Authors, some rights reserved; exclusive licensee American Association for the Advancement of Science. No claim to original U.S. Government Works

Through the tumor necrosis factor (TNF) receptor type II (TNFR2), TNF preferentially activates, expands, and promotes the phenotypic stability of $CD4^+Foxp3^+$ regulatory T (T_{reg}) cells. Those T_{reg} cells that have a high abundance of TNFR2 have the maximal immunosuppressive capacity. We investigated whether targeting TNFR2 could effectively suppress the activity of T_{reg} cells and consequently enhance the efficacy of cancer immunotherapy. We found that, relative to a suboptimal dose of the immunostimulatory Toll-like receptor 9 ligand CpG oligodeoxynucleotide (ODN), the combination of the suboptimal dose of CpG ODN with the TNFR2-blocking antibody M861 more markedly inhibited the growth of subcutaneously grafted mouse CT26 colon tumor cells. This resulted in markedly fewer $TNFR2^+$ T_{reg} cells and more interferon-γ–positive (IFN-γ^+) $CD8^+$ cytotoxic T lymphocytes infiltrating the tumor and improved long-term tumor-free survival in the mouse cohort. Tumor-free mice were resistant to rechallenge by the same but not unrelated (4T1 breast cancer) cells. Treatment with the combination of TNFR2-blocking antibody and a CD25-targeted antibody also resulted in enhanced inhibition of tumor growth in a syngeneic 4T1 mouse model of breast cancer. Thus, the combination of a TNFR2 inhibitor and an immunotherapeutic stimulant may represent a more effective treatment strategy for various cancers.

INTRODUCTION

Overcoming the immunosuppressive tumor microenvironment is key to achieving effective cancer immunotherapy (*1*, *2*). Tumor-infiltrating $CD4^+Foxp3^+$ regulatory T (T_{reg}) cells are potent immunosuppressive cells that represent a major cellular mechanism of tumor immune evasion and play a major role in dampening naturally occurring and therapeutically induced antitumor immune responses (*3*). Accumulation of T_{reg} cells within tumor tissues, and the resultant high ratio of T_{reg} cells to effector T (T_{eff}) cells, is correlated with poor prognosis of cancer patients, including those with lung cancer (*4*), breast cancer (*5*), colorectal cancer (*6*), pancreatic cancer (*7*), and other malignancies. Elimination of T_{reg} activity, by either reducing their number or down-regulating their immunosuppressive function using checkpoint inhibitors, has become an effective strategy to enhance the efficacy of cancer therapy (*8*, *9*).

Tumor necrosis factor (TNF) receptor type II (TNFR2) is predominantly present on the maximally suppressive subset of mouse and human T_{reg} cells (*10*, *11*). There is now compelling evidence that the interaction of TNF with TNFR2 promotes the proliferative expansion, suppressive function, and phenotypical stability of T_{reg} cells (*12*–*18*). In mouse Lewis lung carcinoma and 4T1 breast tumor model, most of the tumor-infiltrating T_{reg} cells are highly suppressive $TNFR2^+$ T_{reg} cells (*10*, *19*). In humans, the proportion of $TNFR2^+$ T_{reg} cells is also increased in the peripheral blood of lung cancer patients and in the tumor-associated ascites of ovarian cancer patients (*20*, *21*). Recent analysis of single-cell RNA sequencing showed that the expression of *TNFR2* is one of the most markedly increased genes on T_{reg} cells, as compared with $CD4^+$ T_{eff} cells and $CD8^+$ cytotoxic T lymphocytes (CTLs) in metastatic melanoma patients, and increased *TNFR2* gene expression is associated with exhaustion of $CD8^+$ CTLs (*22*). Furthermore, the amount of TNFR2 present on the surface of T_{reg} cells is associated with greater lymphatic invasion, a higher incidence of tumor metastasis, a higher clinical stage, and poorer response to treatment in patients with lung cancer and acute myeloid leukemia (AML) (*20*, *23*, *24*). This clinical and experimental evidence suggests that the highly suppressive $TNFR2^+$ T_{reg} cells associated with tumors play a major role in tumor immune evasion. Meanwhile, TNFR2 is also found on several tumor cells, including colon cancer (*25*), Hodgkin lymphoma (*26*), myeloma (*27*), renal carcinoma (*28*), and ovarian cancer (*29*), leading many to consider *TNFR2* an oncogene. Antagonistic antibody targeting TNFR2 induces the death of both T_{reg} cells and OVCAR3 ovarian cancer cells, which have abundant surface TNFR2 (*29*). On the basis of these observations, we proposed that TNFR2 behaves as an immune checkpoint activator and oncoprotein (*30*).

TNF can be induced by various immunotherapies, including dendritic cell (DC)–based interventions, tumor vaccines, and Toll-like receptor (TLR) agonists (*31*–*33*). Such immunotherapy-induced TNF may, in turn, increase TNFR2 on T_{reg} cells (*34*), resulting in the expansion and activation of tumor-associated T_{reg} cells through TNFR2. For example, by activating DCs, the TLR9 agonistic CpG oligodeoxynucleotides (ODNs) have the capacity to induce antitumor immune responses in mouse models (*35*–*37*). CpG ODNs promote the maturation and improve the function of professional antigen-presenting cells while supporting the generation of antigen-specific B cells and CTLs (*38*). Intratumoral injection of CpG ODN also induces the differentiation and reduces the immunosuppressive activity of myeloid-derived suppressor cells (MDSCs) (*39*), therefore enhancing the host's response to cancer (*40*). However, treatment with CpG ODN can also induce human or mouse T_{reg} cells that have potent immunosuppressive function, which, in turn, dampens host immune responses against the tumor (*41*, *42*). CpG ODN treatment can increase the production

[1]Cancer Inflammation Program, Center for Cancer Research, National Cancer Institute, Frederick, MD 21702, USA. [2]Department of Research, Guizhou Provincial People's Hospital, Guiyang, Guizhou 550002, China. [3]State Key Laboratory of Quality Research in Chinese Medicine, Institute of Chinese Medical Sciences, University of Macau, Macao SAR 999078, China.
*Corresponding author. Email: xchen@umac.mo (X.C.); oppenhej@mail.nih.gov (J.J.O.)

of TNF in cultured murine DCs (*43*) or human peripheral blood mononuclear cells (*44*), which is likely responsible for the activation of T_{reg} cells. Therefore, by reducing T_{reg} activity, blockade of TNFR2 may enhance the antitumor effect of an immunotherapeutic such as CpG ODN.

Here, we tested this hypothesis and found that the combination of a blocking antibody (M861) recognizing TNFR2 and CpG ODN more potently inhibited mouse CT26 colon tumor development and induced greater tumor regression in syngeneic mice, resulting in greater long-term tumor-free survival of the mice. In addition, in a mouse 4T1 breast cancer model, a better antitumor effect was observed by simultaneously blocking TNFR2 and CD25. Furthermore, tumor antigen-specific immunity developed in the mice that survived CT26 tumor graftment; they completely (over the time course of the experiment) and selectively resisted a rechallenge by CT26, but not 4T1, tumor cells. This effect was associated with a decrease in the proportion of T_{reg} cells among tumor-infiltrating leukocytes, a reduced surface abundance of TNFR2 on T_{reg} cells, and increased tumor infiltration of interferon-γ (IFN-γ)–producing $CD8^+$ T cells. Thus, the combination of TNFR2 antagonism and immunotherapy may be a promising cancer treatment strategy.

RESULTS

M861 inhibits the stimulatory effect of TNF on T_{reg} cells

Previously, we showed that treatment with TNF preferentially promoted the proliferative expansion of T_{reg} cells, accompanied by increased abundance of TNFR2 on T_{reg} cells in vitro and in lipopolysaccharide (LPS)–treated mice (*18*, *34*). In $CD4^+$ T cells cultured with interleukin-2 (IL-2), treatment with the TNFR2 antibody M861 significantly inhibited TNF-induced proliferation (Fig. 1A) and expansion (Fig. 1B) of T_{reg} cells. M861 also significantly blocked TNF-induced increases in the cell surface abundance of TNFR2 on T_{reg} cells (Fig. 1C). In LPS-challenged mice, although administration of M861 failed to reduce the number of T_{reg} cells in the spleens and lymph nodes within 24 hours, the proportion of $TNFR2^+$ T_{reg} cells was significantly reduced by 64% and the abundance of TNFR2 on splenic T_{reg} cells was significantly reduced by >56% (Fig. 1D). The decrease in $TNFR2^+$ T_{reg} cells was not due to cell death (fig. S1). Therefore, unlike two other antibodies recognizing human TNFR2 described in a recent study (*29*), M861 was not a T_{reg}-depleting antibody. Furthermore, its capacity to reduce TNFR2 abundance appears to be more potent than its inhibition of the proliferative expansion of T_{reg} cells induced by LPS treatment (Fig. 1). Overall, our data favor the idea that M861 is a blocking antibody that inhibits ligand-induced TNFR2 signaling.

Combination therapy with TNFR2-blocking antibody and CpG ODN potently inhibits the growth of CT26 tumors and generated tumor-specific immunity

To examine the effect of TNFR2 blockade on the efficacy of tumor immunotherapy, we treated female CT26 tumor-bearing Balb/c mice with M861 and CpG ODN or various controls (Fig. 2A). Treatment was started when the tumor reached 5 to 6 mm in diameter (day 0). CpG ODNs were administered by intratumoral injection, which was previously reported to achieve an optimal antitumor effect (*39*). To reveal the beneficial effect of combination therapy, we administered M861 with a suboptimal dose of CpG ODN, neither of which markedly inhibited tumor growth alone (Fig. 2B). The combination of M861 and CpG ODN potently inhibited the growth of primary CT26 tumors (Fig. 2B). Eighty percent of mice were tumor-free and survived up to the end of the experiment at 60 days, whereas mice in other groups died from tumor burden within 50 days after tumor inoculation (Fig. 2C). The individual tumor growth curves varied; although a few mice had slow tumor growth with phosphate-buffered saline (PBS), CpG, or M861 alone, the antitumor effect of the M861 and CpG ODN combination is clear (Fig. 2, D to G).

To investigate whether the tumor-free mice developed long-term CT26 tumor-specific immunity, the surviving mice were reinoculated subcutaneously with CT26 tumor cells into the right flanks, and 4T1 tumor cells were inoculated into their left flanks. As controls, both 4T1 tumor cells and CT26 tumor cells were inoculated into naïve mice at the same manner, and as expected, both tumors developed in all naïve mice (Fig. 2H). Whereas all of the CT26 (intratumoral)–surviving mice developed measurable 4T1 tumors by day 26 after inoculation, none of these mice developed CT26 colon tumors (Fig. 2I). These results indicate that the treatment with combination of M861 and CpG ODN induced the development of long-term tumor antigen-specific immunity.

M861 did not induce the death of $TNFR2^+$ T_{reg} cells (fig. S1), indicating that its effect was caused by binding and blocking TNFR2 signaling. The possibility that this antibody also binds and neutralizes soluble shed TNFR2 should be addressed in a future study. It was recently reported that antibodies recognizing human TNFR2, in addition to eliminating T_{reg} cells, could also directly act on TNFR2-expressing tumor cells (*29*). A considerable proportion of CT26 cancer cells are $TNFR2^+$ cells (fig. S2A). However, treatment with M861 (up to 20 μg/ml) did not inhibit the growth of CT26 cells (fig. S2B), indicating that the in vivo inhibitory effect of this antibody on CT26 tumor was not due to any direct effect on tumor cells.

Combination therapy with TNFR2-blocking antibody and CpG ODN reduces the proportion of tumor-infiltrating $TNFR2^+$ T_{reg} cells and increases IFN-γ^+ $CD8^+$ CTLs

Because combination therapy resulted in inhibited CT26 tumor growth and marked tumor regression in many of the mice, we were unable to examine the immune cell profile present in the tumor environment. To obtain a tumor mass for further study, we delayed the treatment until tumors reached ~10 mm in diameter, and the effect of treatments on tumor-infiltrating T_{reg} cells was examined by fluorescence-activated cell sorting (FACS) analysis (Fig. 3, A to C). The proportion of intratumoral T_{reg} cells was increased to ~20% by treatment with CpG ODN alone (Fig. 3D). Furthermore, CpG ODN treatment also significantly increased the amount of TNFR2 on T_{reg} cells by ~20% (Fig. 3E). These results suggest that, in addition to stimulating the expansion of T_{reg} cells as previously reported (*41*, *42*), CpG ODN can also increase the function of T_{reg} cells, as indicated by the increased abundance of TNFR2 (*10*, *45*). Both the proportion of $TNFR2^+$ T_{reg} cells and the abundance of TNFR2 in T_{reg} cells (measured as per cell) were markedly reduced by treatment with the TNFR2-blocking antibody (Fig. 3, E and F). Notably, the CpG ODN–induced expansion of T_{reg} cells and increased abundance of TNFR2 on T_{reg} cells were completely abrogated by M861 treatment (Fig. 3, D and E). The combination therapy markedly increased the production of IFN-γ by $CD8^+$ CTLs, and the proportion of IFN-γ–producing $CD8^+$ T cells was greater than threefold as compared with CpG ODN treatment alone (Fig. 3, C and G). Thus, our data indicate that combination therapy reduced T_{reg} activity and promoted the induction of potent type 1 helper T cell antitumor immune responses.

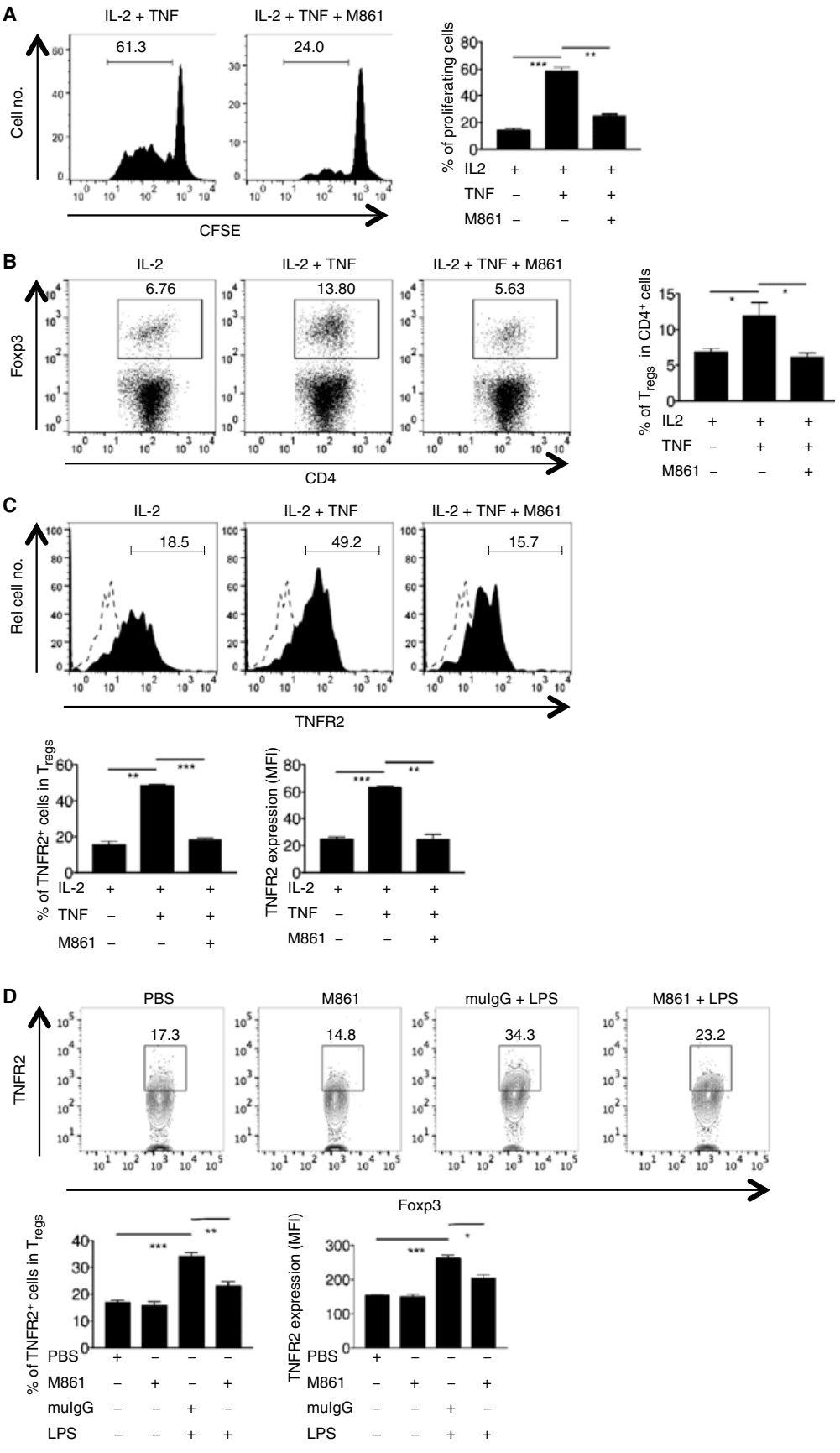

Fig. 1. The in vitro and in vivo effects of an antibody recognizing TNFR2 (M861) on T_{reg} cells. (**A** to **C**) Magnetic-activated cell sorting–purified $CD4^+$ T cells were labeled with carboxyfluorescein diacetate succinimidyl ester (CFSE). The cells were cultured with interleukin-2 (IL-2; 10 ng/ml) alone or with tumor necrosis factor (TNF; 20 ng/ml) and M861 (10 μg/ml), as indicated, for 72 hours. Proliferation of regulatory T (T_{reg}) cells shown by CFSE dilution (A), the proportion of T_{reg} cells in $CD4^+$ cell cultures (B), and the surface abundance of TNF receptor type II (TNFR2) on T_{reg} cells (C) were analyzed with fluorescence-activated cell sorting (FACS), gating for $Foxp3^+$ staining (A and C) or not gated (total cells; B). (**D**) Wild-type Balb/c mice were injected intraperitoneally with phosphate-buffered saline (PBS), lipopolysaccharide (LPS; 200 μg), M861 (100 μg), mouse immunoglobulin G (muIgG), or a combination thereof, as indicated, for 24 hours. The abundance of TNFR2 on the surface of T_{reg} cells in the spleen was analyzed by FACS, gating for $CD4^+Foxp3^+$ staining. FACS plots are representative of three independent experiments. Data are means ± SEM of $n = 5$ mice. Number in each FACS plot indicates the percentage of gated cells. $^*P < 0.05$, $^{**}P < 0.01$, $^{***}P < 0.001$ by Student's *t* test (A to D).

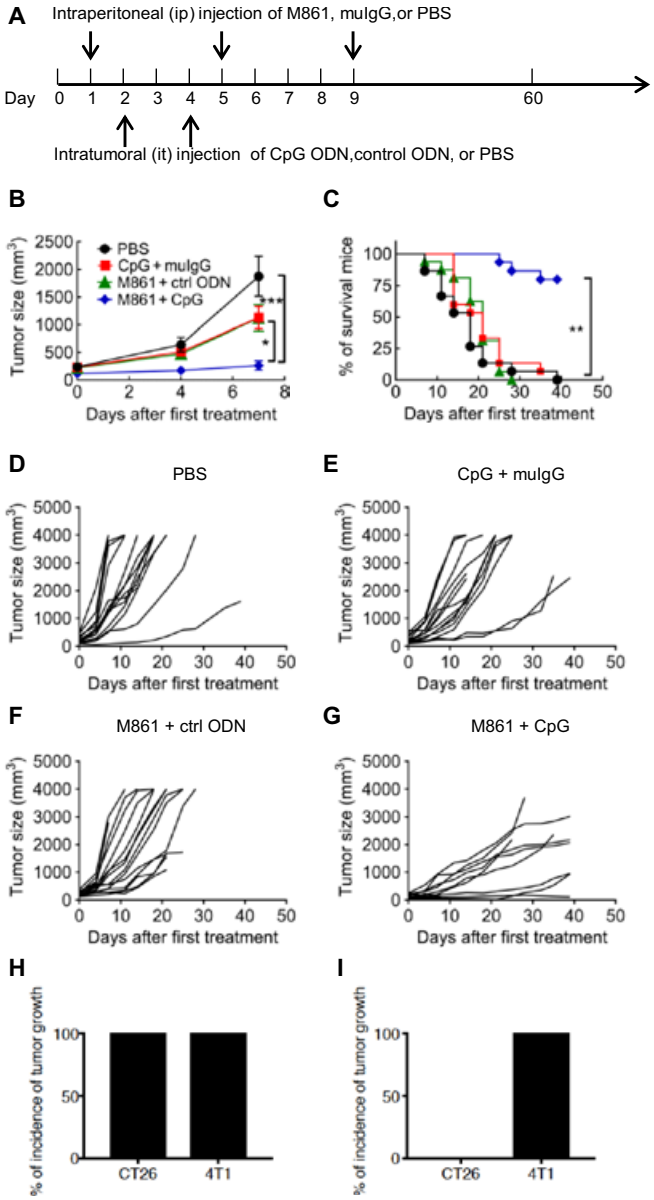

Fig. 2. M861 in combination with CpG ODN potently inhibits the development of mouse CT26 colon tumors. (**A**) Schematic of the experimental protocol. Balb/c mice were inoculated in the right flank with CT26 tumor cells (2×10^5 cells in 0.2 ml of PBS). When tumor reached 5 to 6 mm in diameter (day 0), mice were then treated with PBS, CpG oligodeoxynucleotide (ODN) plus control (ctrl) IgG, M861 plus control ODN, or CpG ODN plus M861. (**B**) Mean growth curves of CT26 tumors in mice treated as described in (A). Data are means ± SEM of 15 mice. (**C**) Survival curves of the CT26 tumor-bearing mice treated as described in (A). (**D** to **G**) CT26 tumor growth curves in each individual CT26 tumor-bearing mouse treated with PBS (D), CpG ODN plus control IgG (E), M861 plus control ODN (F), or M861 plus CpG ODN (G). Data are summary of results pooled from three independent experiments ($n = 15$ mice). The tumor-free mice were reinoculated with CT26 tumor cells into the right flank and 4T1 tumor cells into the left flank 8 weeks after the mice became tumor-free. As a control, normal mice were also inoculated with CT26 tumor cells into the right flank and 4T1 tumor cells into the left flank in the same manner. Data ($n = 8$ mice) are the percentage of tumor incidence on (**H**) normal mice and (**I**) surviving mice on day 26 after (re-)challenge. $^*P < 0.05$, $^{**}P < 0.01$, $^{***}P < 0.001$ by one-way analysis of variance (ANOVA) test (B), log-rank test (C), or Student's *t* test (H and I).

Combination of TNFR2 antagonistic antibody and CD25 antagonistic antibody inhibits the development of mouse 4T1 breast tumors

CD25, the IL-2 receptor α chain, was the first identified surface marker of T_{reg} cells (*46*), and targeting of CD25 has been a conventional approach for T_{reg} elimination (*47*, *48*). PC61 is a CD25-recognizing monoclonal antibody that blocks IL-2 binding to the receptor (*49*), and it was shown that pretreatment with PC61 led to tumor rejection in mouse tumor models (*50*, *51*). We thus compared the effect of TNFR2 antagonistic antibody and CD25 antagonistic antibody on the tumor development. To this end, TR75-54.7, a well-characterized functional blocking TNFR2 antibody (*52*), and PC61 were administered separately or in combination into mice. Three days later, the mice were inoculated with 4T1 tumor cells (Fig. 4A). The results showed that TR75-54.7 more potently inhibited the development of 4T1 tumor than PC61 (Fig. 4, B and C). Although the difference in tumor size was not statistically different between mice treated with two antibodies (Fig. 4B), only TR75-54.7 markedly enhanced the survival of tumor-bearing mice (Fig. 4C), whereas PC61 did not have such effect (Fig. 4C). Moreover, the combination of TR75-54.7 and PC61 was superior to the monotherapy in the inhibition of tumor growth (Fig. 4B). Consequently, the median survival of tumor-bearing mice was longer after combination therapy (38 days), as compared with monotherapy of TR75-54.7 (34 days) or PC61 (27 days) (Fig. 4, C and D; median survival of PBS control group was 24 days). Therefore, TR75-54.7 has more potent antitumor effect than PC61 in mouse 4T1 breast cancer model, whereas the combination of both resulted in the optimal antitumor effect.

DISCUSSION

Our data presented in this study showed that blockade of TNFR2 potently enhanced the effect of immunotherapy with CpG ODN against CT26 tumors, which was attributable to the reduction in T_{reg} activity and consequent mobilization of $CD8^+$ CTLs. Because of the paucity of T_{reg} cells recovered from tumor tissue, we could not determine the functionality of the tumor-infiltrating T_{reg} cells in this study directly. Nevertheless, the marked reduction in TNFR2 abundance on T_{reg} cells, which correlates with T_{reg} function, suggests that M861 reduced the suppressive capacity of T_{reg} cells in the tumor environment. This effect of M861 treatment appears to be specific for tumor-infiltrating T_{reg} cells, given that the proportion of T_{reg} cells, the abundance of TNFR2 on T_{reg} cells, and the suppressive function of T_{reg} cells present in the peripheral lymphoid tissues were not decreased by treatment with the TNFR2-blocking antibody. Although this antibody did not attenuate TNFR2 signaling in unstimulated mice, it potently inhibited the increased abundance of TNFR2 induced by LPS (Fig. 1), suggesting that increased TNFR2 abundance both in the tumor environment and in LPS-challenged mice is similarly induced by the interaction of TNF and TNFR2.

CD25 has been used as an exclusive target for physical depletion of T_{reg} cells to elicit antitumor immunity in both murine cancer models (*47*) and human cancer patients (*48*). Depletion of T_{reg} cells by administration of CD25-blocking antibody (PC61) before tumor challenge provokes effective immune response to syngeneic tumors in otherwise unresponsive mice (*50*, *51*). Our previous study showed that TNFR2 was more closely associated with the suppressive function of T_{reg} cells and the phenotype of tumor-infiltrating T_{reg} cells, as compared with CD25 (*10*, *20*, *45*). Thus, we directly compared the antitumor effect of a better characterized and commercially available

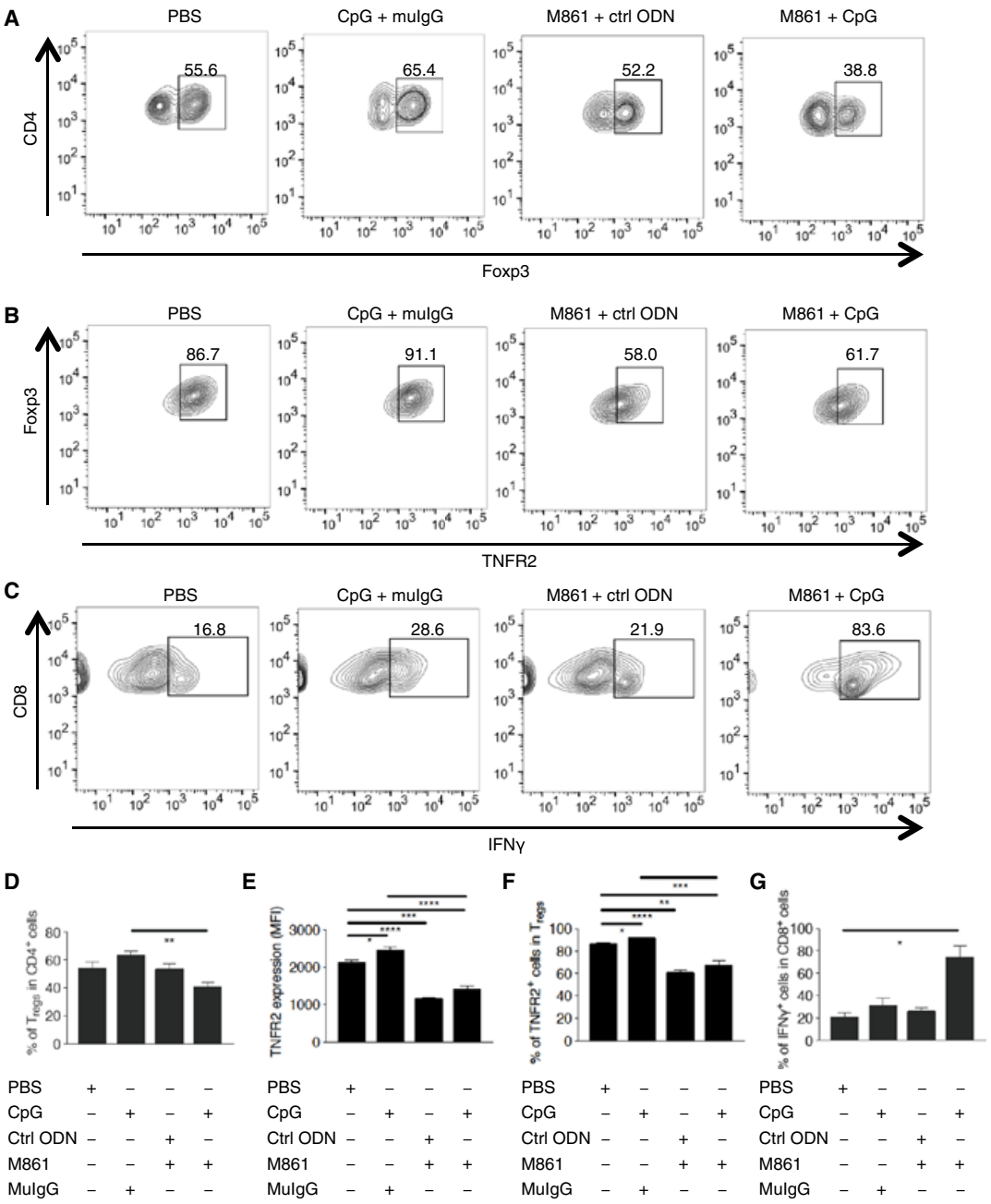

Fig. 3. Effects of M861 in combination with CpG ODN on tumor-infiltrating TNFR2$^+$ T_{reg} cells and IFN-γ$^+$ CD8 CTLs. (**A**) Representative FACS analysis of T_{reg} cells in CD4$^+$ cells from Balb/c mice inoculated with CT26 tumor cells (as described in Fig. 2), treated as indicated when tumor diameter reached 10 mm, and sacrificed for tumor tissue isolation 1 day after the final treatment. The number indicates the percentage of T_{reg} cells in CD4$^+$ cells. (**B**) Representative FACS analysis of TNFR2$^+$ cells in T_{reg} cells from mice described in (A). The number indicates the percentage of TNFR2$^+$ cells in CD4$^+$Foxp3$^+$ cells. (**C**) Representative FACS analysis of IFN-γ$^+$ cells in CD8$^+$ cells from mice described in (A). The number indicates the percentage of interferon-γ–positive (IFN-γ$^+$) cells in CD8$^+$ cells. (**D** to **G**) Summary of the proportion of T_{reg} cells in intratumoral CD4$^+$ cells (D), the mean fluorescence intensity (MFI) of TNFR2 on CD4$^+$Foxp3$^+$ cells (E), the proportion of TNFR2$^+$ cells in CD4$^+$Foxp3$^+$ cells (F), and the proportion of IFN-γ$^+$ cells in CD8$^+$ cells (G), each from mice described in (A). Flow analysis was gated on live CD45$^+$CD3$^+$ cells. Data were quantified from, or are representative of, at least three independent experiments; $n = 5$ mice (A, B, and D to F) or 3 mice (C and G). *$P < 0.05$, **$P < 0.01$, ***$P < 0.001$, ****$P < 0.0001$ by Student's t test.

TNFR2 antagonistic antibody (for example, TR75-54.7) (*52*) and PC61 on mouse 4T1 breast cancer model. The results show that pretreatment with TR75-54.7 is superior to PC61 in the inhibition of tumor growth (Fig. 4). The simultaneous blockade of TNFR2 and CD25 appears to have better effect as compared with monotherapy (Fig. 4). This intriguingly aligned well with our previous observation that, in mice, the sequence of suppressive capacity of T_{reg} subsets was TNFR2$^+$CD25$^+$ cells > TNFR2$^+$CD25$^-$ cells > TNFR2$^-$CD25$^+$ cells. Presumably, the maximal suppressive subset of T_{reg} cells was inhibited by the combination treatment of TR75-54.7 and PC61. This possibility will be experimentally examined in a future study.

CD11b$^+$Gr1$^+$ MDSCs also contribute to tumor immune evasion. Recent studies indicate that the generation, accumulation, and function of MDSCs also require TNF-TNFR2 signaling (*53*, *54*). Furthermore, CpG ODNs reportedly reduce the number of MDSCs in tumor-bearing mice (*55*). Nevertheless, the proportion of MDSCs in the spleen and tumor of CT26 tumor-bearing mice was not decreased by M861 treatment in our study.

Activation and expansion of T_{reg} cells through TNF-TNFR2 interaction represent a general negative feedback loop triggered by many immunological stimulators, including immunotherapeutic agents (*56*). For example, in addition to CpG ODN, in vivo treatment with the TLR4 ligand LPS (*34*) or the TLR2 ligand Pam3CSK4 (*57*) also promotes the activation and expansion of T_{reg} cells, accompanied by the increased abundance of TNFR2 on T_{reg} cells (*34*). Furthermore, cancer immunotherapy with IL-2, a cytokine that increases the abundance

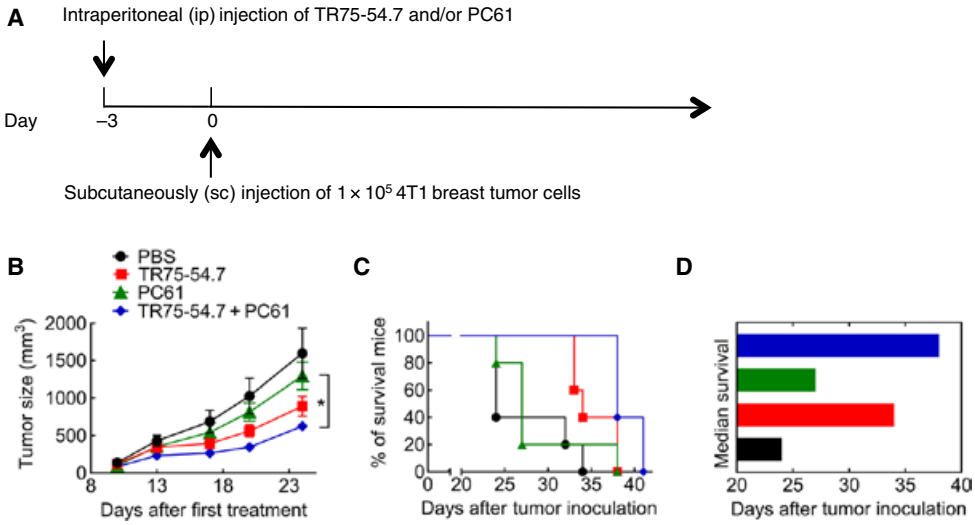

Fig. 4. Effect of TNFR2 antagonistic antibody and CD25 antagonistic antibody on mouse 4T1 breast cancer model. (**A**) Schematic of the experimental protocol. TR75-54.7 and/or PC61 were intraperitoneally injected into Balb/c mice 3 days before inoculation of 4T1 tumor cells (1×10^5 cells in 0.1 ml of PBS). (**B**) Growth kinetics of 4T1 tumors in mice. Data are means ± SEM of five mice. (**C**) Survival curves of the 4T1 tumor-bearing mice. (**D**) Median survival of the 4T1 tumor-bearing mice. *$P < 0.05$ by one-way ANOVA test (B) or log-rank test (C).

of TNFR2 on T_{reg} cells (*18*), results in substantial activation and expansion of T_{reg} cells (*58*, *59*). Even the stimulation of immune checkpoint inhibitors can also expand T_{reg} cells. For example, proliferative expansion of T_{reg} cells is induced by PD-1 blockade in melanoma patients (*60*) and by PD-L1 blockade in HIV patients (*61*). In this proof-of-principle study, we have shown that the antitumor effect of CpG ODN was markedly enhanced, whereas its stimulation of T_{reg} cells was prevented, by TNFR2 blockade. Whether the effect of TNFR2 blockade can augment other types of immunotherapeutics needs to be determined.

Because of their clear therapeutic value in cancer treatment, strategies have been developed to deplete T_{reg} cells or reduce their suppressive functions by targeting CD25 or other immune checkpoint proteins that are preferentially present on tumor-infiltrating T_{reg} cells (such as CTLA-4, TIM-3, LAG-3, PD-1, and GITR) (*62*, *63*). Because a large abundance of TNFR2 is associated with the maximally suppressive T_{reg} cells in tumor-infiltrating lymphocytes (*10*, *19*–*21*), targeting of TNFR2 may have an advantage in eliminating the more functional T_{reg} cells. This idea is supported by studies of ovarian cancer and AML that show that patients treated with reagents that reduce TNFR2 abundance on T_{reg} cells have beneficial antitumor effects (*21*, *23*, *24*, *29*). Further investigation is needed to directly compare the efficacy of targeting of TNFR2 with that of other T_{reg} checkpoint inhibitors.

Together, our findings reveal that an antibody blocking ligand-induced activation of TNFR2 markedly enhances the antitumor efficacy of immunotherapy with CpG ODN in mouse models of colon and breast cancer by reducing the number of tumor-infiltrating $TNFR2^+$ T_{reg} cells while increasing the number of IFN-γ^+ $CD8^+$ CTLs. Thus, combining a TNFR2 antagonist with an immunostimulant may represent a novel and more effective treatment strategy for patients with various cancers.

MATERIALS AND METHODS

Mice

Female wild-type 8- to 12-week-old Balb/c mice were obtained from the Animal Production Area of the National Cancer Institute at Frederick (NCI-Frederick). NCI-Frederick is accredited by the American Association for the Accreditation of Laboratory Animal Care International and follows the Public Health Service Policy for the Care and Use of Laboratory Animals. The animal study was approved by Institutional Animal Care and Use Committee of NCI-Frederick. Animal care was provided in accordance with the procedures outlined in the *Guide for the Care and Use of Laboratory Animals* (National Research Council, revised 1996).

Cells and reagents

The CT26 colon cancer and 4T1 breast cancer cell lines were purchased from the American Type Culture Collection and examined with Molecular Testing of Biological Materials by Animal Health Diagnostic Laboratory (NCI-Frederick) and Luminescence Mycoplasma Test by Animal Molecular Diagnostics Laboratory (NCI-Frederick). Cell lines were cultured in RPMI 1640 medium supplemented with 10% fetal calf serum and 2 mM glutamine at 37°C in a humidified incubator with 5% CO_2. CpG ODN 1668 was purchased from InvivoGen. Anti-mouse antibodies, including anti-mouse CD45, CD4, CD8a, and TNFR2 antibodies, were purchased from BD Biosciences. LIVE/DEAD Fixable Near-IR Dead Cell Stain Kit was purchased from Thermo Fisher Scientific. An antibody recognizing mouse TNFR2 (M861), as well as its control immunoglobulin G (IgG) (mouse IgG1), was a gift from Amgen Inc. Anti-mouse TNFR2 antibody TR75-54.7 and anti-mouse CD25 antibody PC61 were gifts from G. Trinchieri [NCI, National Institutes of Health (NIH)].

CT26 tumor cell inoculation and separation of tumor-infiltrating leukocytes

CT26 tumor cells were subcutaneously injected into the right flank of recipient mice in single-cell suspension with 2×10^5 cells in 0.2 ml of PBS per mouse. After indicated times, tumors were excised, minced, and digested in RPMI 1640 supplemented with collagenase IV (1 mg/ml) and deoxyribonuclease I (0.1 mg/ml). The fragments were pushed through a 70-um pore size cell strainer to create a single-cell suspension. In some experiments, tumor-free mice 8 weeks after anti-TNFR2 and CpG ODN treatment were reinoculated with CT26 cells (2×10^5) into the right flank, and the same number of 4T1 cells was injected subcutaneously into the left flank. Tumor size was calculated by the following formula: (length × width^2)/2. "Survival" represents the time to develop a 4-cm^3 tumor or a moribund state, a humane end point that triggers euthanasia. Mice were monitored daily and were euthanized when signs of morbidity from metastatic disease burden became evident.

Treatment of mouse model of CT26 colon cancer

When the diameter of tumor reached 5 to 6 mm, mice were treated with the following dose schedule: An antibody recognizing TNFR2 (M861) or mouse IgG1 was administered at days 1, 5, and 9 intraperitoneally at 100 μg in 0.2 ml of PBS. CpG ODN or control ODN was administered intratumorally at days 2 and 4 at 20 μg in 0.1 ml of PBS. The same quantity of PBS was administered intraperitoneally or intratumorally as a control. In some experiments, the treatment was started when the diameter of tumor reached 10 mm. One day after the last treatment, mice were sacrificed and tumor and lymphoid tissues were harvested for study.

Treatment of mouse 4T1 breast cancer model

An antibody recognizing TNFR2 (TR75-54.7) and/or an antibody recognizing CD25 (PC61) were administered at 200 μg in 0.2 ml of PBS 3 days before the inoculation of 1×10^5 4T1 breast tumor cells in 0.1 ml of PBS per mouse subcutaneously injected into right mammary fat pads (thoracic No. 2 mammary glands) of recipient female Balb/c mice.

In vitro culture of $CD4^+$ T cells

$CD4^+$ cells were purified from lymphocytes with Mouse CD4 (L3T4) MicroBeads and LS Columns (Miltenyi Biotec). $CD4^+$ cells were labeled with carboxyfluorescein diacetate succinimidyl ester (CFSE) and cultured at 4×10^5 cells per well in a 96-well plate with medium (*12*) alone or IL-2 (10 ng/ml), or with or without TNF (20 ng/ml), or in the presence of M861 (10 μg/ml). After 72 hours, the proliferation of T_{reg} cells (as indicated by CFSE dilution), the proportion of T_{reg} cells, and TNFR2 abundance on T_{reg} cells were analyzed by FACS, gating for $Foxp3^+$ cells.

In vivo treatment with LPS and M861

Normal Balb/c mice were intraperitoneally injected with 200 μg of LPS (Sigma-Aldrich, catalog no. L9764) in PBS. Some mice were injected intraperitoneally with 200 μg of M861 or control Mu IgG1 1 hour before injection of LPS. Mouse spleens and mesenteric lymph nodes were harvested at 24 hours after injection for the FACS analysis of phenotype.

In vitro proliferation of CT26 and 4T1 tumor cells

CT26 and 4T1 tumor cells were seeded into 96-well plate at 5×10^4 cells per well. The cells were cultured with media alone or with M861 (10 or 20 μg/ml). After 72 hours, cells were treated with pulsed 1 mCi [^{3}H]thymidine (PerkinElmer Life Sciences) per well for the last 6 hours of the culture period. The proliferation was evaluated by [^{3}H]thymidine incorporation.

Flow cytometry

After blocking FcR, cells were incubated with appropriately diluted antibodies. The acquisition was performed using a Fortessa cytometer (BD Biosciences), and data analysis was conducted using FlowJo software (Tree Star Inc.). FACS analysis was gated on the live cells only by using a LIVE/DEAD Fixable Dead Cell Stain kit.

Statistical analysis

Two-tailed Student's *t* test was used for the comparison of two indicated groups. One-way analysis of variance (ANOVA) test was used for the comparison of tumor growth between groups at the same day shown in Figs. 2B and 4B. Log-rank test was used for the comparison of survival shown in Figs. 2C and 4C. All statistical analysis was performed with GraphPad Prism 7.0.

SUPPLEMENTARY MATERIALS

www.sciencesignaling.org/cgi/content/full/11/511/eaan0790/DC1
Fig. S1. M861 does not induce the death of T_{reg} cells in LPS-treated mice.
Fig. S2. M861 does not inhibit the proliferation of TNFR2-expressing CT26 tumor cells.

REFERENCES AND NOTES

1. G. T. Motz, G. Coukos, Deciphering and reversing tumor immune suppression. *Immunity* **39**, 61–73 (2013).
2. J. M. Pitt, A. Marabelle, A. Eggermont, J.-C. Soria, G. Kroemer, L. Zitvogel, Targeting the tumor microenvironment: Removing obstruction to anticancer immune responses and immunotherapy. *Ann. Oncol.* **27**, 1482–1492 (2016).
3. A. Tanaka, S. Sakaguchi, Regulatory T cells in cancer immunotherapy. *Cell Res.* **27**, 109–118 (2017).
4. H. Tao, Y. Mimura, K. Aoe, S. Kobayashi, H. Yamamoto, E. Matsuda, K. Okabe, T. Matsumoto, K. Sugi, H. Ueoka, Prognostic potential of FOXP3 expression in non-small cell lung cancer cells combined with tumor-infiltrating regulatory T cells. *Lung Cancer* **75**, 95–101 (2012).
5. J. Shou, Z. Zhang, Y. Lai, Z. Chen, J. Huang, Worse outcome in breast cancer with higher tumor-infiltrating FOXP3+ Tregs: A systematic review and meta-analysis. *BMC Cancer* **16**, 687 (2016).
6. Y.-C. Lin, J. Mahalingam, J.-M. Chiang, P.-J. Su, Y.-Y. Chu, H.-Y. Lai, J.-H. Fang, C.-T. Huang, C.-T. Chiu, C.-Y. Lin, Activated but not resting regulatory T cells accumulated in tumor microenvironment and correlated with tumor progression in patients with colorectal cancer. *Int. J. Cancer* **132**, 1341–1350 (2013).
7. L. Liu, G. Zhao, W. Wu, Y. Rong, D. Jin, D. Wang, W. Lou, X. Qin, Low intratumoral regulatory T cells and high peritumoral $CD8^+$ T cells relate to long-term survival in patients with pancreatic ductal adenocarcinoma after pancreatectomy. *Cancer Immunol. Immunother.* **65**, 73–82 (2016).
8. H. Nishikawa, S. Sakaguchi, Regulatory T cells in cancer immunotherapy. *Curr. Opin. Immunol.* **27**, 1–7 (2014).
9. C. Liu, C. J. Workman, D. A. A. Vignali, Targeting regulatory T cells in tumors. *FEBS J.* **283**, 2731–2748 (2016).
10. X. Chen, J. J. Subleski, H. Kopf, O. M. Z. Howard, D. N. Männel, J. J. Oppenheim, Cutting edge: Expression of TNFR2 defines a maximally suppressive subset of mouse $CD4^+CD25^+FoxP3^+$ T regulatory cells: Applicability to tumor-infiltrating T regulatory cells. *J. Immunol.* **180**, 6467–6471 (2008).
11. X. Chen, J. J. Subleski, R. Hamano, O. M. Z. Howard, R. H. Wiltrout, J. J. Oppenheim, Co-expression of TNFR2 and CD25 identifies more of the functional $CD4^+FOXP3^+$ regulatory T cells in human peripheral blood. *Eur. J. Immunol.* **40**, 1099–1106 (2010).
12. Y. Grinberg-Bleyer, D. Saadoun, A. Baeyens, F. Billiard, J. D. Goldstein, S. Gregoire, G. H. Martin, R. Elhage, N. Derian, W. Carpentier, G. Marodon, D. Klatzmann, E. Piaggio, B. L. Salomon, Pathogenic T cells have a paradoxical protective effect in murine autoimmune diabetes by boosting Tregs. *J. Clin. Invest.* **120**, 4558–4568 (2010).
13. X. Chen, X. Wu, Q. Zhou, O. M. Z. Howard, M. G. Netea, J. J. Oppenheim, TNFR2 is critical for the stabilization of the $CD4^+Foxp3^+$ regulatory T. cell phenotype in the inflammatory environment. *J. Immunol.* **190**, 1076–1084 (2013).
14. B. Zaragoza, X. Chen, J. J. Oppenheim, A. Baeyens, S. Gregoire, D. Chader, G. Gorochov, M. Miyara, B. L. Salomon, Suppressive activity of human regulatory T cells is maintained in the presence of TNF. *Nat. Med.* **22**, 16–17 (2016).
15. M. Chopra, M. Biehl, T. Steinfatt, A. Brandl, J. Kums, J. Amich, M. Vaeth, J. Kuen, R. Holtappels, J. Podlech, A. Mottok, S. Kraus, A.-L. Jordán-Garrote, C. A. Bäuerlein, C. Brede, E. Ribechini, A. Fick, A. Seher, J. Polz, K. J. Ottmüller, J. Baker, H. Nishikii, M. Ritz, K. Mattenheimer, S. Schwinn, T. Winter, V. Schäfer, S. Krappmann, H. Einsele, T. D. Müller, M. J. Reddehase, M. B. Lutz, D. N. Männel, F. Berberich-Siebelt, H. Wajant, A. Beilhack, Exogenous TNFR2 activation protects from acute GvHD via host T reg cell expansion. *J. Exp. Med.* **213**, 1881–1900 (2016).
16. M. Leclerc, S. Naserian, C. Pilon, A. Thiolat, G. H. Martin, C. Pouchy, C. Dominique, Y. Belkacemi, F. Charlotte, S. Maury, B. L. Salomon, J. L. Cohen, Control of GVHD by regulatory T cells depends on TNF produced by T cells and TNFR2 expressed by regulatory T cells. *Blood* **128**, 1651–1659 (2016).
17. A. Pierini, W. Strober, C. Moffett, J. Baker, H. Nishikii, M. Alvarez, Y. Pan, D. Schneidawind, E. Meyer, R. S. Negrin, TNF-α priming enhances $CD4^+FoxP3^+$ regulatory T-cell suppressive function in murine GVHD prevention and treatment. *Blood* **128**, 866–871 (2016).

18. X. Chen, M. Bäumel, D. N. Männel, O. M. Z. Howard, J. J. Oppenheim, Interaction of TNF with TNF receptor type 2 promotes expansion and function of mouse $CD4^+CD25^+$ T regulatory cells. *J. Immunol.* **179**, 154–161 (2007).
19. X. Chen, Y. Yang, Q. Zhou, J. M. Weiss, O. M. Z. Howard, J. M. McPherson, L. M. Wakefield, J. J. Oppenheim, Effective chemoimmunotherapy with anti-TGFβ antibody and cyclophosphamide in a mouse model of breast cancer. *PLOS ONE* **9**, e85398 (2014).
20. F. Yan, R. Du, F. Wei, H. Zhao, J. Yu, C. Wang, Z. Zhan, T. Ding, X. Ren, X. Chen, H. Li, Expression of TNFR2 by regulatory T cells in peripheral blood is correlated with clinical pathology of lung cancer patients. *Cancer Immunol. Immunother.* **64**, 1475–1485 (2015).
21. C. Govindaraj, K. Scalzo-Inguanti, M. Madondo, J. Hallo, K. Flanagan, M. Quinn, M. Plebanski, Impaired Th1 immunity in ovarian cancer patients is mediated by $TNFR2^+$ Tregs within the tumor microenvironment. *Clin. Immunol.* **149**, 97–110 (2013).
22. I. Tirosh, B. Izar, S. M. Prakadan, M. H. Wadsworth II, D. Treacy, J. J. Trombetta, A. Rotem, C. Rodman, C. Lian, G. Murphy, M. Fallahi-Sichani, K. Dutton-Regester, J.-R. Lin, O. Cohen, P. Shah, D. Lu, A. S. Genshaft, T. K. Hughes, C. G. K. Ziegler, S. W. Kazer, A. Gaillard, K. E. Kolb, A.-C. Villani, C. M. Johannessen, A. Y. Andreev, E. M. Van Allen, M. Bertagnolli, P. K. Sorger, R. J. Sullivan, K. T. Flaherty, D. T. Frederick, J. Jané-Valbuena, C. H. Yoon, O. Rozenblatt-Rosen, A. K. Shalek, A. Regev, L. A. Garraway, Dissecting the multicellular ecosystem of metastatic melanoma by single-cell RNA-seq. *Science* **352**, 189–196 (2016).
23. C. Govindaraj, P. Tan, P. Walker, A. Wei, A. Spencer, M. Plebanski, Reducing TNF receptor 2^+ regulatory T cells via the combined action of azacitidine and the HDAC inhibitor, panobinostat for clinical benefit in acute myeloid leukemia patients. *Clin. Cancer Res.* **20**, 724–735 (2014).
24. C. Govindaraj, M. Madondo, Y. Y. Kong, P. Tan, A. Wei, M. Plebanski, Lenalidomide-based maintenance therapy reduces TNF receptor 2 on CD4 T cells and enhances immune effector function in acute myeloid leukemia patients. *Am. J. Hematol.* **89**, 795–802 (2014).
25. K. E. Hamilton, J. G. Simmons, S. Ding, L. Van Landeghem, P. K. Lund, Cytokine induction of tumor necrosis factor receptor 2 is mediated by STAT3 in colon cancer cells. *Mol. Cancer Res.* **9**, 1718–1731 (2011).
26. S. Nakayama, T. Yokote, M. Tsuji, T. Akioka, T. Miyoshi, Y. Hirata, N. Hiraoka, K. Iwaki, A. Takayama, U. Nishiwaki, Y. Masuda, T. Hanafusa, Expression of tumour necrosis factor-α and its receptors in Hodgkin lymphoma. *Br. J. Haematol.* **167**, 574–577 (2014).
27. H. Rauert, T. Stühmer, R. Bargou, H. Wajant, D. Siegmund, TNFR1 and TNFR2 regulate the extrinsic apoptotic pathway in myeloma cells by multiple mechanisms. *Cell Death Dis.* **2**, e194 (2011).
28. J. Wang, R. S. Al-Lamki, Tumor necrosis factor receptor 2: Its contribution to acute cellular rejection and clear cell renal carcinoma. *Biomed. Res. Int.* **2013**, 821310 (2013).
29. H. Torrey, J. Butterworth, T. Mera, Y. Okubo, L. Wang, D. Baum, A. Defusco, S. Plager, S. Warden, D. Huang, E. Vanamee, R. Foster, D. L. Faustman, Targeting TNFR2 with antagonistic antibodies inhibits proliferation of ovarian cancer cells and tumor-associated T_{regs}. *Sci. Signal.* **10**, eaaf8608 (2017).
30. X. Chen, J. J. Oppenheim, Targeting TNFR2, an immune checkpoint stimulator and oncoprotein, is a promising treatment for cancer. *Sci. Signal.* **10**, eaal2328 (2017).
31. I. D. Jung, S. J. Shin, M.-G. Lee, T. H. Kang, H. D. Han, S. J. Lee, W. S. Kim, H. M. Kim, W. S. Park, H. W. Kim, C.-H. Yun, E. K. Lee, T.-C. Wu, Y.-M. Park, Enhancement of tumor-specific T cell-mediated immunity in dendritic cell-based vaccines by *Mycobacterium tuberculosis* heat shock protein X. *J. Immunol.* **193**, 1233–1245 (2014).
32. C. Weir, A. L. Hudson, E. Moon, A. Ross, M. Alexander, L. Peters, V. Langova, S. J. Clarke, N. Pavlakis, R. Davey, V. M. Howell, Streptavidin: A novel immunostimulant for the selection and delivery of autologous and syngeneic tumor vaccines. *Cancer Immunol. Res.* **2**, 469–479 (2014).
33. P. J. Tacken, I. S. Zeelenberg, L. J. Cruz, M. A. van Hout-Kuijer, G. van de Glind, R. G. Fokkink, A. J. A. Lambeck, C. G. Figdor, Targeted delivery of TLR ligands to human and mouse dendritic cells strongly enhances adjuvanticity. *Blood* **118**, 6836–6844 (2011).
34. R. Hamano, J. Huang, T. Yoshimura, J. J. Oppenheim, X. Chen, TNF optimally activatives regulatory T cells by inducing TNF receptor superfamily members TNFR2, 4-1BB and OX40. *Eur. J. Immunol.* **41**, 2010–2020 (2011).
35. S. Nierkens, M. H. den Brok, R. P. M. Sutmuller, O. M. Grauer, E. Bennink, M. E. Morgan, C. G. Figdor, T. J. M. Ruers, G. J. Adema, In vivo colocalization of antigen and CpG within dendritic cells is associated with the efficacy of cancer immunotherapy. *Cancer Res.* **68**, 5390–5396 (2008).
36. K. Furumoto, L. Soares, E. G. Engleman, M. Merad, Induction of potent antitumor immunity by in situ targeting of intratumoral DCs. *J. Clin. Invest.* **113**, 774–783 (2004).
37. L. Guéry, J. Dubrot, C. Lippens, D. Brighouse, P. Malinge, M. Irla, C. Pot, W. Reith, J.-M. Waldburger, S. Hugues, Ag-presenting CpG-activated pDCs prime Th17 cells that induce tumor regression. *Cancer Res.* **74**, 6430–6440 (2014).
38. D. M. Klinman, Immunotherapeutic uses of CpG oligodeoxynucleotides. *Nat. Rev. Immunol.* **4**, 249–259 (2004).
39. Y. Shirota, H. Shirota, D. M. Klinman, Intratumoral injection of CpG oligonucleotides induces the differentiation and reduces the immunosuppressive activity of myeloid-derived suppressor cells. *J. Immunol.* **188**, 1592–1599 (2012).
40. J. Vollmer, A. M. Krieg, Immunotherapeutic applications of CpG oligodeoxynucleotide TLR9 agonists. *Adv. Drug Deliv. Rev.* **61**, 195–204 (2009).
41. E. A. Moseman, X. Liang, A. J. Dawson, A. Panoskaltsis-Mortari, A. M. Krieg, Y.-J. Liu, B. R. Blazar, W. Chen, Human plasmacytoid dendritic cells activated by CpG oligodeoxynucleotides induce the generation of $CD4^+CD25^+$ regulatory T cells. *J. Immunol.* **173**, 4433–4442 (2004).
42. B. Baban, P. R. Chandler, M. D. Sharma, J. Pihkala, P. A. Koni, D. H. Munn, A. L. Mellor, IDO activates regulatory T cells and blocks their conversion into Th17-like T cells. *J. Immunol.* **183**, 2475–2483 (2009).
43. T. Sparwasser, E.-S. Koch, R. M. Vabulas, K. Heeg, G. B. Lipford, J. W. Ellwart, H. Wagner, Bacterial DNA and immunostimulatory CpG oligonucleotides trigger maturation and activation of murine dendritic cells. *Eur. J. Immunol.* **28**, 2045–2054 (1998).
44. J. Ågren, C. Thiemermann, S. J. Foster, J. E. Wang, A. O. Aasen, Cytokine responses to CpG DNA in human leukocytes. *Scand. J. Immunol.* **64**, 61–68 (2006).
45. X. Chen, R. Hamano, J. J. Subleski, A. A. Hurwitz, O. M. Z. Howard, J. J. Oppenheim, Expression of costimulatory TNFR2 induces resistance of $CD4^+FoxP3^-$ conventional T cells to suppression by $CD4^+FoxP3^+$ regulatory T cells. *J. Immunol.* **185**, 174–182 (2010).
46. S. Sakaguchi, N. Sakaguchi, M. Asano, M. Itoh, M. Toda, Immunologic self-tolerance maintained by activated T cells expressing IL-2 receptor alpha-chains (CD25). Breakdown of a single mechanism of self-tolerance causes various autoimmune diseases. *J. Immunol.* **155**, 1151–1164 (1995).
47. Y. Y. Setiady, J. A. Coccia, P. U. Park, In vivo depletion of $CD4^+FOXP3^+$ Treg cells by the PC61 anti-CD25 monoclonal antibody is mediated by $Fc\gamma RIII^+$ phagocytes. *Eur. J. Immunol.* **40**, 780–786 (2010).
48. A. J. Rech, R. Mick, S. Martin, A. Recio, N. A. Aqui, D. J. Powell Jr., T. A. Colligon, J. A. Trosko, L. I. Leinbach, C. H. Pletcher, C. K. Tweed, A. DeMichele, K. R. Fox, S. M. Domchek, J. L. Riley, R. H. Vonderheide, CD25 blockade depletes and selectively reprograms regulatory T cells in concert with immunotherapy in cancer patients. *Sci. Transl. Med.* **4**, 134ra62 (2012).
49. J. W. Lowenthal, P. Corthésy, C. Tougne, R. Lees, H. R. MacDonald, M. Nabholz, High and low affinity IL 2 receptors: Analysis by IL 2 dissociation rate and reactivity with monoclonal anti-receptor antibody PC61. *J. Immunol.* **135**, 3988–3994 (1985).
50. S. Onizuka, I. Tawara, J. Shimizu, S. Sakaguchi, T. Fujita, E. Nakayama, Tumor rejection by in vivo administration of anti-CD25 (interleukin-2 receptor α) monoclonal antibody. *Cancer Res.* **59**, 3128–3133 (1999).
51. J. Shimizu, S. Yamazaki, S. Sakaguchi, Induction of tumor immunity by removing $CD25^+CD4^+$ T cells: A common basis between tumor immunity and autoimmunity. *J. Immunol.* **163**, 5211–5218 (1999).
52. K. C. Sheehan, J. K. Pinckard, C. D. Arthur, L. P. Dehner, D. V. Goeddel, R. D. Schreiber, Monoclonal antibodies specific for murine p55 and p75 tumor necrosis factor receptors: Identification of a novel in vivo role for p75. *J. Exp. Med.* **181**, 607–617 (1995).
53. X. Zhao, L. Rong, X. Zhao, X. Li, X. Liu, J. Deng, H. Wu, X. Xu, U. Erben, P. Wu, U. Syrbe, J. Sieper, Z. Qin, TNF signaling drives myeloid-derived suppressor cell accumulation. *J. Clin. Invest.* **122**, 4094–4104 (2012).
54. X. Hu, B. Li, X. Li, X. Zhao, L. Wan, G. Lin, M. Yu, J. Wang, X. Jiang, W. Feng, Z. Qin, B. Yin, Z. Li, Transmembrane TNF-α promotes suppressive activities of myeloid-derived suppressor cells via TNFR2. *J. Immunol.* **192**, 1320–1331 (2014).
55. C. Zoglmeier, H. Bauer, D. Nörenberg, G. Wedekind, P. Bittner, N. Sandholzer, M. Rapp, D. Anz, S. Endres, C. Bourquin, CpG blocks immunosuppression by myeloid-derived suppressor cells in tumor-bearing mice. *Clin. Cancer Res.* **17**, 1765–1775 (2011).
56. X. Chen, J. J. Oppenheim, TNF-α: An activator of CD4+FoxP3+TNFR2+ regulatory T cells. *Curr. Dir. Autoimmun.* **11**, 119–134 (2010).
57. Q. Chen, T. S. Davidson, E. N. Huter, E. M. Shevach, Engagement of TLR2 does not reverse the suppressor function of mouse regulatory T cells, but promotes their survival. *J. Immunol.* **183**, 4458–4466 (2009).
58. G. C. Sim, N. Martin-Orozco, L. Jin, Y. Yang, S. Wu, E. Washington, D. Sanders, C. Lacey, Y. Wang, L. Vence, P. Hwu, L. Radvanyi, IL-2 therapy promotes suppressive $ICOS^+$ Treg expansion in melanoma patients. *J. Clin. Invest.* **124**, 99–110 (2014).
59. F. M. Lemoine, M. Cherai, C. Giverne, D. Dimitri, M. Rosenzwajg, H. Trebeden-Negre, N. Chaput, B. Barrou, N. Thioun, B. Gattegnio, F. Selles, A. Six, N. Azar, J. P. Lotz, A. Buzyn, M. Sibony, A. Delcourt, O. Boyer, S. Herson, D. Klatzmann, R. Lacave, Massive expansion of regulatory T-cells following interleukin 2 treatment during a phase I-II dendritic cell-based immunotherapy of metastatic renal cancer. *Int. J. Oncol.* **35**, 569–581 (2009).
60. D. M. Woods, R. Rannakrishnan, A. L. Sodré, A. Berglund, J. Weber, PD-1 blockade induces phosphorylated STAT3 and results in an increase of Tregs with reduced suppressive function. *J. Immunol.* **198** (2017).
61. C. Peligero, J. Argilaguet, R. Güerri-Fernandez, B. Torres, C. Ligero, P. Colomer, M. Plana, H. Knobel, F. García, A. Meyerhans, PD-L1 blockade differentially impacts regulatory T cells from HIV-infected individuals depending on plasma viremia. *PLOS Pathog.* **11**, e1005270 (2015).

62. T. L. Whiteside, The role of regulatory T cells in cancer immunology. *Immunotargets Ther.* **4**, 159–171 (2015).
63. H. Pere, C. Tanchot, J. Bayry, M. Terme, J. Taieb, C. Badoual, O. Adotevi, N. Merillon, E. Marcheteau, V. Quillien, C. Banissi, A. Carpentier, F. Sandoval, M. Nizard, F. Quintin-Colonna, G. Kroemer, W. H. Fridman, L. Zitvogel, S. Oudard, E. Tartour, Comprehensive analysis of current approaches to inhibit regulatory T cells in cancer. *Oncoimmunology* **1**, 326–333 (2012).

Acknowledgments: We thank O. M. Z. Howard, K. T. Czarra, T. He, and P. Li for their help in this study. We thank NCI-Frederick Cancer Inflammation Program Fluorescence Cytometry core (K. B. Noer and R. M. Matthai) for expert technical assistance with flow cytometry, and the excellent administrative support from S. D. Livingstone. **Funding:** This work was supported (in part) by the Intramural Research Program of the NIH, NCI, Center for Cancer Research; Department of Science and Technology, Guizhou Province, under grants G[2014]7020 and J[2015]2003; University of Macau under grants SRG2014-00024-ICMS-QRCM, MYRG2016-00023-ICMS-QRCM, and MYRG2017-00120-ICMS; and the Science and Technology Development Fund of Macao SAR (FDCT) under grant 014/2015/A1. **Author contributions:** Y.N., J.H., H.S., A.L.T., D.Y., and X.C. performed experiments and analyzed data. J.J.O., D.M.K., and X.C. designed and guided the study and prepared the manuscript. **Competing interests:** The authors declare that they have no competing interests.

Submitted 1 March 2017
Accepted 16 November 2017
Published 2 January 2018
10.1126/scisignal.aan0790

Citation: Y. Nie, J. He, H. Shirota, A. L. Trivett, D. Yang, D. M. Klinman, J. J. Oppenheim, X. Chen, Blockade of TNFR2 signaling enhances the immunotherapeutic effect of CpG ODN in a mouse model of colon cancer. *Sci. Signal.* **11**, eaan0790 (2018).

Science Signaling

CANCER

2017 © The Authors, some rights reserved; exclusive licensee American Association for the Advancement of Science.

Androgen receptor inhibitor–induced "BRCAness" and PARP inhibition are synthetically lethal for castration-resistant prostate cancer

Likun Li,[1] Styliani Karanika,[1]* Guang Yang,[1] Jiangxiang Wang,[1] Sanghee Park,[1] Bradley M. Broom,[2] Ganiraju C. Manyam,[2] Wenhui Wu,[2] Yong Luo,[1] Spyridon Basourakos,[1] Jian H. Song,[1] Gary E. Gallick,[1] Theodoros Karantanos,[1†] Dimitrios Korentzelos,[1] Abul Kalam Azad,[1] Jeri Kim,[1] Paul G. Corn,[1] Ana M. Aparicio,[1] Christopher J. Logothetis,[1] Particia Troncoso,[3] Timothy Heffernan,[4] Carlo Toniatti,[5] Hyun-Sung Lee,[6] Ju-Seog Lee,[6] Xuemei Zuo,[1] Wenjun Chang,[1‡] Jianhua Yin,[1‡] Timothy C. Thompson[1§]

Cancers with loss-of-function mutations in *BRCA1* or *BRCA2* are deficient in the DNA damage repair pathway called homologous recombination (HR), rendering these cancers exquisitely vulnerable to poly(ADP-ribose) polymerase (PARP) inhibitors. This functional state and therapeutic sensitivity is referred to as "BRCAness" and is most commonly associated with some breast cancer types. Pharmaceutical induction of BRCAness could expand the use of PARP inhibitors to other tumor types. For example, *BRCA* mutations are present in only ~20% of prostate cancer patients. We found that castration-resistant prostate cancer (CRPC) cells showed increased expression of a set of HR-associated genes, including *BRCA1*, *RAD54L*, and *RMI2*. Although androgen-targeted therapy is typically not effective in CRPC patients, the androgen receptor inhibitor enzalutamide suppressed the expression of those HR genes in CRPC cells, thus creating HR deficiency and BRCAness. A "lead-in" treatment strategy, in which enzalutamide was followed by the PARP inhibitor olaparib, promoted DNA damage–induced cell death and inhibited clonal proliferation of prostate cancer cells in culture and suppressed the growth of prostate cancer xenografts in mice. Thus, antiandrogen and PARP inhibitor combination therapy may be effective for CRPC patients and suggests that pharmaceutically inducing BRCAness may expand the clinical use of PARP inhibitors.

INTRODUCTION

Metastatic prostate cancer (PCa) is incurable and the second leading cause of cancer deaths among men in the Western world (*1*). Although patients initially respond to androgen deprivation therapy, most eventually develop castration-resistant prostate cancer (CRPC) and metastasis to bone, the predominant site of advanced lethal PCa (*2*, *3*). Abiraterone acetate and enzalutamide (ENZ), novel androgen receptor (AR) signaling inhibitors (*4*, *5*), each extends the life of metastatic CRPC patients for 4 to 5 months, but neither of these agents is curative. Therefore, more effective therapies are needed, including novel therapeutic combinations and innovative therapy sequencing approaches.

The development of CRPC is accompanied by the accumulation of gene mutations, chromosomal translocations, and enhanced DNA repair activities that enable CRPC cells to survive and proliferate (*6*–*8*). Moreover, increased expression of certain DNA repair genes reflects reduced DNA repair proficiency, and these activities are associated with greater mutagenesis, adverse clinical features, and inferior patient survival rates (*9*). Poly(adenosine diphosphate–ribose) polymerase (PARP) inhibitors, which can abrogate base excision repair or trap PARP on the DNA, are promising therapeutic agents that show synthetic lethality against many types of cancer with BRCA1 or BRCA2 deficiencies (*10*–*13*). Although a favorable response of cancers to PARP inhibition due to BRCA1 or BRCA2 mutations has been demonstrated, PARP inhibitors have not been widely used in cancers with deficiencies of other homologous recombination (HR) genes. Promising clinical studies using PARP inhibitors are under way (*14*–*16*), and it is now essential to further our understanding of the HR pathway to maximize the benefit of PARP inhibitor therapy for CRPC. BRCA germline/somatic mutations/deletions account for only 12 to 20% of CRPC patients (*6*, *14*, *17*, *18*); therefore, pharmaceutically induced HR deficiency becomes an attractive and clinically viable strategy that potentially expands the benefit of PARP inhibitor therapy to CRPC patients who do not have BRCA mutations.

Accumulating evidence revealed the convergence of DNA damage response (DDR) signaling pathways and AR signaling pathways in PCa (*8*, *19*–*22*). We previously found that an AR- and c-Myb–coregulated DDR gene signature is correlated with PCa metastasis, castration resistance, tumor recurrence, and reduced survival in PCa patients (*8*). The presence of a relatively large number of HR genes in this AR- and c-Myb–coregulated DDR gene signature, together with the identification of a CRPC–up-regulated HR gene signature (Fig. 1), led us to consider that pharmaceutically induced down-regulation of

[1]Department of Genitourinary Medical Oncology, The University of Texas MD Anderson Cancer Center, 1515 Holcombe Boulevard, Houston, TX 77030–4009, USA. [2]Department of Bioinformatics and Computational Biology, The University of Texas MD Anderson Cancer Center, Houston, TX 77030–4009, USA. [3]Department of Pathology, The University of Texas MD Anderson Cancer Center, Houston, TX 77030–4009, USA. [4]Institute for Applied Cancer Science, The University of Texas MD Anderson Cancer Center, Houston, TX 77030–4009, USA. [5]ORBIT (Oncology Research for Biologics and Immunotherapy Translation), The University of Texas MD Anderson Cancer Center, Houston, TX 77030–4009, USA. [6]Department of Systems Biology, The University of Texas MD Anderson Cancer Center, Houston, TX 77030–4009, USA.
*Present address: Infectious Diseases Division, Warren Alpert Medical School of Brown University and Rhode Island Hospital, 593 Eddy Street, Physicians Office Building, Third Floor, Suite 328/330, Providence, RI 02903, USA.
†Present address: General Internal Medicine Section, Boston Medical Center, Boston University School of Medicine, 840 Harrison Avenue, Boston, MA 02118, USA.
‡Present address: Department of Epidemiology, Second Military Medical University, Shanghai 200433, China.
§Corresponding author. Email: timthomp@mdanderson.org

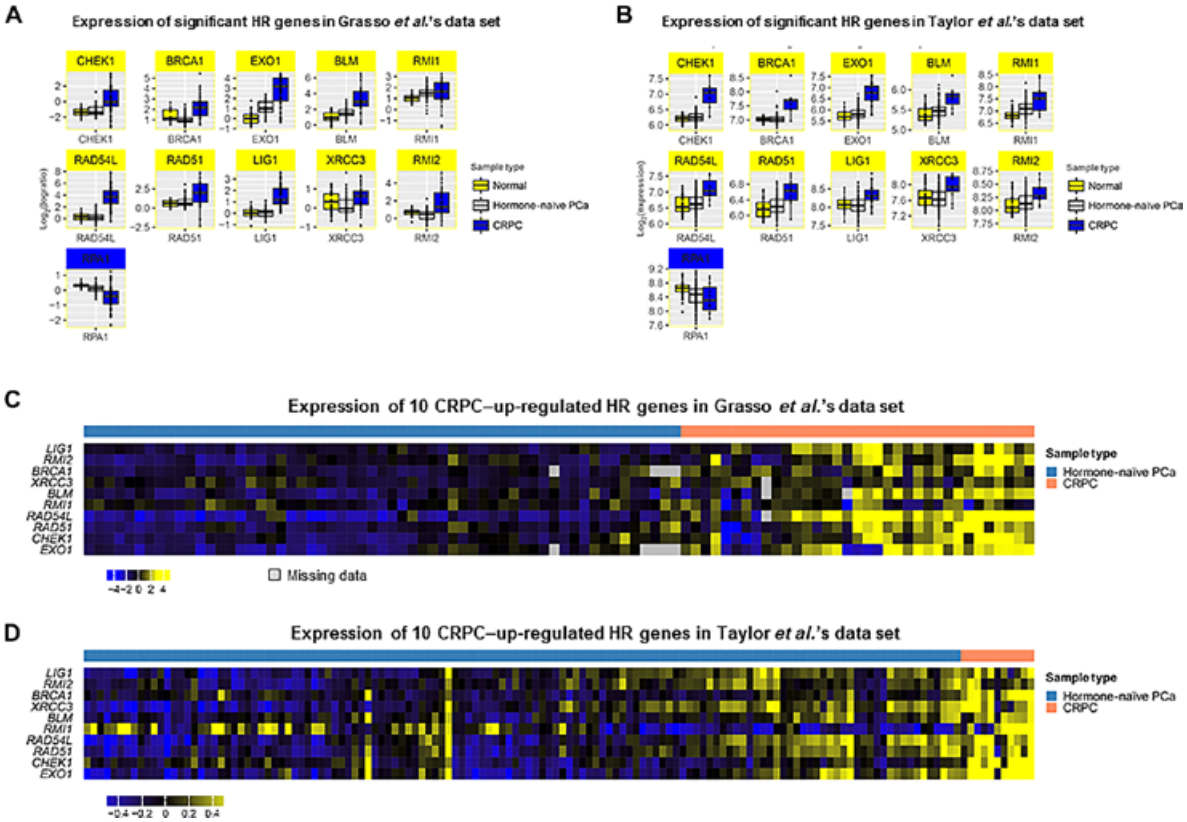

Fig. 1. HR gene expression in human normal prostate and primary PCa and CRPC tissue samples. (**A** and **B**) Box plots showing 10 CRPC–up-regulated (yellow) and 1 CRPC–down-regulated (*RPA1*; blue) HR genes common to two published CRPC data sets. (**C** and **D**) Heat maps showing expression of 10 commonly up-regulated HR genes in two published CRPC data sets.

AR-regulated HR genes may induce HR deficiency and sensitize CRPC to PARP inhibition. Therefore, targeting AR by ENZ and PARP by olaparib (OLA) would generate synthetic lethality in CRPC. Here, we report that ENZ down-regulated a specific set of HR genes, including *BRCA1*, *RAD51AP1*, *RAD51C*, *RAD54L*, and *RMI2*, and this pharmaceutically induced HR deficiency synergizes with the effects of OLA to induce DNA damage–related cell death, inhibit PCa cell clonal growth, and suppress xenograft tumor growth.

RESULTS

Expression of HR-associated genes is up-regulated in CRPC

To extend our previous study showing the correlation of advanced PCa and AR- and c-Myb–coregulated DDR gene signature, in which HR-associated genes are highly represented (*8*), we identified specific HR genes that were up-regulated in CRPC using two public patient data sets (*6*, *17*) and a Gene Ontology–defined set of 37 HR-associated genes. Analysis of these HR genes showed significant differential expression between hormone-naïve primary PCa and CRPC samples. Statistically altered HR genes were identified after Benjamini-Hochberg correction for multiple hypothesis testing ($P < 0.05$), and those common to both data sets were identified (Fig. 1, A and B). There were 10 up-regulated HR genes common to both data sets, including *CHEK1*, *BRCA1*, *EXO1*, *BLM*, *RMI1*, *RAD54L*, *RAD51*, *LIG1*, *XRCC3*, and *RMI2*, and 1 down-regulated HR gene (*RPA1*). Analysis of gene expression in CRPC tissue samples revealed that a set of HR genes is overexpressed in CRPC and positively correlated with CRPC development and adverse clinical outcome (Fig. 1, C and D).

ENZ, OLA, and their combination inhibit HR-associated gene expression in AR-positive PCa cells

To test our hypothesis that pharmaceutically induced down-regulation of AR-regulated HR genes may induce BRCAness and sensitize CRPC to PARP inhibition, we examined the effect of ENZ, OLA, and the combination (ENZ + OLA) on HR gene expression in multiple PCa cell lines with variable androgen dependence. Microarray analysis revealed that expressions of 15 of 37 HR genes were statistically altered in response to drug treatment (after Benjamini-Hochberg correction for multiple hypothesis testing, $P < 0.05$) (Fig. 2A). Among these 15 HR genes, we selected 5 genes, namely, *BRCA1*, *RAD51AP1*, *RAD51C*, *RAD54L*, and *RMI2* for further investigation. Our selections were made on the basis of the following: *BRCA1*, *RAD54L*, and *RMI2* are among the 10 up-regulated HR genes in CRPC in both of the independent clinical data sets (Fig. 1); these 5 genes are among most significantly altered ENZ-targeted, down-regulated HR genes; and these 5 genes are involved in different critical steps in HR-mediated DNA repair (*23*–*26*). Quantitative reverse transcription polymerase chain reaction (qRT-PCR) (Fig. 2, B to D) and Western blotting (Fig. 2E) analyses showed that ENZ treatment inhibited the expression of all five genes in VCaP cells (AR-positive, the most androgen-dependent of the three cell lines used, and derived from a vertebral metastatic lesion of a patient with hormone refractory PCa) and all five genes to a lesser extent in LNCaP cells

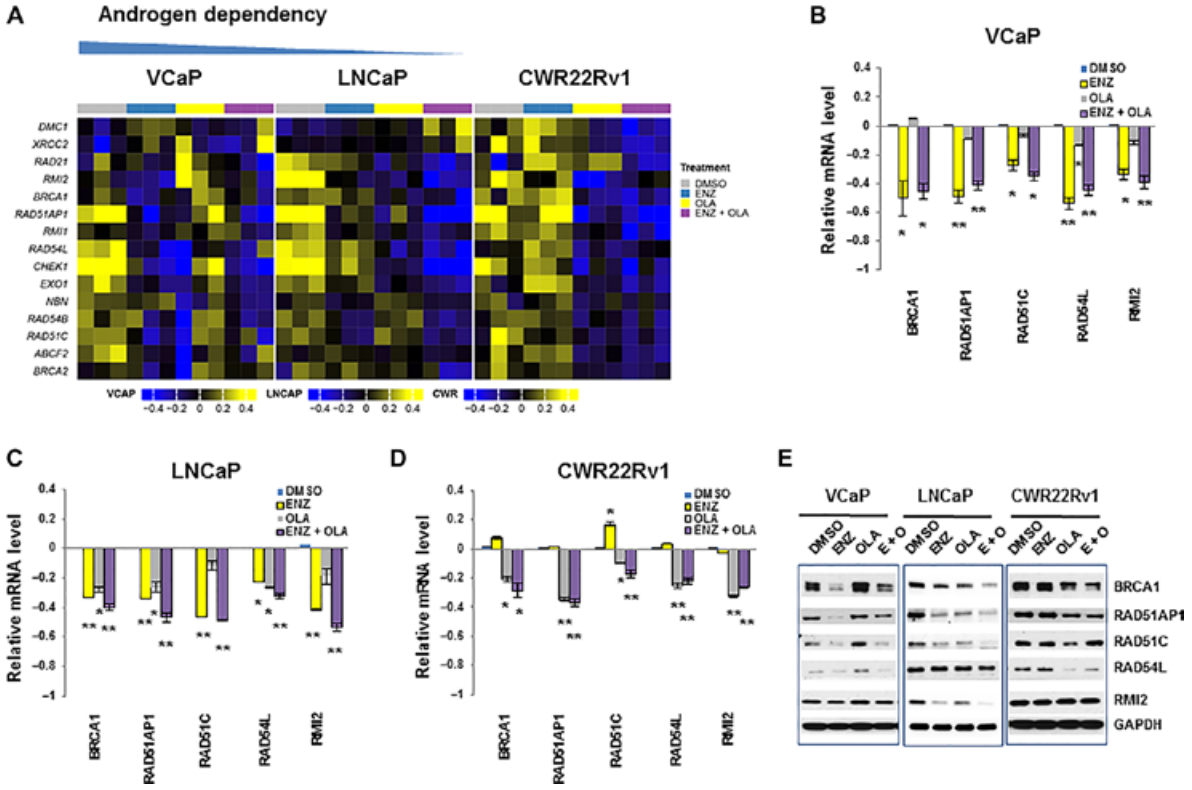

Fig. 2. Cell context–dependent ENZ and OLA down-regulation of HR genes in PCa cells with different androgen dependency. (**A**) Heat map showing the expression of 15 HR-associated genes that were significantly altered by ENZ in AR-positive and androgen-dependent VCaP and LNCaP cells and in AR-positive and androgen-independent CWR22Rv1 cells. Significance ($P < 0.05$) was determined by Benjamini-Hochberg correction for multiple hypothesis testing. (**B** to **D**) qRT-PCR analysis of mRNA expression of five select HR genes in VCaP (B), LNCaP (C), and CWR22Rv1 (D) cells. Data are means ± SD from three experiments. *$P < 0.05$, **$P < 0.01$ (Wilcoxon–Mann-Whitney test). (**E**) Western blotting analysis of five selected HR proteins in the indicated cell lines. E, ENZ; O, OLA. Blots are representative of three or more experiments.

(AR-positive but less androgen-dependent than VCaP and derived from a patient with a supraclavicular lymph node metastatic lesion; this cell line also contains a point mutation in the ligand-binding domain of AR, leading to altered hormone specificity) but did not inhibit any of these genes in CWR22Rv1 cells [AR-positive and androgen-independent and derived from a primary prostate tumor that expresses mutant (H874Y) ARs and secretes low amounts of prostate-specific antigen]. Unexpectedly, OLA treatment suppressed the expression of most of these HR genes in LNCaP cells and all of these HR genes in CWR22Rv1 cells but had very little effect on these HR genes in VCaP cells. Further down-regulation of these HR genes by the combination of ENZ and OLA compared to single agent alone was evident in the LNCaP model (Fig. 2, A to E).

HR genes cooperatively contribute to DNA repair and PCa cell survival

To determine the role of these ENZ–down-regulated HR genes with regard to OLA sensitivity of PCa cells, we performed cell cycle analysis to quantitate sub-G_1 (apoptotic) cells resulting from HR gene silencing and OLA combination treatment. We screened multiple small interfering RNAs (siRNAs) for each HR gene in VCaP cells, selected the two most effective siRNAs for each HR gene to analyze the biological activities in VCaP cells, and then chose the more effective one to use for the analysis in LNCaP and CWR22Rv1 cells. Our results demonstrate that each HR gene differentially contributes to resistance to OLA treatment and PCa cell survival as indicated by the increase in the sub-G_1 cell population in response to knockdown of a specific HR gene (Fig. 3, A to F). Synergy analyses using two-way analysis of variance (ANOVA) (*27*) and Bliss independence model (*28*) indicated that knockdown of BRCA1, RAD51C, or RMI2 synergized with OLA in all three cell lines; knockdown of RAD51AP1 synergized with OLA in VCaP and CWR22Rv1 cells; and knockdown of RAD54L synergized with OLA in LNCaP and CWR22Rv1 cells (Fig. 3, D to F, and table S1).

HR is a multistep biological process (*23*–*26*). We hypothesized that ENZ– and/or OLA–down-regulated HR genes that function at different HR steps cooperatively contribute to DNA repair and PCa cell survival. Therefore, simultaneous knockdown of multiple HR genes should cooperatively enhance the HR deficiency phenotype and synergize the HR defect with OLA. We selected *BRCA1*, *RAD51C*, and *RMI2* to test cooperative functions because these three HR genes are involved in the recruitment of early HR factors to double-strand breaks, formation of the RAD51 nucleoprotein filaments, and resolution of double Holliday junctions, respectively (*23*–*26*) and because the siRNAs for each of these three HR genes showed synergy with OLA treatment in all three cell lines tested (Fig. 3, D to F). Simultaneous knockdown of two or three HR-associated genes markedly increased the abundance of γH2AX protein (a marker of DNA damage) and cleaved PARP (a marker of apoptosis) (Fig. 3G), significantly increased proportion of sub-G_1 cells (Fig. 3H), and significantly reduced capacity for colony formation (Fig. 3I) compared with knockdown of each HR gene singly. Synergistic effects were observed in most of the HR-associated siRNA combinations and HR-associated siRNA and OLA

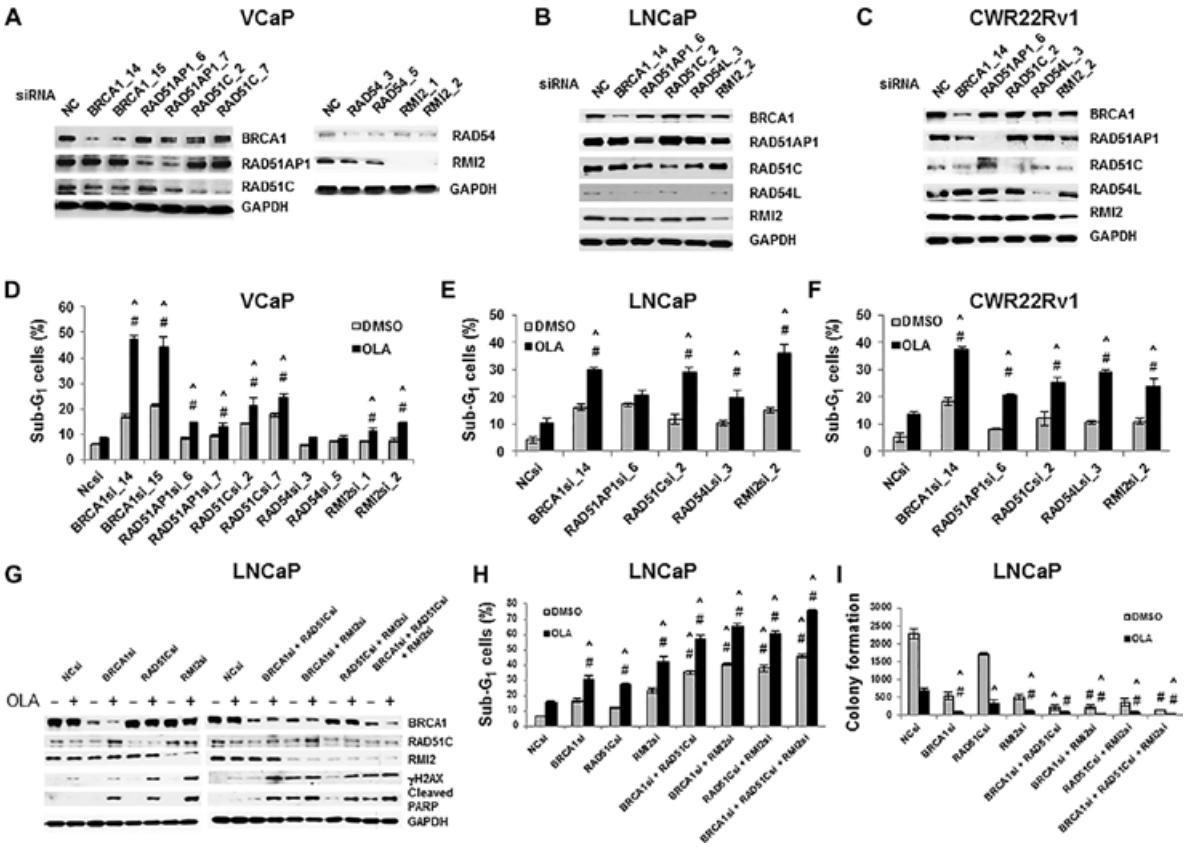

Fig. 3. HR gene silencing synergizes with OLA to increase cytotoxicity to PCa cells. (**A** to **C**) Western blotting analysis for the expression of HR genes in VCaP (A), LNCaP (B), and CWR22Rv1 (C) cells transfected with specific HR gene siRNAs (20 nM). Two siRNAs per HR gene were tested in VCaP cells, as indicated; one each was used in LNCaP and CWR22Rv1. Blots are representative of three or more experiments. (**D** to **F**) Flow cytometry analysis of sub-G_1 cells after siRNA and OLA treatment in VCaP (D), LNCaP (E), and CWR22Rv1 (F) cells transfected as in (A) 24 hours before treatment with dimethyl sulfoxide (DMSO) or OLA (10 μM for 48 hours). (**G**) Western blotting analysis for BRCA1, RAD51C, and RMI2 proteins, γH2AX abundance, and cleaved PARP abundance by RNA interference and OLA, as indicated, in LNCaP cells. Blots are representative of three or more experiments. (**H**) Flow cytometry analysis of sub-G_1 cells for synergistic effects of combinations of three selected HR gene siRNAs in the absence and presence of OLA in LNCaP cells. Data are means ± SD from three experiments. (**I**) Colony assay for synergistic effects of combinations of three selected HR gene siRNAs in the absence and presence of OLA in LNCaP cells. Data are means ± SD from three experiments. #Synergy by two-way ANOVA; ^synergy by Bliss independence analysis (table S1).

combinations (Fig. 3, H and I, and table S1). Dual knockdown of BRCA1 and RMI2 showed the greatest effects (Fig. 3, G to I) among the tested dual siRNA combinations. Together, these results suggest that ENZ-regulated HR genes cooperatively contribute to DNA repair and PCa cell survival.

ENZ and/or OLA inhibits HR efficiency

γH2AX and RAD51 are two markers of DNA damage, DNA repair, and treatment sensitivity in preclinical and clinical samples (*29*). To determine whether ENZ and OLA treatment leads to reduced HR efficiency, we conducted double immunofluorescence staining to assess the formation of γH2AX and RAD51 foci and their colocalization in OLA + ENZ–treated LNCaP cells (Fig. 4A). Quantitative analyses demonstrated that the percentages of cells that contain γH2AX foci were significantly higher in ENZ + OLA–treated cells compared to those in OLA-treated cells (Fig. 4B, left), and the percentage of cells with both γH2AX and RAD51 foci was significantly lower in response to ENZ + OLA treatment than to OLA treatment alone (Fig. 4B, right). Foci ratio of RAD51 to γH2AX was significantly lower in ENZ + OLA–treated cells than in those treated with OLA alone (Fig. 4C). Analysis of drug-treated LNCaP cells using a quantitative PCR (qPCR)–based HR assay showed that ENZ and OLA each reduced HR efficiency and that their combination further reduced HR efficiency (Fig. 4D). Western blotting analysis of drug-treated LNCaP cells indicated that ENZ + OLA combination treatment markedly increased DNA damage or its persistence (γH2AX) and DNA damage–induced apoptosis (cleaved PARP) (Fig. 4E). Together, these data suggest that the cytotoxic effects of the ENZ + OLA combination are mediated by deficient DNA repair.

Lead-in ENZ + OLA strategy synergistically increases apoptosis and inhibits clonogenic growth in PCa cells

To optimize treatment conditions of ENZ and OLA combination, we compared a lead-in ENZ + OLA treatment strategy with a traditional concomitant ENZ + OLA strategy. In the lead-in ENZ + OLA treatment, we pretreated PCa cells with ENZ for 24 hours (lead-in time) and then with ENZ + OLA for 48 hours. This protocol achieved ENZ-mediated down-regulation of HR genes before OLA was applied. In the concomitant ENZ + OLA treatment, cells were treated with DMSO (vehicle control for ENZ) for 24 hours and then with ENZ + OLA for 48 hours.

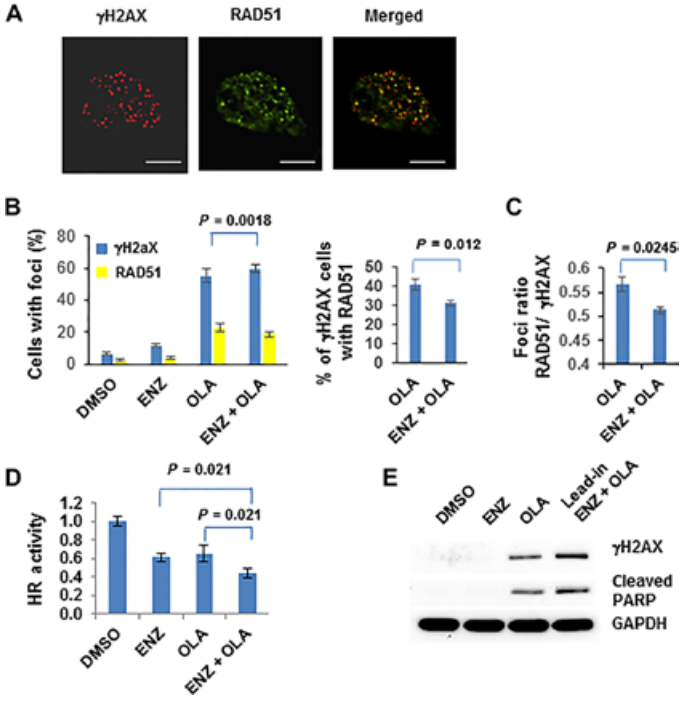

Fig. 4. ENZ and OLA suppress DNA repair in PCa. (**A**) Double immunofluorescence to detect γH2AX (red) and RAD51 (green) foci and their colocalization in OLA + ENZ–treated LNCaP cells. (**B** and **C**) Quantitation (percentage) of γH2AX or RAD51 foci-positive cells and γH2AX and RAD51 foci-double positive cells (B) and the ratio of RAD51 to γH2AX foci in LNCaP cells. (**D**) Relative HR activity was calculated by a two-step normalization: The number of PCR cycles in assay primer group was normalized by that in universal primer group (internal control); the number of PCR cycles in treatment groups was normalized by that of control, with control = 1. Data are means ± SD from three experiments. *P* values were derived from Wilcoxon–Mann-Whitney Test. (**E**) Western blotting analysis of γH2AX and cleaved PARP in lead-in ENZ + OLA–treated cells compared to those in OLA-treated cells. Blots are representative of three experiments.

The resulting data showed that the lead-in ENZ + OLA treatment increased sub-G_1 cells and inhibited colony growth more effectively than traditional concomitant ENZ + OLA treatment in VCaP and LNCaP cells (AR-positive and androgen-dependent), but not in CWR22Rv1 cells (AR-positive and androgen-independent) (Fig. 5, A to D, and table S1).

Because the lead-in ENZ + OLA treatment protocol further increased the number of apoptotic cells compared to the concomitant ENZ + OLA protocol, we considered differential ENZ versus OLA apoptotic activities combined with increased exposure to ENZ during the lead-in treatment phase as underlying cooperative mechanisms for the lead-in effect. Using unambiguous pro- and antiapoptotic gene subsets derived from the Gene Ontology–defined apoptosis gene set (GO: 0006915), we pooled microarray expression data of these pro- and antiapoptotic genes, adjusted *P* value using Benjamini-Hochberg procedure for multiple hypothesis testing, and identified statistically significant ($P < 0.05$) alterations in gene expression in ENZ, OLA, or lead-in ENZ + OLA–treated samples compared to those treated with vehicle (tables S2 and S3). In addition to overlapping subsets of ENZ- and OLA-induced up-regulated proapoptotic genes and overlapping subsets of ENZ- and OLA-induced down-regulated antiapoptotic genes, which could contribute to synergistic effects from ENZ and OLA, we found that two of the antiapoptotic genes, encoding serum/glucocorticoid-regulated kinase 1 (SGK1) and tumor necrosis factor–α (TNF-α)–induced protein 8 (TNFAIP8), were down-regulated by ENZ but up-regulated by OLA, which led us to speculate that the lead-in protocol would enable maximal ENZ-induced suppression and delay OLA up-regulation of these specific antiapoptotic genes. Both SGK1 and TNFAIP8 reportedly participate in apoptosis evasion, cell survival, chemoresistance, and tumor progression (Fig. 5E) (*30*–*34*). Western blotting analysis validated select ENZ– and OLA–up-regulated pro-apoptotic genes and ENZ–down-regulated and OLA–up-regulated *SGK1* and *TNFAIP8* (Fig. 5F). To validate the pro–cell survival roles of SGK1 and TNFAIP8, we knocked down each in LNCaP cells (Fig. 5G) and performed cell cycle analysis to assess sub-G_1 cell distribution. SGK1 knockdown alone caused only a slight increase in the proportion of sub-G_1 cells but significantly increased the proportion of sub-G_1 cells when combined with OLA, whereas TNFAIP8 knockdown alone significantly increased the proportion of sub-G_1 cells that was further increased by combination with OLA (Fig. 5H). Our data suggest that, in addition to down-regulation of specific HR genes, down-regulation of *SGK1* and *TNFAIP8* expression by ENZ before OLA treatment, in part, contributes to the superior therapeutic effect of the lead-in ENZ + OLA strategy.

Lead-in ENZ + OLA treatment strategy synergistically suppresses PCa growth

To test our finding of synergism in the lead-in ENZ + OLA treatment strategy in vivo, we analyzed ENZ or OLA alone and concomitant or lead-in ENZ + OLA combination treatment using a subcutaneous patient-derived xenograft (PDX) tumor model [MDA PCa 133-4, AR-positive, and implanted in precastrated severe combined immunodeficiency (SCID) mice] and two orthotopic PCa cell line xenograft models (VCaP, AR-positive, and androgen-dependent; CWR22Rv1, AR-positive, and androgen-independent) (Fig. 6A). In the MDA 133-4 subcutaneous model, treatment with ENZ or OLA alone was sufficient to suppress tumor growth, indicated by reduced tumor volumes (Fig. 6B) and tumor weights (Fig. 6C), with ENZ demonstrating superior efficacy among the two single agents. The in vivo lead-in treatment with ENZ + OLA, which mimicked that used in cultured cells, achieved significantly greater tumor suppression than treatment with either OLA or ENZ alone or with concomitant ENZ + OLA treatment (Fig. 6, B and C). Synergy analysis revealed a synergistic therapeutic effect in the lead-in ENZ + OLA group (Fig. 6, B and C, and table S1). Analysis of xenograft tumor samples demonstrated significantly reduced BRCA1 protein abundance and Ki67 staining in tumors from mice treated with the lead-in ENZ + OLA protocol compared to those from mice treated with vehicle, ENZ, or OLA alone, or concomitant ENZ + OLA (Fig. 6, D and E). Similar results were observed using VCaP orthotopic xenograft model (Fig. 7). ENZ had superior efficacy in the MDA 133-4 and VCaP models; by contrast, in the CWR22Rv1 model, OLA showed superior efficacy, and the lead-in ENZ + OLA and concomitant ENZ + OLA showed efficacy similar to that of OLA alone (Fig. 8, A to C). Although BRCA1 abundance was relatively unchanged (Fig. 8D), Ki67 labeling was significantly reduced in CWR22Rv1 xenograft samples from OLA- or lead-in ENZ + OLA–treated mice (Fig. 8E).

DISCUSSION

The utilization of PARP inhibitors such as OLA has rapidly evolved from in vitro studies to clinical applications (*16*, *35*, *36*). However, only

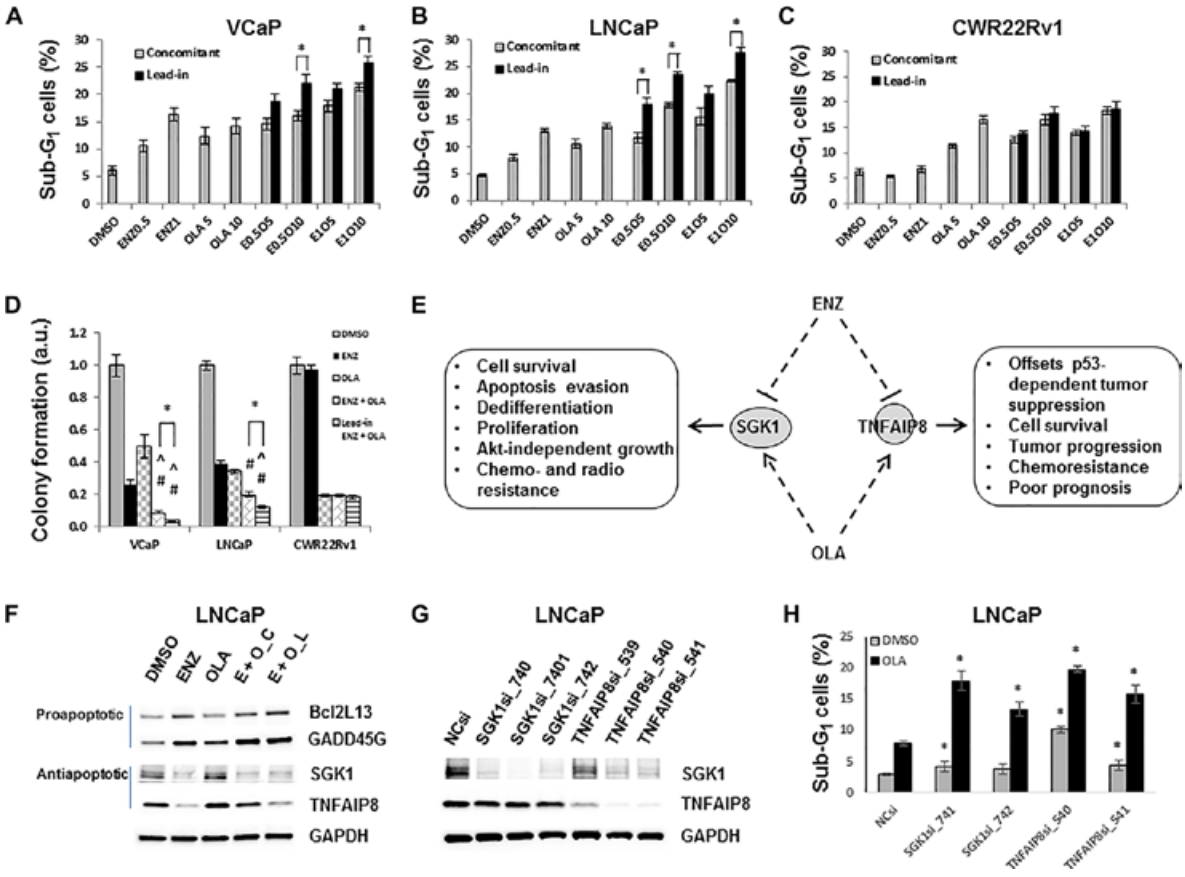

Fig. 5. A superior lead-in effect and its underlying mechanisms. (**A** to **C**) Cell cycle analysis. Cells were pretreated with ENZ (0.5 or 1 μM) or DMSO (vehicle control) for 24 hours, followed by the treatment with DMSO, ENZ (0.5 or 1 μM) or OLA (5 or10 μM), or ENZ + OLA for 48 hours. (**D**) Colony assay. Optimal concentrations of ENZ and OLA were determined for each cell line by drug titration (fig. S2). Cells were pretreated with ENZ (VCaP, 100 nM; LNCaP, 150 nM; CWR22Rv, 1 μM) or DMSO (vehicle) for 24 hours, followed by treatment with ENZ, OLA (VCaP, 2.5 μM; LNCaP, 1.5 μM; CWR22Rv1, 500 nM), ENZ + OLA, or DMSO for 10 to 20 days depending on the cell line. #Synergy by two-way ANOVA; ^synergy by Bliss independence model. a.u., arbitrary units. (**E**) Functional illustration of two ENZ–down-regulated and OLA–up-regulated antiapoptotic genes *SGK1* and *TNFAIP8*. (**F**) Western blotting analysis of selected pro- and antiapoptotic proteins from LNCaP cells treated with DMSO, ENZ, OLA, E + O_C (concomitant), or E + O_L (lead-in). (**G**) Western blotting analysis for SGK1 and TNFAIP8 in control and siRNA-transfected LNCaP cells. Blots are representative of three experiments. (**H**) Sub-G_1 cell analysis in control, SGK1 siRNA-, or TNFAIP8 siRNA-transfected in LNCaP cells. Data are means ± SD from three experiments. *$P < 0.05$ by Wilcoxon–Mann-Whitney test [(A to C) versus the corresponding concomitant condition and (H) versus the control siRNA under DMSO condition].

recently has limited information become available for PCa. Recent reports include the results from preclinical models (*8*, *37*), a phase 1 clinical trial using OLA as single agent (*15*), a phase 1/2 clinical trial using veliparib in combination with temozolomide (*38*, *39*), and a more recent phase 2 trial using OLA (*14*). It is noteworthy that Mateo *et al.* extended the BRCAness concept to mutations/deletions of genes involved in HR regulation (*ATM*), HR factor nuclear localization (*PALB2*), and chromatin remodeling during HR DNA repair (*HDAC2*), which conceptually supports our finding that *BRCA1/2* and other HR genes involved in different stages of HR DNA repair cooperatively contribute to OLA sensitivity and our proposal that pharmaceutically induced HR deficiency as a therapy concept for future clinical applications of OLA. By demonstrating that 10 specific HR genes are up-regulated in CRPC in two public data sets and that these up-regulated HR genes represent therapy targets for ENZ + OLA combination treatment, we introduce a specific biomarker panel for the use of PARP inhibitors and expand the concept of BRCAness to the concept of HR deficiency for CRPC as regard to clinical applications of PARP inhibitors for synthetic lethal therapy.

HR occurs through a series of steps (*23*, *25*, *26*), and the five ENZ–down-regulated HR genes that we identified are involved in almost all the major steps. Our data suggest that each ENZ–down-regulated HR gene has a role in HR and the maintenance of PCa cell survival but that *BRCA1*, *RAD51C*, and *RMI2*, in particular, cooperatively contribute to DNA repair and PCa cell survival, perhaps through their roles during sequential steps in the HR pathway. The superior performance of dual and triple knockdown underscores redundancy among HR mediators that may oppose PARP inhibitor efficacy. Therefore, ENZ-induced suppression of multiple HR genes is a viable strategy to improve the efficacy of PARP inhibitors. The concept, if applied clinically, may extend the benefit of PARP inhibition therapy to CRPC patients who do not bear germline or somatic mutations in or deletion of *BRCA1/2* or other HR genes.

We also demonstrated that lead-in ENZ + OLA has a clear advantage compared to concomitant ENZ + OLA. In addition to down-regulation of a specific set of HR genes by ENZ before OLA treatment, this strategy also allows maximal ENZ suppression of and delay of OLA up-regulation of specific antiapoptotic genes. SGK1 and TNFAIP8 are

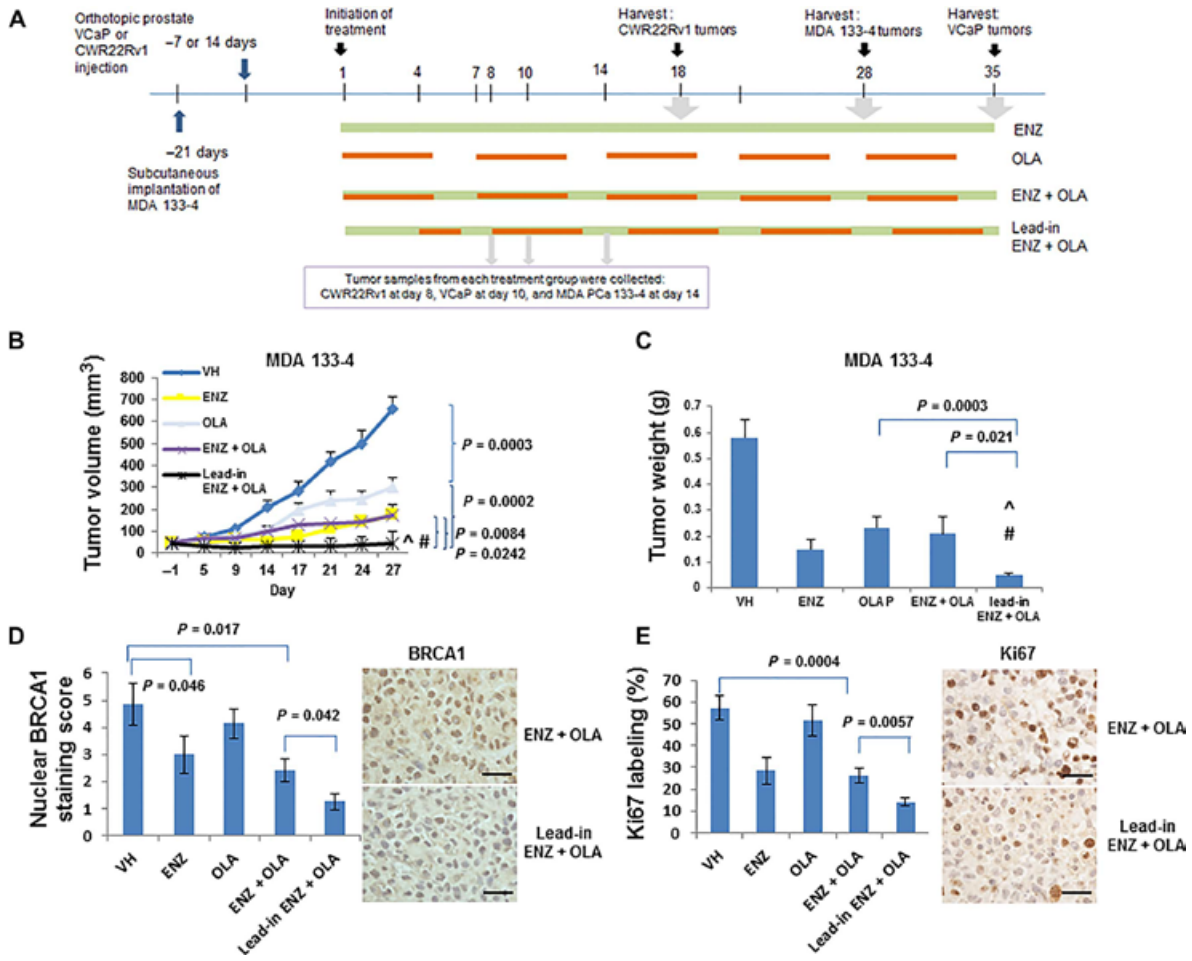

Fig. 6. Scheme of in vivo experiments and results of MDA PCa 133-4 subcutaneous model. (**A**) Scheme of in vivo experiments for VCaP and CWR22Rv1 orthotopic models and MDA 133-4 subcutaneous model. (**B** and **C**) Suppression of MDA PCa 133-4 subcutaneous tumor growth by ENZ and OLA. Tumor growth (B) assessed 1 day before treatment and through 27 days of therapy and tumor weight (C) assessed at day 27 of treatment in MDA 133-4 subcutaneous xenografts. Data are means ± SE from 10 or more mice in each group. *P* values were derived from ANOVA *t* test. #Synergy determined by two-way ANOVA; ^synergy determined by Bliss independence analysis. VH, vehicle. (**D** and **E**) Immunostaining for BRCA1 (D) and Ki67 (E) at day 14 of the indicated treatment. Data are means ± SE from seven or more mice; *P* values were derived from Wilcoxon–Mann-Whitney test.

two ENZ–down-regulated and OLA–up-regulated antiapoptotic genes identified in this study, and knockdown of either gene was proved to have significant synergistic effect with PARP inhibition as regard to apoptotic cell death. These results suggest that down-regulation of SGK1 and TNFAIP8 by ENZ before OLA treatment is, at least, one of the mechanisms underlying the superior effect of lead-in ENZ + OLA over concomitant ENZ + OLA; they are also consistent with growing evidence that links SGK1 and TNFAIP8 to cancer cell survival, metastasis, and chemo- and radioresistance (*30*–*34*).

The results of our xenograft studies provided particularly compelling support for the clinical utility of the ENZ + OLA combination treatment approach for advanced PCa or CRPC. Synergistic growth suppression was associated with ENZ-sensitive models (that is, MDA PCa133-4 and VCaP). The lead-in approach demonstrated clear superiority of the ENZ + OLA combination treatments for the ENZ-sensitive models compared to the traditional concomitant application protocols. Suppression of nuclear *BRCA1* levels by the ENZ + OLA combination was associated with treatment efficacy in these models. Overall, these results have direct relevance for future ENZ + OLA clinical trials, which should be considered in light of our results.

Our data also showed that OLA strongly suppressed HR genes in androgen-independent CWR22Rv1 cells, indicating a cell context–dependent role for OLA in HR gene regulation, and it is noteworthy that our results suggest a transition from AR- to PARP-dependent regulation of HR genes. Future studies are warranted to address these possibilities. Although ENZ failed to synergize with OLA in this cell line model, OLA can down-regulate HR genes in this type of PCa cells and compensate for the loss of ENZ effect.

Overall, our study provides new insights into the molecular functions of ENZ, adds mechanistic rationale to the ENZ + OLA combination therapy, and underscores the importance of an expanded BRCAness concept in future clinical usage of OLA. Our findings support a randomized clinical trial for OLA as single agent or in combination with other agents in unselected patients with CRPC. Future investigations using baseline and OLA-treated patient tissue samples are warranted to link the genomic and transcriptomic landscape, including these ENZ–down-regulated HR genes, with patient response to OLA therapy.

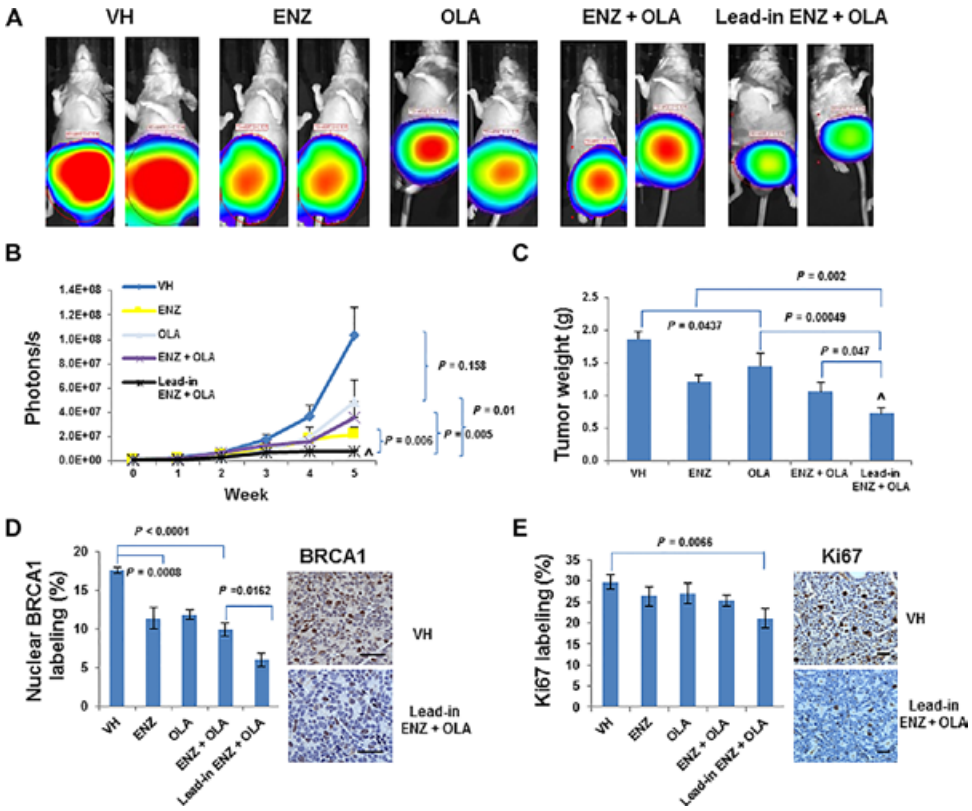

Fig. 7. Suppression of VCaP orthotopic xenograft tumor growth by ENZ and OLA treatment. (**A** to **C**) Representative luminescent images (A), tumor growth (B), and tumor weight (C) of VCaP orthotopic xenografts treated as indicated. Images are representative of experiments, and data are means ± SE from 17 or more mice in each group. *P* values were derived from ANOVA *t* test. ^Synergy determined by Bliss independence analysis. (**D** and **E**) Immunohistochemcal staining for BRCA1 (D) and Ki67 (E) at 7 (BRCA1) or 10 (Ki67) days of the indicated treatment. Data are means ± SD from four or more mice. *P* values were derived from Wilcoxon–Mann-Whitney test.

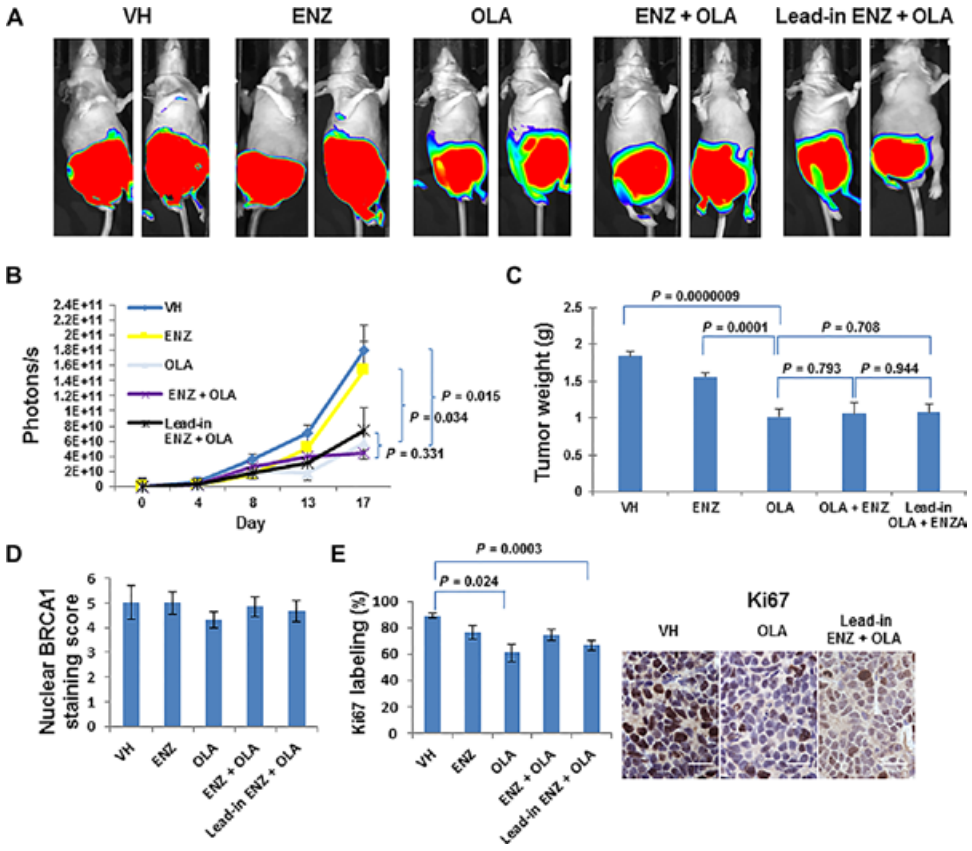

Fig. 8. Suppression of CWR22Rv1 orthotopic xenograft tumor growth by ENZ and OLA treatment. (**A**) Representative bioluminescent images from 10 or more mice in each group. (**B** and **C**) Tumor growth (B) and weight (C) of CWR22Rv1 orthotopic xenografts from mice treated as indicated. Data are means ± SE. ^Synergy by Bliss independence analysis. (**D** and **E**) Immunohistochemical staining for BRCA1 (D) and Ki67 (E) in tumors removed from mice after 8 days of the indicated treatment. Data are means ± SE from six or more mice. *P* values were derived from Wilcoxon–Mann-Whitney test.

MATERIALS AND METHODS

Sources of cell lines and PDXs

VCaP and LNCaP (American Type Culture Collection) and CWR22Rv1 (from F. M. Sirotnak of Memorial Sloan Kettering Cancer Center) cell lines were validated by short tandem repeat DNA fingerprinting with the AmpFlSTR Identifiler PCR Amplification Kit (Applied Biosystems) in MD Anderson's Characterized Cell Line Core Facility. Genetic background (genomic alterations and copy number variations) of these cell lines, VCaP-luc, CWR22Rv1-luc, and MDA 133-4 PDX model was analyzed using MDA T200 platform and summarized in fig. S1.

Gene expression microarray

Complementary DNA (cDNA) microarray was performed using Illumina TotalPrep RNA Amplification Kit (Thermo Scientific) and Illumina Human HT-12 v4.0 Expression BeadChip Kit (Illumina). Microarray data were deposited in the Gene Expression Omnibus (GEO) database (accession number GSE69249).

Bioinformatics and biostatistics analyses

Samples of Grasso *et al.* [GSE35988; (*6*)] were profiled on two different Agilent Whole Genome Microarrays. The two expression matrices (GPL6480 and GPL6848) were combined for bioinformatics/biostatistics analyses because no obvious batch effect was detected by principal component analysis. Samples of Taylor *et al.* [GSE21034; (*17*)] were profiled on Affymetrix Human Exon 1.0 ST arrays, and transcript-level expression matrix (GPL10264) was used for the analyses. The transcript accession numbers were converted to gene symbols using University of California, Santa Cruz reference gene annotation file, and median expression level was used for genes with multiple transcripts. To compare the expression of 37 HR genes between normal prostate and hormone-naïve PCa and CRPC samples, a linear model was fit to each of the genes, followed by Tukey's all-pair comparisons of the independent variable using R package "multcomp." The overall *P* values were adjusted by Benjamini-Hochberg procedure. Genes with significant overall *P* value (<0.05) and also with significant *P* value when comparing CRPC either to hormone-naïve PCa or to normal prostate samples were selected from both Grasso and Taylor data sets. The commonly significantly up-regulated and down-regulated genes were used for box plots (Fig. 1, A and B). The expression profile of the 10 commonly up-regulated genes in the samples of Grasso *et al.* (Fig. 1C) and Taylor *et al.* (Fig. 1D) was shown in semisupervised hierarchical clustering heat maps. A similar statistical analysis was performed in cell line microarray data. The mean expression level was used for genes with multiple probes. The expression profile of genes with significant overall *P* value and also significant *P* value when comparing ENZ + OLA to DMSO for any of the three cell lines was shown in supervised hierarchical clustering heat maps (Fig. 2A). Genes associated with apoptosis were obtained by the Gene Ontology term "apoptosis" (GO: 0006915) and manually curated to characterize the pro- and antiapoptosis gene sets on the basis of PubMed gene descriptions. Difference of gene expression across various treatments was assessed using ANOVA in these gene sets. The *P* values were adjusted for multiple testing by Benjamini-Hochberg (false discovery rate) method. Genes with adjusted *P* values less than 0.05 are defined as significant. Further, Tukey's test was used to perform multiple comparison assessment with all the contrasts of interest in the data set.

Quantitative reverse transcription polymerase chain reaction

Total RNA from cancer cell lines was extracted with the RiboPure RNA extraction kit (Thermo Fisher Scientific). Reverse transcription reactions were carried out with the High-Capacity cDNA Archive Kit (Applied Biosystems) according to the manufacturer's protocol. Real-time PCR was performed using the ABI PRISM 7000 sequence detection system (Applied Biosystems) according to the manufacturer's instructions. The relative quantity of mRNA was determined by the $\Delta\Delta C_T$ (comparative change in cycle threshold) method as described by the manufacturer and normalized to glyceraldehyde-3-phosphate dehydrogenase (GAPDH) RNA in the same cDNA preparation. Primers and probes used for qRT-PCR were purchased from Integrated DNA Technologies and are listed in table S4.

Immunohistochemical analysis

Antibodies to BRCA1 (Abcam, M110) and Ki67 (Santa Cruz Biotechnology, SC15401) were used for immunostaining on formalin-fixed paraffin-embedded tissue slides from the mouse PCa xenografts. Briefly, rehydrated slides were microwave-heated for 20 min in citrate buffer (10 mM, pH 6.0) for antigen retrieval. They were then incubated with 1% H_2O_2 for 10 min to inactivate endogenous horseradish peroxidase (HRP). After blocking with serum-free protein block (Dako, X0909), they were incubated with the primary antibodies (BRCA1, 1:100; Ki67, 1:100) for 90 min at room temperature, followed by incubation with HRP-conjugated secondary antibody (Dako, K4061) for 40 min at room temperature. The immunoreaction products were visualized with 3,3′-diaminobenzidine/H_2O_2 solution. For quantitative analyses, 15 to 20 microscopic fields (at 200×) from each specimen were randomly selected, and immunostaining results were evaluated by investigators (G.Y. and D.K.) who were blinded to the treatment information of a specimen, and the nuclear BRCA1 or Ki67 labeling rates were recorded.

Lead-in ENZ + OLA treatment in cultured cells

VCaP, LNCaP, and CWR22Rv1 cells were pretreated with 1 μM ENZ or DMSO vehicle control for 24 hours, followed by treatment with ENZ (1 μM), OLA (10 μM for VCaP and LNCaP and 5 μM for CWR22Rv1), ENZ + OLA, or DMSO for 48 hours. The selection of OLA concentrations was based on the sensitivity of PCa cell lines to OLA.

Western blotting

Proteins were separated by electrophoresis using 4 to 20% gradient Mini-PROTEAN TGX Gels (Bio-Rad) and transferred onto a nitrocellulose blotting membrane (GE Healthcare Life Sciences). Blots with interested proteins were blocked with tris-buffered saline buffer containing 0.1% Tween 20 and 5% nonfat milk for 1 hour and incubated with specific primary antibody overnight in a cold room rocker. After incubation with HRP-conjugated secondary antibody, blots were incubated with SuperSignal West Dura Extended Duration Substrate (Thermo Scientific) for 2 min and imaged with ChemiDoc MP Imaging System (Bio-Rad). Antibodies against BRCA1 (1:2000), RAD51AP1 (1:200), RAD51C (1:200), RAD54 (1:200), RMI2 (1:2000), and TNFAIP8 (1:500) were purchased from Abcam. Antibodies against γH2AX (1:250), cleaved PARP (1:500), SGK1 (1:250), and GAPDH (1:10,000) were purchased from Cell Signaling Technology.

HR assay

HR assays were performed using LNCaP cells and an HR Assay Kit (Norgen Biotek) according to the manufacturer's suggested protocol. Briefly, LNCaP cells were transfected with dl-1 and dl-2 vectors that carried a mutated lacZ gene in each plasmid using FuGENE Transfection Reagent (Roche). After 6 hours of plasmid transfection, cells were pretreated with ENZ or DMSO vehicle control for 18 hours and then

treated with DMSO, ENZ, OLA, or ENZ + OLA for 24 hours. Total DNA was isolated, and qPCR analysis was performed using universal primers (for internal normalization) and assay-specific primers. The PCR cycle numbers for each sample using assay-specific primers was first normalized with respect to that in each sample using universal primers and then normalized with respect to control (control = 1).

RNA interference

Cells were seeded 1 day before siRNA transfection [six-well format (for RNA or protein preparation): VCaP, 1×10^6 per well; LNCaP, 5×10^5 per well; CWR22Rv1, 2×10^5 per well; 24-well format (for cell cycle analysis): one-fifth of cell numbers of six-well format). siRNA transfection was performed with 20 nM siRNA using RNAiMAX (Life Technologies) according to the manufacturer's protocol. The sources and sequences of siRNAs are listed in table S5.

Flow cytometry analysis

Flow cytometry analysis was performed as described previously (*8*). Briefly, cells were seeded onto 24-well plates 1 day before the drug treatment or siRNA transfection. Flow cytometry analysis was performed 48 hours after the drug treatment or siRNA transfection. In the case of siRNA and drug combination, siRNA transfection was performed 1 day before the drug treatment, and flow cytometry analysis was performed 48 hours after the drug treatment. Cells were harvested and prepared as a single-cell suspension, washed with phosphate-buffered saline, incubated with a staining buffer containing 0.1% sodium citrate, 0.1% Triton X-100, and propidium iodine (50 mg/ml) for 30 min at 4°C, and proceeded to cell cycle analysis with a FACSCanto II flow cytometer (BD Biosciences). Cell cycle profiles and quantitative data were obtained using FlowJo software (Tree Star Inc.).

Clonogenic assay

PCa cells were seeded at a low density in six-well plates (VCaP, 1×10^5 per well; LNCaP, 2×10^4 per well; CWR22Rv1, 5×10^3 per well) and grown in normal growth medium for 10 to 20 days, and colonies were stained with 0.5% crystal violet and counted as described previously (*8*). Experiments were performed in triplicate, and data were means ±SD from three or more independent experiments.

Xenograft tumor assays

For the MDA 133-4 PDX model, equal-sized tumor pieces were implanted into subcutaneous pockets in the flanks of 6- to 8-week-old male CB17 SCID mice (Charles River Laboratories International Inc.). VCaP cells (3×10^6) and CWR22Rv1 cells (2×10^6) were injected orthotopically into the prostates. When tumors reached an approximate volume of 30 mm^3, tumor-bearing mice were randomly placed in experimental subgroups to receive ENZ, OLA, ENZ + OLA (concomitant or lead-in: 4-day pretreatment of ENZ before combined treatment with ENZ + OLA), or a vehicle control (ENZ, 10 mg/kg every day orally; OLA, 40 mg/kg per day, 5 days each week, intraperitoneally). Subcutaneous tumor growth was monitored twice per week by caliper measurement, and orthotopic tumor growth was monitored weekly by bioluminescent images. Mice were sacrificed, and tumor wet weights were determined. A subset of mice was euthanized, tumor specimens were collected, and formalin-fixed paraffin-embedded tissue slides were prepared for immunohistochemical analysis of BRCA1 and Ki67 from tumors taken before or after 8 to 14 days of treatment.

Statistical analysis

ANOVA was used to assess the difference of gene expression, and Benjamini-Hochberg correction for multiple hypothesis testing was used to adjust the *P* values in the determination of statistically altered HR genes in human PCa patient samples and in drug-treated PCa cell line samples and statistically altered pro- or antiapoptotic genes in drug-treated PCa cell line samples. Wilcoxon–Mann-Whitney test was used for data with non-normal distributions or data with small sample sizes, including qRT-PCR, cell cycle analysis, colony assay, and immunohistochemical analyses. ANOVA *t* test was used for analysis of tumor growth and tumor wet weights. Synergistic effects were determined by two-way ANOVA tests (*27*) and by the Bliss independence model (*28*).

SUPPLEMENTARY MATERIALS

www.sciencesignaling.org/cgi/content/full/10/480/eaam7479/DC1
Fig. S1. Sequence and copy number variation analysis using T200 platform.
Fig. S2. Titration of ENZ and OLA for colony assays.
Table S1. Determination of synergy.
Table S2. Expression of proapoptotic genes.
Table S3. Expression of antiapoptotic genes.
Table S4. Primers and probes for qRT-PCR.
Table S5. siRNA sources and sequences.

REFERENCES AND NOTES

1. R. Siegel, D. Naishadham, A. Jemal, Cancer statistics. *CA Cancer J. Clin.* **62**, 10–29 (2012).
2. D. A. Loblaw, K. S. Virgo, R. Nam, M. R. Somerfield, E. Ben-Josef, D. S. Mendelson, R. Middleton, S. A. Sharp, T. J. Smith, J. Talcott, M. Taplin, N. J. Vogelzang, J. L. Wade III, C. L. Bennett, H. I. Scher, Initial hormonal management of androgen-sensitive metastatic, recurrent, or progressive prostate cancer: 2006 Update of an American Society of Clinical Oncology practice guideline. *J. Clin. Oncol.* **25**, 1596–1605 (2007).
3. J. Sturge, M. P. Caley, J. Waxman, Bone metastasis in prostate cancer: Emerging therapeutic strategies. *Nat. Rev. Clin. Oncol.* **8**, 357–368 (2011).
4. C. L. Derleth, E. Y. Yu, Targeted therapy in the treatment of castration-resistant prostate cancer. *Oncology* **27**, 620–628 (2013).
5. N. J. Vogelzang, Two paths forward in metastatic castration-resistant prostate cancer. *Oncology* **27**, 638–639 (2013).
6. C. S. Grasso, Y.-M. Wu, D. R. Robinson, X. Cao, S. M. Dhanasekaran, A. P. Khan, M. J. Quist, X. Jing, R. J. Lonigro, J. C. Brenner, I. A. Asangani, B. Ateeq, S. Y. Chun, J. Siddiqui, L. Sam, M. Anstett, R. Mehra, J. R. Prensner, N. Palanisamy, G. A. Ryslik, F. Vandin, B. J. Raphael, L. P. Kunju, D. R. Rhodes, K. J. Pienta, A. M. Chinnaiyan, S. A. Tomlins, The mutational landscape of lethal castration-resistant prostate cancer. *Nature* **487**, 239–243 (2012).
7. S. C. Baca, D. Prandi, M. S. Lawrence, J. M. Mosquera, A. Romanel, Y. Drier, K. Park, N. Kitabayashi, T. Y. MacDonald, M. Ghandi, E. Van Allen, G. V. Kryukov, A. Sboner, J. P. Theurillat, T. D. Soong, E. Nickerson, D. Auclair, A. Tewari, H. Beltran, R. C. Onofrio, G. Boysen, C. Guiducci, C. E. Barbieri, K. Cibulskis, A. Sivachenko, S. L. Carter, G. Saksena, D. Voet, A. H. Ramos, W. Winckler, M. Cipicchio, K. Ardlie, P. W. Kantoff, M. F. Berger, S. B. Gabriel, T. R. Golub, M. Meyerson, E. S. Lander, O. Elemento, G. Getz, F. Demichelis, M. A. Rubin, L. A. Garraway, Punctuated evolution of prostate cancer genomes. *Cell* **153**, 666–677 (2013).
8. L. Li, W. Chang, G. Yang, C. Ren, S. Park, T. Karantanos, S. Karanika, J. Wang, J. Yin, P. K. Shah, H. Takahiro, M. Dobashi, W. Zhang, E. Efstathiou, S. N. Maity, A. M. Aparicio, E. M. L. Ning Tapia, P. Troncoso, B. Broom, L. Xiao, H.-S. Lee, J.-S. Lee, P. G. Corn, N. Navone, T. C. Thompson, Targeting poly(ADP-ribose) polymerase and the c-Myb–regulated DNA damage response pathway in castration-resistant prostate cancer. *Sci. Signal.* **7**, ra47 (2014).
9. S. P. Pitroda, I. M. Pashtan, H. L. Logan, B. Budke, T. E. Darga, R. R. Weichselbaum, P. P. Connell, DNA repair pathway gene expression score correlates with repair proficiency and tumor sensitivity to chemotherapy. *Sci. Transl. Med.* **6**, 229ra242 (2014).
10. L. W. Ellisen, PARP inhibitors in cancer therapy: Promise, progress, and puzzles. *Cancer Cell* **19**, 165–167 (2011).
11. C. J. Lord, A. Ashworth, The DNA damage response and cancer therapy. *Nature* **481**, 287–294 (2012).
12. Y. Shen, M. Aoyagi-Scharber, B. Wang, Trapping poly(ADP-ribose) polymerase. *J. Pharmacol. Exp. Ther.* **353**, 446–457 (2015).

13. E. Castro, J. Mateo, D. Olmos, J. S. de Bono, Targeting DNA repair: The role of PARP inhibition in the treatment of castration-resistant prostate cancer. *Cancer J.* **22**, 353–356 (2016).
14. J. Mateo, S. Carreira, S. Sandhu, S. Miranda, H. Mossop, R. Perez-Lopez, D. N. Rodrigues, D. Robinson, A. Omlin, N. Tunariu, G. Boysen, N. Porta, P. Flohr, A. Gillman, I. Figueiredo, C. Paulding, G. Seed, S. Jain, C. Ralph, A. Protheroe, S. Hussain, R. Jones, T. Elliott, U. McGovern, D. Bianchini, J. Goodall, Z. Zafeiriou, C. T. Williamson, R. Ferraldeschi, R. Riisnaes, B. Ebbs, G. Fowler, D. Roda, W. Yuan, Y. M. Wu, X. Cao, R. Brough, H. Pemberton, R. A'Hern, A. Swain, L. P. Kunju, R. Eeles, G. Attard, C. J. Lord, A. Ashworth, M. A. Rubin, K. E. Knudsen, F. Y. Feng, A. M. Chinnaiyan, E. Hall, J. S. de Bono, DNA-repair defects and olaparib in metastatic prostate cancer. *N. Engl. J. Med.* **373**, 1697–1708 (2015).
15. S. K. Sandhu, W. R. Schelman, G. Wilding, V. Moreno, R. D. Baird, S. Miranda, L. Hylands, R. Riisnaes, M. Forster, A. Omlin, N. Kreischer, K. Thway, H. Gevensleben, L. Sun, J. Loughney, M. Chatterjee, C. Toniatti, C. L. Carpenter, R. Iannone, S. B. Kaye, J. S. de Bono, R. M. Wenham, The poly(ADP-ribose) polymerase inhibitor niraparib (MK4827) in *BRCA* mutation carriers and patients with sporadic cancer: A phase 1 dose-escalation trial. *Lancet Oncol.* **14**, 882–892 (2013).
16. C. L. Scott, E. M. Swisher, S. H. Kaufmann, Poly (adp-ribose) polymerase inhibitors: Recent advances and future development. *J. Clin. Oncol.* **33**, 1397–1406 (2015).
17. B. S. Taylor, N. Schultz, H. Hieronymus, A. Gopalan, Y. Xiao, B. S. Carver, V. K. Arora, P. Kaushik, E. Cerami, B. Reva, Y. Antipin, N. Mitsiades, T. Landers, I. Dolgalev, J. E. Major, M. Wilson, N. D. Socci, A. E. Lash, A. Heguy, J. A. Eastham, H. I. Scher, V. E. Reuter, P. T. Scardino, C. Sander, C. L. Sawyers, W. L. Gerald, Integrative genomic profiling of human prostate cancer. *Cancer Cell* **18**, 11–22 (2010).
18. D. Robinson, E. M. Van Allen, Y.-M. Wu, N. Schultz, R. J. Lonigro, J.-M. Mosquera, B. Montgomery, M.-E. Taplin, C. C. Pritchard, G. Attard, H. Beltran, W. Abida, R. K. Bradley, J. Vinson, X. Cao, P. Vats, L. P. Kunju, M. Hussain, F. Y. Feng, S. A. Tomlins, K. A. Cooney, D. C. Smith, C. Brennan, J. Siddiqui, R. Mehra, Y. Chen, D. E. Rathkopf, M. J. Morris, S. B. Solomon, J. C. Durack, V. E. Reuter, A. Gopalan, J. Gao, M. Loda, R. T. Lis, M. Bowden, S. P. Balk, G. Gaviola, C. Sougnez, M. Gupta, E. Y. Yu, E. A. Mostaghel, H. H. Cheng, H. Mulcahy, L. D. True, S. R. Plymate, H. Dvinge, R. Ferraldeschi, P. Flohr, S. Miranda, Z. Zafeiriou, N. Tunariu, J. Mateo, R. Perez-Lopez, F. Demichelis, B. D. Robinson, M. Schiffman, D. M. Nanus, S. T. Tagawa, A. Sigaras, K. W. Eng, O. Elemento, A. Sboner, E. I. Heath, H. I. Scher, K. J. Pienta, P. Kantoff, J. S. de Bono, M. A. Rubin, P. S. Nelson, L. A. Garraway, C. L. Sawyers, A. M. Chinnaiyan, Integrative clinical genomics of advanced prostate cancer. *Cell* **161**, 1215–1228 (2015).
19. S. Karanika, T. Karantanos, L. Li, P. G. Corn, T. C. Thompson, DNA damage response and prostate cancer: Defects, regulation and therapeutic implications. *Oncogene* **34**, 2815–2822 (2015).
20. H. Q. Ta, D. Gioeli, The convergence of DNA damage checkpoint pathways and androgen receptor signaling in prostate cancer. *Endocr. Relat. Cancer* **21**, R395–R407 (2014).
21. J. F. Goodwin, M. J. Schiewer, J. L. Dean, R. S. Schrecengost, R. de Leeuw, S. Han, T. Ma, R. B. Den, A. P. Dicker, F. Y. Feng, K. E. Knudsen, A hormone–DNA repair circuit governs the response to genotoxic insult. *Cancer Discov.* **3**, 1254–1271 (2013).
22. W. R. Polkinghorn, J. S. Parker, M. X. Lee, E. M. Kass, D. E. Spratt, P. J. Iaquinta, V. K. Arora, W.-F. Yen, L. Cai, D. Zheng, B. S. Carver, Y. Chen, P. A. Watson, N. P. Shah, S. Fujisawa, A. G. Goglia, A. Gopalan, H. Hieronymus, J. Wongvipat, P. T. Scardino, M. J. Zelefsky, M. Jasin, J. Chaudhuri, S. N. Powell, C. L. Sawyers, Androgen receptor signaling regulates DNA repair in prostate cancers. *Cancer Discov.* **3**, 1245–1253 (2013).
23. K. K. Khanna, S. P. Jackson, DNA double-strand breaks: Signaling, repair and the cancer connection. *Nat. Genet.* **27**, 247–254 (2001).
24. N. Suwaki, K. Klare, M. Tarsounas, RAD51 paralogs: Roles in DNA damage signalling, recombinational repair and tumorigenesis. *Semin. Cell Dev. Biol.* **22**, 898–905 (2011).
25. C. Liu, S. Srihari, K.-A. Lê Cao, G. Chenevix-Trench, P. T. Simpson, M. A. Ragan, K. K. Khanna, A fine-scale dissection of the DNA double-strand break repair machinery and its implications for breast cancer therapy. *Nucleic Acids Res.* **42**, 6106–6127 (2014).
26. R. Prakash, Y. Zhang, W. Feng, M. Jasin, Homologous recombination and human health: The roles of BRCA1, BRCA2, and associated proteins. *Cold Spring Harb. Perspect. Biol.* **7**, a016600 (2015).
27. B. K. Slinker, The statistics of synergism. *J. Mol. Cell. Cardiol.* **30**, 723–731 (1998).
28. C. I. Bliss, The toxicity of poisons appled jointly. *Ann. Appl. Biol.* **26**, 585–615 (1939).
29. H. Willers, L. Gheorghiu, Q. Liu, J. A. Efstathiou, L. J. Wirth, M. Krause, C. von Neubeck, DNA damage response assessments in human tumor samples provide functional biomarkers of radiosensitivity. *Semin. Radiat. Oncol.* **25**, 237–250 (2015).
30. C. Talarico, V. Dattilo, L. D'Antona, M. Menniti, C. Bianco, F. Ortuso, S. Alcaro, S. Schenone, N. Perrotti, R. Amato, SGK1, the new player in the game of resistance: Chemo-radio molecular target and strategy for inhibition. *Cell Physiol. Biochem.* **39**, 1863–1876 (2016).
31. P. Castel, M. Scaltriti, The emerging role of serum/glucocorticoid-regulated kinases in cancer. *Cell Cycle* **16**, 5–6 (2016).
32. J. M. Lowe, T.-A. Nguyen, S. A. Grimm, K. A. Gabor, S. D. Peddada, L. Li, C. W. Anderson, M. A. Resnick, D. Menendez, M. B. Fessler, The novel p53 target TNFAIP8 variant 2 is increased in cancer and offsets p53-dependent tumor suppression. *Cell Death Differ.* **24**, 181–191 (2016).
33. T. Liu, H. Gao, M. Yang, T. Zhao, Y. Liu, G. Lou, Correlation of TNFAIP8 overexpression with the proliferation, metastasis, and disease-free survival in endometrial cancer. *Tumour Biol.* **35**, 5805–5814 (2014).
34. T. F. Day, R. R. Mewani, J. Starr, X. Li, D. Chakravarty, H. Ressom, X. Zou, O. Eidelman, H. B. Pollard, M. Srivastava, U. N. Kasid, Transcriptome and proteome analyses of TNFAIP8 knockdown cancer cells reveal new insights into molecular determinants of cell survival and tumor progression. *Methods Mol. Biol.* **1513**, 83–100 (2017).
35. R. Plummer, Poly(ADP-ribose)polymerase (PARP) inhibitors: From bench to bedside. *Clin. Oncol.* **26**, 250–256 (2014).
36. E. S. Ratner, A. C. Sartorelli, Z. P. Lin, Poly (ADP-ribose) polymerase inhibitors: On the horizon of tailored and personalized therapies for epithelial ovarian cancer. *Curr. Opin. Oncol.* **24**, 564–571 (2012).
37. J. C. Brenner, B. Ateeq, Y. Li, A. K. Yocum, Q. Cao, I. A. Asangani, S. Patel, X. Wang, H. Liang, J. Yu, N. Palanisamy, J. Siddiqui, W. Yan, X. Cao, R. Mehra, A. Sabolch, V. Basrur, R. J. Lonigro, J. Yang, S. A. Tomlins, C. A. Maher, K. S. Elenitoba-Johnson, M. Hussain, N. M. Navone, K. J. Pienta, S. Varambally, F. Y. Feng, A. M. Chinnaiyan, Mechanistic rationale for inhibition of poly(ADP-ribose) polymerase in ETS gene fusion-positive prostate cancer. *Cancer Cell* **19**, 664–678 (2011).
38. J.-m. Lee, J. A. Ledermann, E. C. Kohn, PARP Inhibitors for BRCA1/2 mutation-associated and BRCA-like malignancies. *Ann. Oncol.* **25**, 32–40 (2014).
39. S. Tangutoori, P. Baldwin, S. Sridhar, PARP inhibitors: A new era of targeted therapy. *Maturitas* **81**, 5–9 (2015).

Funding: This work was supported, in part, by the National Cancer Institute grants R0150588 (to T.C.T.) and 5P50 CA140388, the Prostate Cancer Specialized Program of Research Excellence at The University of Texas MD Anderson Cancer Center, the National Cancer Institute Support Grant CA16672, and the MD Anderson Cancer Center Support Grant. G.C.M. is supported by a grant from the Michael and Susan Dell Foundation. **Author contributions:** T.C.T. and L.L. conceived and designed the study and wrote the paper. L.L., J.W., X.Z., W.C., and J.Y. performed the cell culture studies. S.K., S.P., J.W., Y.L., S.B., J.H.S., G.E.G., and T.K. performed the xenograft model experiments. G.Y. and D.K. performed the immunohistochemical analysis. B.M.B., G.C.M., W.W., and A.K.A. performed the gene expression analysis of CRPC patient tissue samples and integrated genomic analysis of cell lines and xenograft models. J.K., P.G.C., A.M.A., and C.J.L. provided clinical insight and concept development. P.T. performed the pathology evaluation of human PCa samples. J.-S.L. and H.-S.L. performed the microarray experiments. T.H. and C.T. provided intellectual contributions. G.E.G. revised the manuscript. All authors contributed to the data analysis. **Competing interests:** The authors declare that they have no competing financial interests. **Data and materials availability:** Microarray data are deposited in the GEO (www.ncbi.nlm.nih.gov/geo/) (accession number GSE69249).

Submitted 11 January 2017
Accepted 5 May 2017
Published 23 May 2017
10.1126/scisignal.aam7479

Citation: L. Li, S. Karanika, G. Yang, J. Wang, S. Park, B. M. Broom, G. C. Manyam, W. Wu, Y. Luo, S. Basourakos, J. H. Song, G. E. Gallick, T. Karantanos, D. Korentzelos, A. K. Azad, J. Kim, P. G. Corn, A. M. Aparicio, C. J. Logothetis, P. Troncoso, T. Heffernan, C. Toniatti, H.-S. Lee, J.-S. Lee, X. Zuo, W. Chang, J. Yin, T. C. Thompson, Androgen receptor inhibitor–induced "BRCAness" and PARP inhibition are synthetically lethal for castration-resistant prostate cancer. *Sci. Signal.* **10**, eaam7479 (2017).

CANCER

Identifying DNA methylation biomarkers for non-endoscopic detection of Barrett's esophagus

Copyright © 2018 The Authors, some rights reserved; exclusive licensee American Association for the Advancement of Science. No claim to original U.S. Government Works

Helen R. Moinova,[1] Thomas LaFramboise,[2,3] James D. Lutterbaugh,[1] Apoorva Krishna Chandar,[1] John Dumot,[1] Ashley Faulx,[1] Wendy Brock,[1] Omar De la Cruz Cabrera,[4] Kishore Guda,[2] Jill S. Barnholtz-Sloan,[2] Prasad G. Iyer,[5] Marcia I. Canto,[6] Jean S. Wang,[7] Nicholas J. Shaheen,[8] Prashanti N. Thota,[9] Joseph E. Willis,[2,10,11]*† Amitabh Chak,[1,2,11]*† Sanford D. Markowitz[1,2,3,11]*†

We report a biomarker-based non-endoscopic method for detecting Barrett's esophagus (BE) based on detecting methylated DNAs retrieved via a swallowable balloon-based esophageal sampling device. BE is the precursor of, and a major recognized risk factor for, developing esophageal adenocarcinoma. Endoscopy, the current standard for BE detection, is not cost-effective for population screening. We performed genome-wide screening to ascertain regions targeted for recurrent aberrant cytosine methylation in BE, identifying high-frequency methylation within the *CCNA1* locus. We tested *CCNA1* DNA methylation as a BE biomarker in cytology brushings of the distal esophagus from 173 individuals with or without BE. *CCNA1* DNA methylation demonstrated an area under the curve of 0.95 for discriminating BE-related metaplasia and neoplasia cases versus normal individuals, performing identically to methylation of *VIM* DNA, an established BE biomarker. When combined, the resulting two biomarker panel was 95% sensitive and 91% specific. These results were replicated in an independent validation cohort of 149 individuals who were assayed using the same cutoff values for test positivity established in the training population. To progress toward non-endoscopic esophageal screening, we engineered a well-tolerated, swallowable, encapsulated balloon device able to selectively sample the distal esophagus within 5 min. In balloon samples from 86 individuals, tests of *CCNA1* plus *VIM* DNA methylation detected BE metaplasia with 90.3% sensitivity and 91.7% specificity. Combining the balloon sampling device with molecular assays of *CCNA1* plus *VIM* DNA methylation enables an efficient, well-tolerated, sensitive, and specific method of screening at-risk populations for BE.

INTRODUCTION

The incidence of esophageal adenocarcinoma (EAC) has more than quadrupled in the past 30 years (*1*–*4*), and the prognosis for EAC patients remains poor, with a less than 20% survival at 5 years (*4*, *5*). Barrett's esophagus (BE), a premalignant intestinal-type columnar metaplasia that replaces the normal squamous mucosa of the distal esophagus, is the only known precursor for EAC, but its detection currently requires performing esophagogastroduodenoscopy (EGD). Because of the high cost of EGD and the lack of a randomized controlled trial demonstrating cost-effective reduction in EAC, endoscopy screening for BE has not been routinely recommended (*6*, *7*). Thus, in about 95% of cases of EAC, the presence of the antecedent BE remains undetected and unknown (*8*). Hence, there is a need for additional methods for BE detection that are less expensive than EGD and can be widely and readily implemented in an at-risk population. Molecular biomarkers for detecting BE are potentially valuable in this regard.

Acquisition of aberrant cytosine methylation within CpG-rich genomic islands is a common accompaniment of many cancers and can serve as a neoplasia biomarker (*9*–*13*). We have previously reported that de novo DNA methylation of the CpG island overlapping the first exon of the vimentin gene (mVIM) is a highly sensitive BE biomarker that is present in biopsies of about 90% of BE patients, suggesting utility of mVIM as a potential biomarker for BE screening (*14*). In an initial pilot study, we further found that mVIM could be detected in esophageal brushings, suggesting that mVIM can serve as a molecular cytology biomarker to enable non-endoscopic detection of BE (*14*). Reduced representation bisulfite sequencing (RRBS) is a whole-genome approach that allows for unbiased assessment of DNA methylation within CpG-dense regions of the human genome, which encompass most promoters and other regulatory regions (*15*, *16*). RRBS thus provides the potential to identify an extended biomarker panel with increased effectiveness for detecting BE.The aims of this study were hence to identify methylated DNA biomarkers of esophageal neoplasia, to define the sensitivity and specificity of such markers in comparison to and/or in combination with mVIM for detecting BE metaplasias and related neoplasias, and to further test the efficacy of these biomarkers for detecting BE in samples obtained via a non-endoscopic swallowable balloon-based esophageal sampling device as compared to samples obtained via endoscopy-directed brushings.

[1]Department of Medicine, Case Western Reserve University and University Hospitals Cleveland Medical Center, Cleveland, OH 44106, USA. [2]Case Comprehensive Cancer Center, Case Western Reserve University, Cleveland, OH 44106, USA. [3]Department of Genetics and Genome Sciences, Case Western Reserve University and University Hospitals Cleveland Medical Center, Cleveland, OH 44106, USA. [4]Department of Mathematical Sciences, Kent State University, Kent, OH 44242, USA. [5]Barrett's Esophagus Unit, Division of Gastroenterology and Hepatology, Mayo Clinic, Rochester, MN 55905, USA. [6]Division of Gastroenterology and Hepatology, Department of Medicine, Johns Hopkins Medical Institutions, Baltimore, MD 21205, USA. [7]Division of Gastroenterology, Department of Medicine, Washington University School of Medicine, St. Louis, MO 63110, USA. [8]Center for Esophageal Diseases and Swallowing, Division of Gastroenterology and Hepatology, University of North Carolina at Chapel Hill, Chapel Hill, NC 27599, USA. [9]Digestive Disease and Surgery Institute, Cleveland Clinic, Cleveland, OH 44195, USA. [10]Department of Pathology, Case Western Reserve University and University Hospitals Cleveland Medical Center, Cleveland, OH 44106, USA. [11]University Hospitals Seidman Cancer Center, University Hospitals Cleveland Medical Center, Cleveland, OH 44106, USA.
*Corresponding author. Email: SXM10@cwru.edu (S.D.M.); josephe.willis@uhhospitals.org (J.E.W.); amitabh.chak@uhhospitals.org (A.C.)
†These authors contributed equally to this work.

RESULTS

RRBS discovery of DNA methylation biomarkers of esophageal neoplasia

We performed RRBS analysis on a set of 26 esophageal cancer (EAC) biopsies and their respective matched normal squamous biopsies, 15 biopsy or brushing samples of BE, and 5 esophageal cancer cell lines (fig. S1). Of 3,091,193 analyzable CpGs, 26,601 CpGs showed methylation below 10% in all the informative normal squamous samples (requiring at least four informative normal samples, each having a sequencing depth of at least 20×). When compared in BE, 1970 of these CpGs showed >30% methylation in at least four samples comprising 45% or more of informative cases (all having a sequencing depth of >10×). Of these 1970 CpGs methylated in BE, 1011 CpGs additionally demonstrated >30% methylation in at least eight informative EAC biopsies (all having a sequencing depth of >10×). These 1011 CpGs that were differentially methylated between normal squamous versus BE and EAC samples were clustered into 412 differentially methylated CpG patches, defined as clusters of differentially methylated CpGs each less than 200 base pairs (bp) apart. The best 26 of these patches were selected for further inspection (table S1). Of these, the best candidate for discriminating BE-related lesions from normal esophagus was a patch of seven CpGs located on chromosome 13, in the CpG island spanning the promoter and 5′ untranslated region of *CCNA1* (Fig. 1A). Seventy percent of the BEs characterized by RRBS showed average methylation exceeding 30% across this patch (Fig. 1B). Moreover, all three informative esophageal cancer cell lines showed nearly 100% methylation across this patch, suggesting that both *CCNA1* alleles were densely methylated and that the methylation signal in the biopsies was derived from the abnormal Barrett's epithelial cells (Fig. 1B).

CCNA1 and VIM DNA methylation in esophageal biopsies

To further interrogate the *CCNA1*-associated DNA methylation patch, we designed a next-generation sequencing (NGS)–based assay for targeted resequencing of this differentially methylated region (Fig. 1A). We targeted a cluster of 21 consecutive CpG residues that overlap with the methylated patch identified by RRBS (Fig. 1A). The NGS approach allows for determining the methylation status for each of these 21 CpGs across a single individual DNA read and thereby calculating the percent of CpG methylation present across this region for each individual *CCNA1* locus DNA molecule, thus enabling each DNA read to be classified as "methylated" versus "unmethylated." This approach further provides a metric of tissue methylation, corresponding to the percent of all the individual *CCNA1* DNA molecules identified as methylated (percent of *CCNA1* "methylated reads"), that can further be referenced as exceeding or not exceeding the upper limit of the normal range. This patch-based algorithm suppresses background from random methylation of individual CpGs and provides enhanced discrimination of normal versus diseased tissue (fig. S2).

We used this method to characterize an expanded set of esophageal biopsies (fig. S1) and to compare the performance of DNA methylation at the *CCNA1* versus *VIM* loci, reflecting our previous identification of *VIM* region methylation as a high-performance biomarker of esophageal neoplasia (*14*). *CCNA1* locus methylation (mCCNA1) was significantly increased in all BE-related lesions versus normal ($P < 0.001$; Fig. 2A), with mCCNA1 detected in 81% percent of nondysplastic BE (NDBE), 68% percent of BE with high-grade dysplasia (HGD), and 90% percent of EAC but in only 1% of normal squamous samples (classifying a tissue as methylated if it had >10% of methylated *CCNA1* reads and classifying a *CCNA1* read as methylated when methylation was detected at ≥16 of 21 target CpG positions). These results were similar to those obtained by bisulfite sequencing analysis of these samples for *VIM* locus methylation (mVIM; Fig. 2B), in which >10% methylation was demonstrated by 100% of NDBE, 63% percent of BE with HGD, and 76.5% percent of EAC but by only 1% of normal squamous samples (classifying *VIM* reads as methylated when methylated at ≥8 of 10 target CpG positions).

CCNA1 and VIM DNA methylation for detecting BE and EAC in cytology brushings

To model a "molecular cytology" assay for detecting BE, we used the NGS bisulfite sequencing assay to measure *CCNA1* DNA methylation (mCCNA1) in a training set of esophageal cytology brushings (fig. S1). Brushings of the gastroesophageal (GE) junction were obtained from 62 control subjects with or without symptomatic GE reflux disease (GERD) but without BE. These controls included persons with normal endoscopic findings ($n = 54$) plus individuals with erosive esophagitis ($n = 8$). Brushings were also obtained from 111 patients including 62 individuals with cancer, either EAC ($n = 48$) or GE junction

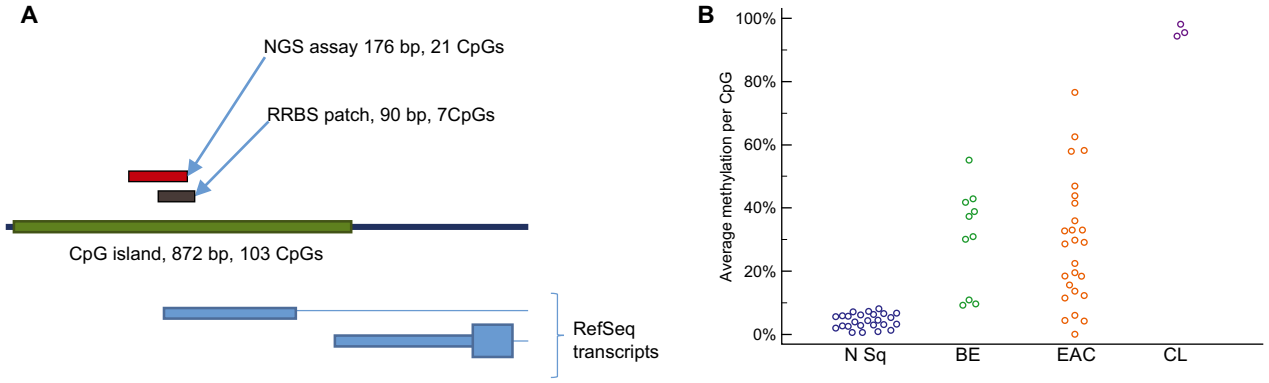

Fig. 1. *CCNA1* region methylation in esophageal neoplasia. (**A**) Location of the differentially methylated region in the *CCNA1* promoter on chromosome 13. The patch of CpGs found to be differentially methylated in reduced representation bisulfite sequencing (RRBS) and the amplicon assayed by next-generation sequencing (NGS) are indicated above the map of the CpG island (green), with structures of *CCNA1* RefSeq transcripts indicated below. (**B**) Average methylation of CpGs in the *CCNA1* RRBS-defined patch of seven CpGs in biopsies of normal squamous (N Sq) mucosa, Barrett's esophagus (BE), and esophageal adenocarcinoma (EAC) and in esophageal cell lines (CL).

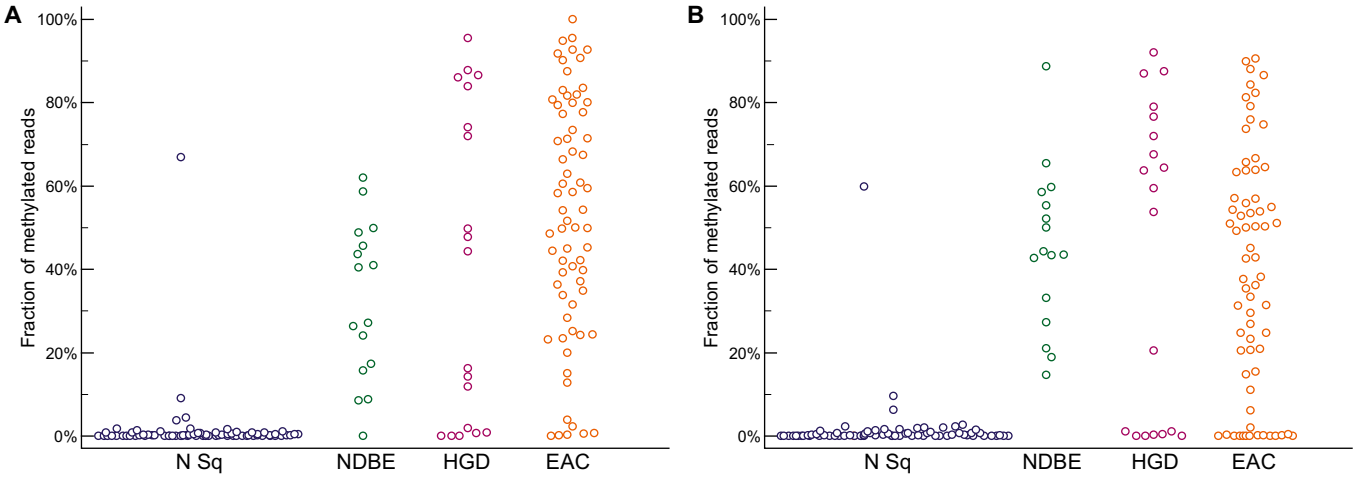

Fig. 2. NGS bisulfite sequencing assay of DNA methylation in esophageal biopsies. (**A**) *CCNA1* locus methylation (mCCNA1) in esophageal neoplasia and control patients. N Sq, normal squamous biopsies; NDBE, nondysplastic BE; HGD, BE with high-grade dysplasia. Fraction of methylated reads in each sample is indicated on the *y* axis. $P < 0.001$ for one-way analysis of variance (ANOVA) comparison and $P < 0.001$ for post hoc Student-Newman-Keuls test of N Sq versus BE, HGD, and EAC. (**B**) *VIM* locus methylation (mVIM) in esophageal neoplasia and control patients. Fraction of methylated reads in each sample is indicated on the *y* axis. $P < 0.001$ for one-way ANOVA comparison and $P < 0.001$ for post hoc Student-Newman-Keuls test of N Sq versus BE, HGD, and EAC.

adenocarcinoma ($n = 14$), and 49 individuals with BE. Of BE cases, 12 had nondysplastic short-segment BE (SSBE; < 3 cm), 19 had nondysplastic long-segment BE (LSBE; ≥3 cm), 8 had low-grade dysplasia (LGD), and 10 had HGD. Eighty-three percent of study participants were white. The disease group was older than controls ($P < 0.0001$) and included more males, reflecting the epidemiology of BE. There was no significant difference in the prevalence of smoking between cases and controls (table S2).

Figure 3A shows the receiver operating characteristic (ROC) curve for mCCNA1 in these training set samples, in which the assay demonstrated an area under the curve (AUC) of 0.95. An optimal cutpoint, in which a sample was detected as positive if it had >3.12% methylated *CCNA1* templates, maximized the sum of sensitivity plus specificity. At this cutpoint, mCCNA1 demonstrated 90.7% sensitivity for detecting BE or cancer with 98.4% specificity. As a comparator, Fig. 3B shows the ROC curve for the same samples assayed for mVIM by bisulfite sequencing analysis. Similar to mCCNA1, the mVIM assay showed an AUC of 0.95. The optimal cutpoint for this assay, of 1.05% mVIM content, provided a sensitivity of 90.7% and a specificity of 93.2% (Fig. 3B). These mVIM results are consistent with our previous observation in a pilot set of 34 esophageal brushings that were analyzed for mVIM by quantitative methylation-specific (qMS)–polymerase chain reaction (PCR) (*14*).

To validate the performance of mCCNA1 and mVIM in molecular cytology applications, we examined a second independent set of esophageal cytology brushings from 149 new individuals recruited at five different cancer centers from across the United States (fig. S1). These individuals included 30 controls with normal esophageal morphology and 119 cases with BE or cancer (table S2). Similarly to the training set, and reflecting the biology of BE, participants in the validation set were 93% white. Training and validation populations did not significantly differ by gender or smoking history, but controls were older in the validation than in training set (table S2). As shown in Fig. 3 (C and D), the validation population again showed an AUC of 0.95 for mCCNA1 and 0.96 for mVIM. Moreover, sensitivity and specificity of mCCNA1 and mVIM in the validation population replicated those of the training population, using the same cutoffs for test positivity as prespecified by the training data set (Fig. 3, C and D versus A and B, and table S3).

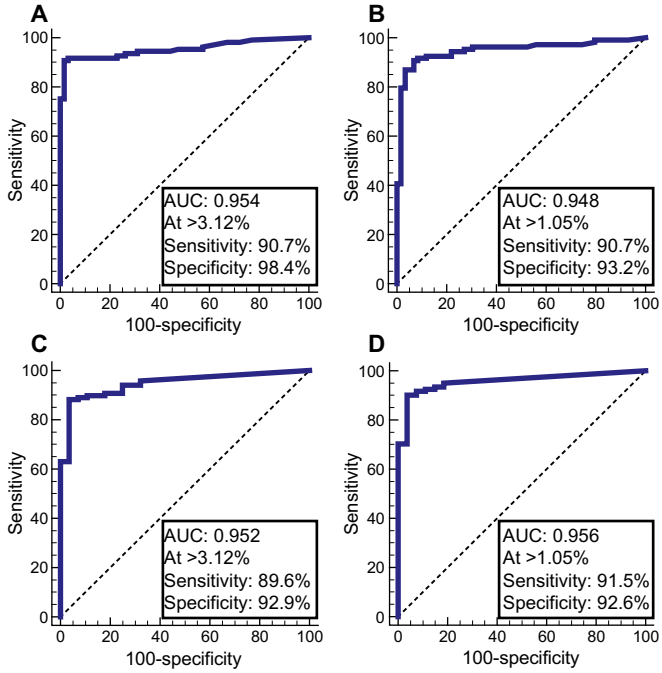

Fig. 3. ROC curves of mCCNA1 and mVIM assayed in esophageal cytology brushings from control normal-appearing GE junctions versus BE and EAC cases. (**A** and **B**) Training samples. (A) mCCNA1, $n = 61$ controls and 108 cases. (B) mVIM, $n = 59$ controls and 107 cases. (**C** and **D**) Validation samples. (C) mCCNA1, $n = 28$ controls and 115 cases. (D) mVIM, $n = 27$ controls and 117 cases. Area under the curve (AUC) and the sensitivity and specificity of the assays at the indicated cutpoint are listed for each graph, with the cutpoint value of percent methylation that defines a positive test denoted by "At >."

BE progresses from nondysplastic metaplasias to LGD and then HGD that ultimately give rise to EAC (*17*, *18*). Given the equivalent

performance of mVIM and mCCNA1 in the training and validation populations, we performed a pooled analysis to examine these markers' performance at each of the stages of progression of BE-related neoplasias. As shown in Table 1, mCCNA1 and mVIM markers were both highly sensitive for detecting each of the stages of BE-related disease, including early NDBE metaplasias, dysplasias (LGD and HGD), and cancers. mVIM performed better than mCCNA1 in detecting NDBE (91.5% versus 79.7%), whereas mCCNA1 showed a slightly higher sensitivity for dysplastic BE (94.5% versus 91.1%) and cancer (94.9% versus 90.7%). When considered in combination, mVIM and mCCNA1 jointly detected 92% of NDBE, 96% of dysplastic BE, and 96% of cancers while maintaining specificity above 90% for negatively classifying brushings from the normal GE junction (Table 1). The combination of mVIM and mCCNA1 was more sensitive than either marker individually, even when the specificity of each individual marker was adjusted to match that of the combination (table S4).

Smoking-induced methylation in the upper esophagus

Esophageal brushings under endoscopic guidance provided for directed sampling of the distal esophagus. However, certain non-endoscopic approaches to esophageal sampling, for example, using sponge-based devices, require sampling the entire esophagus. To simulate this process, we obtained additional cytology brushings of the proximal normal squamous esophagus from all participants in our training population. To avoid contamination, these proximal brushings were obtained before any brushings of the GE junction. Unexpectedly, a subset of these proximal squamous mucosa brushings tested positive for mVIM or mCCNA1, demonstrating methylation values above the cutpoint for normal GE junction as determined by the training set of brushings. Positive tests were obtained in 21% of proximal squamous samples assayed by mVIM and 6% assayed by *CCNA1* (Fig. 4, A and B). Insight into the basis for methylation in the proximal esophagus came from noting that the great majority of methylation-positive samples were obtained from current or former smokers, with smokers accounting for 75% of samples testing mVIM-positive ($P = 0.0155$) and 100% of samples testing mCCNA1-positive ($P = 0.0094$). Further review determined that most of the methylation-positive normal squamous biopsies from our initial experiments (Fig. 2) also came from smokers, although the numbers were too few to support statistical analyses. These findings suggest that using methylated DNA markers for non-endoscopic detection of BE will be enhanced by device designs that allow for selective sampling of the distal esophagus and for protection of samples from contamination by the proximal esophagus. Reassuringly, for such a selective sampling approach, reanalysis of brushings from the distal esophagus showed smoking to have no significant effect on the extent of *VIM* and of *CCNA1* methylation detectable in either the normal GE junction of control individuals or in cases with BE or Barrett's related neoplasia (table S5).

Detecting BE and EAC via non-endoscopic balloon sampling

To enable non-endoscopic targeted sampling of the distal esophagus, we designed and built an encapsulated, inflatable, surface-textured balloon. The device is swallowed in a pill-sized 16 × 9–mm capsule attached to a thin 2.16-mm silicone catheter (Fig. 5, A and B). After delivery to the stomach, the balloon is inflated by injecting 5 cm^3 of air through the catheter (Fig. 5C) and then gently withdrawn 3 to 6 cm back through the distal esophagus to sample the luminal epithelial surface. The balloon is then deflated and inverted back into the capsule (Fig. 5D), thus protecting the acquired biosample from further dilution or contamination in the proximal esophagus and the oropharynx. After retrieval of the capsule through the mouth, DNA is extracted from the balloon surface for molecular analysis.

One hundred fifty-six patients underwent unsedated distal esophageal sampling with the balloon device before scheduled EGD. Most of the participants were male (71%) and white (83%), with an average age of 64.1 years (SD = 12.5 years). Twenty-eight (18%) were unable to swallow the device. However, the 128 successful participants in trial reported little to no anxiety, pain, or choking and only low to intermediate gagging (table S6). On average, the balloon reached the stomach in 3.3 min (range, 1.0 to 7.7 min) with excellent tolerance in 72% of cases (table S6). Ninety-three percent of individuals who participated

Table 1. mVIM and mCCNA1 performance in the combined set of all distal esophagus brushings. *VIM* and *CCNA1* gene methylation was assayed in DNA samples from cytology brushings of the distal esophagus from the following: unaffected controls brushed at the gastroesophageal junction (control GEJ); cases of NDBE, further subclassified as short-segment BE (SSBE) of 1 to 3 cm or long-segment BE (LSBE) of ≥3 cm; BE with low-grade dysplasia (LGD); BE with HGD; EAC (including junctional cancer of the esophagus). Samples were scored as *VIM*-methylated for mVIM >1.05% and as *CCNA1*-methylated for mCCNA1 >3.12% [using receiver operating characteristic (ROC) defined cutpoints from Fig.3, A and B]. Cases were positive for the panel of mCCNA1 plus mVIM if either marker tested positive. Controls were negative for the panel when both mCCNA1 and mVIM were negative. Controls with one negative marker and one marker with assay failure were excluded. Entries indicate percent sensitivity or specificity (%) and total number of individuals tested (*n*).

	mVIM		mCCNA1		Either mVIM or mCCNA1	
	%	*n*	%	*n*	%	*n*
Specificity control GEJ	93.0	86	96.6	89	90.5	84
Sensitivity all cases	91.1	224	90.1	223	94.8	229
Sensitivity all NDBE	91.5	71	79.7	69	91.7	72
Sensitivity SSBE	87.1	31	76.7	30	87.1	31
Sensitivity LSBE	95.0	40	82.1	39	95.1	41
Sensitivity all dysplastic BE	91.1	56	94.5	55	96.5	57
Sensitivity LGD	93.9	33	90.6	32	94.1	34
Sensitivity HGD	87.0	23	100.0	23	100.0	23
Sensitivity EAC	90.7	97	94.9	99	96.0	100

in esophageal balloon testing would repeat the procedure if necessary, whereas 95% would recommend it to others (table S6).

From the 128 balloons processed, an adequate DNA amount of at least 60 ng was obtained in 116 instances (91%). Thirty individuals were additionally excluded from further analysis because of either having a history of previous esophageal ablation for Barrett's dysplasia ($n = 23$), having gastric intestinal metaplasia (IM; $n = 4$), or having esophageal IM of <1 cm in length (ultrashort BE; $n = 3$). The 86 evaluable individuals (table S7) included 36 controls free of IM but with erosive esophagitis ($n = 3$) or other indications for upper endoscopy ($n = 33$). The evaluable individuals also included 50 cases, 42 with BE (31 nondysplastic, 6 LGD, 4 HGD, and 1 indefinite for dysplasia) and 8 with EAC or junctional cancers (Table 2). In these balloon samples, mVIM and mCCNA1 discriminated cases and controls with performance nearly identical to that found in the cytology brushing samples, with ROC curves for balloon samples demonstrating an AUC of 0.92 for mCCNA1 and 0.91 for mVIM (Figs. 6A versus 3A and 6B versus 3B). Balloon samples of the normal GE junction showed less background methylation of *CCNA1* than did cytology brushings, and at a cutpoint of 1% for mCCNA1, the assay detected 72% of cases while retaining 100% specificity (Table 2). mVIM demonstrated essentially the same cutpoint in balloon samples (1%) as in cytology brushings, and the mVIM assay detected 80% of cases with a specificity of 91.7% (Table 2). When the two markers were jointly applied to the balloon samples, the panel detected 90.3% of NDBE cases with a specificity of 91.7% (Table 2). The combination had a slightly higher sensitivity of 94.4% for detecting LSBE (≥3 cm) but still detected SSBE of 1- to 3-cm length with 84.6% sensitivity. Although the study included only a few cases of dysplasia or cancer, the combination of mVIM and mCCNA1 did detect 9 of 11 dysplasias and seven of eight cancers, yielding a sensitivity of 88% for detection of all BE, dysplasias, and cancers studied (Table 2). Overall, the encapsulated balloon device successfully sampled the distal esophagus with excellent tolerability and acceptability and, when combined with bisulfite sequencing for mVIM plus mCCNA1, demonstrated high sensitivity and specificity for detecting BE.

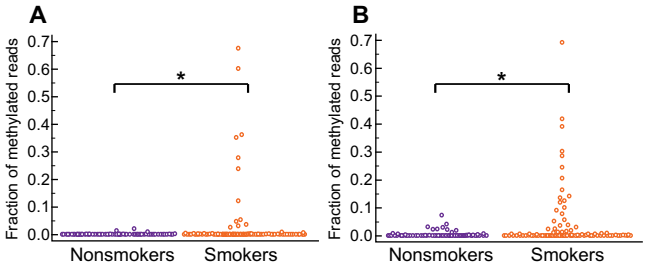

Fig. 4. DNA methylation in the proximal squamous esophagus of smokers versus nonsmokers. (**A**) mCCNA1, *$P = 0.0094$; (**B**) mVIM, *$P = 0.0155$. Patients were classified as smokers if they had any history of ever smoking. *P* values for differences between smokers and nonsmokers were computed using the Mann-Whitney rank sum test.

Methylation in other upper gastrointestinal tract pathologies

To identify potential confounding sources of *VIM* and *CCNA1* DNA methylation, we performed a retrospective analysis of archival formalin-fixed paraffin-embedded (FFPE) esophageal and gastric specimens that captured common pathologies of the upper gastrointestinal (GI) tract (Table 3). As expected, FFPE biopsies of BE were highly methylated, with 90% testing positive for mVIM, 75% testing positive for mCCNA1, and 90% testing positive for the two-marker panel. Clinical criteria for BE require identifying 1 cm or more of esophageal IM. However, the two-marker panel additionally detected 80% of early esophageal IMs, identifying 80% of IM lesions <1 cm and still confined to the endoscopic GE junction (70% positive for mVIM and 67% positive for mCCNA1). Moreover, among individuals with BE, mVIM or mCCNA1 methylation could also be detected in 30% of biopsy samples of columnar mucosa that had no histologic IM (regions of gastric metaplasia; Table 3), suggesting that the IM in these BE cases arose in an antecedent field of methylation-positive columnar cells. In contrast, among individuals without BE or IM, assays for mVIM and for mCCNA1 were negative in all GE junction samples ($n = 55$), which included 15 cases with chronic carditis typified by columnar mucosa without IM (Table 3), and methylation was additionally negative in all distal esophagus samples ($n = 24$). Together, these findings suggest that aberrant methylation occurs at the earliest stages of BE development, in those columnar mucosae that are actively evolving toward IM. Methylation is not simply a consequence of inflammation, because mVIM and mCCNA1 tests were all negative in each of 15 cases of eosinophilic esophagitis, as well as in the above-mentioned chronic carditis samples. Methylation was, however, additionally detected in a subset of gastric IM lesions, 22% of which were positive for at least one of the two markers. Moreover, 2 of 13 individuals with *Helicobacter pylori* gastritis, who were at increased risk for but did not have gastric IM, were also positive for *VIM* or *CCNA1* methylation. However, 24 normal gastric fundic mucosa without IM were negative for mVIM in all samples and negative for mCCNA1 in all but one sample. Positive tests for mVIM and mCCNA1 are thus highly associated with IM, predominantly IM of the esophagus but sometimes IM of the stomach.

Consistent with the predictions from this FFPE archive, positive methylation was detected on two of three balloon samples from cases of ultrashort BE (<1 cm), which were unevaluable in the primary analysis (two positive for mVIM and none for mCCNA1). Similarly, positive methylation was detected in balloon samples from four of four cases of gastric IM that were also unevaluable for the primary analysis (four positive for mVIM and two for mCCNA1). This finding of DNA methylation markers that are shared between gastric metaplasias and very early esophageal metaplasias is consistent with other genomic and cell biology lines of evidence that also point to a common origin between EACs and intestinal-type gastric cancers (*19*, *20*).

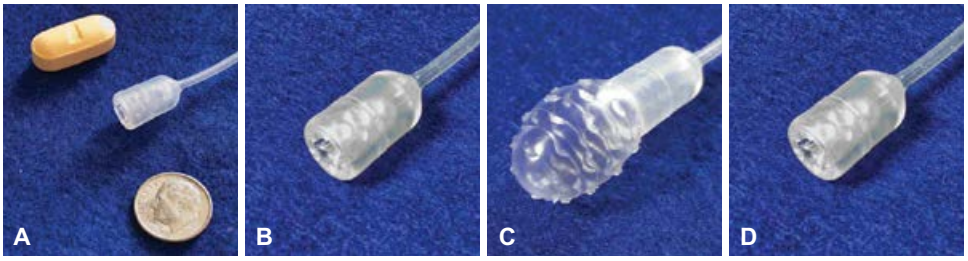

Fig. 5. Non-endoscopic balloon device. (**A**) Device capsule and catheter in comparison to a vitamin pill and a dime. (**B**) Capsule containing inverted balloon in configuration for swallowing. (**C**) Capsule with inflated balloon in configuration for esophageal sampling. (**D**) Capsule containing inverted balloon in configuration for device and biospecimen retrieval.

Table 2. mVIM and mCCNA1 performance in esophageal balloon samples. *VIM* and *CCNA1* gene methylation was assayed in DNA samples from non-endoscopic balloon sampling of the distal esophagus from unaffected controls [individuals with gastroesophageal reflux disease (GERD), erosive esophagitis, or no pathology detected during endoscopy]; cases of NDBE, further subclassified as SSBE of 1 to 3 cm or LSBE of ≥3 cm; BE with LGD; BE with HGD; EAC (including junctional cancer of the esophagus). Samples were scored as *VIM*-methylated for mVIM >1.0% and as *CCNA1*-methylated for mCCNA1 >1.0% (using ROC-defined cutpoints from Fig.6). Samples were positive for the panel of mCCNA1 plus mVIM if either marker tested positive. Entries indicate percent sensitivity or specificity (%) and total number of individuals tested (*n*). We note that only four HGDs were studied, and in this small sample size, differences in the rate of mVIM and mCCNA1 detection of HGD versus detection of NBDE or EAC are not statistically significant ($P > 0.088$ for any between group comparisons).

	mVIM		mCCNA1		Either mVIM or mCCNA1	
	%	*n*	%	*n*	%	*n*
Specificity unaffected controls	91.7	36	100.0	36	91.7	36
Sensitivity all cases	80.0	50	72.0	50	88.0	50
Sensitivity all NDBE	80.6	31	71.0	31	90.3	31
Sensitivity SSBE	69.2	13	53.8	13	84.6	13
Sensitivity LSBE	88.9	18	83.3	18	94.4	18
Sensitivity all dysplastic BE	72.7	11	72.7	11	81.8	11
Sensitivity LGD	83.3	6	100.0	6	100.0	6
Sensitivity HGD	50.0	4	50.0	4	50.0	4
Sensitivity EAC	87.5	8	75.0	8	87.5	8

VIM methylation was additionally identifiable in esophageal balloon samples from certain individuals in whom dysplastic BE had been previously ablated. Specifically, analysis of balloon samples from 23 endoscopically normal individuals who were unevaluable for the primary study, because of their having had ablation of previous dysplastic BE lesions, also demonstrated positive mVIM signals present in eight (35%) patients ($P < 0.017$ for increased mVIM positivity in post-ablation versus evaluable control individuals; table S8). This finding suggests that the endoscopically normal post-ablation GE junction, and/or post-ablation neosquamous epithelium, may retain molecular abnormalities associated with previous IM and may hence harbor continued cellular precursors of BE. It will be intriguing to determine whether, on longitudinal follow-up, these individuals who retain *VIM* methylation after BE ablation will demonstrate a higher risk for BE recurrence. Curiously, only 2 of these 23 post-ablation individuals were positive for *CCNA1* methylation.

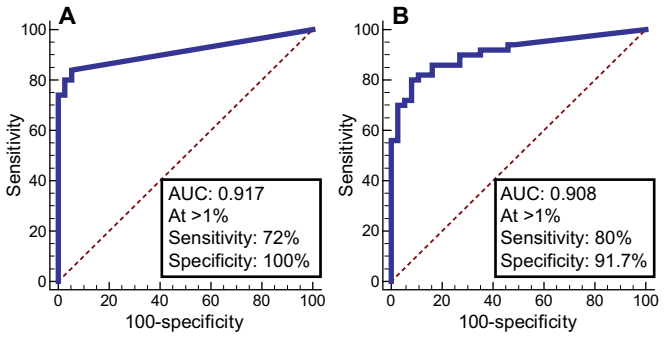

Fig. 6. ROC curves of mCCNA1 and mVIM assayed on esophageal balloon samplings of the distal esophagus. (**A**) mCCNA1, $n = 36$ controls and 50 cases. (**B**) mVIM, $n = 36$ controls and 50 cases. AUC and the sensitivity and specificity of the assays at the indicated cutpoints are listed for each graph, with the cutpoint value of percent methylation that defines a positive test denoted by "At >."

Biological implications

These studies in the esophagus help to inform the larger understanding of the genesis of aberrant DNA methylation in human neoplasias. Our data strongly point to epithelial cells as the source of both *VIM* and *CCNA1* methylation signals. First, *VIM* and *CCNA1* methylation were both detected in epithelial fractions from microdissected FFPE samples of early and late BE lesions (Table 3). Second, EAC cell lines demonstrated nearly complete biallelic methylation (>97% of alleles methylated) in five of five cell lines for *CCNA1* and in four of five cell lines for VIM (fig. S3). Third, testing in whole-organ gastroesophagus porcine explants showed that the balloon device samples a nearly exclusively epithelial cell population (fig. S4). Consistent with this, no breaches of the surface epithelium (no abrasions) were detected in the human participants in this study, all of whom underwent upper endoscopic examination immediately after the balloon procedure. The basis for the aberrant methylation of *VIM* and *CCNA1* genomic loci that we commonly found in BE-related lesions remains obscure. As noted above, smoking was associated with increased mVIM and mCCNA1 only in the proximal (upper) but not in the distal esophagus (Fig. 4 and table S5). Moreover, there is no clear functional implication of *CCNA1* methylation in BE, because expression of this cyclin family gene is normally restricted primarily to the testis, with lesser expression in the brain, and because *CCNA1* expression is not present in either unmethylated normal squamous esophagus or methylated EAC cells (fig. S3). Similarly, *VIM* expression is also absent in the unmethylated normal esophagus (fig. S3). However, *VIM* expression is associated with epithelial to mesenchymal transition (EMT) of cancer cells (*21*), and although *VIM* expression was absent in all four *VIM*-methylated EAC cell lines, *VIM* expression was detected in unmethylated FLO1 EAC cells (fig. S3), suggesting that *VIM* methylation may provide a mechanism for cancer cells to suppress EMT.

Table 3. mVIM and mCCNA1 detection in FFPE biopsies of upper gastrointestinal tract pathologies. mVIM and mCCNA1 were assayed in microdissected formalin-fixed paraffin-embedded (FFPE) biopsies that captured each of the histologies shown. IM, intestinal metaplasia. Samples were scored as methylated for mVIM >1.05% and mCCNA1 >3.12% (the cutpoints established in ROC analysis of esophageal brushings assayed for each marker). Samples were positive for the panel of mCCNA1 plus mVIM if either marker tested positive. Entries indicate percent positive samples (%) and total number of individuals tested (*n*).

	mCCNA1		mVIM		Either mVIM or mCCNA1	
	%	*n*	%	*n*	%	*n*
BE (IM)	75	20	90	21	90	21
GEJ/cardia with IM (<1-cm extent)	67	9	70	10	80	10
Non-IM columnar metaplasia concurrent with BE	11	9	30	10	30	10
GEJ/cardia without IM (including 15 cases with chronic carditis)	0	53	0	54	0	55
Distal normal squamous esophagus from control patients without glandular metaplasia	0	24	0	24	0	24
Eosinophilic esophagitis	0	12	0	15	0	15
Gastric fundic mucosa without IM	4	24	0	24	4	24
Intestinal metaplasia of stomach	14	7	11	9	22	9
H. pylori gastritis without IM	15	13	8	13	15	13

DISCUSSION

This study demonstrates the feasibility of non-endoscopic office-based molecular cytology screening for BE and EAC. First, we have identified cytosine methylation of the *CCNA1* locus as a methylation marker of BE. Second, we have shown that molecular cytology assays of distal esophageal brushings, by bisulfite sequencing detection of the two-marker panel of mVIM and mCCNA1 DNAs, detect BE and EAC with sensitivity and specificity both greater than 90%. Third, we have shown that a swallowable balloon device can obtain DNA samples from the distal esophagus in a rapid simple unsedated outpatient examination and, when combined with bisulfite sequencing for detecting DNA methylation, maintains both sensitivity and specificity for detecting BE and EAC at close to 90%. The combination of this sampling device and molecular diagnostic assay demonstrates the feasibility of non-endoscopic molecular cytology screening for BE as a method for ultimately preventing EAC development.

EAC has steadily increased in incidence over recent decades. With an 82% 5-year mortality rate, this cancer is the most rapidly increasing cause of cancer mortality from solid tumors in the American population (*5*). BE is a precursor lesion from which EAC develops, and ablation of BE with HGD and/or LGD is recommended to prevent EAC (*22*, *23*). However, the great majority of EACs are diagnosed in patients who have never had previous BE screening. This reflects that most patients with GERD symptoms do not undergo upper endoscopy and, moreover, that 40% of EACs develop in patients with no previous symptoms (*24*, *25*). Thus, the success of ablation approaches in preventing EAC will remain limited without an acceptable and cost-effective method to effectively screen at-risk populations and detect those individuals who are harboring BE. Non-endoscopic balloon sampling paired with molecular assay for mVIM and mCCNA1 offers a technology to address this need for simple noninvasive BE screening.

Given the need, other investigators have also advanced alternative approaches for BE screening. One such approach uses sponge-based devices for esophageal sampling (*26*, *27*). One advantage of the balloon device is that it deploys rapidly by inflation, eliminating the waiting time for the coating on typical sponge devices to dissolve. In addition, as the balloon retracts into its capsule after sampling, it enables directed sampling of the distal esophagus and provides protection of the sample from dilution or contamination from the proximal esophagus or oral cavity. Moreover, the smaller dimensions of the retracted balloon provide for easier and more comfortable retrieval. Balloon sampling of the esophagus was first demonstrated by Falk and colleagues (*28*), with the current balloon-based device now incorporating additional design enhancements that include optimized surface texturing and the addition of a protective capsule for delivery and retrieval.

Immunohistochemical detection of trefoil factor 3 has also been proposed as a biomarker for detection of BE, with a reported sensitivity of 79.9% when used with a cytosponge collection device (*29*). Attractions of DNA-based biomarkers include absence of subjectivity in interpretation and ease of automation for processing large sample numbers. Although direct comparison between the approaches will be of interest, the finding of 91% sensitivity for detecting BE metaplasia by mVIM plus mCCNA1 assays performed on balloon samples suggests that this approach is likely at least as robust and may offer ease of examination and easier scalability to large populations. The lower background of *CCNA1* methylation in control individuals sampled by esophageal balloons, as compared to cytology brushings, is intriguing and perhaps reflects a useful advantage arising from the somewhat more superficial cell layer sampled by the balloon versus by cytology brushings.

We note that this study does have some limitations. The balloon device investigation was conducted at a single tertiary care institution, and establishing generality will require replication at other centers and in community-based populations. Our study population is also predominantly male Caucasians, suggesting caution in extrapolating these results to females and other ethnic groups, in which BE is less

common. In addition, we suffered failures of some participants to swallow the balloon device or of the device to obtain adequate sample. Remedying this limitation will need to be a focus of future enhancements to the device design. Last, we lack longitudinal follow-up to be able to interpret implications of finding positive tests for mVIM and mCCNA1 in endoscopically normal individuals without IM of stomach or esophagus or in higher-risk individuals who are post ablation of dysplastic BE.

In summary, this study suggests that the combination of a balloon-based sampling device with bisulfite sequencing of the *VIM* and *CCNA1* loci provides a highly sensitive and specific yet minimally invasive screening procedure that could be clinically useful for detection and screening of BE.

MATERIALS AND METHODS

Study design

The study protocol was approved by University Hospitals Cleveland Medical Center and Cleveland Clinic Institutional Review Boards for Human Subject Investigation. Clinical trial registration numbers at ClinicalTrials.gov are NCT02451124 for the non-endoscopic balloon trial and NCT00288119 for the endoscopic cytology brushings study. Subjects referred for outpatient EGD were approached for study participation. Consent for obtaining esophageal brushings and biopsies for research was obtained from subjects before their EGD. Cases were classified as subjects with newly diagnosed BE, those undergoing surveillance of BE, or those with a new diagnosis of esophageal or GE junctional adenocarcinoma undergoing an endoscopic procedure. BE was defined according to current American College of Gastroenterology guidelines as at least 1 cm of endoscopically visible columnar mucosa in the distal esophagus with IM confirmed on histology (*7*). Lesions <1 cm were classified as ultrashort BE and analyzed separately. Control subjects had no endoscopic evidence of BE and no histological evidence of IM if a clinical biopsy was obtained from either the distal esophagus or GE junction.

The overall study was a nonrandomized observational study. Esophageal brushings were first used to validate findings from esophageal biopsies of methylated vimentin and *CCNA1* as biomarkers for detection of BE. Balloon-based esophageal samples were then obtained as a second validation sample. Study size was not prespecified, and results are reported for esophageal brushing samples accrued from June 2011 to February 2017 and for all balloon samples accrued from July 2015 to August 2016. No subjects were excluded from reporting. The primary endpoint of detection of BE and related progressed lesions was prespecified before study initiation. All laboratory samples were assayed by investigators blinded to the clinical status of the subjects.

Reduced representation bisulfite sequencing

RRBS was performed as previously described (*15*). Genomic DNA isolated from frozen esophageal biopsies or cell lines was digested with Msp I (New England Biolabs, no. R0106T). End repair, A-tailing, and adapter ligation were carried out using the NEXTFlex Bisulfite-Seq library prep kit (Bioo Scientific, cat. no. NOVA-5119-02) with additional use of methylated NEXTFlex bisulfite sequencing barcoded adapters (Bioo Scientific, cat. no. NOVA-511912) to allow for multiplexing multiple samples on a single sequencing lane. After adapter ligation, the library was size-fractionated on an agarose gel, and DNA fragments between 170 and 350 bp (corresponding to the initial unligated 40- to 220-bp Msp I digest fragments) were isolated and purified from the gel using Macherey-Nagel gel extraction and PCR purification kit (cat. no. 740609.250). After elution from the columns, DNA was bisulfite-converted using the EpiTect Bisulfite Conversion Kit (QIAGEN, cat. no. 59104). Adapter-ligated and converted libraries were then PCR-amplified and purified using Macherey-Nagel gel extraction and PCR purification kit.

Sequencing was performed on an Illumina HiSeq 2500 using paired-end 100-bp reads. Individual BAM files for each sample were generated for alignment. DNA sequencing reads from each RRBS experiment were aligned to bisulfite-converted and unconverted versions of the human reference genome (hg18) using Bowtie2, and percent methylation for each CpG was calculated by dividing the number of methylated Cs by the total coverage of that base. These analyses were facilitated by the Bismark software (*30*), which was specifically developed for processing RRBS data. The overall pipeline converts raw RRBS FASTQ files to tables of read depth and percent methylation at each individual CpG site for each patient sample.

Endoscopic sampling

During the endoscopy, one cytology brushing (US Endoscopy) was obtained from the proximal squamous esophagus, 20 to 25 cm from the incisors, as soon as the esophagus was intubated. The second cytology brushing was obtained from endoscopic BE or cancer lesions. In endoscopic normal controls, the GE junction was brushed to sample the glandular mucosa as well as distal squamous mucosa. Standard-of-care clinical biopsies were obtained from suspected BE and cancer cases. Data were collected from subjects regarding demographics, indications for EGD, GERD symptoms, exposures, and past medical history. All diagnoses (Table 1) were established by endoscopic report and histopathology review of clinical biopsy samples. Demographic data for all patients are provided in table S2. Brushes were immediately clipped with wire cutters into empty nuclease-free 0.5-ml cryo-safe tubes and immediately snap-frozen on dry ice for transport to storage at −80°C until use. Genomic DNA was extracted from endoscopic brushes using the DNeasy Blood and Tissue Kit (QIAGEN, cat. no. 69504). The protocol for the purification of total DNA from animal tissues (Spin-Column Protocol) was used with the modification of increasing the digestion time to overnight. Final elution volume was 100 µl. DNA yields from clinical samples were quantitated using the Qubit fluorometer (Invitrogen).

FFPE tissues specimens

Archival normal and neoplastic tissue specimens were obtained from the Department of Pathology at University Hospitals Cleveland Medical Center under a tissue procurement protocol approved by University Hospitals Cleveland Medical Center Institutional Review Board. Before use, diagnostic slides of all samples were reviewed by a gastrointestinal pathologist (J.E.W.) for confirmation of the recorded diagnoses. After confirmation of diagnoses, specimens for this study were prepared via punch biopsies of tissue blocks. The presence of IM in designated esophageal biopsies was required for a diagnosis of BE according to published guidelines (*7*).

DNA was purified using QIAamp DNA Micro Kit (QIAGEN) according to the manufacturer's protocol with the following modifications: The starting extraction volume was increased to 200 µl of ATL buffer and 50 µl of proteinase K. The cores were digested for 4 days at 60°. An additional 6 µl of proteinase K was added on days 2 and 3 of incubation. The DNA was eluted from columns in 100 µl of low–tris-EDTA (TE) elution buffer and used immediately for bisulfite conversion or frozen at −80°C until use.

Non-endoscopic esophageal brushing via a balloon device

We designed an encapsulated, inflatable, surface-featured balloon for targeted sampling of the distal esophagus. The device was delivered in a 16 × 9–mm capsule that also protected the acquired biospecimen from potential contamination with proximal esophagus material during withdrawal. Subjects referred for outpatient EGD were approached for study participation. Patients underwent unsedated distal esophageal sampling with the balloon device before scheduled EGD. After a patient swallowed the capsule with the balloon and the capsule was allowed to reach the stomach, the balloon was inflated with 5 to 5.5 cm^3 of air using the attached tubing and syringe. On average, the balloon reached the stomach in 3.3 min (range, 1 to 7 min). The inflated balloon was pulled slowly for 3 to 6 cm from the point where the constriction of the esophageal sphincter was felt by the endoscopist and then deflated using an attached syringe, thus retracting the balloon inside the capsule and protecting the sample. After the capsule was removed, the balloon was reinflated, cut off from the capsule, and immediately frozen. DNA was extracted from balloons using the same protocol as for endoscopic brushings but with the modification of increasing the volumes of kit buffers ATL and AL to 1 ml, to completely cover the balloons. After the procedure, each patient filled out a standardized tolerance and acceptance questionnaire (table S9) (*31*).

Bisulfite conversion of the genomic DNA

To create a template for PCR and then DNA methylation analysis, DNA samples were subjected to treatment with sodium bisulfite, which converts unmethylated cytosine bases into uracil, while leaving methylated cytosines intact, using an EpiTect kit (QIAGEN) according to the manufacturer's protocol. The person performing the methylation analysis was blinded to the clinical history of the samples until after all procedures and calculations were completed.

Bisulfite sequencing–based methylation detection

Bisulfite-converted DNA samples from cytology brushings were analyzed by NGS. Bisulfite-specific, methylation-indifferent PCR primers were constructed as a mixture of primers against converted products of fully methylated or fully unmethylated templates and were used to amplify a differentially methylated region of the vimentin exon 1 CpG island [previously described, (*32*)] or *CCNA1* (table S10). Platinum Taq reaction mix (Invitrogen) was supplemented with 1 mM $MgCl_2$, 0.2 mM deoxyribonucleotide triphosphates (New England Biolabs), 0.5 M betaine (Sigma), and a mix of the four primers, each at 0.1 μM final concentration. PCR was performed using a touchdown protocol, where after the activation of Taq polymerase at 95°C for 5 min, the initial cycling conditions were 95°C for 45 s, 67°C for 45 s, and 72°C for 45 s. The annealing temperature was decreased by 3°C every three cycles to a final of 55°C. An additional 33 cycles of PCR were performed at the annealing temperature of 55°C. Successful amplification was confirmed by agarose gel electrophoresis. PCR products were purified using NucleoSpin Gel and PCR Clean-up kit (Macherey-Nagel) and quantitated by Qubit. The NEXTflex Rapid DNA-Seq Kit (Bioo Scientific) was used to prepare indexed libraries for NGS sequencing (Illumina-compatible), and NGS was performed using a MiSeq platform at the McGill University and Génome Québec Innovation Centre, Montréal, Canada. FFPE DNA samples were bisulfite-converted and sequenced by EpiQuest (Zymo Research), using the same protocol as above.

Analysis of non-endoscopic balloon DNA samples was done the same way as for brushing samples above, except that the PCR amplification primers (table S10) were indexed by adding 96 different 7-bp index tags to the 5′ end of both forward and reverse primers (table S11). The amplification with indexed primers was carried out under the same conditions as for nonindexed primers, and the PCR products were subsequently mixed together, before preparing a library for NGS using a nonindexed library adapter.

DNA sequencing reads from each sample were aligned to bisulfite-converted and unconverted versions of the human reference genome (hg18) using Bowtie2. *VIM* aligned reads were classified as methylated if they indicated that 8 or more CpG dinucleotides were methylated (out of total of 10 CpGs present between the primers in the *VIM* PCR fragment). *CCNA1* aligned reads were classified as methylated if they indicated that 16 or more CpG dinucleotides were methylated (out of a total of 21 CpGs present between the primers in the *CCNA1* PCR fragment). These analyses were facilitated by use of Bismark software (*30*), which was specifically developed for processing bisulfite sequencing data.

Statistical methods

Between-group comparisons of continuous variables were performed using unpaired Student's *t* test (for two groups) or one-way analysis of variance (ANOVA) for groups of three or more, followed by the post hoc Student-Newman-Keuls test for all pairwise comparisons. The Mann-Whitney rank sum test was used to determine the *P* value for comparison of smokers and nonsmokers. Fisher's exact test was used for comparison of demographic composition of cases/controls in brushing and balloon studies. ROC curves and all associated statistics were generated using MedCalc software. The optimal cutpoints were calculated as maximizing the sum of sensitivity plus specificity.

SUPPLEMENTARY MATERIALS

www.sciencetranslationalmedicine.org/cgi/content/full/10/424/eaao5848/DC1

Fig. S1. Flowchart of study analyses.
Fig. S2. Comparison of methylation of individual CpGs versus CpG patches in discriminating esophageal lesions.
Fig. S3. Comparing *VIM* and *CCNA1* expression versus methylation.
Fig. S4. Morphology of touch preps from balloon brushings of three intact porcine esophagus samples from esophagogastric organ explants.
Table S1. Location of 26 differentially methylated patches identified by RRBS comparison of normal esophageal squamous mucosa versus Barrett's lesions.
Table S2. Demographic characteristics of training and validation esophageal brushing populations.
Table S3. mVIM and mCCNA1 performance in training and validation esophageal brushing samples.
Table S4. Comparison of sensitivities of mVIM plus mCCNA1 versus mVIM or mCCNA1, all at equal specificities.
Table S5. Influence of smoking on *VIM* and *CCNA1* methylation in proximal versus distal esophagus.
Table S6. Participant evaluation of the non-endoscopic balloon sampling of the esophagus.
Table S7. Demographic characteristics of subjects in non-endoscopic balloon study.
Table S8. Methylation in post-ablation subjects.
Table S9. Post-examination questionnaire.
Table S10. Bisulfite-specific methylation-independent PCR primer sequences.
Table S11. Index tags for bisulfite-specific methylation-independent PCR primer sequences.
References (*33*–*66*)

REFERENCES AND NOTES

1. W. J. Blot, S. S. Devesa, R. W. Kneller, J. F. Fraumeni Jr., Rising incidence of adenocarcinoma of the esophagus and gastric cardia. *JAMA* **265**, 1287–1289 (1991).
2. S. S. Devesa, W. J. Blot, J. F. Fraumeni Jr., Changing patterns in the incidence of esophageal and gastric carcinoma in the United States. *Cancer* **83**, 2049–2053 (1998).
3. M. Pera, A. J. Cameron, V. F. Trastek, H. A. Carpenter, A. R. Zinsmeister, Increasing incidence of adenocarcinoma of the esophagus and esophagogastric junction. *Gastroenterology* **104**, 510–513 (1993).

4. H. Pohl, H. G. Welch, The role of overdiagnosis and reclassification in the marked increase of esophageal adenocarcinoma incidence. *J. Natl. Cancer Inst.* **97**, 142–146 (2005).
5. R. L. Siegel, K. D. Miller, A. Jemal, Cancer statistics, 2016. *CA Cancer J. Clin.* **66**, 7–30 (2016).
6. American Gastroenterological Association, American Gastroenterological Association medical position statement on the management of Barrett's esophagus. *Gastroenterology* **140**, 1084–1091 (2011).
7. N. J. Shaheen, G. W. Falk, P. G. Iyer, L. B. Gerson, ACG clinical guideline: Diagnosis and management of Barrett's esophagus. *Am. J. Gastroenterol.* **111**, 30–50 (2016).
8. G. S. Dulai, S. Guha, K. L. Kahn, J. Gornbein, W. M. Weinstein, Preoperative prevalence of Barrett's esophagus in esophageal adenocarcinoma: A systematic review. *Gastroenterology* **122**, 26–33 (2002).
9. W.-D. Chen, Z. J. Han, J. Skoletsky, J. Olson, J. Sah, L. Myeroff, P. Platzer, S. Lu, D. Dawson, J. Willis, T. P. Pretlow, J. Lutterbaugh, L. Kasturi, J. K. V. Willson, J. S. Rao, A. Shuber, S. D. Markowitz, Detection in fecal DNA of colon cancer–specific methylation of the nonexpressed vimentin gene. *J. Natl. Cancer Inst.* **97**, 1124–1132 (2005).
10. W. M. Grady, J. Willis, P. J. Guilford, A. K. Dunbier, T. T. Toro, H. Lynch, G. Wiesner, K. Ferguson, C. Eng, J.-G. Park, S.-J. Kim, S. Markowitz, Methylation of the CDH1 promoter as the second genetic hit in hereditary diffuse gastric cancer. *Nat. Genet.* **26**, 16–17 (2000).
11. D. M. Marzese, D. S. B. Hoon, Emerging technologies for studying DNA methylation for the molecular diagnosis of cancer. *Expert Rev. Mol. Diagn.* **15**, 647–664 (2015).
12. H. R. Moinova, W.-D. Chen, L. Shen, D. Smiraglia, J. Olechnowicz, L. Ravi, L. Kasturi, L. Myeroff, C. Plass, R. Parsons, J. Minna, J. K. V. Willson, S. B. Green, J.-P. Issa, S. D. Markowitz, HLTF gene silencing in human colon cancer. *Proc. Natl. Acad. Sci. U.S.A.* **99**, 4562–4567 (2002).
13. C. Noehammer, W. Pulverer, M. R. Hassler, M. Hofner, M. Wielscher, K. Vierlinger, T. Liloglou, D. McCarthy, T. J. Jensen, A. Nygren, H. Gohlke, G. Trooskens, M. Braspenning, W. Van Criekinge, G. Egger, A. Weinhaeusel, Strategies for validation and testing of DNA methylation biomarkers. *Epigenomics* **6**, 603–622 (2014).
14. H. Moinova, R. S. Leidner, L. Ravi, J. Lutterbaugh, J. S. Barnholtz-Sloan, Y. Chen, A. Chak, S. D. Markowitz, J. E. Willis, Aberrant vimentin methylation is characteristic of upper gastrointestinal pathologies. *Cancer Epidemiol. Biomarkers Prev.* **21**, 594–600 (2012).
15. H. Gu, Z. D. Smith, C. Bock, P. Boyle, A. Gnirke, A. Meissner, Preparation of reduced representation bisulfite sequencing libraries for genome-scale DNA methylation profiling. *Nat. Protoc.* **6**, 468–481 (2011).
16. C. Bock, E. M. Tomazou, A. B. Brinkman, F. Müller, F. Simmer, H. Gu, N. Jäger, A. Gnirke, H. G. Stunnenberg, A. Meissner, Quantitative comparison of genome-wide DNA methylation mapping technologies. *Nat. Biotechnol.* **28**, 1106–1114 (2010).
17. E. Richmond, A. Umar, Mechanisms of esophageal adenocarcinoma formation and approaches to chemopreventive intervention. *Semin. Oncol.* **43**, 78–85 (2016).
18. A. Singh, A. Chak, Advances in the management of Barrett's esophagus and early esophageal adenocarcinoma. *Gastroenterol. Rep. (Oxf)* **3**, 303–315 (2015).
19. Y. Hayakawa, N. Sethi, A. R. Sepulveda, A. J. Bass, T. C. Wang, Oesophageal adenocarcinoma and gastric cancer: Should we mind the gap? *Nat. Rev. Cancer* **16**, 305–318 (2016).
20. Cancer Genome Atlas Research Network, Integrated genomic characterization of oesophageal carcinoma. *Nature* **541**, 169–175 (2017).
21. S. Lamouille, J. Xu, R. Derynck, Molecular mechanisms of epithelial–mesenchymal transition. *Nat. Rev. Mol. Cell Biol.* **15**, 178–196 (2014).
22. C. L. Greene, E. M. Tomazou, A. B. Brinkman, F. Müller, F. Simmer, H. Gu, N. Jäger, A. Gnirke, H. G. Stunnenberg, A. Meissner, Emerging concepts for the endoscopic management of superficial esophageal adenocarcinoma. *J. Gastrointest. Surg.* **20**, 851–860 (2016).
23. A. J. Small, J. L. Araujo, C. L. Leggett, A. H. Mendelson, A. Agarwalla, J. A. Abrams, C. J. Lightdale, T. C. Wang, P. G. Iyer, K. K. Wang, A. K. Rustgi, G. G. Ginsberg, K. A. Forde, P. A. Gimotty, J. D. Lewis, G. W. Falk, M. Bewtra, Radiofrequency ablation is associated with decreased neoplastic progression in patients with Barrett's esophagus and confirmed low-grade dysplasia. *Gastroenterology* **149**, 567–576.e3 (2015).
24. A. Chak, A. Faulx, C. Eng, W. Grady, M. Kinnard, H. Ochs-Balcom, G. Falk, Gastroesophageal reflux symptoms in patients with adenocarcinoma of the esophagus or cardia. *Cancer* **107**, 2160–2166 (2006).
25. J. Lagergren, R. Bergström, A. Lindgren, O. Nyrén, Symptomatic gastroesophageal reflux as a risk factor for esophageal adenocarcinoma. *N. Engl. J. Med.* **340**, 825–831 (1999).
26. S. Kadri, P. Lao-Sirieix, R. C. Fitzgerald, Developing a nonendoscopic screening test for Barrett's esophagus. *Biomark. Med.* **5**, 397–404 (2011).
27. S. R. Kadri, P. Lao-Sirieix, M. O'Donovan, I. Debiram, M. Das, J. M. Blazeby, J. Emery, A. Boussioutas, H. Morris, F. M. Walter, P. Pharoah, R. H. Hardwick, R. C. Fitzgerald, Acceptability and accuracy of a non-endoscopic screening test for Barrett's oesophagus in primary care: Cohort study. *BMJ* **341**, c4372 (2010).
28. G. W. Falk, R. Chittajallu, J. R. Goldblum, C. V. Biscotti, K. R. Geisinger, R. E. Petras, S. Birgisson, T. W. Rice, J. E. Richter, Surveillance of patients with Barrett's esophagus for dysplasia and cancer with balloon cytology. *Gastroenterology* **112**, 1787–1797 (1997).
29. C. S. Ross-Innes, C. S. Ross-Innes, I. Debiram-Beecham, M. O'Donovan, E. Walker, S. Varghese, P. Lao-Sirieix, L. Lovat, M. Griffin, K. Ragunath, R. Haidry, S. S. Sami, P. Kaye, M. Novelli, B. Disep, R. Ostler, B. Aigret, B. V. North, P. Bhandari, A. Haycock, D. Morris, S. Attwood, A. Dhar, C. Rees, M. D. D. Rutter, P. D. Sasieni, R. C. Fitzgerald, Evaluation of a minimally invasive cell sampling device coupled with assessment of trefoil factor 3 expression for diagnosing Barrett's esophagus: A multi-center case–control study. *PLOS MED.* **12**, e1001780 (2015).
30. F. Krueger, S. R. Andrews, Bismark: A flexible aligner and methylation caller for Bisulfite-Seq applications. *Bioinformatics* **27**, 1571–1572 (2011).
31. A. F. Peery, T. Hoppo, K. S. Garman, E. S. Dellon, N. Daugherty, S. Bream, A. F. Sanz, J. Davison, M. Spacek, D. Connors, A. L. Faulx, A. Chak, J. D. Luketich, N. J. Shaheen, B. A. Jobe; Barret's Esophagus Risk Consotium, Feasibility, safety, acceptability, and yield of office-based, screening transnasal esophagoscopy (with video). *Gastrointest. Endosc.* **75**, 945–953.e2 (2012).
32. M. Li, W.-d. Chen, N. Papadopoulos, S. N. Goodman, N. C. Bjerregaard, S. Laurberg, B. Levin, H. Juhl, N. Arber, H. Moinova, K. Durkee, K. Schmidt, Y. He, F. Diehl, V. E. Velculescu, S. Zhou, L. A. Diaz Jr., K. W. Kinzler, S. D. Markowitz, B. Vogelstein, Sensitive digital quantification of DNA methylation in clinical samples. *Nat. Biotechnol.* **27**, 858–863 (2009).
33. A. Ooki, Z. Maleki, J.-J. Tsay, C. Goparaju, M. Brait, N. Turaga, H. S. Nam, W. N. Rom, H. I. Pass, D. Sidransky, R. Guerrero-Preston, M. O. Hoque, A panel of novel detection and prognostic methylated DNA markers in primary non-small cell lung cancer and serum DNA. *Clin. Cancer Res.* **23**, 7141–7152 (2017).
34. S. Shen, G. Wang, Q. Shi, R. Zhang, Y. Zhao, Y. Wei, F. Chen, D. C. Christiani, Seven-CpG-based prognostic signature coupled with gene expression predicts survival of oral squamous cell carcinoma. *Clin. Epigenetics* **9**, 88 (2017).
35. H. Tanaka, M. Kanda, M. Koike, N. Iwata, D. Shimizu, K. Ezaka, S. Sueoka, Y. Tanaka, H. Takami, R. Hashimoto, C. Tanaka, S. Yamada, T. Fujii, G. Nakayama, H. Sugimoto, M. Fujiwara, Y. Kodera, Adherens junctions associated protein 1 serves as a predictor of recurrence of squamous cell carcinoma of the esophagus. *Int. J. Oncol.* **47**, 1811–1818 (2015).
36. D. Cogdell, W. Chung, Y. Liu, J. M. McDonald, K. Aldape, J. P. Issa, G. N. Fuller, W. Zhang, Tumor-associated methylation of the putative tumor suppressor AJAP1 gene and association between decreased AJAP1 expression and shorter survival in patients with glioma. *Chin. J. Cancer* **30**, 247–253 (2011).
37. E.-J. Lee, P. Rath, J. Liu, D. Ryu, L. Pei, S. K. Noonepalle, A. Y. Shull, Q. Feng, N. S. Litofsky, D. C. Miller, D. C. Anthony, M. D. Kirk, J. Laterra, L. Deng, H.-B. Xin, X. Wang, J.-H. Choi, H. Shi, Identification of global DNA methylation signatures in glioblastoma-derived cancer stem cells. *J. Genet. Genomics* **42**, 355–371 (2015).
38. K. Matsusaka, A. Kaneda, G. Nagae, T. Ushiku, Y. Kikuchi, R. Hino, H. Uozaki, Y. Seto, K. Takada, H. Aburatani, M. Fukayama, Classification of Epstein–Barr virus–positive gastric cancers by definition of DNA methylation epigenotypes. *Cancer Res.* **71**, 7187–7197 (2011).
39. H.-C. Lai, Y.-C. Wang, M.-H. Yu, R.-L. Huang, C.-C. Yuan, K.-J. Chen, C.-C. Wu, K.-J. Chiang, T.-K. Chao, DNA methylation as a biomarker for the detection of hidden carcinoma in endometrial atypical hyperplasia. *Gynecol. Oncol.* **135**, 552–559 (2014).
40. Y.-C. Chen, R.-L. Huang, Y.-K. Huang, Y.-P. Liao, P.-H. Su, H.-C. Wang, C.-C. Chang, Y.-W. Lin, M.-H. Yu, T.-Y. Chu, H.-C. Lai, Methylomics analysis identifies epigenetically silenced genes and implies an activation of β-catenin signaling in cervical cancer. *Int. J. Cancer* **135**, 117–127 (2014).
41. M. O. Kitchen, R. T. Bryan, R. D. Emes, J. R. Glossop, C. Luscombe, K. K. Cheng, M. P. Zeegers, N. D. James, A. J. Devall, C. A. Mein, L. Gommersall, A. A. Fryer, W. E. Farrell, Quantitative genome-wide methylation analysis of high-grade non-muscle invasive bladder cancer. *Epigenetics* **11**, 237–246 (2016).
42. M. Murakami, T. Yoshimoto, K. Nakabayashi, K. Tsuchiya, I. Minami, R. Bouchi, H. Izumiyama, Y. Fujii, K. Abe, C. Tayama, K. Hashimoto, T. Suganami, K. Hata, K.-i. Kihara, Y. Ogawa, Integration of transcriptome and methylome analysis of aldosterone-producing adenomas. *Eur. J. Endocrinol.* **173**, 185–195 (2015).
43. E. Kostareli, D. Holzinger, O. Bogatyrova, T. Hielscher, G. Wichmann, M. Keck, B. Lahrmann, N. Grabe, C. Flechtenmacher, C. R. Schmidt, T. Seiwert, G. Dyckhoff, A. Dietz, D. Höfler, M. Pawlita, A. Benner, F. X. Bosch, P. Plinkert, C. Plass, D. Weichenhan, J. Hess, HPV-related methylation signature predicts survival in oropharyngeal squamous cell carcinomas. *J. Clin. Invest.* **123**, 2488–2501 (2013).
44. C. P. E. Lange, M. Campan, T. Hinoue, R. F. Schmitz, A. E. van der Meulen-de Jong, H. Slingerland, P. J. M. J. Kok, C. M. van Dijk, D. J. Weisenberger, H. Shen, R. A. E. M. Tollenaar, P. W. Laird, Genome-scale discovery of DNA-methylation biomarkers for blood-based detection of colorectal cancer. *PLOS ONE* **7**, e50266 (2012).
45. V. Kloten, M. Rose, S. Kaspar, S. von Stillfried, R. Knüchel, E. Dahl, Epigenetic inactivation of the novel candidate tumor suppressor gene *ITIH5* in colon cancer predicts unfavorable overall survival in the CpG island methylator phenotype. *Epigenetics* **9**, 1290–1301 (2014).
46. M. Rose, N. T. Gaisa, P. Antony, D. Fiedler, A. Heidenreich, W. Otto, S. Denzinger, S. Bertz, A. Hartmann, A. Karl, R. Knüchel, E. Dahl, Epigenetic inactivation of *ITIH5* promotes

bladder cancer progression and predicts early relapse of pT1 high-grade urothelial tumours. *Carcinogenesis* **35**, 727–736 (2014).
47. V. Kloten, B. Becker, K. Winner, M. G. Schrauder, P. A. Fasching, T. Anzeneder, J. Veeck, A. Hartmann, R. Knüchel, E. Dahl, Promoter hypermethylation of the tumor-suppressor genes *ITIH5*, *DKK3*, and *RASSF1A* as novel biomarkers for blood-based breast cancer screening. *Breast Cancer Res.* **15**, R4 (2013).
48. J. Dittmann, A. Ziegfeld, L. Jansen, M. Gajda, V. Kloten, E. Dahl, I. B. Runnebaum, M. Dürst, C. Backsch, Gene expression analysis combined with functional genomics approach identifies ITIH5 as tumor suppressor gene in cervical carcinogenesis. *Mol. Carcinog.* **56**, 1578–1589 (2017).
49. S. Zhang, X.-L. Feng, L. Shi, C.-J. Gong, Z.-J. He, H.-J. Wu, T.-Y. Ling, Genome-wide analysis of DNA methylation in tongue squamous cell carcinoma. *Oncol. Rep.* **29**, 1819–1826 (2013).
50. G. Ma, H. Liu, Q. Hua, M. Wang, M. Du, Y. Lin, Y. Ge, W. Gong, Q. Zhao, F. Qiang, G. Tao, Z. Zhang, H. Chu, KCNMA1 cooperating with PTK2 is a novel tumor suppressor in gastric cancer and is associated with disease outcome. *Mol. Cancer* **16**, 46 (2017).
51. D. K. Vanaja, M. Ehrich, D. Boom, J. C. Cheville, R. J. Karnes, D. J. Tindall, C. R. Cantor, C. Y. Young, Hypermethylation of genes for diagnosis and risk stratification of prostate cancer. *Cancer Invest.* **27**, 549–560 (2009).
52. J. M. Yi, M. Dhir, A. A. Guzzetta, C. A. Iacobuzio-Donahue, K. Heo, K. M. Yang, H. Suzuki, M. Toyota, H.-M. Kim, N. Ahuja, DNA methylation biomarker candidates for early detection of colon cancer. *Tumour Biol.* **33**, 363–372 (2012).
53. J.-H. Bae, J. Park, K. M. Yang, T.-O. Kim, J. M. Yi; IBD Study Group of Korean Association for Study of Intestinal Diseases (KASID), Detection of DNA hypermethylation in sera of patients with Crohn's disease. *Mol. Med. Rep.* **9**, 725–729 (2014).
54. D. Li, Z. Xu, J. Liu, X. Pu, Y. Luo, X. Zheng, [Restriction landmark genomic scanning for screening aberrant CpG methylations in prostate cancer]. *Nan Fang Yi Ke Da Xue Xue Bao* **36**, 103–108 (2016).
55. L. M. R. B. Arantes, A. C. de Carvalho, M. E. Melendez, C. C. Centrone, J. F. Góis-Filho, T. N. Toporcov, D. N. Caly, E. H. Tajara, E. M. Goloni-Bertollo, A. L. Carvalho; GENCAPO, Validation of methylation markers for diagnosis of oral cavity cancer. *Eur. J. Cancer* **51**, 632–641 (2015).
56. K. Chalertpet, W. Pakdeechaidan, V. Patel, A. Mutirangura, P. Yanatatsaneejit, Human papillomavirus type 16 E7 oncoprotein mediates *CCNA1* promoter methylation. *Cancer Sci.* **106**, 1333–1340 (2015).
57. J. Klajic, F. Busato, H. Edvardsen, N. Touleimat, T. Fleischer, I. Bukholm, A.-L. Børresen-Dale, P. E. Lønning, J. Tost, V. N. Kristensen, DNA methylation status of key cell-cycle regulators such as *CDKNA2*/p16 and *CCNA1* correlates with treatment response to doxorubicin and 5-fluorouracil in locally advanced breast tumors. *Clin. Cancer Res.* **20**, 6357–6366 (2014).
58. L. Maldonado, M. Brait, C. Michailidi, E. Munari, T. Driscoll, L. Schultz, T. Bivalacqua, M. Schoenberg, D. Sidransky, G. J. Netto, M. O. Hoque, An epigenetic marker panel for recurrence risk prediction of low grade papillary urothelial cell carcinoma (LGPUCC) and its potential use for surveillance after transurethral resection using urine. *Oncotarget* **5**, 5218–5233 (2014).
59. Y. Li, J. Xu, H. Ju, Y. Xiao, H. Chen, J. Lv, T. Shao, J. Bai, Y. Zhang, L. Wang, X. Wang, H. Ren, X. Li, A network-based, integrative approach to identify genes with aberrant co-methylation in colorectal cancer. *Mol. Biosyst.* **10**, 180–190 (2014).
60. H. Bae, B. Kim, H. Lee, S. Lee, H.-S. Kang, S. Jung Kim, Epigenetically regulated Fibronectin leucine rich transmembrane protein 2 (FLRT2) shows tumor suppressor activity in breast cancer cells. *Sci. Rep.* **7**, 272 (2017).
61. M. Kusakabe, T. Kutomi, K. Watanabe, N. Emoto, N. Aki, H. Kage, E. Hamano, H. Kitagawa, T. Nagase, A. Sano, Y. Yoshida, T. Fukami, T. Murakawa, J. Nakajima, S. Takamoto, S. Ota, M. Fukayama, Y. Yatomi, N. Ohishi, D. Takai, Identification of *G0S2* as a gene frequently methylated in squamous lung cancer by combination of in silico and experimental approaches. *Int. J. Cancer* **126**, 1895–1902 (2010).
62. Y. Wu, J. Davison, X. Qu, C. Morrissey, B. Storer, L. Brown, R. Vessella, P. Nelson, M. Fang, Methylation profiling identified novel differentially methylated markers including *OPCML* and *FLRT2* in prostate cancer. *Epigenetics* **11**, 247–258 (2016).
63. S. Windhorst, K. Song, A. F. Gazdar, Inositol-1,4,5-trisphosphate 3-kinase-A (ITPKA) is frequently over-expressed and functions as an oncogene in several tumor types. *Biochem. Pharmacol.* **137**, 1–9 (2017).
64. Y.-W. Wang, X. Ma, Y.-A. Zhang, M.-J. Wang, Y. Yatabe, S. Lam, L. Girard, J.-Y. Chen, A. F. Gazdar, *ITPKA* gene body methylation regulates gene expression and serves as an early diagnostic marker in lung and other cancers. *J. Thorac. Oncol.* **11**, 1469–1481 (2016).
65. H. Takamaru, E. Yamamoto, H. Suzuki, M. Nojima, R. Maruyama, H. O. Yamano, K. Yoshikawa, T. Kimura, T. Harada, M. Ashida, R. Suzuki, H.-o. Yamamoto, M. Kai, T. Tokino, T. Sugai, K. Imai, M. Toyota, Y. Shinomura, Aberrant methylation of *RASGRF1* is associated with an epigenetic field defect and increased risk of gastric cancer. *Cancer Prev. Res. (Phila.)* **5**, 1203–1212 (2012).
66. N. Uehiro, F. Sato, F. Pu, S. Tanaka, M. Kawashima, K. Kawaguchi, M. Sugimoto, S. Saji, M. Toi, Circulating cell-free DNA-based epigenetic assay can detect early breast cancer. *Breast Cancer Res.* **18**, 129 (2016).

Acknowledgments: We acknowledge the contribution of staff of the McGill University and Génome Québec Innovation Centre, Montréal, Canada for NGS sequencing and thank Nottingham Spirk, North Coast Medical Development, and M. Haag and S. Weidenbecher for support and assistance in development of the balloon device. **Funding:** This study was supported by NIH grants P50CA150964, U54CA163060, UO1CA152756, UL1TR000439, and UH2CA205105; American Cancer Society grant 123436-RSG-12-159-01-DMC; and awards from the Case-Coulter Foundation Partnership for Translational Research and the Ohio Third Frontier Technology Validation and Start-Up Fund. **Author contributions:** S.D.M. and A.C. designed the study; A.C., J.D., P.N.T., A.F., and J.S.B.-S. wrote and submitted the clinical protocol and treated the patients; P.G.I., M.I.C., J.S.W., and N.J.S. recruited the patients and obtained research tissue samples; A.K.C. and W.B. archived and managed the clinical samples; J.E.W. performed the pathology review of FFPE samples; J.D.L. prepared and archived DNA for all samples used in the study; H.R.M. and K.G. performed the experiments; O.D.I.C.C. and T.L. performed the NGS analyses; H.R.M. and S.D.M. analyzed the data; and H.R.M., S.D.M., and A.C. wrote the manuscript. All authors reviewed and approved the final manuscript. **Competing interests:** A.C., J.E.W., and S.D.M. have awarded patents on the use of methylated vimentin for detection of BE and other GI cancers and have also pending patent on a balloon-based device for non-endoscopic sampling of the esophagus. A.C., J.E.W., S.D.M., T.L., O.D.I.C.C., and H.R.M. have pending patents on methylated *CCNA1*. Patent rights have been assigned to Case Western Reserve University and are managed under institutional conflict of interest policies. Awarded patents include U.S. Patent 9580754 (Methods and compositions for detecting gastrointestinal and other cancers), U.S. Patent 8415100 (Methods and compositions for detecting gastrointestinal and other cancers), and U.S. Patent 8221977 (Methods and compositions for detecting colon cancers). Pending patents include PCT/US2014/070060 (Device for collecting a biological sample), PCT/US2010/030084 (Digital quantification of DNA methylation), PCT/US2015/068131 (Methods and compositions for detecting esophageal neoplasias and metaplasias), and PCT/US2017/040708 (Methods and compositions for detecting esophageal neoplasias and/or metaplasias in the esophagus). S.D.M. has consulting relationships with Rodeo Therapeutics, Janssen Pharmaceuticals, and GlaxoSmithKline. A.C. has consulting relationships with US Endoscopy and C2 Therapeutics. N.J.S. consults for Shire, Ambu, and Boston Scientific and has research funding from Medtronic, C2 Therapeutics, CSA Medical, EndoStim, CDx Diagnostics, and Interpace Diagnostics. P.G.I. consults for Medtronic and has research funding from Exact Sciences, IntroMedic, and C2 Therapeutics. M.I.C. consults for PENTAX Medical Corporation and Cook Medical and has research funding from C2 Therapeutics Inc. J.D. consults for US Endoscopy and CSA Medical and has research funding from C2 Therapeutics. No other financial conflicts of interest pertain to the authors of this paper.

Submitted 7 August 2017
Accepted 8 November 2017
Published 17 January 2018
10.1126/scitranslmed.aao5848

Citation: H. R. Moinova, T. LaFramboise, J. D. Lutterbaugh, A. K. Chandar, J. Dumot, A. Faulx, W. Brock, O. De la Cruz Cabrera, K. Guda, J. S. Barnholtz-Sloan, P. G. Iyer, M. I. Canto, J. S. Wang, N. J. Shaheen, P. N. Thota, J. E. Willis, A. Chak, S. D. Markowitz, Identifying DNA methylation biomarkers for non-endoscopic detection of Barrett's esophagus. *Sci. Transl. Med.* **10**, eaao5848 (2018).

CANCER

A precision therapy against cancers driven by *KIT/PDGFRA* mutations

Copyright © 2017 The Authors, some rights reserved; exclusive licensee American Association for the Advancement of Science. No claim to original U.S. Government Works

Erica K. Evans,[1] Alexandra K. Gardino,[1] Joseph L. Kim,[1] Brian L. Hodous,[1] Adam Shutes,[1] Alison Davis,[1] Xing Julia Zhu,[1] Oleg Schmidt-Kittler,[1] Doug Wilson,[1] Kevin Wilson,[1] Lucian DiPietro,[1]* Yulian Zhang,[1]† Natasja Brooijmans,[1] Timothy P. LaBranche,[1] Agnieszka Wozniak,[2] Yemarshet K. Gebreyohannes,[2] Patrick Schöffski,[2] Michael C. Heinrich,[3] Daniel J. DeAngelo,[4] Stephen Miller,[1] Beni Wolf,[1] Nancy Kohl,[1]‡ Timothy Guzi,[1] Nicholas Lydon,[1] Andy Boral,[1] Christoph Lengauer[1]§

Targeting oncogenic kinase drivers with small-molecule inhibitors can have marked therapeutic benefit, especially when administered to an appropriate genomically defined patient population. Cancer genomics and mechanistic studies have revealed that heterogeneous mutations within a single kinase can result in various mechanisms of kinase activation. Therapeutic benefit to patients can best be optimized through an in-depth understanding of the disease-driving mutations combined with the ability to match these insights to tailored highly selective drugs. This rationale is presented for BLU-285, a clinical stage inhibitor of oncogenic KIT and PDGFRA alterations, including activation loop mutants that are ineffectively treated by current therapies. BLU-285, designed to preferentially interact with the active conformation of KIT and PDGFRA, potently inhibits activation loop mutants KIT D816V and PDGFRA D842V with subnanomolar potency and also inhibits other well-characterized disease-driving KIT mutants both in vitro and in vivo in preclinical models. Early clinical evaluation of BLU-285 in a phase 1 study has demonstrated marked activity in patients with diseases associated with *KIT* (aggressive systemic mastocytosis and gastrointestinal stromal tumor) and *PDGFRA* (gastrointestinal stromal tumor) activation loop mutations.

INTRODUCTION

Targeted inhibition of oncogenic kinases has transformed the care of a subset of cancer patients whose malignancy is driven by activating mutations and thus vulnerable to therapeutic inhibition of the activated oncoprotein. Successful examples of this approach include erlotinib and crizotinib for mutant *EGFR*- and *ALK*-/*ROS*-driven lung cancers, respectively (*1*–*3*), vemurafenib for mutant *BRAF* melanomas (*4*), and imatinib for both *BCR-ABL*–driven chronic myeloid leukemia and *KIT* mutant gastrointestinal stromal tumor (GIST) (*5*, *6*). However, effectively inhibiting a disease-driving kinase is complicated because various mechanisms of kinase activation, including alteration of conformational states or changes in dimerization potential, influence kinase inhibitor binding. Evaluation of individual oncogenic mutations is therefore critical to effectively pair an unmet medical need with the design of an appropriately targeted agent.

The KIT receptor belongs to the class III receptor tyrosine kinase (RTK) family that also includes the structurally related proteins PDGFRA (platelet-derived growth factor receptor A), PDGFRB, FLT3 (FMS-like tyrosine kinase 3), and CSF1R (colony-stimulating factor 1 receptor). Normally, stem cell factor (SCF) binds to and activates KIT by inducing dimerization, autophosphorylation, and initiation of downstream signaling (*7*). In several tumor types, however, somatic activating mutations in *KIT* drive ligand-independent constitutive activity; these mutations have been most extensively studied in GIST (*8*, *9*).

[1]Blueprint Medicines, Cambridge, MA 02139, USA. [2]Laboratory of Experimental Oncology, Department of Oncology, KU Leuven, Belgium 3000. [3]VA Health Care System and Knight Cancer Institute, Oregon Health and Science University, Portland, OR 97239, USA. [4]Department of Medical Oncology, Dana-Farber Cancer Institute, Boston, MA 02215, USA.
*Present address: Relay Therapeutics, Cambridge, MA 02142, USA.
†Present address: Actinium Pharmaceuticals Inc., New York, NY 10016, USA.
‡Present address: Nancy Kohl Consulting, Wellesley, MA 02482, USA.
§Corresponding author. Email: clengauer@blueprintmedicines.com

Nearly 80% of metastatic GISTs have a primary activating mutation in either the extracellular region (exon 9) or the juxtamembrane (JM) domain (exon 11) of *KIT*, and up to an additional 10% are mutated in the highly related kinase PDGFRA (*10*). The recognition that many KIT mutant tumors respond to treatment with imatinib has transformed the treatment of GIST. First-line imatinib treatment provides a median progression-free survival (PFS) of 18 to 24 months (*11*). However, most GIST patients eventually relapse due to a secondary mutation in *KIT* that markedly decreases the binding affinity of imatinib. These resistance mutations invariably arise within the adenosine 5′-triphosphate (ATP)–binding pocket (exons 13 and 14) or the activation loop (exons 17 and 18) of the kinase (*8*). Activation loop mutations accumulate with increasing frequency after second-line therapy (sunitinib), which also has inadequate activity on activation loop mutant proteins (*12*, *13*). In 5 to 6% of unresectable or metastatic GIST patients, an activation loop mutation in *PDGFRA* at amino acid 842 occurs as the primary mutation (*14*, *15*) and is insensitive to imatinib and all other approved GIST agents (*16*, *17*). With no effective treatments available, the prognosis for patients with metastatic PDGFRA D842V GIST is particularly dire, with PFS of only 3 to 5 months and overall survival of 15 months (*16*, *18*).

Beyond GIST, the D816V mutant in the activation loop of KIT, which is structurally identical to the D842V mutant in PDGFRA (*15*), is found in more than 90% of patients (*19*, *20*) with systemic mastocytosis (SM), a rare hematologic disease of clonal mast cells (*21*). In advanced forms of SM, organ function is compromised by the accumulation of excess mast cells, and overall survival is decreased. Although the indolent subtype of the disease does not affect survival, many patients suffer from debilitating symptoms associated with mast cell degranulation, histamine release, and a reduced quality of life. Midostaurin has recently been approved by the U.S. Food and Drug Administration (FDA) for the treatment of advanced SM,

but whether its mechanism of action relies upon KIT D816V inhibition is unclear (*22*).

We embarked on an in-depth mechanistic evaluation of KIT/PDGFRA-directed small-molecule inhibitors across a comprehensive collection of clinically relevant KIT primary and resistance mutants. The results of these studies illustrate a continuum of activation states for KIT mutants. This understanding has guided the discovery and development of BLU-285, a highly potent and selective small-molecule inhibitor of KIT and PDGFRA activated mutants. BLU-285 demonstrated robust in vitro and in vivo activity in various *KIT*-driven preclinical models and has provided promising initial clinical activity in patients with GIST and SM.

RESULTS

KIT activation loop mutants display affinity for type I inhibitors

Inhibitors that bind to the inactive conformation of kinases are categorized as type II inhibitors (*23*), and the three agents currently FDA-approved for the treatment of GIST (imatinib, sunitinib, and regorafenib) share this binding mode. The ability of type II inhibitors to suppress exon 9 and 11 KIT mutants (*24*, *25*) indicates that these alterations provide only a minor shift in equilibrium in favor of the active over the inactive conformation of the kinase (*26*, *27*). In contrast, mutations in the activation loops of KIT and PDGFRA induce a more prominent equilibrium shift toward the active conformation, which is incompatible with type II inhibitor binding (*26*). We therefore pursued a strategy to develop a selective type I inhibitor or an active conformation inhibitor of KIT and PDGFRA to address activation loop mutants.

Analysis of screening data against a panel of wild-type (WT) and mutant KIT proteins with a set of commercial and proprietary kinase-directed small-molecule inhibitors revealed not only the binding of type I scaffolds to the D816V activation loop mutant but also to the V559D exon 11 JM domain mutant and to KIT WT proteins (fig. S1). As anticipated, type II inhibitors displayed poor affinity for the D816V mutant. To extend our understanding of type I versus type II inhibitor binding preferences across a larger spectrum of clinically relevant KIT mutants, an additional exon 11 mutant (V560G), as well as several exon 17 and 18 activation loop mutants (D816E, D820E, and A829P), were added to the evaluation (Fig. 1). Binding data analysis confirmed that KIT WT does not demonstrate a strong preference for one inhibitor type over the other, although it does show marked sensitivity to some type II inhibitors. The KIT V560G mutant bound tightly to type II inhibitors, whereas KIT activation loop mutants (D816E, D816V, D820E, and A829P) displayed either a slight bias toward or a pronounced affinity for type I inhibitors. Notably, the KIT D816V mutant consistently displayed a marked preference for type I inhibitors over that of type II inhibitors. These data validated a focus on type I inhibitors for suppressing KIT D816V activity and additional activation loop mutants and also provided an explanation for the difficulty that previous drug discovery efforts have encountered when focused on type II molecules for activation loop inhibition.

BLU-285 is a potent and selective inhibitor of KIT and PDGFRA activation loop mutants

Extensive exploration of diverse chemical scaffolds against the mutant KIT panel coupled with optimization of drug metabolism and pharmacokinetic properties yielded BLU-285 (Fig. 2A). BLU-285 demonstrated exquisite activity on KIT activation loop mutants, with biochemical IC_{50} measured in the subnanomolar range for all activation loop mutants tested including KIT D816V (IC_{50} = 0.27 nM) and PDGFRA D842V (IC_{50} = 0.24 nM) (Fig. 2B). Broad screening against a large panel of human kinases at 3 μM revealed that BLU-285 had very limited potential for activity outside of KIT and PDGFRA. BLU-285 was also more than 150-fold more potent on KIT D816V than several important kinase antitargets such as VEGFR2 (vascular endothelial growth factor receptor 2), SRC, and FLT3 (Fig. 2C and tables S1 and S2). This large difference in BLU-285 activity between KIT D816V and other kinases suggested that off-target inhibition in vivo would be unlikely and that BLU-285 was a highly selective inhibitor of KIT and PDGFRA activation loop mutants.

Comparatively, the type II inhibitors imatinib, sunitinib, and regorafenib only weakly inhibited KIT D816V or PDGFRA D842V enzyme activity (Fig. 2B). Of these approved agents for GIST, the overall kinome selectivity profile of BLU-285 was most similar to imatinib (Fig. 2C), which has an impressive tolerability profile in the clinic relative to the others (*5*, *6*, *28*). Type I inhibitors midostaurin and crenolanib, an investigational compound in clinical trials for the treatment of GIST patients with primary *PDGFRA* D842 mutations (*29*), registered biochemical activity against the activation loop mutants in the low-digit nanomolar range. However, both showed extensive activity across the human kinome, which may be associated with a more complex safety profile in the clinic and a smaller therapeutic window (Fig. 2C).

BLU-285 is active across a spectrum of clinically observed KIT mutants

To assess the breadth of activity of BLU-285 against *KIT* mutations identified in patients, we tested BLU-285 biochemically against a large panel of KIT primary and acquired resistance mutants representing various diseases and stages of progression. BLU-285 demonstrated potency across a spectrum of KIT mutants and superior potency to imatinib on all mutants tested, revealing broad potential for this type I inhibitor in GIST (Fig. 3). Activity was greatest against the KIT exon 11/17 (V560G/D816V) double mutant (Fig. 3). Mutations in the JM domain and activation loop each serve to release autoinhibitory conformations of the kinase domain (*26*), and together, they may virtually lock in the active kinase conformation to which BLU-285 preferentially binds, thereby enhancing its potency. Other KIT activation loop mutants showed sensitivity to BLU-285 with IC_{50} < 2 nM, reflecting a strong bias of these mutants for the active kinase conformation. BLU-285 also demonstrated low nanomolar potency against JM domain mutants, suggesting that exon 11 mutations in *KIT*-driven GIST are sensitive to both type I and type II inhibitors.

ATP-binding site mutations in *KIT* exons 13 (V654A) and 14 (T670I), which cause resistance to imatinib, were less sensitive to BLU-285, signifying preference for a WT ATP-binding site for optimal compound binding. However, like the KIT activation loop mutants, both ATP site mutants were more sensitive to BLU-285 inhibition in the presence of JM domain mutants as compared to the ATP site mutants alone (Fig. 3). These findings further reinforce the positive effect of JM domain mutants on BLU-285 accessibility to the active conformation of the enzyme. Finally, BLU-285 showed greater potency against all disease-relevant KIT mutants than against KIT WT.

BLU-285 is highly active in KIT mutant cell lines

To confirm the activities observed in biochemical assays, we used *KIT*-driven cell lines to assess BLU-285 target engagement (Table 1).

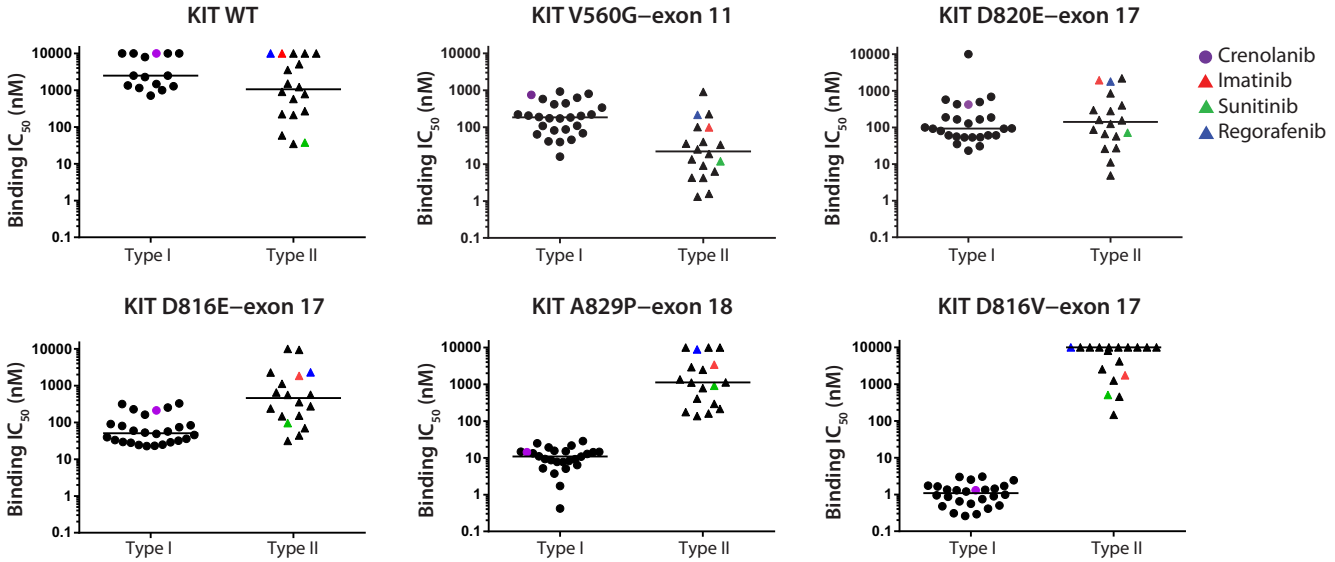

Fig. 1. Inhibitor binding analysis reveals type I preference for KIT activation loop mutants. Half-maximal inhibitory concentration (IC_{50}; in nanomolar) of type I (15 for KIT WT and 26 for mutant KIT) and 18 type II compounds bound to various KIT proteins as measured by LanthaScreen in the absence of ATP. Median values are depicted by horizontal lines. Reference compounds are depicted as follows: imatinib, red triangle; sunitinib, green triangle; regorafenib, blue triangle; crenolanib, purple circle).

A

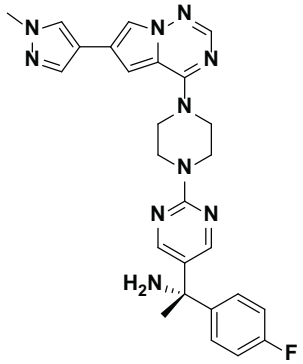

B

Compound	Inhibitor type	KIT WT IC_{50} (nM)	KIT del557-558 exon 11 IC_{50} (nM)	KIT D816V exon 17 IC_{50} (nM)	PDGFRA D842V exon 18 IC_{50} (nM)
BLU-285	Type I	73	0.6	0.27	0.24
Imatinib	Type II	261	12	8150	759
Sunitinib	Type II	37	7	207	120
Regorafenib	Type II	204	17	3640	810
Crenolanib	Type I	36	2.1	1.5	0.2
Midostaurin	Type I	26	2.2	2.9	4.9

C

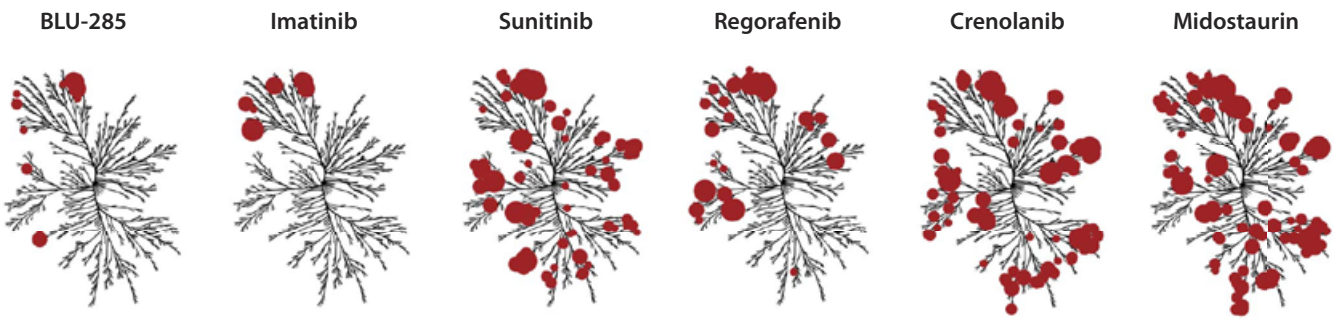

Fig. 2. BLU-285 is a potent and highly selective inhibitor of KIT and PDGFRA activation loop mutants. (**A**) Chemical structure of BLU-285. (**B**) Biochemical potency against KIT WT and the KIT del557-558 (exon 11), D816V (exon 17), and PDGFRA D842V (exon 18) mutants for BLU-285 and several compounds in use or being explored for the treatment of GIST and SM. (**C**) Binding data for compounds screened at 3 μM against 392 kinases are depicted as red circles on the kinome tree. The size of the circle indicates binding potency. Kinome illustration reproduced courtesy of Cell Signaling Technology (www.cellsignal.com).

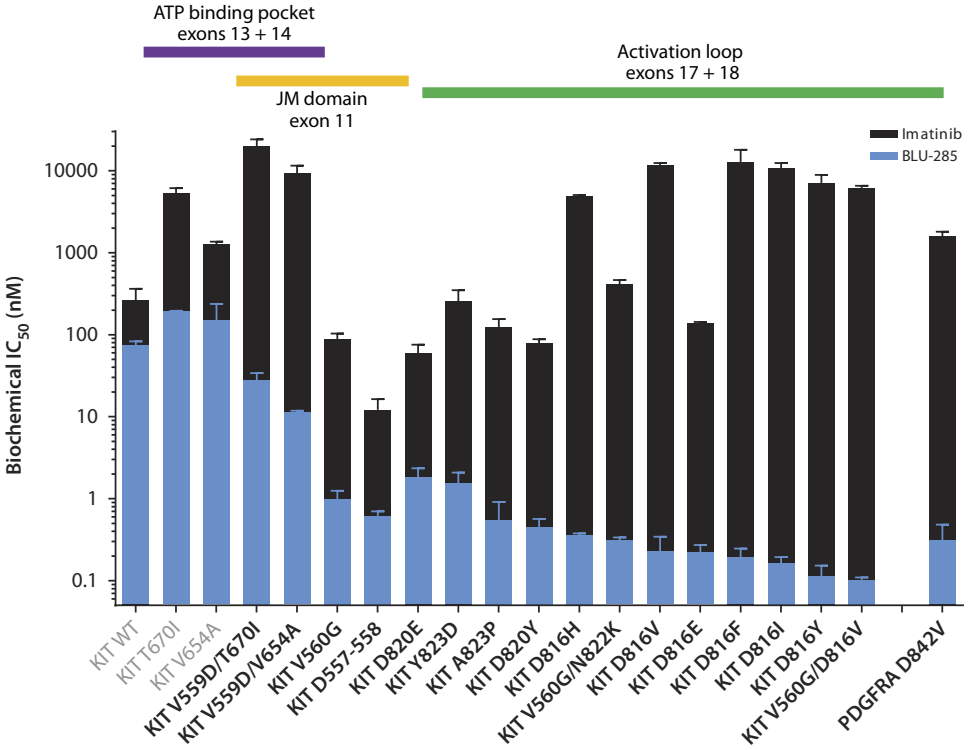

Fig. 3. BLU-285 is active against a spectrum of KIT and PDGFRA disease-relevant mutants. Biochemical data highlights BLU-285 activity across 19 KIT and PDGFRA mutant proteins. Data are depicted as bars that represent the mean IC_{50} value + SD for BLU-285 (light blue) and imatinib (black). Clinically observed KIT and PDGFRA mutants are clustered by their location within the primary protein sequence. The exon location and associated structural region for each mutant are listed above, and disease relevant mutants are shown in bold.

The most marked effect was seen in HMC1.2 cells, which carry the dual exon 11/17 (V560G/D816V) *KIT* mutations (*30*). BLU-285 potently inhibited both KIT autophosphorylation (IC_{50} = 4 nM) and downstream signaling in this cell line (Table 1 and fig. S2). BLU-285 was also highly active on the murine KIT D814Y mutant (equivalent to human D816Y) mastocytoma line P815 (IC_{50} = 22 nM) and on KIT exon 17 N822K in the human Kasumi-1 acute myeloid leukemia line (IC_{50} = 40 nM; Table 1) (*31*, *32*). BLU-285 inhibited autophosphorylation in the HMC1.1 cell line expressing the KIT JM domain V560G mutant (IC_{50} = 100 nM) but with less potency than that observed in KIT exon 17 mutant cell lines. Finally, BLU-285 showed the weakest activity against KIT WT, inhibiting autophosphorylation with an IC_{50} of 192 nM in SCF-stimulated M-07e human megakaryoblastic leukemia cells, pointing to a potential safety margin for inhibition of mutant KIT over endogenous KIT WT signaling and other class III RTKs.

Antiproliferative effects of BLU-285 in *KIT*-dependent cell lines correlated well with on-target potencies against individual KIT mutants (Table 1). Together, these in vitro cellular data reflected the biochemical activity of BLU-285 on KIT mutant and WT enzymes, where BLU-285 potency correlated with the activation status of the enzyme. A similar pattern was observed with PDGFRA in which cellular potency tracked with biochemical activity and the activated state of the protein; BLU-285 was most potent against the PDGFRA D842V activation loop mutant, which distinguished this compound from other established agents used for the treatment of GIST (Table 1 and fig. S3).

BLU-285 demonstrates antitumor activity in preclinical models of *KIT*-driven diseases

In vivo activity of BLU-285 was assessed across a panel of *KIT*-driven disease models. The P815 mastocytoma cell line was used to establish a *KIT* mutant exon 17 subcutaneous allograft model. BLU-285, administered orally, once daily from 0.3 to 30 mg/kg, exhibited dose-dependent antitumor activity in this model (Fig. 4A). BLU-285 was well tolerated at all doses, showing no adverse effects on body weight (Fig. 4B). Dasatinib, used at the maximum tolerated dose (MTD) in vivo as a comparator based on its reported biochemical activity against multiple KIT D816 mutants (*33*), demonstrated inferior activity compared to BLU-285, likely due to its poor pharmacokinetics and issues with tolerability (Fig. 4B) (*34*). Pharmacokinetic and pharmacodynamic (PK/PD) analyses of plasma exposure and target engagement in tumor samples showed that phospho-KIT (pKIT) inhibition could be sustained over 24 hours (Fig. 4C and fig. S4). BLU-285 at a 10 mg/kg dose caused 75% pKIT inhibition with significant antitumor activity [$P < 0.001$, analysis of variance (ANOVA)], whereas BLU-285 at 30 mg/kg drove sustained pKIT inhibition to 90% and led to full tumor regression (table S3). These data demonstrated that complete target coverage by BLU-285 was achievable at exposures that were well tolerated.

Next, the activity of BLU-285 was assessed in a patient-derived xenograft (PDX) from a refractory GIST lesion bearing *KIT* exon 11/17 (del557-558/Y823D) alterations. As anticipated, this model was resistant to imatinib (Fig. 4D, top). These data are reflective of the clinical experience because patients with this *KIT* exon 11/17 double mutation usually progress on imatinib and sunitinib therapies, leaving regorafenib as their final approved therapeutic option. Administration of regorafenib (30 mg/kg), equivalent to the recommended human dose of 160 mg (*35*), resulted in tumor stasis in this model, as did BLU-285 (3 mg/kg). In contrast, BLU-285 at doses of 10 and 30 mg/kg resulted in tumor regression (Fig. 4D, top) and were well tolerated (fig. S5). Pharmacodynamic analysis of tumors harvested 24 hours after BLU-285 administration revealed a dose-dependent inhibition of KIT autophosphorylation correlating with tumor response (Fig. 4D). Microscopic evaluation showed that in addition to decreases in tumor size, the BLU-285 (10 and 30 mg/kg) cohorts exhibited 27 and 50% reductions in nuclear density (fig. S6). This decrease resulted from myxoid degeneration, a phenomenon observed in GIST and select other mesenchymal tumors, which is characterized by replacement of tumor cells by connective tissue mucosubstances. Myxoid degeneration is known to occur in GIST tumors responding to imatinib or undergoing spontaneous regression (*10*, *36*).

The potent activity of BLU-285 toward KIT exon 11 JM domain mutants in the biochemical and cellular settings warranted preclinical

Table 1. Inhibition of KIT/PDGFRA autophosphorylation and proliferation in cell lines.

				pKIT inhibition IC_{50} (nM)			
Cell line	**Mutation**	**Exon**	**Tissue**	**BLU-285**	**Imatinib**	**Sunitinib**	**Regorafenib**
M-07e	KIT WT	—	Human megakaryoblastic leukemia	192	336	3	63
HMC1.1	KIT V560G	11	Human mast cell leukemia	100	21	1	38
Kasumi	KIT N822K	17	Human acute myeloid leukemia	40	129	6	111
P815	KIT D816Y	17	Murine mastocytoma	22	1236	611	128
HMC1.2	KIT V560G/D816V	11/17	Human mast cell leukemia	4	9144	14,488	314
CHO	PDGFRA WT	—	Engineered	95	<100		
CHO	PDGFRA V561D	12	Engineered	40	<100		
CHO	PDGFRA D842V	18	Engineered	30	3145		
				Proliferation IC_{50} (nM)			
Cell line	**KIT mutation**	**Exon**	**Tissue**	**BLU-285**	**Imatinib**	**Sunitinib**	**Regorafenib**
M-07e	WT	—	Human megakaryoblastic leukemia	417	604	132	678
HMC1.1	V560G	11	Human mast cell leukemia	344	36	13	115
Kasumi	N822K	17	Human acute myeloid leukemia	75	382	31	211
P815	D816Y	17	Murine mastocytoma	202	2,811	230	1,974
HMC1.2	V560G/D816V	11/17	Human mast cell leukemia	125	11,355	1506	>25,000

exploration in a model of primary GIST bearing the *KIT* exon 11 del557-559insF alteration. This PDX model was sensitive to imatinib, as expected (Fig. 4E, top). Notably, doses of 30 and 100 mg/kg BLU-285 led to tumor regression similar to that observed with imatinib, and at 10 mg/kg, BLU-285 produced tumor stasis. Again, histological assessment of tumors showed a decrease in cellularity and myxoid degeneration in the imatinib and BLU-285 treatment groups, coincident with tumor regression (fig. S7). Therefore, although BLU-285 was most potent in the KIT activation loop mutant models, robust in vivo activity against the primary KIT exon 11 GIST mutants was achieved at slightly higher yet well-tolerated exposures (fig. S8). Assuming similar dose-exposure tolerability in patients, these results suggest that in addition to activity on activation loop mutants alone and the exon 11/17 double mutants in refractory GIST, BLU-285 may be able to prevent the emergence of the primary *KIT* exon 11 mutant clone in the clinical setting of acquired resistance.

Finally, a GIST PDX model bearing the *KIT* exon 11/13 (del557-558/V654A) double mutation was studied. This model was resistant to imatinib and sensitive to sunitinib as expected (Fig. 4F, top). A dose of BLU-285 (10 mg/kg) was not efficacious, reflecting the reduced activity of BLU-285 against this KIT exon 11/13 (V559D/V654A) double mutant observed biochemically (Fig. 3). In contrast, BLU-285 at the dose of 30 mg/kg resulted in marked tumor regression, concomitant with roughly 60% inhibition of KIT autophosphorylation (Fig. 4F, bottom). These results confirm a dose-dependent in vivo activity of BLU-285 against *KIT* exon 11/13 lesions, suggesting broad activity of BLU-285 across the clinically relevant *KIT* mutational spectrum observed in GIST.

BLU-285 exhibits clinical activity in early studies

To investigate the impact of BLU-285 on *KIT*- and *PDGFRA*-driven malignancies, we progressed BLU-285 into phase 1, first-in-human (FIH) dose-escalation studies in patients with advanced, unresectable GIST (NCT02508532) and advanced SM (NCT02561988). These two patient populations lack effective therapies and are each characterized by a high incidence of *KIT* and/or *PDGFRA* activation loop mutations.

A 65-year-old female with primary gastric PDGFRA D842V mutant GIST, who had progressed on previous imatinib, dasatinib, and crenolanib therapy, was enrolled at the first dose level (30 mg) (*37*). BLU-285 was administered orally, once daily in cycles of 28 days, and radiographic response was assessed per Response Evaluation Criteria in Solid Tumors (RECIST1.1) on day 1 of cycle 3. After 8 weeks of treatment with BLU-285, a 31% reduction in tumor size was observed by computed topography (CT) scan and confirmed by central radiographic review (Fig. 5A). A second CT scan 2 months later confirmed a partial response with 48% reduction in tumor size, and response was maintained for at least 15 cycles and continued at the time of manuscript preparation. Interrogation of circulating tumor DNA (ctDNA) collected before and at 2-week intervals after BLU-285 administration demonstrated a rapid and sustained reduction of *PDGFRA* D842V allele burden detected in the plasma (Fig. 5A).

Similar early antitumor activity was observed in a 48-year-old patient with a GIST tumor bearing a rare primary *KIT* D820Y activation loop mutation with clinical progression on previous imatinib, sunitinib, and regorafenib therapy (*37*). This patient was treated once daily with 60 mg of BLU-285; RECIST1.1 evaluation revealed a 25% tumor shrinkage at the first assessment that was confirmed on day 1 of cycle 5, with a

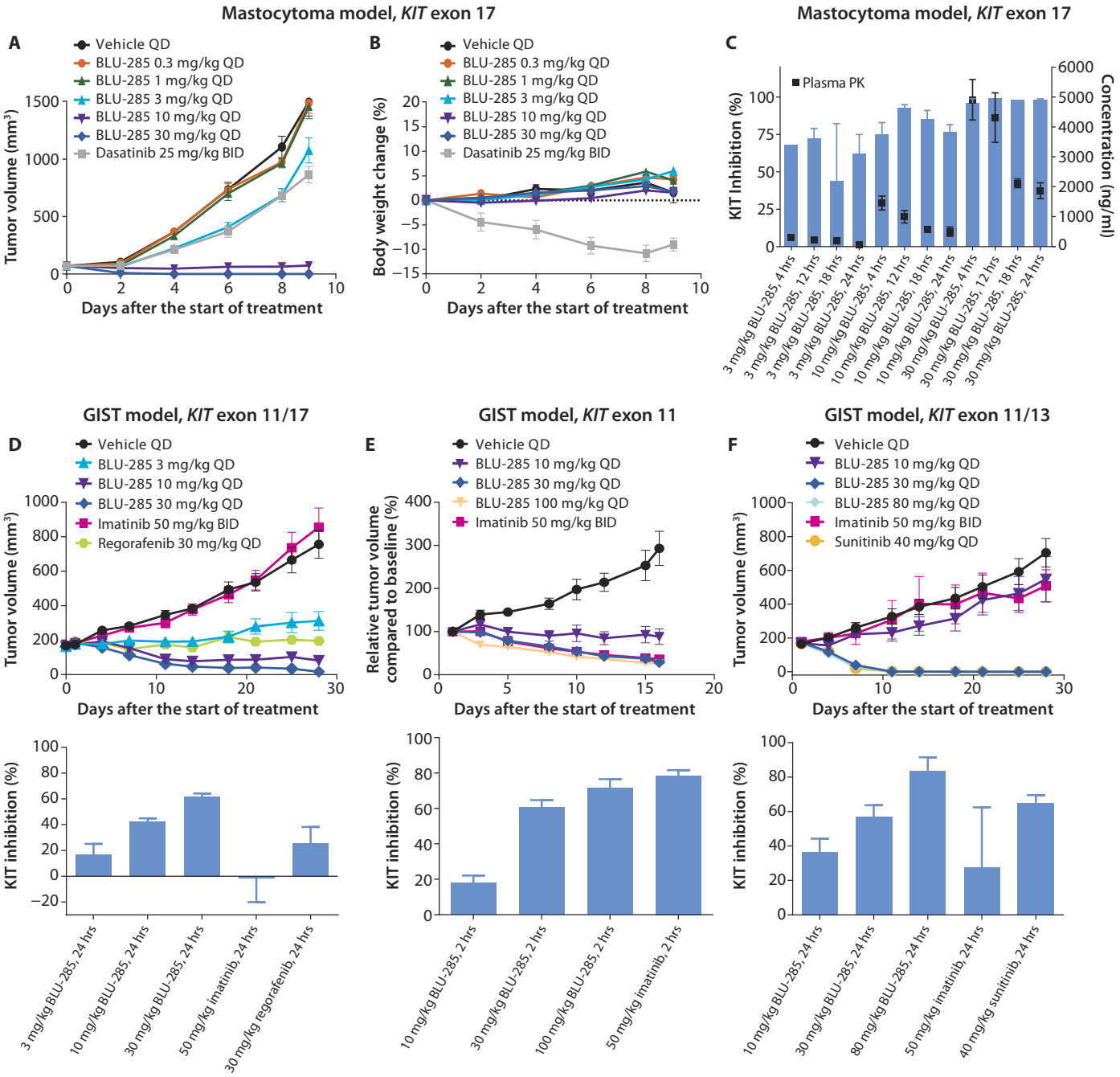

Fig. 4. BLU-285 demonstrates antitumor activity across multiple *KIT*-driven in vivo disease models. BLU-285 antitumor activity in both primary and refractory *KIT*-driven disease models. (**A** to **C**) Antitumor activity (A), body weight (B), and PK/PD (C) relationship for BLU-285 and dasatinib in a P815 KIT D814Y mastocytoma allograft model. (**D** to **F**) Antitumor activity of BLU-285 and reference compounds (top) and pharmacodynamic analysis of KIT inhibition (bottom) in human GIST PDX models of disease with (D) *KIT* exon 11/17 delW557K558/Y823D, (E) *KIT* exon 11 delW557-V559insF, and (F) *KIT* exon 11/13 delW557K558/V654A mutations. QD, once daily; BID, twice daily.

28% reduction and maintained through cycle 15 (32% reduction), as assessed by central radiographic review (Fig. 5B).

Finally, in advanced SM, robust clinical activity was observed in a patient treated with 60 mg of BLU-285 (*38*). Bone marrow mast cell infiltration, a hallmark of SM, was measured at baseline and again after two cycles of BLU-285. A marked decrease in bone marrow mast cells was observed, indicating an effect on aberrant mast cell survival within the bone marrow environment and suggestive of rapid therapeutic activity (Fig. 5C). This early activity of BLU-285 on both GIST and SM with *PDGFRA* and *KIT* activation loop mutations suggests the promise of this targeted therapy for several typically treatment refractory patient populations.

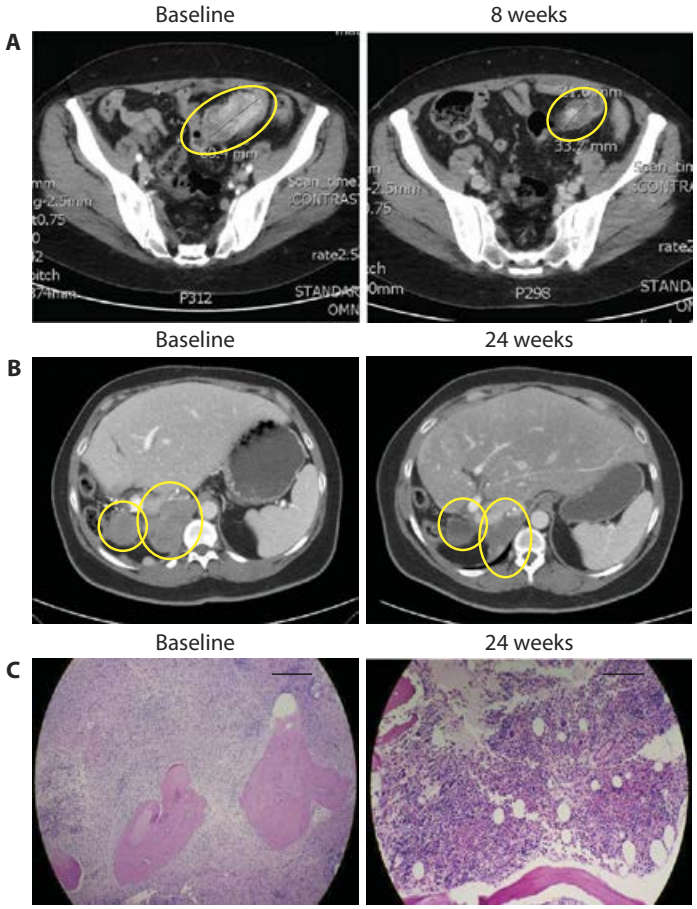

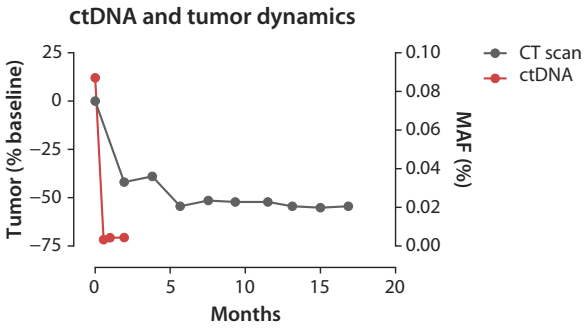

Fig. 5. Clinical data with BLU-285 confirm early evidence of activity in patients with diseases driven by *KIT* and *PDGFRA* activation loop mutations. (**A**) BLU-285 [30 mg per os (PO), QD] induces rapid radiographic clinical response per RECIST1.1 (31% tumor reduction at week 8) and decline in *PDGFRA* D842V ctDNA in a patient with *PDGFRA* D842V–mutant GIST that progressed on previous imatinib, dasatinib, and crenolanib therapy. The images show CT scans with tumor circled in yellow. The graph shows tumor burden as measured by the sum of the longest dimension for the target lesions (per RECIST1.1) and mutant allele frequency (MAF). (**B**) Radiographic clinical response per RECIST1.1 with BLU-285 (60 mg PO, QD) in a patient with primary KIT D820Y–mutant GIST that had previously progressed on imatinib, sunitinib, and regorafenib. The images show CT scans with a pelvic tumor mass highlighted within yellow circles that demonstrated a 28% tumor reduction at day 1 of cycle 5. A partial response of 32% tumor reduction was confirmed by central radiographic review at cycle 15. (**C**) BLU-285 (30 mg PO, QD) markedly decreased bone marrow mast cell burden in a patient with *KIT* D816V–driven aggressive SM. At baseline, diffuse bone marrow infiltration with malignant mast cells obliterated normal hematopoiesis (left). After BLU-285 treatment, there was a marked reduction in malignant mast cells and return of normal trilineage hematopoiesis (right). Scale bars, 1000 μm (left) and 200 μm (right).

DISCUSSION

Until now, patients with diseases associated with KIT or PDGFRA activation loop mutant kinases have had few meaningful treatment options. Drug discovery efforts to address these genetic drivers have primarily focused on repurposing multikinase inhibitors with ancillary KIT/PDGFRA activity, engineering activation loop mutant activity into imatinib-like type II scaffolds, or developing target-directed antibodies, both naked and conjugated to cytotoxics. Unfortunately, these approaches have all failed to date because of an inability to sufficiently inhibit *KIT* and *PDGFRA* activation loop mutations without concomitant dose-limiting toxicities. With no viable therapeutic options in hand, doctors are left filling this medical void by administering to patients either ineffective drugs or agents whose use lacks sound scientific rationale. For example, many patients with either PDGFRA D842V GIST or KIT D816V SM receive imatinib despite a mountain of preclinical and clinical data that demonstrate its ineffectiveness. The delivery of such therapies introduces unnecessary risk to patients and increasingly unjustifiable health care expense (*39*).

BLU-285 was designed as a potent and highly selective inhibitor of KIT and PDGFRA activation loop mutant kinases. In contrast to the approved type II agents with KIT inhibitory activity, BLU-285, a type I inhibitor that binds the active conformation of the kinase, was able to inhibit all activation loop aberrations tested, including the difficult-to-target PDGFRA D842V and structurally homologous KIT D816V mutants. As anticipated from this precision targeted approach, BLU-285 rapidly demonstrated signs of clinical activity in patients harboring these particular mutations, even at the lowest dose levels tested. On the basis of these observations, BLU-285 has the potential to address the medical need for these genomically defined patient populations.

Preclinical profiling against numerous KIT primary activating mutants and several secondary resistance mutants identified in imatinib- or imatinib/sunitinib-resistant GIST patients demonstrated that BLU-285 maintained activity against a broad spectrum of additional disease-relevant KIT mutants, with only slightly shifted potencies both in vitro and in vivo. This is unsurprising, given that the various activating mutations all serve, albeit to differing degrees, to shift the conformational equilibrium of KIT to the active form, thus enhancing its affinity for BLU-285. By escalating doses of BLU-285 in ongoing clinical studies in patients with GIST and SM, we will likely be able to determine the extent and spectrum of additional *KIT* and *PDGFRA* activating mutations that can be inhibited adequately to result in meaningful clinical outcomes.

Although the full spectrum of clinical mutants covered by BLU-285 will be characterized with emerging data over time, it may not be feasible for any single inhibitor to address all of the various mutations identified in *KIT* and *PDGFRA* in a kinome-selective manner. In addition, similar to most other targeted therapies against kinase drivers, new on-target resistance mutations may manifest themselves upon prolonged treatment. Although forthcoming clinical trial data will illuminate any gaps that exist in BLU-285 coverage, combination strategies designed to complement or enhance the activity of BLU-285 in oncogenic *KIT*- and *PDGFRA*-driven disease should also be considered. Given the high degree of kinome selectivity and a seemingly favorable clinical safety profile in early trials, BLU-285 is a promising candidate for both

targeted single agent and combination regimens in *KIT/PDGFRA*-driven malignancies.

MATERIALS AND METHODS

Study design

The aim of this study was to design and characterize BLU-285, a potent, selective small-molecule inhibitor of KIT/PDGFRA activating mutants including activation loop mutants. BLU-285 activity was assessed in enzymatic assays with recombinant KIT/PDGFRA WT or mutant protein, cell lines driven by mutant KIT activation, and in vivo preclinical *KIT*-driven models. All animal studies were performed under Institutional Animal Care and Use Committee (IACUC) guidelines established at each respective institution where study was conducted. The sample size for animal experiments (n = 6 to 11) was based on the results of preliminary experiments, with exact numbers described in Materials and Methods. Mice were randomly assigned to the treatment and control groups; investigators were not blinded during evaluation of the preclinical in vivo experiments. The BLU-285 FIH phase 1 clinical trial was an open-label, nonrandomized study built to assess safety, MTD, pharmacokinetics, pharmacodynamics, and preliminary antitumor activity of BLU-285.

LanthaScreen binding assays

Serially diluted compounds, KIT protein, and anti–glutathione *S*-transferase–Europium antibody were incubated with tracer as follows: KIT WT, V560G, and D820E proteins with tracer 222 and KIT D816E, A829P, and D816V with Tracer 178. Plates were incubated at 25°C for 60 min and read on a PerkinElmer EnVision with two excitation flashes and two emission reads: λ_{ex} = 350 nm, λ_{em} = 665 nm; λ_{ex} = 350 nm, λ_{em} = 615 nm.

IC_{50} generation

Raw data were normalized to 0 and 100% inhibition controls using dimethyl sulfoxide (DMSO) and staurosporine, respectively. IC_{50} values were calculated using a three- or four-parameter logistic nonlinear regression model.

BLU-285 synthesis

The synthesis of BLU-285 is described in issued patent WO2015/057873; example 7, compound 44.

KINOMEscan binding assays

Compounds were screened at 3 μM concentration against a panel of 392 WT kinase constructs using the KINOMEscan assay platform at DiscoveRx, as previously described (*40*).

Hotspot kinase profiling assays

In vitro kinase profiling of KIT and PDGFRA constructs was performed at Reaction Biology Corporation. Kinase/substrate pairs, serially diluted compounds, and any additional cofactors required were prepared in a reaction buffer at their respective Michaelis constant (K_m) for ATP. ^{33}P-ATP (10 mCi/ml) was added to initiate the reaction, followed by the detection of kinase activity by a filter-binding method.

Cell culture

HMC1.1 and HMC1.2 cell lines were licensed from J. Butterfield (Mayo Clinic) (*41*). Cells were grown in Iscove's modified Dulbecco's medium containing 20 or 10% fetal calf serum supplemented with iron (HyClone). Kasumi-1, P815, and Chinese hamster ovary (CHO)–K1 cells (American Type Culture Collection) were grown in vendor-recommended medium. M-07e cells (DSMZ) were grown in Dulbecco's modified Eagle's medium containing granulocyte-macrophage colony-stimulating factor (5 ng/ml) for maintenance or in SCF (5 ng/ml) for cell-based assays. PDGFRA WT and mutant kinase constructs were transiently transfected into CHO cells, as previously described (*29*). All cells underwent short tandem repeat authentication; cells were discarded after 20 passages.

Immunoblot analysis

After treatment of cells with compounds, cells were lysed in Phospho-Safe lysis buffer with protease/phosphatase inhibitors. Total protein concentration was determined using a bicinchoninic acid (BCA) assay (Pierce). Primary antibodies include total KIT (#3308, Cell Signaling Technology), pTyr719-KIT (#3391, Cell Signaling Technology), total PDGFRA (sc-338), pTyr754-PDGFRA (sc-12911), total AKT (#2920, Cell Signaling Technology), pSer473-AKT (#4060, Cell Signaling Technology), total ERK (#9107, Cell Signaling Technology), pTyr/Thr 202/204-ERK (#4370, Cell Signaling Technology), and β-actin (ab3280, Abcam). Secondary antibodies were from Rockland Antibodies and Assays [IRDye 800–conjugated rabbit immunoglobulin G (IgG) and IRDye 700–conjugated mouse IgG]. Immunoblots were imaged using an Odyssey LI-COR Fluorescent imaging system. PDGFRA autophosphorylation was assessed by immunoprecipitation, followed by immunoblotting for phospho-PDGFRA and total PDGFRA, as previously described (*14*). To quantitate the percent of pKIT/PDGFR inhibition in cells, the pKIT/total KIT ratio was calculated for each concentration of compound and normalized to the average of DMSO-treated cells.

Autophosphorylation assays

AlphaLISA

Cells were seeded in a 384-well plate and incubated overnight at 37°C. Compounds were serially diluted in 100% DMSO, added to cells at a final DMSO concentration of 0.25%, and incubated at 37°C for 90 min. Cells were lysed with AlphaLISA Lysis Buffer supplemented with protease/phosphatase inhibitors with shaking for 30 min at 4°C. Total biotinylated human KIT (#3308, Cell Signaling Technology), murine KIT (ab112167, Abcam), and phosphoY719-KIT (#3391, Cell Signaling Technology) antibodies and AlphaLISA donor and acceptor beads were added to lysates. Plates were read on an EnVision using an AlphaScreen protocol.

Enzyme-linked immunosorbent assay

A PathScan phospho c-kit (panTyr) sandwich enzyme-linked immunosorbent assay (#7294, Cell Signaling Technology) was used to assess the percent inhibition of autophosphorylation of KIT WT. M-07e cells were seeded into a 96-well plate in serum/cytokine-free medium, followed by the addition of compounds for 60 min at 37°C. The cells were stimulated with human SCF (50 ng/ml) and scanned on an EnVision plate reader.

Cellular proliferation

Cells were plated in serum-containing medium and incubated overnight at 37°C. Compounds were serially diluted and added to cells at a final DMSO concentration of 0.25% and incubated at 37°C for 72 hours. Cell Titer-Glo reagent was added and read on the EnVision using a 384-well luminescence protocol.

Animal studies

All animal studies were performed under IACUC guidelines established at each respective institution where the study was conducted. BLU-285

was formulated in 0.5% carboxymethyl cellulose + 1% Tween 80. Dasatinib (Selleckchem) was formulated in 50% propylene glycol. Imatinib (Carbosynth) was formulated in sterile water. Regorafenib (Carbosynth) was formulated in a PEG400/125 mM methanesulfonic acid (MSA) mixture at 80:20 ratio. MSA (125 mM) was prepared in water. Sunitinib (Carbosynth) was formulated in 50 mM citrate buffer (pH 3.5). The P815 xenograft study was performed at WuXi AppTec in Shanghai, China. BALB/c nude mice were inoculated with 1×10^6 P815 cells subcutaneously at the right flank. When the average tumor size reached about 75 mm^3, treatment with test article began. Ten animals were treated per group. Tumors were measured to assess antitumor activity. For PK/PD analysis, plasma and tumors were collected from three mice per group. The GIST exon 11/17 (model 2007031011) and exon 11/13 (model GS11331) xenograft studies were performed at Crown Biosciences. Nonobese diabetic–severe combined immunodeficient mice were inoculated with 100,000 to 125,000 viable cells subcutaneously into the rear flank. Animals were randomized when average tumor volume reached 150 to 200 mm^3, followed by oral dosing of compounds. Eleven animals were treated per group. Plasma and tumor samples were collected from three animals per group. The GIST exon 11 (model UZLX-GIST3) xenograft (*42*) study was performed in the Laboratory of Experimental Oncology at KU Leuven, Belgium. Tumors were bilaterally implanted onto the rear flanks of adult nude *nu/nu* NMRI mice and randomized upon reaching an average tumor volume of ~500 mm^3. Six animals were treated per group for a total of 12 individual tumor measurements. One animal per group was sacrificed for PK/PD analysis, and the other five were used to evaluate antitumor activity.

Xenograft tumor pharmacodynamic analysis

Frozen tumor slices were homogenized in 400 µl of PhosphoSafe lysis buffer with protease/phosphatase inhibitors. Protein concentration was determined using a BCA assay. Fifty micrograms of lysate was subject to SDS–polyacrylamide gel electrophoresis, followed by immunoblotting.

BLU-285 phase 1 study

Open label, nonrandomized, global, FIH phase 1, dose-escalation studies with BLU-285 in advanced, unresectable GIST (NCT02508532) and advanced SM (NCT02561988) were initiated to define the safety, MTD, pharmacokinetics, pharmacodynamics, and preliminary antitumor activity of BLU-285 in each indication. Initial sample size for each study was about 60 patients (25 patients in dose escalation and 35 in dose expansion) as appropriate for FIH studies designed to identify an MTD and assess preliminary antitumor activity. All statistical analyses of safety, pharmacokinetic, pharmacodynamic, and efficacy data were descriptive in nature because the primary objective of the studies was to define the safety and MTD of BLU-285. The studies were reviewed and approved by the institutional review board at each clinical site. Written informed consent was obtained from all patients before study entry. Key eligibility criteria for the GIST study included adult patients (≥18 years of age) with unresectable GIST who had received ≥2 kinase inhibitors, including imatinib, or patients with tumors bearing a *PDGFRA* D842 mutation regardless of previous therapy; Eastern Cooperative Oncology Group (ECOG) performance status of 0 to 2; and adequate bone marrow, hepatic, renal, and cardiac function. BLU-285 was administered orally, once daily, on a 4-week cycle using a 3 + 3 dose-escalation design. Adverse events per Common Terminology Criteria for Adverse Events (CTCAE), pharmacokinetics, ctDNA levels (Sysmex Inostics), and centrally reviewed radiographic response per RECIST1.1 were assessed. Presented data are preliminary and represent a cutoff of 28 April 2017. Key eligibility criteria for the advanced SM study included adult patients (≥18 years of age) with aggressive SM, SM with associated hematologic neoplasm and one or more C-findings, or mast cell leukemia per World Health Organization diagnostic criteria; ECOG performance status of 0 to 3; and adequate bone marrow, hepatic, renal, and cardiac function. BLU-285 was administered orally, once daily, on a 4-week cycle using a 3 + 3 dose escalation design. Adverse events per CTCAE, pharmacokinetics, ctDNA levels, and markers of mast cell burden, including serum tryptase and bone marrow mast cell content, were assessed. Presented data are preliminary with data cutoff of 1 December 2016.

Statistical analysis

Results for in vivo preclinical models were expressed as mean ± SEM. Multiple group comparisons were made using Wilcoxon's matched pair test, Mann-Whitney *U* test, or one-way ANOVA, followed by Tukey's multiple comparisons test. $P < 0.05$ was considered statistically significant. Analyses of preliminary efficacy data in the phase 1 BLU-285 clinical trial are descriptive in nature.

SUPPLEMENTARY MATERIALS

www.sciencetranslationalmedicine.org/cgi/content/full/9/414/eaao1690/DC1

Fig. S1. Analysis of compound binding reveals broad type I activity across various forms of KIT.
Fig. S2. BLU-285 inhibits KIT signaling in a *KIT* exon 11/17 human cell line.
Fig. S3. BLU-285 exhibits differential activity on PDGFRA WT and V561D and D842V mutants.
Fig. S4. Pharmacodynamic analysis of KIT signaling in a P815 allograft model of SM demonstrates in vivo target engagement.
Fig. S5. BLU-285 is well tolerated in a *KIT* mutant exon 11/17 PDX model of relapsed GIST.
Fig. S6. Histology of GIST PDX *KIT* mutant exon 11/17 tumors confirms tumor regression.
Fig. S7. Histology of GIST PDX *KIT* mutant exon 11 tumors was correlated with tumor size regression.
Fig. S8. BLU-285 is well tolerated in a *KIT* mutant exon 11 PDX model of primary GIST.
Table S1. Human kinases with more than 90% binding by BLU-285, imatinib, sunitinib, regorafenib, crenolanib, and midostaurin are listed.
Table S2. BLU-285 has selectivity for KIT D816V over several kinase antitargets.
Table S3. Antitumor activity of BLU-285 and type II inhibitors across various *KIT* mutant–driven models of disease highlights robust activity of BLU-285.

REFERENCES AND NOTES

1. C. Zhou, Y.-L. Wu, G. Chen, J. Feng, X.-Q. Liu, C. Wang, S. Zhang, J. Wang, S. Zhou, S. Ren, S. Lu, L. Zhang, C. Hu, C. Hu, Y. Luo, L. Chen, M. Ye, J. Huang, X. Zhi, Y. Zhang, Q. Xiu, J. Ma, L. Zhang, C. You, Erlotinib versus chemotherapy as first-line treatment for patients with advanced *EGFR* mutation-positive non–small-cell lung cancer (OPTIMAL, CTONG-0802): A multicentre, open-label, randomised, phase 3 study. *Lancet Oncol.* **12**, 735–742 (2011).
2. E. L. Kwak, Y.-J. Bang, D. R. Camidge, A. T. Shaw, B. Solomon, R. G. Maki, S.-H. I. Ou, B. J. Dezube, P. A. Jänne, D. B. Costa, M. Varella-Garcia, W.-H. Kim, T. J. Lynch, P. Fidias, H. Stubbs, J. A. Engelman, L. V. Sequist, W. Tan, L. Gandhi, M. Mino-Kenudson, G. C. Wei, S. M. Shreeve, M. J. Ratain, J. Settleman, J. G. Christensen, D. A. Haber, K. Wilner, R. Salgia, G. I. Shapiro, J. W. Clark, A. J. Iafrate, Anaplastic lymphoma kinase inhibition in non–small-cell lung cancer. *N. Engl. J. Med.* **363**, 1693–1703 (2010).
3. A. T. Shaw, S.-H. I. Ou, Y.-J. Bang, D. R. Camidge, B. J. Solomon, R. Salgia, G. J. Riely, M. Varella-Garcia, G. I. Shapiro, D. B. Costa, R. C. Doebele, L. P. Le, Z. Zheng, W. Tan, P. Stephenson, S. M. Shreeve, L. M. Tye, J. G. Christensen, K. D. Wilner, J. W. Clark, A. J. Iafrate, Crizotinib in *ROS1*-rearranged non–small-cell lung cancer. *N. Engl. J. Med.* **371**, 1963–1971 (2014).
4. G. Bollag, P. Hirth, J. Tsai, J. Zhang, P. N. Ibrahim, H. Cho, W. Spevak, C. Zhang, Y. Zhang, G. Habets, E. A. Burton, B. Wong, G. Tsang, B. L. West, B. Powell, R. Shellooe, A. Marimuthu, H. Nguyen, K. Y. J. Zhang, D. R. Artis, J. Schlessinger, F. Su, B. Higgins, R. Iyer, K. D'Andrea, A. Koehler, M. Stumm, P. S. Lin, R. J. Lee, J. Grippo, I. Puzanov, K. B. Kim, A. Ribas, G. A. McArthur, J. A. Sosman, P. B. Chapman, K. T. Flaherty, X. Xu, K. L. Nathanson, K. Nolop, Clinical efficacy of a RAF inhibitor needs broad target blockade in *BRAF*-mutant melanoma. *Nature* **467**, 596–599 (2010).

5. S. G. O'Brien, F. Guilhot, R. A. Larson, I. Gathmann, M. Baccarani, F. Cervantes, J. J. Cornelissen, T. Fischer, A. Hochhaus, T. Hughes, K. Lechner, J. L. Nielsen, P. Rousselot, J. Reiffers, G. Saglio, J. Shepherd, B. Simonsson, A. Gratwohl, J. M. Goldman, H. Kantarjian, K. Taylor, G. Verhoef, A. E. Bolton, R. Capdeville, B. J. Druker; IRIS Investigators, Imatinib compared with interferon and low-dose cytarabine for newly diagnosed chronic-phase chronic myeloid leukemia. *N. Engl. J. Med.* **348**, 994–1004 (2003).
6. G. D. Demetri, M. von Mehren, C. D. Blanke, A. D. Van den Abbeele, B. Eisenberg, P. J. Roberts, M. C. Heinrich, D. A. Tuveson, S. Singer, M. Janicek, J. A. Fletcher, S. G. Silverman, S. L. Silberman, R. Capdeville, B. Kiese, B. Peng, S. Dimitrijevic, B. J. Druker, C. Corless, C. D. M. Fletcher, H. Joensuu, Efficacy and safety of imatinib mesylate in advanced gastrointestinal stromal tumors. *N. Engl. J. Med.* **347**, 472–480 (2002).
7. J. Lennartsson, L. Rönnstrand, Stem cell factor receptor/c-Kit: From basic science to clinical implications. *Physiol. Rev.* **92**, 1619–1649 (2012).
8. C. R. Antonescu, P. Besmer, T. Guo, K. Arkun, G. Hom, B. Koryotowski, M. A. Leversha, P. D. Jeffrey, D. Desantis, S. Singer, M. F. Brennan, R. G. Maki, R. P. DeMatteo, Acquired resistance to imatinib in gastrointestinal stromal tumor occurs through secondary gene mutation. *Clin. Cancer Res.* **11**, 4182–4190 (2005).
9. C. M. Barnett, M. C. Heinrich, Management of tyrosine kinase inhibitor-resistant gastrointestinal stromal tumors. *Am. Soc. Clin. Oncol. Educ. Book* **32**, 663–668 (2012).
10. C. R. Antonescu, The GIST paradigm: Lessons for other kinase-driven cancers. *J. Pathol.* **223**, 251–261 (2011).
11. C. D. Blanke, C. Rankin, G. D. Demetri, C. W. Ryan, M. von Mehren, R. S. Benjamin, A. K. Raymond, V. H. C. Bramwell, L. H. Baker, R. G. Maki, M. Tanaka, J. R. Hecht, M. C. Heinrich, C. D. M. Fletcher, J. J. Crowley, E. C. Borden, Phase III randomized, intergroup trial assessing imatinib mesylate at two dose levels in patients with unresectable or metastatic gastrointestinal stromal tumors expressing the kit receptor tyrosine kinase: S0033. *J. Clin. Oncol. Off. J. Am. Soc. Clin. Oncol.* **26**, 626–632 (2008).
12. M. C. Heinrich, R. G. Maki, C. L. Corless, C. R. Antonescu, A. Harlow, D. Griffith, A. Town, A. Mckinley, W.-B. Ou, J. A. Fletcher, C. D. M. Fletcher, X. Huang, D. P. Cohen, C. M. Baum, G. D. Demetri, Primary and secondary kinase genotypes correlate with the biological and clinical activity of sunitinib in imatinib-resistant gastrointestinal stromal tumor. *J. Clin. Oncol.* **26**, 5352–5359 (2008).
13. B. Liegl, I. Kepten, C. Le, M. Zhu, G. D. Demetri, M. C. Heinrich, C. D. M. Fletcher, C. L. Corless, J. A. Fletcher, Heterogeneity of kinase inhibitor resistance mechanisms in GIST. *J. Pathol.* **216**, 64–74 (2008).
14. M. C. Heinrich, C. L. Corless, A. Duensing, L. McGreevey, C.-J. Chen, N. Joseph, S. Singer, D. J. Griffith, A. Haley, A. Town, G. D. Demetri, C. D. M. Fletcher, J. A. Fletcher, *PDGFRA* activating mutations in gastrointestinal stromal tumors. *Science* **299**, 708–710 (2003).
15. S. Hirota, A. Ohashi, T. Nishida, K. Isozaki, K. Kinoshita, Y. Shinomura, Y. Kitamura, Gain-of-function mutations of platelet-derived growth factor receptor α gene in gastrointestinal stromal tumors. *Gastroenterology* **125**, 660–667 (2003).
16. P. A. Cassier, E. Fumagalli, P. Rutkowski, P. Schöffski, M. Van Glabbeke, M. Debiec-Rychter, J.-F. Emile, F. Duffaud, J. Martin-Broto, B. Landi, A. Adenis, F. Bertucci, E. Bompas, O. Bouché, S. Leyvraz, I. Judson, J. Verweij, P. Casali, J.-Y. Blay, P. Hohenberger; European Organisation for Research and Treatment of Cancer, Outcome of patients with platelet-derived growth factor receptor alpha–mutated gastrointestinal stromal tumors in the tyrosine kinase inhibitor era. *Clin. Cancer Res.* **18**, 4458–4464 (2012).
17. M. C. Heinrich, C. L. Corless, G. D. Demetri, C. D. Blanke, M. von Mehren, H. Joensuu, L. S. McGreevey, C.-J. Chen, A. D. Van den Abbeele, B. J. Druker, B. Kiese, B. Eisenberg, P. J. Roberts, S. Singer, C. D. M. Fletcher, S. Silberman, S. Dimitrijevic, J. A. Fletcher, Kinase mutations and imatinib response in patients with metastatic gastrointestinal stromal tumor. *J. Clin. Oncol. Off. J. Am. Soc. Clin. Oncol.* **21**, 4342–4349 (2003).
18. C. Yoo, M.-H. Ryu, J. Jo, I. Park, B.-Y. Ryoo, Y.-K. Kang, Efficacy of imatinib in patients with platelet-derived growth factor receptor alpha–mutated gastrointestinal stromal tumors. *Cancer Res. Treat.* **48**, 546–552 (2016).
19. T. Kristensen, H. Vestergaard, M. B. Møller, Improved detection of the *KIT* D816V mutation in patients with systemic mastocytosis using a quantitative and highly sensitive real-time qPCR assay. *J. Mol. Diagn.* **13**, 180–188 (2011).
20. A. C. Garcia-Montero, M. Jara-Acevedo, C. Teodosio, M. L. Sanchez, R. Nunez, A. Prados, I. Aldanondo, L. Sanchez, M. Dominguez, L. M. Botana, F. Sanchez-Jimenez, K. Sotlar, J. Almeida, L. Escribano, A. Orfao, *KIT* mutation in mast cells and other bone marrow hematopoietic cell lineages in systemic mast cell disorders: A prospective study of the Spanish Network on Mastocytosis (REMA) in a series of 113 patients. *Blood* **108**, 2366–2372 (2006).
21. A. Pardanani, T. L. Reeder, T. K. Kimlinger, J. Y. Baek, C.-Y. Li, J. H. Butterfield, A. Tefferi, Flt-3 and c-kit mutation studies in a spectrum of chronic myeloid disorders including systemic mast cell disease. *Leuk. Res.* **27**, 739–742 (2003).
22. J. Gotlib, H. C. Kluin-Nelemans, T. I. George, C. Akin, K. Sotlar, O. Hermine, F. T. Awan, E. Hexner, M. J. Mauro, D. W. Sternberg, M. Villeneuve, A. Huntsman Labed, E. J. Stanek, K. Hartmann, H.-P. Horny, P. Valent, A. Reiter, Efficacy and safety of midostaurin in advanced systemic mastocytosis. *N. Engl. J. Med.* **374**, 2530–2541 (2016).
23. J. Zhang, P. L. Yang, N. S. Gray, Targeting cancer with small molecule kinase inhibitors. *Nat. Rev. Cancer* **9**, 28–39 (2009).
24. C. D. Mol, D. R. Dougan, T. R. Schneider, R. J. Skene, M. L. Kraus, D. N. Scheibe, G. P. Snell, H. Zou, B.-C. Sang, K. P. Wilson, Structural basis for the autoinhibition and STI-571 inhibition of c-Kit tyrosine kinase. *J. Biol. Chem.* **279**, 31655–31663 (2004).
25. C. D. Mol, K. B. Lim, V. Sridhar, H. Zou, E. Y. T. Chien, B.-C. Sang, J. Nowakowski, D. B. Kassel, C. N. Cronin, D. E. McRee, Structure of a c-Kit product complex reveals the basis for kinase transactivation. *J. Biol. Chem.* **278**, 31461–31464 (2003).
26. K. S. Gajiwala, J. C. Wu, J. Christensen, G. D. Deshmukh, W. Diehl, J. P. DiNitto, J. M. English, M. J. Greig, Y.-A. He, S. L. Jacques, E. A. Lunney, M. McTigue, D. Molina, T. Quenzer, P. A. Wells, X. Yu, Y. Zhang, A. Zou, M. R. Emmett, A. G. Marshall, H.-M. Zhang, G. D. Demetri, KIT kinase mutants show unique mechanisms of drug resistance to imatinib and sunitinib in gastrointestinal stromal tumor patients. *Proc. Natl. Acad. Sci. U.S.A.* **106**, 1542–1547 (2009).
27. C. L. Corless, C. M. Barnett, M. C. Heinrich, Gastrointestinal stromal tumours: Origin and molecular oncology. *Nat. Rev. Cancer* **11**, 865–878 (2011).
28. E. Ben Ami, G. D. Demetri, A safety evaluation of imatinib mesylate in the treatment of gastrointestinal stromal tumor. *Expert Opin. Drug Saf.* **15**, 571–578 (2016).
29. M. C. Heinrich, D. Griffith, A. McKinley, J. Patterson, A. Presnell, A. Ramachandran, M. Debiec-Rychter, Crenolanib inhibits the drug-resistant PDGFRA D842V mutation associated with imatinib-resistant gastrointestinal stromal tumors. *Clin. Cancer Res.* **18**, 4375–4384 (2012).
30. M. Sundström, H. Vliagoftis, P. Karlberg, J. H. Butterfield, K. Nilsson, D. D. Metcalfe, G. Nilsson, Functional and phenotypic studies of two variants of a human mast cell line with a distinct set of mutations in the *c-kit* proto-oncogene. *Immunology* **108**, 89–97 (2003).
31. S. Demehri, A. Corbin, M. Loriaux, B. J. Druker, M. W. Deininger, Establishment of a murine model of aggressive systemic mastocytosis/mast cell leukemia. *Exp. Hematol.* **34**, 284–288 (2006).
32. A. Beghini, I. Magnani, C. B. Ripamonti, L. Larizza, Amplification of a novel c-Kit activating mutation Asn^{822}-Lys in the Kasumi-1 cell line: A t(8;21)-Kit mutant model for acute myeloid leukemia. *Hematol J.* **3**, 157–163 (2002).
33. M. M. Schittenhelm, S. Shiraga, A. Schroeder, A. S. Corbin, D. Griffith, F. Y. Lee, C. Bokemeyer, M. W. N. Deininger, B. J. Druker, M. C. Heinrich, Dasatinib (BMS-354825), a dual SRC/ABL kinase inhibitor, inhibits the kinase activity of wild-type, juxtamembrane, and activation loop mutant KIT isoforms associated with human malignancies. *Cancer Res.* **66**, 473–481 (2006).
34. S. Verstovsek, A. Tefferi, J. Cortes, S. O'Brien, G. Garcia-Manero, A. Pardanani, C. Akin, S. Faderl, T. Manshouri, D. Thomas, H. Kantarjian, Phase II study of dasatinib in Philadelphia chromosome–negative acute and chronic myeloid diseases, including systemic mastocytosis. *Clin. Cancer Res.* **14**, 3906–3915 (2008).
35. T. Van Looy, Y. K. Gebreyohannes, A. Wozniak, J. Cornillie, J. Wellens, H. Li, U. Vanleeuw, G. Floris, M. Debiec-Rychter, R. Sciot, P. Schöffski, Characterization and assessment of the sensitivity and resistance of a newly established human gastrointestinal stromal tumour xenograft model to treatment with tyrosine kinase inhibitors. *Clin. Sarcoma Res.* **4**, 10 (2014).
36. H. Joensuu, P. J. Roberts, M. Sarlomo-Rikala, L. C. Andersson, P. Tervahartiala, D. Tuveson, S. L. Silberman, R. Capdeville, S. Dimitrijevic, B. Druker, G. D. Demetri, Effect of the tyrosine kinase inhibitor STI571 in a patient with a metastatic gastrointestinal stromal tumor. *N. Engl. J. Med.* **344**, 1052–1056 (2001).
37. M. C. Heinrich, R. L. Jones, M. von Mehren, P. Schoffski, S. Bauer, O. Mir, P. A. Cassier, F. Eskens, H. Shi, T. Alvarez-Diez, O. Schmidt-Kittler, M. E. Healy, B. B. Wolf, S. George, Clinical activity of BLU-285 in advanced gastrointestinal stromal tumor (GIST). *J. Clin. Oncol. Off. J. Am. Soc. Clin. Oncol.* **35**, 11011 (2017).
38. M. W. Drummond, D. J. DeAngelo, M. W. Deininger, D. Radia, A. T. Quiery, E. O. Hexner, H. Shi, T. Alvarez-Diez, E. K. Evans, M. E. Healy, B. B. Wolf, S. Verstovsek, Preliminary safety and clinical activity in a phase 1 study of Blu-285, a potent, highly-selective inhibitor of KIT D816V in Advanced Systemic Mastocytosis (SM). *Blood* **128**, 477 (2016).
39. P. Schöffski, A. Wozniak, O. Schöffski, L. van Eycken, M. Debiec-Rychter, Overcoming cost implications of mutational analysis in patients with gastrointestinal stromal tumors: A pragmatic approach. *Oncol. Res. Treat.* **39**, 811–816 (2016).
40. M. I. Davis, J. P. Hunt, S. Herrgard, P. Ciceri, L. M. Wodicka, G. Pallares, M. Hocker, D. K. Treiber, P. P. Zarrinkar, Comprehensive analysis of kinase inhibitor selectivity. *Nat. Biotechnol.* **29**, 1046–1051 (2011).
41. J. H. Butterfield, D. Weiler, G. Dewald, G. J. Gleich, Establishment of an immature mast cell line from a patient with mast cell leukemia. *Leuk. Res.* **12**, 345–355 (1988).
42. T. Van Looy, A. Wozniak, G. Floris, R. Sciot, H. Li, J. Wellens, U. Vanleeuw, J. A. Fletcher, P. W. Manley, M. Debiec-Rychter, P. Schöffski, Phosphoinositide 3-kinase inhibitors combined with imatinib in patient-derived xenograft models of gastrointestinal stromal tumors: Rationale and efficacy. *Clin. Cancer Res.* **20**, 6071–6082 (2014).

Acknowledgments: We thank our colleagues at Blueprint Medicines for the thoughtful discussions and constructive feedback throughout the course of the BLU-285 program and for the critical review of the manuscript. We also thank the scientists at WuXi AppTec and CrownBio for their excellent in vivo study support and execution, A. Tsimboukis for the graphic design contributions, and all of the patients and their families, the doctors, and the nurses for their participation in the ongoing phase 1 clinical trials with BLU-285. **Funding:** This work was funded by Blueprint Medicines. In addition, contributions from the Heinrich laboratory were funded, in part, by a VA Merit Review grant (2I01BX000338-05) to M.C.H. **Author contributions:** E.K.E., A.K.G., J.L.K., and C.L. wrote and revised the manuscript. A.S. performed the enzymatic binding and activity assays. A.K.G., A.D., and X.J.Z. performed the cellular assays. B.L.H., D.W., K.W., L.D., Y.Z., J.L.K., N.B., N.L., and T.G. contributed to the design and synthesis of BLU-285. J.L.K. and N.B. provided the structural biology and computational chemistry insights to support BLU-285 generation. E.K.E., A.K.G., N.K., A.W., Y.K.G., and P.S. designed and performed the in vivo xenograft studies. T.P.L. and Y.K.G. performed immunohistochemistry analysis. M.C.H. contributed to the target engagement studies in CHO cells. A.B. and B.W. led the BLU-285 clinical trial design. D.J.D., P.S., and M.C.H. cared for the patients on BLU-285 trial. S.M. and O.S.-K. analyzed ctDNA from the clinical samples. **Competing interests:** E.K.E., A.K.G., J.L.K., B.L.H., A.D., X.J.Z., O.S.-K., D.W., K.W., N.B., T.P.L., S.M., B.W., T.G., N.L., A.B., and C.L. are current employees and shareholders of Blueprint Medicines. N.L. is a shareholder of Blueprint Medicines. Y.Z., B.L.H., J.L.K., K.W., and D.W. are inventors on patent WO2015/057873 held by Blueprint Medicines, which includes BLU-285. All other authors declare that they have no competing interests.

Submitted 23 June 2017
Accepted 2 October 2017
Published 1 November 2017
10.1126/scitranslmed.aao1690

Citation: E. K. Evans, A. K. Gardino, J. L. Kim, B. L. Hodous, A. Shutes, A. Davis, X. J. Zhu, O. Schmidt-Kittler, D. Wilson, K. Wilson, L. DiPietro, Y. Zhang, N. Brooijmans, T. P. LaBranche, A. Wozniak, Y. K. Gebreyohannes, P. Schöffski, M. C. Heinrich, D. J. DeAngelo, S. Miller, B. Wolf, N. Kohl, T. Guzi, N. Lydon, A. Boral, C. Lengauer, A precision therapy against cancers driven by *KIT/PDGFRA* mutations. *Sci. Transl. Med.* **9**, eaao1690 (2017).

Robotics for Science, Science for **Robotics**

Transforming the Future of Robotics in Research !

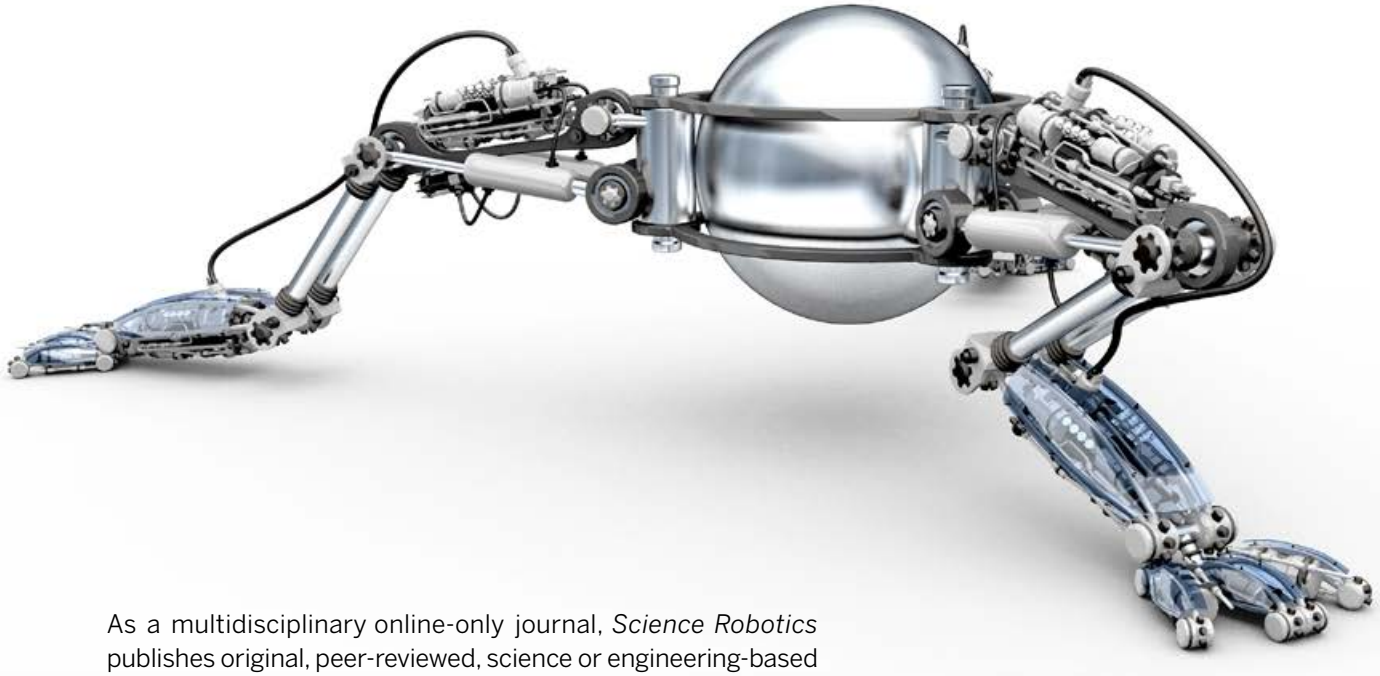

As a multidisciplinary online-only journal, *Science Robotics* publishes original, peer-reviewed, science or engineering-based research articles that advance the field of robotics. The journal provides a central forum for communication of new ideas, general principles, and original developments in research and field applications of robotics for all environments.

Science Robotics

AAAS

ScienceRobotics.org

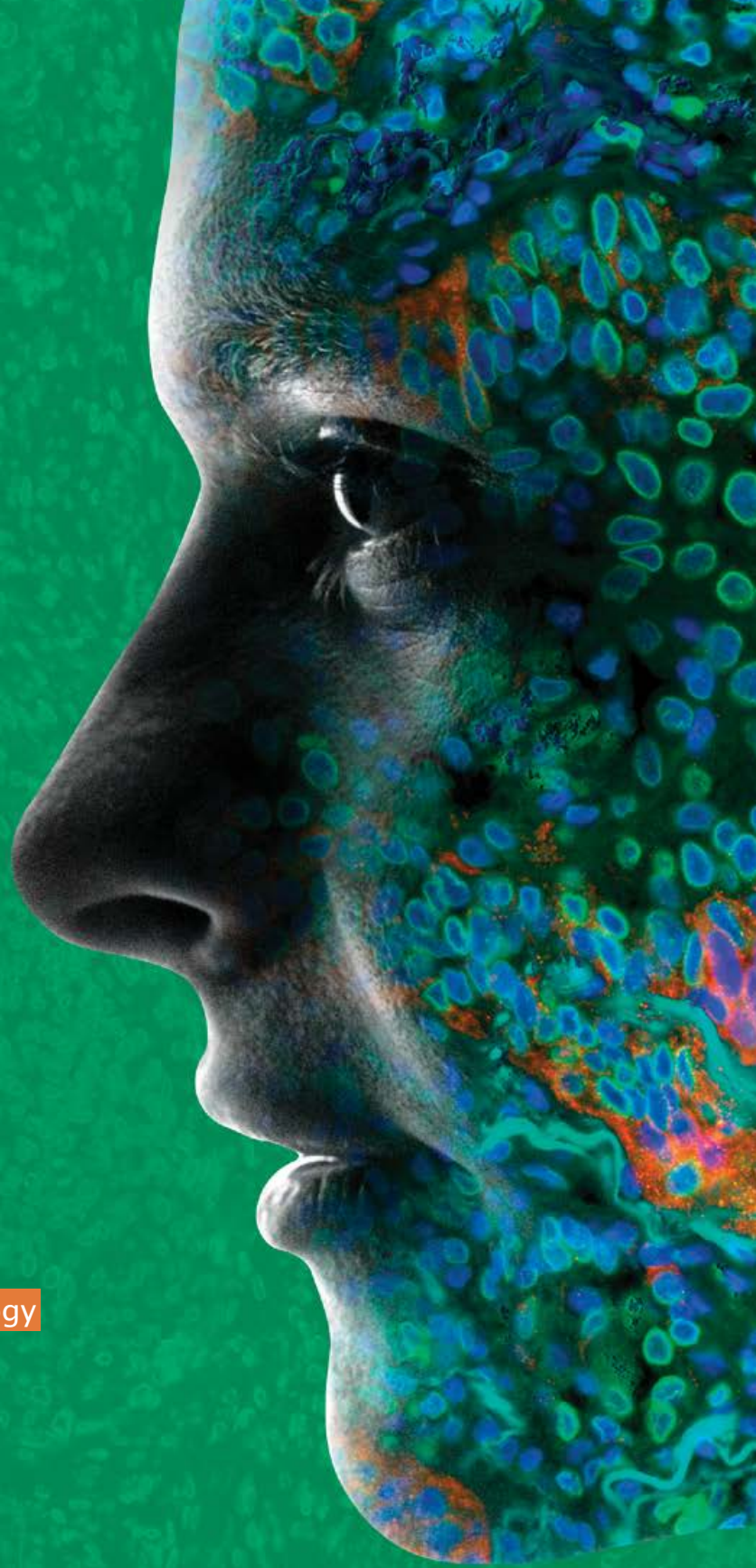

Light your way.

Get the full picture with trusted tumor immune response results from our in-house validated antibodies.

When it comes to your tumor immune response research, blind spots are unacceptable. Independent testing has demonstrated that 75% of antibodies in today's market are non-specific or simply do not work at all.* But at Bethyl, we've manufactured and validated every antibody we make on site to ensure target specificity and sensitivity. All to guarantee our antibodies will function as designed in your assay 100% of the time. More than 10,000 independent citations over the past 15 years have proven that, at Bethyl, we put a lot in every drop.

See our data at bethyl.com/immuno-oncology

**Weller, MG, Analytical Chemistry Insights:11, 21-27 (2016).*

Antibodies shown: Rabbit anti-PD-L1 (red, A700-020) & Lamin-A/C (green, A303-430A) in FFPE lung.
©2018 Bethyl Laboratories, Inc. All rights reserved.

BETHYL
LABORATORIES, INC

Really Good Antibodies